Clean electric cars pose a messy recycling puzzle p. 780

Reversible ketone-based redox flow batteries pp. 788 & 836

Touch feedback boosts brain-computer interface pp. 791 & 831

Science

$15
21 MAY 2021
sciencemag.org

AAAS



SYMBIOTIC FUNGUS

Mutual support by plant and fungus aided ancient move to land pp. 789 & 864

Gordon Research Conferences

Advancing the Frontiers of Science and a Commitment to Diversity

Did you know that GRC offers two diversity fellowship programs for eligible applicants?

The Carl Storm Underrepresented Minority Fellowship (CSURM)

This program was established by the GRC Board of Trustees to honor Director Emeritus Carl Storm's many years of service to GRC and to support his commitment to increasing diversity at the conferences. This fellowship program provides an opportunity for URM graduate students, postdocs, faculty and scientists to receive funding assistance to attend their first GRC.



The Carl Storm International Diversity Fellowship

This program was established by the GRC Board of Trustees to honor Director Emeritus Carl Storm's many years of service to GRC and to support his commitment to increasing diversity at the conferences. This fellowship program allows conference chairs to nominate graduate students and postdocs from China, Africa, India, Central America, South America, Russia, and Ukraine. Funding is available on a first-come, first-served basis.





Apply now for 2021 and 2022 conferences!
By completing a brief form, eligible applicants can obtain additional information about these funding opportunities!



Visit www.grc.org today!



Science shines amid COVID in 2020:

From artificial sun to quantum computers, scientists break through our toughest challenges with bravery and boldness

What is a breakthrough? Is a discovery occurring at a particular moment in time? Or is it a continuum of creativity? Perhaps breakthroughs should not be measured as single, momentous flashes of brilliance, but rather as a series of cascading challenges and solutions that lead to a better understanding of our world and ourselves. And when we escape this narrow definition of "breakthroughs," we can expand the borders of science and stretch our creativity.

The year 2020 saw the COVID-19 pandemic ravaging the world, attacking societies at their core and impacting economies in ways no one could ever imagine. As Ma Huateng–also known as Pony Ma, chairman of the board and CEO of Tencent–pointed out, "This reminds us that in the vastness of the cosmos, human knowledge of ourselves and nature is still limited, and only by relentlessly exploring the unknown can we better meet the challenges of the future. Scientists, like lighthouses illuminating the way forward, now bear an even more important mission for human explorations of nature, and a significant responsibility bestowed by our times."

30 years ago, *Science* began celebrating its annual Breakthrough of the Year, shining a bright light on the brilliance and bravery of ordinary humans engaging in the extraordinary. Here, we pay homage to this long tradition by highlighting breakthroughs that demonstrate ingenuity, often ignited under pressure. From new COVID-19 vaccines developed in record time to the discovery of the chemical agent that provokes locusts to swarm, to ambitious missions to the moon and Mars, one element of all these breakthroughs is clear: The problems were vexing, daunting, and dangerous even, but scientists and engineers welcomed the challenge. Working around the clock in high-stakes and sometimes treacherous conditions, our fellow humans didn't back down when systems and schedules broke down and problems broke out–they broke through and triumphed in the moment. Scientific discovery waits for no one, after all, and it certainly did not wait for the pandemic to dissipate.

The selected breakthroughs were sourced from the News team at *Science* with input from editors in the *Science*/AAAS Custom Publishing Office. A shortlist of topics was provided to Tencent–a world-leading Internet company and artificial intelligence leader, which leveraged its social, data, and analysis services and collected votes from over 1.58 million young users via Tencent Kandian and Tencent Penguin Tutoring. After fully gauging the interests of these teens, the editorial and news teams of *Science* chose the final 10 breakthrough topics.

Scientific breakthroughs in 2020 were breathtaking, considering the dynamic complexity of rallying teams and aligning resources during such an unpredictable and tumultuous time. Last year, we achieved quantum supremacy when a quantum computer completed a task in minutes that would have taken a conventional supercomputing system 2.5 billion years. We imaged individual atoms within proteins using cryo-electron microscopy (cryo-EM), a cutting-edge technique in structural biology. We discovered that our climate change mitigation efforts are working: The hole in the ozone layer is healing. We created the first living robots using stem cells from frog embryos and algorithms, and we demonstrated room-temperature superconductivity. We sent exciting missions to the moon and Mars. And perhaps most significantly, in less than a year, we developed and delivered vaccines for COVID-19, a spectacular feat that both tested and clarified the power of science, technology, engineering, and mathematics (STEM).

It is quite fitting that Tencent, one of the world's largest and most innovative firms, is joining hands with *Science* for this celebration. The company owns WeChat, a social media platform with over 1 billion users, and has a diverse presence across various sectors. Tencent is actively involved in nurturing and inspiring young minds to lead future STEM innovation.

Every endeavor, especially science and engineering research, requires bravery and an inexhaustible reservoir of resiliency and rock-solid capabilities in the face of seemingly insurmountable odds. These breakthroughs showcase everyday scientists who did extraordinary things as they overcame barriers and broke free of limitations, turning difficulties into opportunities and challenges into change.

Tencent 腾讯

IMAGE: © BARTLOMIEJ K. WROBLEWSKI/ SHUTTERSTOCK.COM

Cottrell Scholars 2021: the Future *of* Science

Research Corporation for Science Advancement, America's first foundation dedicated wholly to science, has named 25 early-career scholars in chemistry, physics, and astronomy as its 2021 Cottrell Scholars. Each awardee receives $100,000. Recipients are recognized for high-quality research, innovative educational initiatives, and academic leadership.

Three accomplished Cottrell Scholars (far right) further along in their careers have also received recognition for their achievements. The IMPACT Award is given for national impact in science through leadership and service. STAR Awards reward excellence in science teaching and research.

For additional information visit rescorp.org or call 520.571.1111.

Cottrell Scholar Awardees

1. Vinayak Agarwal, chemistry, Georgia Institute of Technology / Unlocking Marine Eukaryotic Natural Product Biosynthetic Schemes in Research and Education

2. Jeanine Amacher, chemistry, Western Washington University / Investigating Sortase Enzyme Activity and Specificity Using Natural Sequence Variation and Ancestral Sequence Reconstruction

3. Jeffrey Bandar, chemistry, Colorado State University / Salt-Promoted Electron Transfer Processes for Reductive Cross-Coupling Reactions

4. Rachel S. Bezanson, astronomy, University of Pittsburgh / Building Bridges in the Steel City: Leveraging the Nearby to Follow Galaxies Across Cosmic Time

5. Laura Blecha, physics, University of Florida / The Making of a Gravitational Wave Source: Probing the Role of Galaxy Assembly in Black Hole Binary and Triple Formation

6. Justin R. Caram, chemistry, University of California, Los Angeles / Chemical Physics Informed Design of SWIR Emissive Molecules

7. Joel F. Destino, chemistry, Creighton University / Bottoms Up: Investigating the Growth and Glass-Forming Properties of Germania-Containing Colloids

8. Daniela Fera, chemistry, Swarthmore College / Dissecting the Interactions and Conformations of Protein Kinases to Understand Biochemical Signaling

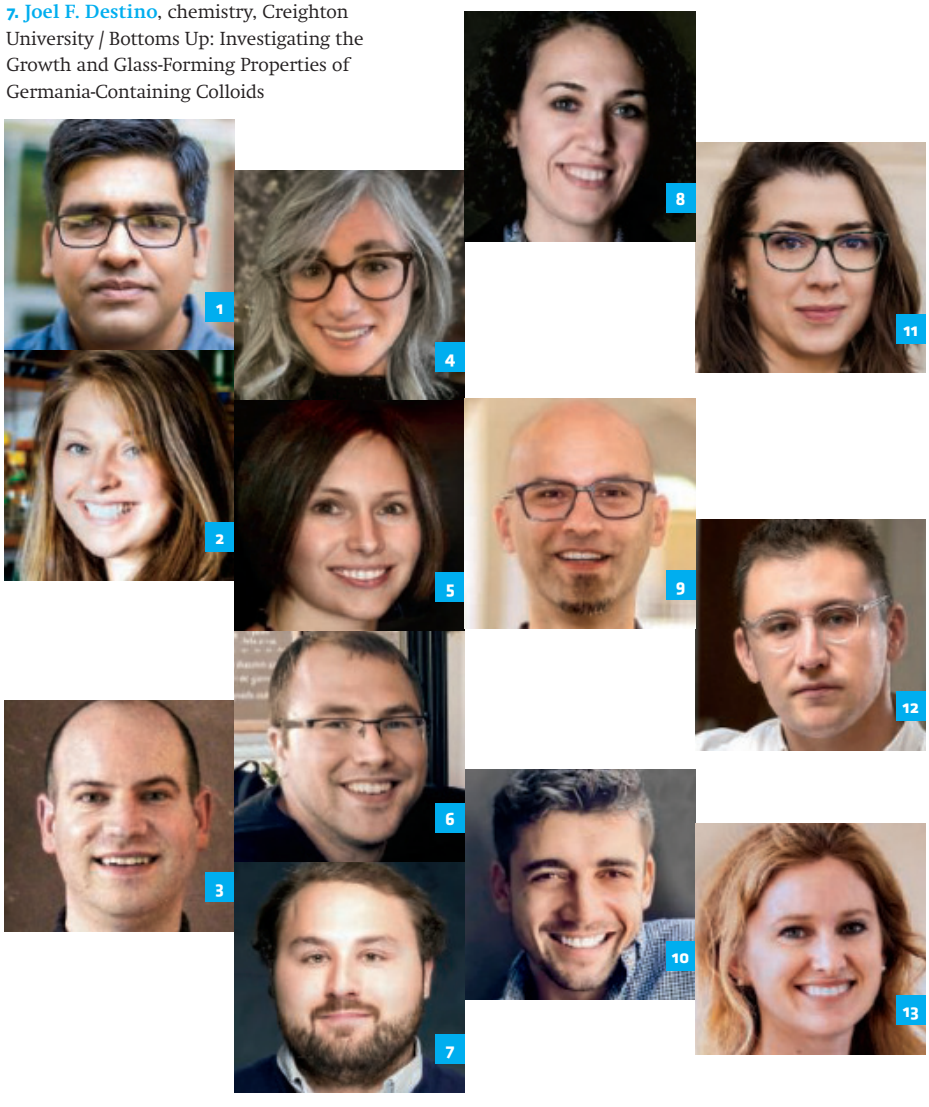
9. Alex Frañó, physics, University of California, San Diego / Creating Artificial Angstrom-scale Periodic Potentials Using X-ray Standing Waves and Enhancing Creativity in Physics Education

10. Thomas L. Gianetti, chemistry, University of Arizona / Developing a Photo-Rechargeable and Symmetrical Organic Redox Flow Battery

11. Natalie M. Gosnell, astronomy, Colorado College / Constraining the Complexities of Stellar Activity with Sub-Subgiant Stars

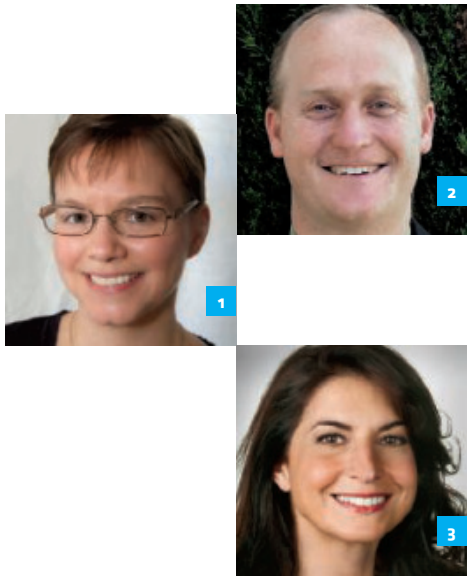
12. Christopher H. Hendon, chemistry, University of Oregon / Inorganic Defects in Metal-Organic Frameworks

13. Alexis C. Komor, chemistry, University of California, San Diego / Harnessing Precision Genome Editing Tools to Study DNA Repair Proteins in Live Cells



IMPACT and STAR Awardees

1. IMPACT awardee Penny Beuning, chemistry, Northeastern University / Cottrell Scholar 2009
2. STAR awardee Tim Clark, chemistry, University of San Diego / Cottrell Scholar 2007
3. STAR awardee Hanadi Sleiman, chemistry, McGill University / Cottrell Scholar 2002



14. Eli M. Levenson-Falk, physics, University of Southern California / Creating Custom Quantum Environments with Superconducting Circuits (For Beginners)
15. Rosario Porras-Aguilar, physics, University of North Carolina at Charlotte / Label-Free Reconfigurable Microscopy with High Specificity **16. Davit Potoyan**, chemistry, Iowa State University / Uncovering Principles of Bio-molecular Condensation: from Single Molecules to Cellular Organelles
17. Tyler D. Robinson, astronomy, Northern Arizona University / Understanding the True Utility of Prior Mass Constraints in Characterizing Exoplanet Atmospheres and Diversifying STEM at NAU
18. Brian J. Shuve, physics, Harvey Mudd College / Matter-Antimatter Asymmetry from Dark Matter Freeze-In **19. Marcelle Soares-Santos**, physics, University of Michigan / Cosmology with Merging Black Holes and Neutron Stars **20. Ruby May A. Sullan**, chemistry, University of Toronto – Scarborough / Multifunctional and Stimuli-Responsive Nanotherapeutic Platform for Targeted Disruption of Bacterial Biofilms

21. Alexandra Velian, chemistry, University of Washington / Synthesis of Functional Metal Chalcogenide Lattices Using Symmetry-Encoded, Atomically Precise Clusters **22. Rongsheng (Ross) Wang**, chemistry, Temple University / A Fluorine Displacement Based Bioorthogonal Labeling Approach to Interrogate Non-Histone Substrates of "Histone" Deacetylases
23. Leah S. Witus, chemistry, Macalester College / Investigation of Beta-Hairpin Hydrolytic Peptides and Development of an Advanced Undergraduate Scientific Communication Course
24. Joseph M. Zadrozny, chemistry, Colorado State University / Harnessing Ligand-Shell Nuclear Spins to Control Molecular Spin Coherence
25. Gail Zasowski, astronomy, University of Utah / Understanding the Chemical Enrichment of Our Universe: Unifying Evidence from the Milky Way and Other Galaxies



RESEARCH CORPORATION
for SCIENCE ADVANCEMENT
A foundation dedicated to science since 1912.

CONTENTS

21 MAY 2021
VOLUME 372
ISSUE 6544



780

NEWS

IN BRIEF

770 News at a glance

IN DEPTH

773 Blind spots thwart global coronavirus tracking
With sequencing concentrated in wealthy countries, variants can arise unseen
By M. Wadman

774 A psychedelic win raises questions for PTSD therapy
MDMA tested along with talk therapy, but the ideal pairing has yet to be studied
By K. Servick
PODCAST

776 Gene therapy that once led to tragedy scores success
Treatment reverses rare liver disease in small clinical trial, highlighting field's progress
By J. Kaiser

777 Bills giving NSF big budget boost gain traction
Two panels shrink size of proposed technology directorate as Senate debate begins *By J. Mervis*

778 Romania left out of high-powered laser project
Legal dispute mars international launch of Extreme Light Infrastructure in Eastern Europe *By E. Cartlidge*

779 China overhauls its public health bureaucracy
Early stumbles in pandemic response prompt new top-level agency to better handle future threats *By D. Normile*

FEATURES

780 A dead battery dilemma
With millions of electric vehicles set to hit the road, scientists are seeking better battery recycling methods *By I. Morse*

INSIGHTS

PERSPECTIVES

784 Emerging H5N8 avian influenza viruses
The global spread of H5N8 avian influenza viruses is a public health concern
By W. Shi and G. F. Gao

786 The growing challenge of vegetation change
Analysis of past change puts risks of plant carbon management in a long-term context
By J. T. Overpeck and D. D. Breshears
REPORT p. 860

788 Tanking up energy through atypical charging
Designed ketone molecules can undergo two-electron charge storage in aqueous solutions
By B. Hu and T. L. Liu
REPORT p. 836

789 Plant lipids enticed fungi to mutualism
Evolution of lipid transfer from plants to fungi allowed plants to colonize land
By H. J. Bouwmeester
REPORT p. 864

791 Putting touch into action
Bidirectional brain-machine interfaces boost movement restoration in a paralyzed user
By A. A. Faisal
REPORT p. 831

792 Putting a brake on hunger
Targeting activation of the melanocortin-4 receptor for weight loss in obesity
By S. Farooqi
RESEARCH ARTICLE p. 808

POLICY FORUM

794 The impact of early childhood interventions on mothers
Failure to measure the impacts on women's time and other maternal outcomes implicitly sets their value at zero *By D. K. Evans* et al.
PODCAST



784

PHOTOS: (TOP TO BOTTOM) ARGONNE NATIONAL LABORATORY; CHRISTIAN CHARISIUS/PICTURE-ALLIANCE/DPA/AP IMAGES



BOOKS *ET AL.*

798 What AI can learn from the biological brain
Brain development could hold lessons for building better artificial neural networks
By K. M. Jóźwik

799 Long live humankind
Data collection and analysis earn top spots among factors that have drastically increased life expectancy *By A. A. van Raalte*

LETTERS

801 Stop the decline of China's wild otters
By Q. Wei et al.

801 The Chinhai spiny newt needs a safer habitat
By A. Xu et al.

802 Green strategies for sustainable packaging
By S. You et al.

802 Errata

RESEARCH

IN BRIEF

803 From *Science* and other journals

REVIEW

806 Human evolution
Modern theories of human evolution foreshadowed by Darwin's *Descent of Man*
P. J. Richerson et al.
REVIEW SUMMARY; FOR FULL TEXT: DOI.ORG/10.1126/SCIENCE.ABA3776

RESEARCH ARTICLES

807 Neuroscience
Experience replay is associated with efficient nonlocal learning *Y. Liu* et al.
RESEARCH ARTICLE SUMMARY; FOR FULL TEXT: DOI.ORG/10.1126/SCIENCE.ABF1357

808 Structural biology
Structure reveals the activation mechanism of the MC4 receptor to initiate satiation signaling *H. Israeli* et al.
PERSPECTIVE p. 792

815 Coronavirus
Genomics and epidemiology of the P.1 SARS-CoV-2 lineage in Manaus, Brazil *N. R. Faria* et al.
REPORT p. 821

REPORTS

821 Coronavirus
Spatiotemporal pattern of COVID-19 spread in Brazil *M. C. Castro* et al.
RESEARCH ARTICLE p. 815

826 Electron microscopy
Electron ptychography achieves atomic-resolution limits set by lattice vibrations
Z. Chen et al.

831 Neuroscience
A brain-computer interface that evokes tactile sensations improves robotic arm control
S. N. Flesher et al.
PERSPECTIVE p. 791

836 Flow batteries
Reversible ketone hydrogenation and dehydrogenation for aqueous organic redox flow batteries *R. Feng* et al.
PERSPECTIVE p. 788

840 Translation
Imaging translation dynamics in live embryos reveals spatial heterogeneities *J. Dufourt* et al.

844 Quantum gases
Observation of superfluidity in a strongly correlated two-dimensional Fermi gas
L. Sobirey et al.

847 Organic chemistry
Photocatalytic C–H activation and the subtle role of chlorine radical complexation in reactivity *Q. Yang* et al.

852 Nanomaterials
Biphenylene network: A nonbenzenoid carbon allotrope *Q. Fan* et al.

856 Conservation
Balancing conservation priorities for nature and for people in Europe *L. M. J. O'Connor* et al.

860 Paleoecology
Global acceleration in rates of vegetation change over the past 18,000 years
O. Mottl et al.
PERSPECTIVE p. 786

864 Plant science
Lipid exchanges drove the evolution of mutualism during plant terrestrialization
M. K. Rich et al.
PERSPECTIVE p. 789

DEPARTMENTS

769 Editorial
"The Descent of Man," 150 years on
By Agustín Fuentes

874 Working Life
The problem with 'follow your dream'
By Ananya Sen

ON THE COVER

Confocal microscopy image of a symbiotic fungus (*Rhizophagus irregularis*) colonizing the tissues of the nonvascular plant *Marchantia paleacea* (plant cell walls, cyan; fungus, green; plant chloroplasts, red). Chloroplasts transfer atmospheric carbon, as lipids, from the plant to the fungus, thus feeding it. The fungus, in turn, provides nutrients and water to the plant. This symbiosis has supported terrestrial plants since they began colonizing dry land 450 million years ago. See pages 789 and 864. *Credit: Cécile Pouzet (FRAIB/CNRS)*



Science Staff 764
Science Careers 869

SCIENCE (ISSN 0036-8075) is published weekly on Friday, except last week in December, by the American Association for the Advancement of Science, 1200 New York Avenue, NW, Washington, DC 20005. Periodicals mail postage (publication No. 484460) paid at Washington, DC, and additional mailing offices.

Copyright © 2021 by the American Association for the Advancement of Science. The title SCIENCE is a registered trademark of the AAAS.

Domestic individual membership, including subscription (12 months): $165 ($74 allocated to subscription). Domestic institutional subscription (51 issues): $2148; Foreign postage extra: Air assist delivery: $98. First class, airmail, student, and emeritus rates on request. Canadian rates with GST available upon request, GST #125488122. Publications Mail Agreement Number 1069624. **Printed in the U.S.A.**
Change of address: Allow 4 weeks, giving old and new addresses and 8-digit account number. **Postmaster:** Send change of address to AAAS, P.O. Box 96178, Washington, DC 20090–6178. **Single-copy sales:** $15 each plus shipping and handling available from backissues.sciencemag.org; bulk rate on request. **Authorization to reproduce** material for internal or personal use under circumstances not falling within the fair use provisions of the Copyright Act can be obtained through the Copyright Clearance Center (CCC), www.copyright.com. The identification code for *Science* is 0036-8075. *Science* is indexed in the *Reader's Guide to Periodical Literature* and in several specialized indexes.

PHOTO: JURGEN AND CHRISTINE SOHNS/MINDEN PICTURES

Science AAAS

Editor-in-Chief Holden Thorp, hthorp@aaas.org

Executive Editor Monica M. Bradford

Editors, Research Valda Vinson, Jake S. Yeston **Editor, Insights** Lisa D. Chong

DEPUTY EDITORS Julia Fahrenkamp-Uppenbrink (UK), Stella M. Hurtley (UK), Phillip D. Szuromi, Sacha Vignieri **SR. EDITORIAL FELLOW** Andrew M. Sugden (UK) **SR. EDITORS** Gemma Alderton (UK), Caroline Ash (UK), Brent Grocholski, Pamela J. Hines, Di Jiang, Marc S. Lavine (Canada), Yevgeniya Nusinovich, Ian S. Osborne (UK), Beverly A. Purnell, L. Bryan Ray, H. Jesse Smith, Keith T. Smith (UK), Jelena Stajic, Peter Stern (UK), Valerie B. Thompson, Brad Wible, Laura M. Zahn **ASSOCIATE EDITORS** Michael A. Funk, Priscilla N. Kelly, Tage S. Rai, Seth Thomas Scanlon (UK), Yury V. Suleymanov **LETTERS EDITOR** Jennifer Sills **LEAD CONTENT PRODUCTION EDITORS** Harry Jach, Lauren Kmec **CONTENT PRODUCTION EDITORS** Amelia Beyna, Jeffrey E. Cook, Chris Filiatreau, Julia Katris, Nida Masiulis, Suzanne M. White **SR. EDITORIAL COORDINATORS** Carolyn Kyle, Beverly Shields **EDITORIAL COORDINATORS** Aneera Dobbins, Joi S. Granger, Jeffrey Hearn, Lisa Johnson, Maryrose Madrid, Ope Martins, Shannon McMahon, Jerry Richardson, Hilary Stewart (UK), Alana Warnke, Alice Whaley (UK), Anita Wynn **PUBLICATIONS ASSISTANTS** Jeremy Dow, Alexander Kief, Ronmel Navas, Brian White **EXECUTIVE ASSISTANT** Jessica Slater **ASI DIRECTOR, OPERATIONS** Janet Clements (UK) **ASI SR. OFFICE ADMINISTRATOR** Jessica Waldock (UK)

News Editor Tim Appenzeller

NEWS MANAGING EDITOR John Travis **INTERNATIONAL EDITOR** Martin Enserink **DEPUTY NEWS EDITORS** Elizabeth Culotta, Lila Guterman, David Grimm, Eric Hand (Europe), David Malakoff **SR. CORRESPONDENTS** Daniel Clery (UK), Jon Cohen, Jeffrey Mervis, Elizabeth Pennisi **ASSOCIATE EDITORS** Jeffrey Brainard, Catherine Matacic **NEWS REPORTERS** Adrian Cho, Jennifer Couzin-Frankel, Jocelyn Kaiser, Rodrigo Pérez Ortega (Mexico City), Kelly Servick, Robert F. Service, Erik Stokstad, Paul Voosen, Meredith Wadman **INTERN** Sofia Moutinho **CONTRIBUTING CORRESPONDENTS** Warren Cornwall, Andrew Curry (Berlin), Ann Gibbons, Sam Kean, Eli Kintisch, Kai Kupferschmidt (Berlin), Andrew Lawler, Mitch Leslie, Eliot Marshall, Virginia Morell, Dennis Normile (Tokyo), Elisabeth Pain (Careers), Charles Piller, Michael Price, Tania Rabesandratana (Barcelona), Joshua Sokol, Emily Underwood, Gretchen Vogel (Berlin), Lizzie Wade (Mexico City) **CAREERS** Donisha Adams, Rachel Bernstein (Editor), Katie Langin (Associate Editor) **COPY EDITORS** Julia Cole (Senior Copy Editor), Cyra Master (Copy Chief) **ADMINISTRATIVE SUPPORT** Meagan Weiland

Creative Director Beth Rakouskas

DESIGN MANAGING EDITOR Marcy Atarod **GRAPHICS MANAGING EDITOR** Alberto Cuadra **PHOTOGRAPHY MANAGING EDITOR** William Douthitt **WEB CONTENT STRATEGY MANAGER** Kara Estelle-Powers **MULTIMEDIA MANAGING PRODUCER** Joel Goldberg **DESIGN EDITOR** Chrystal Smith **DESIGNER** Christina Aycock **GRAPHICS EDITOR** Nirja Desai **INTERACTIVE GRAPHICS EDITOR** Kelly Franklin **SENIOR SCIENTIFIC ILLUSTRATORS** Valerie Altounian, Chris Bickel **SENIOR GRAPHICS SPECIALISTS** Holly Bishop, Nathalie Cary **SENIOR PHOTO EDITOR** Emily Petersen **PHOTO EDITOR** Kaitlyn Dolan **WEB DESIGNER** Jennie Pajerowski **SOCIAL MEDIA STRATEGIST** Jessica Hubbard **VIDEO PRODUCER** Meagan Cantwell **SENIOR PODCAST PRODUCER** Sarah Crespi

Chief Executive Officer and Executive Publisher Sudip Parikh

Publisher, Science Family of Journals Bill Moran

DIRECTOR, BUSINESS SYSTEMS AND FINANCIAL ANALYSIS Randy Yi **DIRECTOR, BUSINESS OPERATIONS & ANALYSIS** Eric Knott **DIRECTOR OF ANALYTICS** Enrique Gonzales **MANAGER, BUSINESS OPERATIONS** Jessica Tierney **SENIOR BUSINESS ANALYST** Cory Lipman, Meron Kebede **FINANCIAL ANALYST** Alexander Lee **ADVERTISING SYSTEM ADMINISTRATOR** Tina Burks **SENIOR SALES COORDINATOR** Shirley Young **DIGITAL/PRINT STRATEGY MANAGER** Jason Hillman **SENIOR MANAGER, PUBLISHING AND CONTENT SYSTEMS** Marcus Spiegler **ASSISTANT MANAGER DIGITAL/PRINT** Rebecca Doshi **SENIOR CONTENT SPECIALISTS** Steve Forrester, Jacob Hedrick, Antoinette Hodal, Lori Murphy **PRODUCTION SPECIALIST** Kristin Wowk **DIGITAL PRODUCTION MANAGER** Lisa Stanford **CONTENT SPECIALIST** Kimberley Oster **ADVERTISING PRODUCTION OPERATIONS MANAGER** Deborah Tompkins **DESIGNER, CUSTOM PUBLISHING** Jeremy Huntsinger **SR. TRAFFIC ASSOCIATE** Christine Hall **SPECIAL PROJECTS ASSOCIATE** Sarah Dhere

ASSOCIATE DIRECTOR, BUSINESS DEVELOPMENT Justin Sawyers **GLOBAL MARKETING MANAGER** Allison Pritchard **DIGITAL MARKETING MANAGER** Aimee Aponte **JOURNALS MARKETING MANAGER** Shawana Arnold **MARKETING ASSOCIATES** Tori Velasquez, Mike Romano, Ashley Hylton **DIGITAL MARKETING SPECIALIST** Asleigh Rojanavongse **SENIOR DESIGNER** Kim Huynh

DIRECTOR AND SENIOR EDITOR, CUSTOM PUBLISHING Sean Sanders **ASSISTANT EDITOR, CUSTOM PUBLISHING** Jackie Oberst

DIRECTOR, PRODUCT & PUBLISHING DEVELOPMENT Chris Reid **DIRECTOR, BUSINESS STRATEGY AND PORTFOLIO MANAGEMENT** Sarah Whalen **ASSOCIATE DIRECTOR, PRODUCT MANAGMENT** Kris Bishop **PRODUCT DEVELOPMENT MANAGER** Scott Chernoff **PUBLISHING TECHNOLOGY MANAGER** Michael Di Natale **SR. PRODUCT ASSOCIATE** Robert Koepke **SPJ ASSOCIATE** Samantha Bruno Fuller

DIRECTOR, INSTITUTIONAL LICENSING Iquo Edim **ASSOCIATE DIRECTOR, RESEARCH & DEVELOPMENT** Elisabeth Leonard **MARKETING MANAGER** Kess Knight **SENIOR INSTITUTIONAL LICENSING MANAGER** Ryan Rexroth **INSTITUTIONAL LICENSING MANAGER** Marco Castellan **MANAGER, AGENT RELATIONS & CUSTOMER SUCCESS** Judy Lillibridge **SENIOR OPERATIONS ANALYST** Lana Guz **FULFILLMENT COORDINATOR** Melody Stringer **SALES COORDINATOR** Josh Haverlock

DIRECTOR, GLOBAL SALES Tracy Holmes **US EAST COAST AND MID WEST SALES** Stephanie O'Connor **US WEST COAST SALES** Lynne Stickrod **US SALES MANAGER, SCIENCE CAREERS** Claudia Paulsen-Young **US SALES REP, SCIENCE CAREERS** Tracy Anderson **ASSOCIATE DIRECTOR, ROW** Roger Goncalves **SALES REP, ROW** Sarah Lelarge **SALES ADMIN ASSISTANT, ROW** Bryony Cousins **DIRECTOR OF GLOBAL COLLABORATION AND ACADEMIC PUBLISHING RELATIONS, ASIA** Xiaoying Chu **ASSOCIATE DIRECTOR, INTERNATIONAL COLLABORATION** Grace Yao **SALES MANAGER** Danny Zhao **MARKETING MANAGER** Kilo Lan **ASCA CORPORATION, JAPAN** Kaoru Sasaki (Tokyo), Miyuki Tani (Osaka) **COLLABORATION/CUSTOM PUBLICATIONS/JAPAN** Adarsh Sandhu

DIRECTOR, COPYRIGHT, LICENSING AND SPECIAL PROJECTS Emilie David **RIGHTS AND LICENSING COORDINATOR** Jessica Adams **RIGHTS AND PERMISSIONS ASSOCIATE** Elizabeth Sandler **CONTRACTS AND LICENSING ASSOCIATE** Lili Catlett

MAIN HEADQUARTERS
Science/AAAS
1200 New York Ave. NW
Washington, DC 20005

SCIENCE INTERNATIONAL
Clarendon House
Clarendon Road
Cambridge, CB2 8FH, UK

SCIENCE CHINA
Room 1004, Culture Square
No. 59 Zhongguancun St.
Haidian District, Beijing, 100872

SCIENCE JAPAN
ASCA Corporation
Sibaura TY Bldg. 4F, 1-14-5
Shibaura Minato-ku
Tokyo, 108-0073 Japan

EDITORIAL
science_editors@aaas.org

NEWS
science_news@aaas.org

INFORMATION FOR AUTHORS
sciencemag.org/authors/science-information-authors

REPRINTS AND PERMISSIONS
sciencemag.org/help/reprints-and-permissions

MEDIA CONTACTS
scipak@aaas.org

MULTIMEDIA CONTACTS
SciencePodcast@aaas.org
ScienceVideo@aaas.org

INSTITUTIONAL SALES AND SITE LICENSES
sciencemag.org/librarian

PRODUCT ADVERTISING & CUSTOM PUBLISHING
advertising.sciencemag.org/products-services
science_advertising@aaas.org

CLASSIFIED ADVERTISING
advertising.sciencemag.org/science-careers
advertise@sciencecareers.org

JOB POSTING CUSTOMER SERVICE
employers.sciencecareers.org
support@sciencecareers.org

MEMBERSHIP AND INDIVIDUAL SUBSCRIPTIONS
sciencemag.org/subscriptions

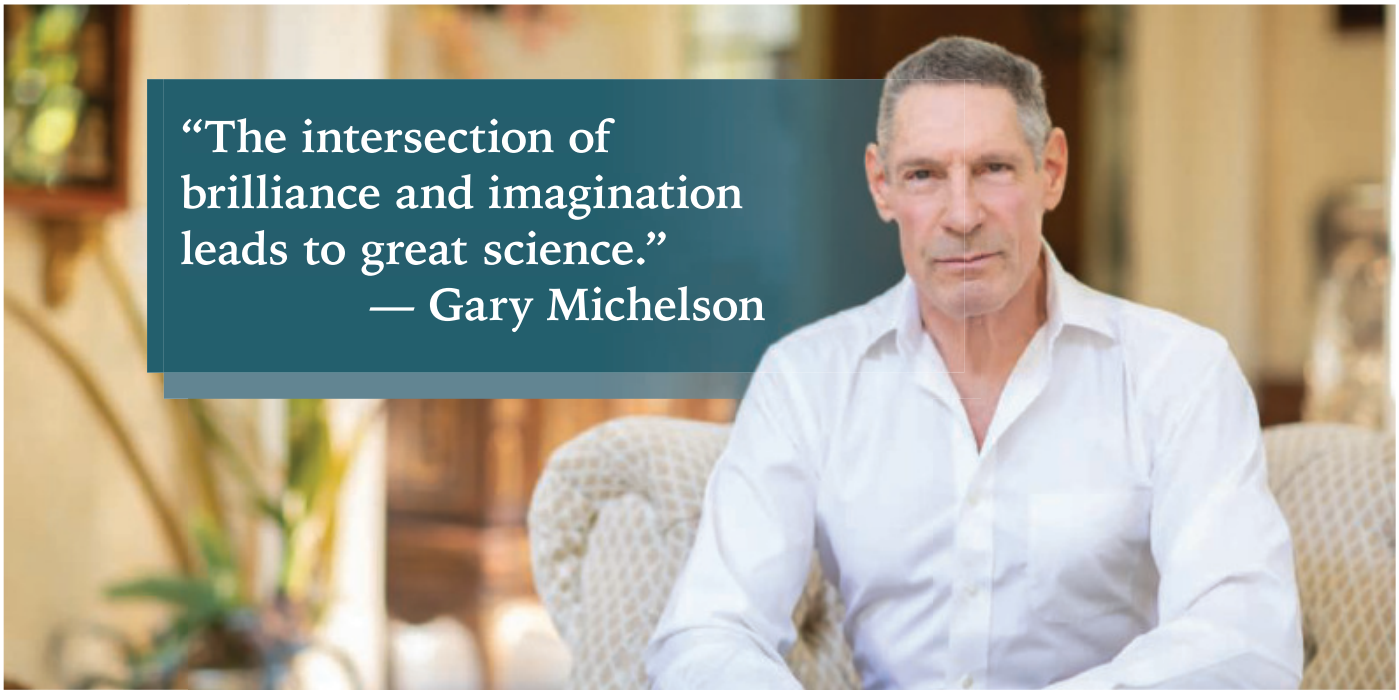
MEMBER BENEFITS
aaas.org/membercentral

AAAS BOARD OF DIRECTORS
CHAIR Claire M. Fraser
PRESIDENT Susan G. Amara
PRESIDENT-ELECT Gilda A. Barabino
TREASURER Carolyn N. Ainslie
CHIEF EXECUTIVE OFFICER Sudip Parikh
BOARD Cynthia M. Beall, Rosina M. Bierbaum, Ann Bostrom, Janine Austin Clayton, Laura H. Greene, Kaye Husbands Fealing, Maria M. Klawe, Robert B. Millard, William D. Provine

BOARD OF REVIEWING EDITORS (Statistics board members indicated with **(S)**)

Erin Adams, *U. of Chicago*
Takuzo Aida, *U. of Tokyo*
Leslie Aiello, *Wenner-Gren Foundation*
Deji Akinwande, *UT Austin*
Judith Allen, *U. of Manchester*
Marcella Alsan, *Harvard U.*
Sebastian Amigorena, *Institut Curie*
James Analytis, *UC Berkeley*
Trevor Archer, *NIEHS, NIH*
Paola Arlotta, *Harvard U.*
David Awschalom, *U. of Chicago*
Clare Baker, *U. of Cambridge*
Delia Baldassarri, *NYU*
Nenad Ban, *ETH Zürich*
Nandita Basu, *U. of Waterloo*
Franz Bauer, *Pontificia U. Católica de Chile*
Ray H. Baughman, *UT Dallas*
Carlo Beenakker, *Leiden U.*
Yasmine Belkaid, *NIAID, NIH*
Philip Benfey, *Duke U.*
Kiros T. Berhane, *Columbia U.*
Bradley Bernstein, *Mass. General Hospital*
Joseph J. Berry, *NREL*
Alessandra Biffi, *Harvard Med.*
Chris Bowler, *École Normale Supérieure*
Ian Boyd, *U. of St. Andrews*
Emily Brodsky, *UC Santa Cruz*
Ron Brookmeyer, *UCLA* **(S)**
Christian Büchel, *UKE Hamburg*
Dennis Burton, *Scripps Res.*
Carter Tribley Butts, *UC Irvine*
György Buzsáki, *NYU School of Med.*
Mariana Byndloss, *Vanderbilt U. Med. Ctr*
Annmarie Carlton, *UC Irvine*
Ling-Ling Chen, *SIBCB, CAS*
M. Keith Chen, *UCLA*
Zhijian Chen, *UT Southwestern Med. Ctr.*
Ib Chorkendorff, *Denmark TU*
Amander Clark, *UCLA*
James J. Collins, *MIT*
Robert Cook-Deegan, *Arizona State U.*
Virginia Cornish *Columbia U.*
Carolyn Coyne, *Duke U.*
Roberta Croce, *VU Amsterdam*
Ismaila Dabo, *Penn State U.*
Jeff L. Dangl, *UNC*
Chiara Daraio, *Caltech*
Nicolas Dauphas, *U. of Chicago*
Christian Davenport, *U. of Michigan*
Frans de Waal, *Emory U.*
Claude Desplan, *NYU*
Sandra Díaz, *U. Nacional de Córdoba*
Ulrike Diebold, *TU Wien*
Stefanie Dimmeler, *Goethe-U. Frankfurt*
Hong Ding, *Inst. of Physics, CAS*
Dennis Discher, *UPenn*
Jennifer A. Doudna, *UC Berkeley*
Ruth Drdla-Schutting, *Med. U. Vienna*
Raissa M. D'Souza, *UC Davis*
Bruce Dunn, *UCLA*
William Dunphy, *Caltech*
Scott Edwards, *Harvard U.*
Todd Ehlers, *U. of Tübingen*
Jennifer Elisseeff, *Johns Hopkins U.*
Andrea Encalada, *U. San Francisco de Quito*
Nader Engheta, *U. of Penn.*
Karen Ersche, *U. of Cambridge*
Beate Escher, *UFZ & U. of Tübingen*
Barry Everitt, *U. of Cambridge*
Vanessa Ezenwa, *U. of Georgia*
Michael Feuer, *GWU*
Toren Finkel, *U. of Pitt. Med. Ctr.*
Gwenn Flowers, *Simon Fraser U.*
Peter Fratzl, *Max Planck Inst. Potsdam*
Elaine Fuchs, *Rockefeller U.*
Jay Gallagher, *U. of Wisconsin*
Daniel Geschwind, *UCLA*
Ramon Gonzalez, *U. of South Florida*
Sandra González-Bailón, *UPenn*
Nicolas Gruber, *ETH Zürich*
Hua Guo, *U. of New Mexico*
Taekjip Ha, *Johns Hopkins U.*
Sharon Hammes-Schiffer, *Yale U.*
Wolf-Dietrich Hardt, *ETH Zürich*
Louise Harra, *U. Coll. London*
Jian He, *Clemson U.*
Carl-Philipp Heisenberg, *IST Austria*
Ykä Helariutta, *U. of Cambridge*
Janet G. Hering, *Eawag*
Heather Hickman, *NIAID, NIH*
Hans Hilgenkamp, *U. of Twente*
Kai-Uwe Hinrichs, *U. of Bremen*
Deirdre Hollingsworth, *U. of Oxford*
Randall Hulet, *Rice U.*
Auke Ijspeert, *EPFL*
Akiko Iwasaki, *Yale U.*
Stephen Jackson, *USGS & U. of Arizona*
Erich Jarvis, *Rockefeller U.*
Peter Jonas, *IST Austria*
Matt Kaeberlein, *U. of Wash.*
William Kaelin Jr., *Dana-Farber Cancer Inst.*
Daniel Kammen, *UC Berkeley*
V. Narry Kim, *Seoul Nat. U.*
Robert Kingston, *Harvard Med.*
Nancy Knowlton, *Smithsonian Institution*
Etienne Koechlin, *École Normale Supérieure*
Alex L. Kolodkin, *Johns Hopkins U.*
Julija Krupic, *U. of Cambridge*
Paul Kubes, *U. of Calgary*
Gabriel Lander, *Scripps Res.* **(S)**
Mitchell A. Lazar, *UPenn*
Wendell Lim, *UCSF*
Luis Liz-Marzán, *CIC biomaGUNE*
Omar Lizardo, *UCLA*
Jonathan Losos, *Wash. U. in St. Louis*
Ke Lu, *Inst. of Metal Res., CAS*
Christian Lüscher, *U. of Geneva*
Jean Lynch-Stieglitz, *Georgia Inst. of Tech.*
David Lyons, *U. of Edinburgh*
Fabienne Mackay, *QIMR Berghofer*
Anne Magurran, *U. of St. Andrews*
Asifa Majid, *U. of York*
Oscar Marín, *King's Coll. London*
Charles Marshall, *UC Berkeley*
Christopher Marx, *U. of Idaho*
David Masopust, *U. of Minnesota*
Geraldine Masson, *CNRS*
Jason Matheny, *Georgetown U.*
Heidi McBride, *McGill U.*
C. Robertson McClung, *Dartmouth*
Rodrigo Medellín, *U. Nacional Autónoma de México*
Jane Memmott, *U. of Bristol*
C. Jessica Metcalf, *Princeton U.*
Baoxia Mi, *UC Berkeley*
Tom Misteli, *NCI, NIH*
Alison Motsinger-Reif, *NIEHS, NIH* **(S)**
Suresh Naidu, *Columbia U.*
Danielle Navarro, *U. of New South Wales*
Daniel Nettle, *Newcastle U.*
Daniel Neumark, *UC Berkeley*
Beatriz Noheda, *U. of Groningen*
Helga Nowotny, *Vienna Sci., Res. & Tech. Fund*
Rachel O'Reilly, *U. of Birmingham*
Pilar Ossorio, *U. of Wisconsin*
Andrew Oswald, *U. of Warwick*
Isabella Pagano, *Istituto Nazionale di Astrofisica*
Elizabeth Levy Paluck, *Princeton U.*
Jane Parker, *Max Planck Inst. Cologne*
Giovanni Parmigiani, *Dana-Farber Cancer Inst.* **(S)**
Daniel Pauly, *U. of British Columbia*
Ana Pêgo, *U. do Porto*
Samuel Pfaff, *Salk Inst.*
Julie Pfeiffer, *UT Southwestern Med. Ctr.*
Philip Phillips, *UIUC*
Matthieu Piel, *Institut Curie*
Kathrin Plath, *UCLA*
Martin Plenio, *Ulm U.*
Katherine Pollard, *UCSF*
Elvira Poloczanska, *Alfred-Wegener-Inst.*
Julia Pongratz, *Ludwig Maximilians U.*
Philippe Poulin, *CNRS*
Jonathan Pritchard, *Stanford U.*
Lei Stanley Qi, *Stanford U.*
Trevor Robbins, *U. of Cambridge*
Joeri Rogelj, *Imperial Coll. London*
Amy Rosenzweig, *Northwestern U.*
Mike Ryan, *UT Austin*
Miquel Salmeron, *Lawrence Berkeley Nat. Lab*
Nitin Samarth, *Penn State U.*
Erica Ollmann Saphire, *La Jolla Inst.*
Joachim Saur, *U. zu Köln*
Alexander Schier, *Harvard U.*
Wolfram Schlenker, *Columbia U.*
Susannah Scott, *UC Santa Barbara*
Anuj Shah, *U. of Chicago*
Vladimir Shalaev, *Purdue U.*
Jie Shan, *Cornell U.*
Beth Shapiro, *UC Santa Cruz*
Jay Shendure, *U. of Wash.*
Steve Sherwood, *U. of New South Wales*
Brian Shoichet, *UCSF*
Robert Siliciano, *JHU School of Med.*
Lucia Sivilotti, *U. Coll. London*
Alison Smith, *John Innes Centre*
Richard Smith, *UNC* **(S)**
Mark Smyth, *QIMR Berghofer*
John Speakman, *U. of Aberdeen*
Tara Spires-Jones, *U. of Edinburgh*
Allan C. Spradling, *Carnegie Institution for Sci.*
V. S. Subrahmanian, *Dartmouth*
Ira Tabas, *Columbia U.*
Eriko Takano, *U. of Manchester*
Patrick Tan, *Duke-NUS Med. School*
Sarah Teichmann, *Wellcome Sanger Inst.*
Rocio Titiunik, *Princeton U.*
Shubha Tole, *Tata Inst. of Fundamental Res.*
Maria-Elena Torres Padilla, *Helmholtz Zentrum München*
Kimani Toussaint, *Brown U.*
Wim van der Putten, *Netherlands Inst. of Ecology*
Henrique Veiga-Fernandes, *Champalimaud Fdn*
Reinhilde Veugelers, *KU Leuven*
Bert Vogelstein, *Johns Hopkins U.*
David Wallach, *Weizmann Inst.*
Jane-Ling Wang, *UC Davis* **(S)**
Jessica Ware, *Amer. Mus. of Natural Hist.*
David Waxman, *Fudan U.*
Chris Wikle, *U. of Missouri* **(S)**
Terrie Williams, *UC Santa Cruz*
Ian A. Wilson, *Scripps Res.* **(S)**
Yu Xie, *Princeton U.*
Jan Zaanen, *Leiden U.*
Kenneth Zaret, *UPenn School of Med.*
Bing Zhu, *Inst. of Biophysics, CAS*
Xiaowei Zhuang, *Harvard U.*
Maria Zuber, *MIT*

Science serves as a forum for discussion of important issues related to the advancement of science by publishing material on which a consensus has been reached as well as including the presentation of minority or conflicting points of view. Accordingly, all articles published in *Science*—including editorials, news and comment, and book reviews—are signed and reflect the individual views of the authors and not official points of view adopted by AAAS or the institutions with which the authors are affiliated.



Inventor and philanthropist Gary Michelson invests big in scientific research

Designed to fund early-career scientists at the peak of their creativity and inventiveness, Michelson Prizes and research grants underwrite bold, blue-sky ideas.

In 2018, when Laura Mackay and Ansuman Satpathy met as two fellow winners of the Michelson Medical Research Foundation's Next Generation Grants, the scientific connection was immediately apparent for these two researchers from opposite ends of the Pacific Ocean.

Mackay, an immunologist from the University of Melbourne in Australia, studies tissue-resident memory T cells—unique immune cells that sit within the site of a past infection to stand guard as sentinels. Satpathy, an immunologist from Stanford University in Palo Alto, California, had developed a suite of high-throughput genomic technologies to characterize immune cells. Over research presentations and meals at the Michelson Prizes symposium, the two realized that Satpathy's technologies could help crack the code of what makes Mackay's favorite cells tick—and a collaboration was born.

"Fast forward to now, and this is one of my favorite collaborations—it wouldn't have happened without us meeting," says Mackay. Their partnership is just one example of how Michelson Prizes are catalysts for research breakthroughs by creative early-career scientists with innovative ideas.

Funding leaps, not increments

The career of Michelson Medical Research Foundation founder Gary Michelson, a now-retired orthopedic surgeon and inventor, was characterized by taking risks with innovative thinking that paid off in a big way.

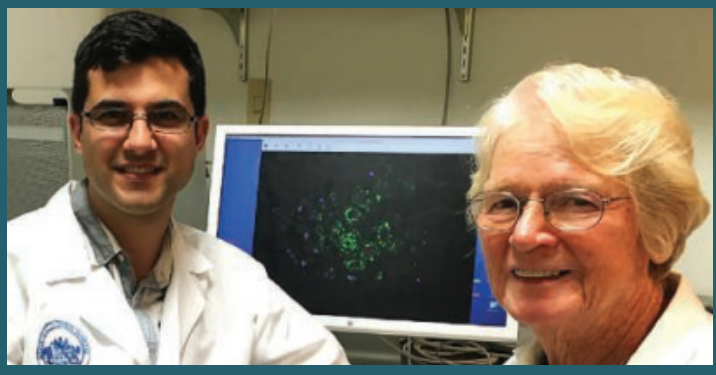
Now he is applying those same principles to philanthropic investment in medical research. "Great science is not incremental. Great science leaps!" he says. "Go big. Or go home," he adds with a smile.

Michelson and his foundations are channeling those principles, along with financial support, into the careers and innovations of early-career researchers—those aged 35 or younger—through a program of prizes and research grants. The overarching goal is to elevate these researchers' career trajectories and to catalyze pathways that are high-risk, but also potentially high-reward.

History shows that significant scientific discoveries often leap from the mind of a single person—usually before the age of 35—as is the case with about 85% of Nobel prizewinners in the sciences, says Michelson from his home in Los Angeles. He sees gaps in traditional biomedical research funding that philanthropies can help fill.

"We had the desire to identify the most brilliant scientists under 35 and to fund research that was too bold and daring to achieve traditional funding," he explains when recalling

PHOTOS: PROVIDED BY MICHELSON PHILANTHROPIES



Funding pie-in-the-sky ideas

Reproductive biologists Patricia Donahoe (right) and David Pépin know the power of winning a Michelson grant to fuel research, the significance of which might otherwise have been missed. While studying Mullerian inhibiting substance (MIS) for its antiovarian cancer effects in mice, they made a serendipitous finding about its potential use as a powerful contraceptive. While delivering high doses of MIS to female mice harboring transplanted human ovarian cancers, Pépin noticed that the mouse ovaries were very small. Upon further investigation, the substance appeared to arrest the ovulation process at a point far upstream from where traditional steroid hormone–based contraception works.

A colleague urged them to contact the Michelson Found Animals Foundation, which has an ongoing award contest of USD 25 million for anyone who develops a single-injection, lifetime contraceptive that would work in domestic pets, both cats and dogs. Donahoe and Pépin won a 3-year, USD 750,000 initial grant from Michelson in 2015 to study their MIS contraceptive idea in mice, and have since received continuations bringing their total award to over USD 1.5 million.

"We were criticized and could not obtain traditional sources of funding for this work" because the idea was considered risky, says Donahoe, director of the Pediatric Surgical Research Laboratories at Massachusetts General Hospital in Boston, where Pépin is an assistant professor. She notes that translational research in reproduction and contraception generally remains underfunded. "We could never have pursued this research without the funding from the Michelson Foundation."

The team went on to show that with a single dose of MIS delivered to mice by gene therapy, they could produce complete contraception for the lifetime of the female mice. They have since tested the technology in rats and cats, and are beginning a study in dogs. The work has implications not only as an alternative to invasive surgeries for pet contraception but also for reversible human contraception and for preserving fertility in women undergoing chemotherapy or enhancing fertility treatments.

As a surgeon, Donahoe sees the importance of collaborations between clinicians and Ph.D. researchers for advancing medical research like this. "Philanthropic funding for laboratories is extraordinarily important–without it, fundamental advances and their translation to clinical applications could be missed."

the establishment of the Michelson Prizes in 2017. The Michelson Prizes take an unconventional approach, akin to a venture capital model, by investing starter funding in a handful of promising young scientists' ideas. The Prizes also value disruptive concepts and inventive processes.

"The intersection of brilliance and imagination leads to great science, and early-career researchers are at their peak energy level—passionate, innovative. They color outside of the lines and take chances," Michelson says. "For all those reasons, they are excellent people to invest in."

Both Satpathy and Mackay won Michelson Prizes for their work in the field of immunology. The program is administered in partnership with the Human Vaccines Project, a nonprofit global consortium based in New York and dedicated to decoding the human immune system and harnessing immune responses for disease prevention and medical cures.

"COVID-19 shined a light on how poorly we understand the human immune system," says Wayne Koff, president and CEO of the Human Vaccines Project, noting that immune responses to COVID ranged from asymptomatic and mild disease to severe and fatal disease. Both Koff and Michelson see the human immune system as the "common denominator" to solving medical problems as diverse as cancer, infectious disease, Alzheimer's disease, and aging.

The USD 150,000 **Michelson Next Generation Grants** seek to support emerging investigators with transformative ideas that are applicable across many different diseases. The 2021 funding round will make awards in two research areas: (1) tackling challenges to successful vaccine development and expanding understanding of immune processes; and (2) expanding understanding of the effects of climate change on immune function, with a focus on research that contributes to vaccine and immunotherapy development. The deadline to apply is June 18, 2021 (for more information, go to www.humanvaccinesproject.org/MichelsonPrizes).

"We are not looking for the next influenza vaccine, but rather gene editing in the immunology space, or the application of a new artificial intelligence [AI] model, or a revolutionary protein engineering method," says Koff. The awards are designed to help launch fledgling research ideas so they can reach their full potential and lay foundations for further

PHOTOS: PROVIDED BY MICHELSON PHILANTHROPIES



(L to R) Wayne Koff, Laura Mackay, and Ansuman Satpathy

funding. The awards also stimulate collaborations such as the one between the Satpathy and Mackay labs.

Immunology investments

Satpathy won the Michelson Prize at a critical juncture, when he was a postdoctoral fellow and hoping to establish an independent laboratory that would marry his interests in immunology and genomic technologies.

"The research funding gave me the bandwidth and freedom to pursue my most ambitious ideas," he says. But, he adds, the recognition and the network of colleagues that the Prize opened up were even more valuable. "The scientific network is way more important when working at the interface of two disciplines, or [when trying] to bring new knowledge into your lab or to bounce ideas off of established experts."

Now an assistant professor of pathology at Stanford University School of Medicine, Satpathy uses high-throughput, single-cell genomics tools to understand the molecular regulators of immune cells. His work could reveal the key molecular switches guiding the responses of immune cells in conjunction with cancer immunotherapies.

Mackay used her Michelson Prize to study the basic biology of tissue-resident memory T cells, or TRM cells. After an infection of the skin or organs such as the liver, TRMs remain embedded to guard against another infection. She wanted to know how TRMs protect against infections, how researchers could enhance TRM generation in the body, and which molecular pathways would make them long-lasting. Her work could lead to ways to engineer TRMs into powerful disease fighters.

"The Prize gave me a boost at exactly the time I needed it," says Mackay. "The visibility of an international award and the funding to do high-risk science was incredible." She recently earned early tenure at the Peter Doherty Institute for Infection and Immunity in Melbourne after just 5 years in her independent position.

Championing early-career investigators

"Philanthropy offers a lifeline for young scientists," says Mackay, who notes that many talented early-career researchers can get swept out of the system.

Now, a new Michelson partnership with AAAS/*Science* will offer more visibility and opportunity for young researchers. The USD 30,000 **Michelson Philanthropies & *Science* Prize for Immunology** will be given for transformative work achieved in the past 3 years by an early-career researcher in the broad field of immunology, including within a variety of cross-cutting disciplines such as AI, protein engineering, bioinformatics, nanotechnology, and tropical medicine, to name a few.

"Like AAAS/*Science*, Michelson Philanthropies believes in recognizing and supporting researchers in what may be the most critical phase of their career," says Bill Moran, publisher of the *Science* family of journals.

Michelson's wife Alya cochairs the Michelson Philanthropies group of foundations. They are members of the Giving Pledge, the group created by Bill Gates and Warren Buffett that comprises billionaires committed to giving the majority of their wealth to philanthropy.

Together, the Michelsons have dedicated a significant portion of their philanthropy to medical research because it offers the greatest return to society, both economically and in terms of easing human suffering.

Their investment in Satpathy's high-risk ideas has already appreciated—and is appreciated—in significant ways: "There's a high likelihood that the research won't work out, but the foundation supported me sticking through it and continuing onto the next project," Satpathy says. "That's empowering to a young researcher."

Sponsored by

MICHELSON
PHILANTHROPIES

PHOTOS: PROVIDED BY MICHELSON PHILANTHROPIES

RECENT PHD IN MOLECULAR MEDICINE?

Gain international recognition, win 30,000 USD, and have your thesis essay published in Science.

The Science & SciLifeLab Prize for Young Scientists is a global prize aimed at rewarding scientists at an early stage of their careers, awarded in four categories.

Research in molecular medicine aims at building on the molecular understanding of disease in humans to develop preventive, diagnostic and therapeutic approaches, including individualized medicine.

Entrants for the 2021 prize must have received their PhD after January 1, 2019.

APPLY FOR THE *SCIENCE* & SCILIFELAB PRIZE FOR YOUNG SCIENTISTS

APPLY BEFORE JULY 15, 2021

SCIENCEPRIZE.SCILIFELAB.SE

Science & SciLifeLab PRIZE For Young Scientists

Science AAAS

SciLifeLab

Knut och Alice Wallenbergs Stiftelse

EDITORIAL

"The Descent of Man," 150 years on



Agustín Fuentes is a professor of anthropology at Princeton University, Princeton, NJ, USA. afuentes2@princeton.edu

In 1871, Charles Darwin tackled "the highest and most interesting problem for the naturalist…the descent of man." Challenging the status quo, Darwin deployed natural and sexual selection, and his recently adopted "survival of the fittest," producing scenarios for the emergence of humankind. He explored evolutionary histories, anatomy, mental abilities, cultural capacities, race, and sex differences. Some conclusions were innovative and insightful. His recognition that differences between humans and other animals were of degree, not of kind, was trailblazing. His focus on cooperation, social learning, and cumulative culture remains core to human evolutionary studies. However, some of Darwin's other assertions were dismally, and dangerously, wrong. "Descent" is a text from which to learn, but not to venerate.

Darwin saw humans as part of the natural world, animals that evolved (descended) from ancestral primates according to processes and patterns similar for all life. For Darwin, to know the human body and mind, we must know other animals and their (and our) descent with modification across lineages and time. But despite these ideal frames and some innovative inferences, "Descent" is often problematic, prejudiced, and injurious. Darwin thought he was relying on data, objectivity, and scientific thinking in describing human evolutionary outcomes. But for much of the book, he was not. "Descent," like so many of the scientific tomes of Darwin's day, offers a racist and sexist view of humanity.

> "'Descent' is a text from which to learn, but not to venerate."

Darwin portrayed Indigenous peoples of the Americas and Australia as less than Europeans in capacity and behavior. Peoples of the African continent were consistently referred to as cognitively depauperate, less capable, and of a lower rank than other races. These assertions are confounding because in "Descent" Darwin offered refutation of natural selection as the process differentiating races, noting that traits used to characterize them appeared nonfunctional relative to capacity for success. As a scientist this should have given him pause, yet he still, baselessly, asserted evolutionary differences between races. He went beyond simple racial rankings, offering justification of empire and colonialism, and genocide, through "survival of the fittest." This too is confounding given Darwin's robust stance against slavery.

In "Descent," Darwin identified women as less capable than (White) men, often akin to the "lower races." He described man as more courageous, energetic, inventive, and intelligent, invoking natural and sexual selection as justification, despite the lack of concrete data and biological assessment. His adamant assertions about the centrality of male agency and the passivity of the female in evolutionary processes, for humans and across the animal world, resonate with both Victorian and contemporary misogyny.

In Darwin's own life he learned from an African-descendant South American naturalist, John Edmonstone in Edinburgh, and experienced substantive relations with the Fuegians aboard the *HMS Beagle*. His daughter Henrietta was a key editor of "Descent." Darwin was a perceptive scientist whose views on race and sex should have been more influenced by data and his own lived experience. But Darwin's racist and sexist beliefs, echoing the views of scientific colleagues and his society, were powerful mediators of his perception of reality.

Today, students are taught Darwin as the "father of evolutionary theory," a genius scientist. They should also be taught Darwin as an English man with injurious and unfounded prejudices that warped his view of data and experience. Racists, sexists, and white supremacists, some of them academics, use concepts and statements "validated" by their presence in "Descent" as support for erroneous beliefs, and the public accepts much of it uncritically.

"The Descent of Man" is one of the most influential books in the history of human evolutionary science. We can acknowledge Darwin for key insights but must push against his unfounded and harmful assertions. Reflecting on "Descent" today one can look to data demonstrating unequivocally that race is not a valid description of human biological variation, that there is no biological coherence to "male" and "female" brains or any simplicity in biological patterns related to gender and sex, and that "survival of the fittest" does not accurately represent the dynamics of evolutionary processes. The scientific community can reject the legacy of bias and harm in the evolutionary sciences by recognizing, and acting on, the need for diverse voices and making inclusive practices central to evolutionary inquiry. In the end, learning from "Descent" illuminates the highest and most interesting problem for human evolutionary studies today: moving toward an evolutionary science of humans instead of "man."

–Agustín Fuentes

PHOTO: AAAS

10.1126/science.abj4606

NEWS

> “The real waste—when the vaccine is readily available to anyone who wants it—is a life lost to COVID-19.”
>
> **Ohio Governor Mike DeWine,** about criticism of the state’s novel incentive for people to get COVID-19 vaccinations: a drawing to award $1 million in state funds to each of five vaccinated people.

IN BRIEF

Edited by
Jeffrey Brainard



Tourists visited the Lincoln Memorial the day after the federal government relaxed its guidance on wearing masks.

PHOTO: JIM WATSON/AFP/GETTY IMAGES

COVID-19

CDC loosens mask guidance, drawing praise and flak

Scientists and physicians gave mixed reviews to the abrupt relaxation of masking guidance by the U.S. Centers for Disease Control and Prevention (CDC) last week. Some applauded, but others criticized the agency’s advice that fully vaccinated people no longer need to wear masks indoors or outdoors, with some exceptions. “CDC’s been great in ’21, but on this one they declared victory too early,” tweeted Bob Wachter, chair of medicine at the University of California, San Francisco. But the Infectious Diseases Society of America Foundation said: “We support the CDC recommendations, which are based on the latest scientific evidence.” Critics noted that CDC’s guidance relies on unvaccinated people to wear masks, but many already ignore the precaution. With only 38% of the country fully vaccinated, this places a large number of people at high risk, they argued. Defending the agency’s decision, CDC Director Rochelle Walensky cited declining COVID-19 case counts and new evidence of vaccines’ high effectiveness in preventing symptomatic and asymptomatic disease. She also noted that the three vaccines authorized for use in the United States have proved effective against several coronavirus variants circulating there.

Japan’s pandemic response lags

PUBLIC HEALTH | Two months before the scheduled start of the Olympic Games in Tokyo, COVID-19 cases are rising steeply in Japan while immunization is moving at a glacial pace, and calls are growing for the government to cancel the games. Japan’s more than 683,000 cases of COVID-19 and 11,500 deaths are better than in many other countries, but scientists say officials lifted a succession of lenient lockdowns prematurely. Meanwhile less than 2% of the population is fully vaccinated. Critics blame the lagging inoculation rate partly on regulations requiring time-consuming additional studies of Japanese subjects for vaccines proved efficacious elsewhere. So

far, only the vaccine made by Pfizer and BioNTech has gained approval. Because of staffing shortages and logistical problems, the country of 126 million people has reportedly used only 25% or less of the vaccine doses it has imported. Recent polls indicate that 60% to 80% of Japanese support canceling the Olympic Games, but the government says they will go ahead as planned, without overseas spectators. A decision on allowing domestic ones has been delayed until June.

China's rover reaches Mars safely

PLANETARY SCIENCE | China on 15 May became the second country, after the United States, to land a spacecraft on Mars and have it survive, state media reported. The Tianwen-1 lander fell through the thin air, using parachutes and retrorockets to land softly. Its six-wheeled rover, named Zhurong after a mythical god of fire, was expected to roll off the lander platform this week and operate for about 90 days. Scientists expect 13 instruments, split between the rover and an orbiter, to yield insights into Mars's geology, atmosphere, weather, and magnetic field. The rover carries a ground-penetrating radar that may spot subsurface permafrost, a clue to stores of water that could have once hosted life.

1918 pandemic yields new clues

VIROLOGY | Century-old tissue specimens stored in formalin have offered scientists new clues about the early evolution of the virus that caused the devastating 1918–19 influenza pandemic. In a lung sample from a young woman who died in Munich at some point in 1918, enough snippets of viral RNA were found to piece together the virus' entire genome, researchers write in a preprint posted on bioRxiv on 14 May. It's only the third fully sequenced virus from the pandemic, and the first from outside North America. The team also assembled partial viral genomes using samples from two young German soldiers who both succumbed to the flu in Berlin on 27 June 1918, during the pandemic's first wave. Scientists have speculated that the virus originated in birds and became better adapted to humans by the second, more lethal wave that swept the planet in the fall of 1918; the new study offers clues that support that view. "It's absolutely fantastic work," says Hendrik Poinar, who runs an ancient DNA lab at McMaster University. As more groups gain the technical expertise to do these difficult reconstructions, he says, "you'll see an explosion of ancient viral genomes from these sorts of collections."

PHOTO: BENEDEK/ISTOCK.COM



One of Earth's hottest recorded surface temperatures was in Arizona's Sonoran Desert.

METEOROLOGY

Death Valley dethroned as world's hottest place

A hunt for Earth's hottest spot has ended in an improbable tie between two deserts hemmed in by heat-trapping mountains. Surface temperatures in the Lut Desert in Iran and the Sonoran Desert along the Mexican-U.S. border recently topped out at a sizzling 80.8°C, about 10° hotter than the previous high. Based on readings from NASA satellites, Lut hit its all-time high in 2018, a record the Sonoran matched the next summer, Yunxia Zhao of the University of California, Irvine, and colleagues reported on 10 May in the *Bulletin of the American Meteorological Society*. That's bad news for desert creatures being pushed to the edge of their heat tolerances, says ecologist David Mildrexler of Eastern Oregon Legacy Lands. By tradition, meteorologists base official heat records only on ground thermometers that measure air temperatures in the shade, and so Earth's official heat record, although disputed, remains a reading of 56.7°C in California's Death Valley in 1913.

Cosmic ray factories revealed

ASTROPHYSICS | Using an observatory on the edge of the Tibetan Plateau, astronomers have spotted the highest energy light ever, gamma ray photons up to 1.4 petaelectronvolts. They traced these extreme photons back to 12 likely sources in the Milky Way Galaxy, including the supernova remnant at the heart of the Crab nebula and, surprisingly, a nursery of baby stars, the research team reports this week in *Nature*. Cosmic rays are charged particles, including protons and other atomic nuclei, which have been accelerated to nearly the speed of light. Their sources have been poorly understood because interstellar magnetic fields bend them on their path to Earth. However, the rays emit gamma rays that follow a straight path, which astronomers can detect indirectly and trace to their origin. The new results come from data collected at China's Large High Altitude Air Shower Observatory during its first year of operation. Once completed with additional detectors, the observatory could help theorists understand how the cosmic ray sources generate such high-energy light.

Financial ties mar clinical advice

MEDICINE | Many medical societies and agencies aren't following decade-old guidance to tamp down conflicts of interest (COIs) among experts who write standards for patient care, an analysis has found. At issue are "clinical practice guidelines," which often synthesize research findings and recommend certain treatments, and which many physicians follow closely. In 2011, the U.S. Institute of Medicine urged steps including that those crafting the guidelines—in cardiology, radiology, and other fields—disclose COIs and divest themselves of relevant financial investments. But many organizations have not adopted such policies, says a review of 46 professional societies and government groups, including the U.S. Centers for Disease Control and Prevention, published in April in *PLOS ONE*. Of the 36 organizations with a publicly available COI policy

for those writing clinical guidelines, 92% did require COI disclosure. But only five required guideline authors to eliminate relevant financial ties. Several required authors with conflicts to recuse themselves from developing or voting on guidelines about relevant issues.

Hopkins gets big gift for diversity

PHILANTHROPY | Billionaire Michael Bloomberg will donate $150 million to Johns Hopkins University and six other institutions to increase the number of Ph.D. students from groups underrepresented in science, the university announced last week. The gift, one of the largest of its kind to any university, will fund about 100 Hopkins students who graduated from historically Black colleges. The gift was announced months after a Hopkins research team reported that the institution's founder, 19th century entrepreneur Johns Hopkins, who historically has been called an abolitionist, held enslaved people in his home. In the 21st century, the institution has struggled with diversity: From 2011 to 2019, just 4% of 2860 Ph.D. students in all fields identified as Black. The new funding will also allow undergraduates access to summer and postbaccalaureate opportunities for education and research at Hopkins. "Johns Hopkins now has the opportunity and imperative to … act ambitiously to begin correcting the longstanding inequity in Ph.D. education," said its president, Ronald Daniels, in a statement.

First nuke forged quasicrystal

MINERALOGY | On 16 July 1945, in Alamogordo, New Mexico, the predawn sky lit up "with the brightness of 20 Suns," as one observer put it, as the first nuclear weapon test released the equivalent of 21 kilotons of TNT—creating a new era, and a rare material. A shock wave and 1500°C heat fused iron, lead, and copper from equipment at the site with sand, creating red "trinitite" glass that rained from the sky. Now, researchers report this week in the *Proceedings of the National Academy of Sciences* that some of the red trinitite contained the first ever humanmade quasicrystals. These exotic minerals possess a nonrepeating arrangement of atoms, unlike in ordinary crystals. In other locations, scientists have also found naturally occurring quasicrystals created by heat and pressure from meteorite impacts.

Trump cost-benefit rule reversed

REGULATION | Continuing its efforts to erase industry-friendly rules adopted by former President Donald Trump, the Biden administration last week said it would repeal a rule that had altered how the U.S. Environmental Protection Agency (EPA) calculated the costs and benefits of air pollution regulations. Critics said the rule made it easier for industry groups to challenge new federal regulations because it required EPA to justify them based only on the benefits produced directly by pollution limits, ignoring any indirect "co-benefits"—for example, a reduction in dangerous soot particles caused by limits on other air pollutants. Co-benefits had greatly boosted the estimated overall gains from some air pollution regulations. Current EPA Administrator Michael Regan said revoking the Trump rule was part of the new administration's "commitment to science."

U.S. to license more pot growers

BIOMEDICINE | The Drug Enforcement Administration (DEA) said last week it will soon end the University of Mississippi's 53-year monopoly on supplying marijuana for U.S. research and give licenses to several other growing facilities. The action came after U.S. medical researchers sued DEA, seeking a larger supply of genetically diverse cannabis to explore its value for treating conditions including post-traumatic stress disorder and chronic pain. Under regulations published in December 2020 and processes outlined by DEA in a memo last week to growers, the agency will purchase the cannabis from growers and provide it to researchers, although in some cases growers will supply small amounts directly to labs. Although consuming marijuana is legal for medical purposes in 36 states and for recreational use in 17 states, possession remains a criminal offense under federal law.



In 2020, Chile's voters backed writing a new constitution, following months of protests against inequality.

PHOTO: MARTIN BERNETTI/AFP/GETTY IMAGES

DEMOCRACY

Scientists will help rewrite Chile's constitution

At least two scientists will take part in drafting a new national constitution for Chile, replacing the current, dictatorship-era document with a charter crafted by a citizen assembly. Nearly 20 people with backgrounds in science and research were on the ballot in an election held 15–16 May for representatives to a constitutional convention; the winners include microbiologist Cristina Dorador of the University of Antofagasta and epidemiologist María Elisa Quinteros Cáceres of the University of Talca. The constitution drafted by the convention will be put to a national vote in 2022. Scientists in Chile say they want the document to recognize the importance of scientific evidence in creating policy, encourage more government spending on research, and expand access to affordable education and health care.

SCIENCEMAG.ORG/NEWS
Read more news from *Science* online.



Testing for COVID-19 at Johannesburg's airport in January. A variant of concern that arose in South Africa has spread around the world.

PHOTO: GUILLEM SARTORIO/BLOOMBERG/GETTY IMAGES

IN DEPTH

COVID-19

Blind spots thwart global coronavirus tracking

With sequencing concentrated in wealthy countries, variants can arise unseen

By **Meredith Wadman**

Last month, Gytis Dudas was tracking a concerning new coronavirus variant that had triggered an outbreak of COVID-19 in his native Lithuania and appeared sporadically elsewhere in Europe and in the United States. Exploring an international database of coronavirus genomes, Dudas found a crucial clue: One sample of the new SARS-CoV-2 variant came from a person who had recently flown to France from Cameroon. A collaborator, Guy Baele of KU Leuven, soon identified six more viral sequences from people in Europe who had traveled there from Cameroon. But then their quest to pinpoint the variant's origins hit a wall: Cameroon had only uploaded 48 viral genomes to the global sequence repository called GISAID. None included the variant.

Science's COVID-19 reporting is supported by the Heising-Simons Foundation.

With dogged legwork, Baele and Dudas, an evolutionary biologist at the Gothenburg Global Biodiversity Centre, learned another team had gathered as-yet-unpublished sequences from a COVID-19 outbreak among staff at a great ape program in the Central African Republic—near the Cameroonian border. Six people there carried the new variant.

Baele, Dudas, and their colleagues reconstructed the variant's evolutionary tree and geographic spread, and concluded that it most likely arose in Cameroon, as they reported in a preprint on 8 May. They note that the variant carries a suite of mutations seen in other "variants of concern" that are more infectious or dangerous.

"It looked like the typical thing that should raise all red flags," says Sébastien Calvignac-Spencer, an evolutionary biologist at the Robert Koch Institute whose team sequenced samples from the ape station. But Cameroon and neighboring countries, where the team inferred the variant might already be prevalent, had been blind to it.

The researchers say the story of this variant, designated B.1.620, holds a warning for the world: "The sequencing effort in Cameroon and other African countries is not enough," says coauthor Ahidjo Ayouba, a biologist at the French National Research Institute for Sustainable Development at the University of Montpellier. He is traveling to his native Cameroon next month to set up the country's first next-generation sequencer. The emergence of new variants with deleterious mutations in countries with no regular sequencing "may become an alarming norm," the researchers caution in their preprint.

It is not just Africa. Of 152 countries for which data were available as of 10 May, 100 had uploaded sequence data to GISAID for less than 1% of their reported cases (see map, p. 774). Among those, 51 countries, including large nations such as India, Indonesia, Russia, and Brazil, had uploaded sequences for less than 0.1% of cases. Ten wealthy nations accounted for 82% of the more than 1.4 million sequences in GISAID's database. "We are working to change that," says Frank Konings, leader of the World Health Organization's (WHO's) Virus Evolution Working Group.

Most countries with scarce sequencing also currently have little or no access to vaccines, and some have severe outbreaks. As the virus replicates unchecked, those regions can become breeding grounds for new mutants, which can then spread around the world. India, for example, is coping with a world-leading surge of cases. On 11 May, WHO labeled the new variant B.1.617, which arose in India and has spread to dozens of countries, a variant of concern. "Where the pandemic is currently unchecked is where we can expect that variants are on the rise," Dudas says. "It would be much more interesting to sequence the last 1000 cases in

the Central African Republic than the next 100,000 cases in Germany."

Globally, the obstacles to systematic surveillance are daunting. State-of-the-art sequencers cost $335,000, and local scientists must be trained to use them. Many areas lack the roads, planes, and refrigeration needed to speedily transport samples. In India, "The issue is sampling: Somebody has to collect and ship the samples and provide the clinical data. That takes some time," says Anurag Agrawal, director of the Council of Scientific and Industrial Research's Institute for Genomics and Integrative Biology in New Delhi. And costly sequencing reagents need to be continually imported and may not always be available.

"We ordered … reagents [from a U.S. company] in November [2020]. They are arriving now!" says Senjuti Saha, a microbiologist at the Child Health Research Foundation in Dhaka, Bangladesh. "This is not an exception, rather it's the rule."

Saha is nonetheless pleased with a multilab effort that has allowed the country to scale up sequencing to 0.2% of 780,000 confirmed COVID-19 cases. "I don't think [that number is] great," she says. "But it was zero before. And we have never done this before."

The effort is already paying off, most recently on 8 May, when two Bangladeshi patients who recently returned from India were found to be carrying B.1.617. Two days later, after a long meeting with scientists, Bangladeshi officials tightened quarantine at the border.

Other countries face geographical challenges. In December 2020, Brazilian scientists identified P.1, now a variant of concern globally, during a massive outbreak in Manaus, the capital of Amazonas state. But sequencing coverage is poor in places like the neighboring rainforest state of Acre and in Brazil's northeast, says Ana Vasconcelos, a computational biologist at the National Laboratory for Scientific Computing in Petrópolis. She says just 25 genomes have been uploaded from Acre. She enlisted colleagues there to provide 100 samples, then found there was no dry ice, needed for transport. She finally received the samples last week, with the help of a French nongovernmental organization, the Mérieux Foundation.

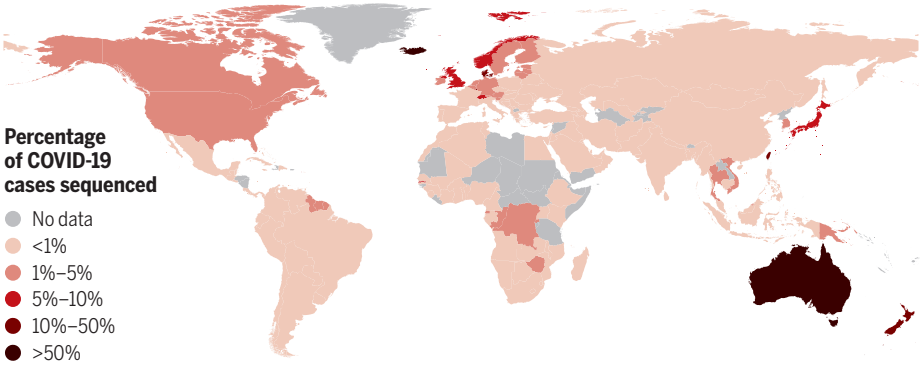
Some experts have suggested nations aim to sequence virus from 5% of cases, but others say such goals are wrongheaded. "The world is getting too obsessed with numbers," says Tulio de Oliveira, a computational biologist and director of the KwaZulu-Natal Research and Innovation Sequencing Platform at the University of KwaZulu-Natal, Durban. For example, he and South African colleagues identified the variant of concern that originated in South Africa soon after it arose by strategically sampling regions that had outbreaks.

De Oliveira and a huge team of other African scientists have now turned sparse sequence data in Africa into a big picture of how the virus has evolved within the continent. In a preprint posted on 13 May, based on nearly 9000 genomes collected in 33 African countries they found that SARS-CoV-2 arrived in African countries with travelers, mainly from Europe. As people traveled within Africa, the virus spread and then evolved into several key variants. "Although distorted by low sampling numbers and blind-spots," the authors write, "the findings highlight that Africa must not be left behind in the global pandemic response, otherwise it could become a breeding ground for new variants."

That's true worldwide, Calvignac-Spencer says. "It's not really possible that we go on being so selfish with genomic surveillance, with vaccines," he says. "It's not understanding our own best interests." ■

A patchy picture

Sequencing of the pandemic coronavirus is minimal in most countries around the world, so scientists often have little insight into emerging new variants.



MENTAL HEALTH

A psychedelic win raises questions for PTSD therapy

MDMA tested along with talk therapy, but the ideal pairing has yet to be studied

By **Kelly Servick**

The news last week that the compound 3,4-methylenedioxymethamphetamine (MDMA), popularly called ecstasy, alleviated post-traumatic stress disorder (PTSD) in a phase 3 trial was a milestone in efforts to turn psychedelic drugs into mainstream treatments. It also highlighted a therapeutic marriage that is getting increasing attention: providing a mind-altering drug while a patient receives care from a trained therapist. "This is really kind of a new zeitgeist in psychiatry," says Barbara Rothbaum, a clinical psychologist at Emory University.

Researchers funded by the nonprofit Multidisciplinary Association for Psychedelic Studies (MAPS) reported in *Nature Medicine* that after "MDMA-assisted therapy," two-thirds of treated participants no longer met the diagnostic criteria for PTSD. MAPS hopes to confirm the results in an ongoing second study and seek approval for the therapy from the U.S. Food and Drug Administration (FDA) as early as 2023. In 2017, the agency granted MDMA a "breakthrough" designation, which comes with extra guidance during the trial process and an expedited review.

The idea that psychedelic drugs and talk therapy work in synergy raises complex questions about how to optimize—and regulate—the drug experience. "It's not understood what the role of MDMA or [another] psychedelic is in facilitating the psychotherapy, and what's happening neurobiologically," says Atheir Abbas, a neuroscientist and psychiatrist at Oregon Health & Science University. Because taking psychedelics without guidance can lead to negative experiences, "a guided, more psychotherapy-oriented approach is probably warranted," he says. "But it's not clear what aspects of that guidance are critical."

CREDITS: (MAP) K. FRANKLIN/*SCIENCE*; (DATA) GISAID, PREPARED BY C. ROEMER; OUR WORLD IN DATA REPOSITORY VIA JOHNS HOPKINS CENTER FOR SYSTEMS SCIENCE AND ENGINEERING



Experimental post-traumatic stress disorder treatment with the psychedelic drug MDMA emphasizes supervision from specially trained therapists.

As MDMA and other tightly controlled psychedelic compounds inch closer to regulatory approval, careful supervision from therapists may help overcome their reputation as illicit substances and fears of indiscriminate use. "MAPS has done very well to really emphasize that they're not just trying to promote a compound," says Rachel Yehuda, who directs the Center for Psychedelic Psychotherapy and Trauma Research at the Icahn School of Medicine at Mount Sinai.

MAPS researchers have worked for more than 3 decades to turn MDMA into a prescription medicine. The substance doesn't produce the vivid hallucinations associated with either LSD or psilocybin, found in magic mushrooms. But it increases the brain's levels of certain neurotransmitters, including serotonin and dopamine, to create a sense of well-being and heightened empathy. That might allow trauma survivors who face intrusive flashbacks to reflect on disturbing memories with less fear and judgement. "It gives you this fascinating ability toward self-compassion," says Jennifer Mitchell, a neuroscientist at the University of California, San Francisco, and an investigator in the MAPS trial.

The psychotherapy the trial used looks different from the most thoroughly studied PTSD psychotherapies. Many of these direct a patient to confront painful memories. In one such approach, called prolonged exposure therapy, "we have them go back in their mind's eye to the time of the traumatic event and recount it out loud, in the present tense, over and over," Rothbaum says. "It's a good therapy, but it's also a hard therapy."

In the MAPS approach, therapists are advised not to steer the conversation toward trauma, but to create a safe space to "support the participant's own unfolding experience," according to MAPS's manual. The manual also describes carefully curated surroundings for patients, advising "fresh flowers and artwork." Rothbaum, who studies and practices prolonged exposure therapy, describes MAPS sessions as "the sweetest therapy in the world for PTSD."

In the trial, 79 participants underwent three 90-minute preparatory therapy sessions; three 8-hour "experimental sessions" with either MDMA or a placebo, spaced about 1 month apart; and nine 90-minute "integration sessions" to process their experiences. Of 42 people who got MDMA, 67% no longer met the diagnostic criteria for PTSD 2 months after their last experimental session. For the placebo group, that rate was 32%. Improvements in the placebo recipients were comparable to those observed in studies of existing approaches such as exposure therapy, says MAPS's chief scientific officer, Berra Yazar-Klosinski.

Yehuda, who has long worried that prolonged exposure therapy can retraumatize some patients and discourage them from continuing treatment, says the research offers a new direction. But MDMA-assisted therapy needs to go head to head in clinical trials with established psychotherapies and the antidepressant drugs already approved for PTSD, says Arash Javanbakht, who directs the Stress, Trauma, and Anxiety Research Clinic at Wayne State University. Others want to test MDMA alongside more mainstream talk therapies. Rothbaum's team hopes to launch a pilot study this year that combines the drug with prolonged exposure therapy. Psychologist Anne Wagner of the mental health clinic Remedy is preparing to launch a pilot study that brings an approach called cognitive processing therapy into the pre- and post-MDMA sessions. Adding this more structured psychotherapy might improve results for some patients, she says.

Should MDMA win FDA approval, the MAPS psychotherapy approach is likely to dominate at least at first. FDA doesn't regulate psychotherapy, but Yazar-Klosinski says FDA has indicated any approval would stipulate that the drug be used alongside therapy from trained providers. (FDA declined to comment on how it might address supportive therapy in an approval.) A subsidiary of MAPS would manufacture the drug and hopes to receive a 5-year exclusivity period on marketing the drug for PTSD. It would sell MDMA only to providers who undergo MAPS's 100-hour training program.

Uncertainty about the right talk therapy pairings extends to research on other psychedelic drugs. Albert Garcia-Romeu, a psychologist at Johns Hopkins University School of Medicine, is testing psilocybin-assisted addiction treatment. For a recent study of cigarette smokers, the team made "kind of our best guess" to pair the drug with cognitive behavioral therapy, a common addiction talk therapy, he says.

Potential FDA decisions on psilocybin and MDMA are still years off. But in November 2020, Oregon became the first state to legalize psilocybin for therapeutic use. It has appointed an advisory board to help make a plan for regulating the compound by December 2022.

Oregon's measure describes a system of state-licensed providers and "a multisession, facilitator-guided, psychotherapy-type experience," says Abbas, who sits on the advisory board but was speaking only for himself. What type of psychotherapy experience should that be? And what qualifies a facilitator? "That's something the board is likely to have to tackle." ■

PHOTO: MULTIDISCIPLINARY ASSOCIATION FOR PSYCHEDELIC STUDIES



Josh McQuillin, shown in 2019, 1 year after being treated, says gene therapy has transformed his life.

PHOTO: RILEY BRANDT/UNIVERSITY OF CALGARY

BIOMEDICINE

Gene therapy that once led to tragedy scores success

Treatment reverses rare liver disease in small clinical trial, highlighting field's progress

By **Jocelyn Kaiser**

Twenty-two years ago, one of scientists' first attempts at gene therapy ended in tragedy when a young man died. The story of Jesse Gelsinger, who had a rare liver disorder, became a textbook example of irresponsible medical research. For years, the case hobbled efforts to treat diseases by adding new DNA to a sick person's cells. Now, a fresh effort to cure Gelsinger's disease is bearing fruit, in the latest sign of the field's resurgence.

The small, ongoing trial for ornithine transcarbamylase (OTC) deficiency, sponsored by the company Ultragenyx, hasn't helped everyone with the inherited disease, which causes dangerously high ammonia levels in the blood and affects an estimated one in 50,000 people. Still, there have been no serious safety problems. Many of the 11 participants have been able to relax dietary restrictions and drop medications, including three who no longer need those measures at all, researchers reported last week at the virtual meeting of the American Society of Gene & Cell Therapy (ASGCT).

"It's very heartening that this went well and there were no untoward effects and partial efficacy," says geneticist Ada Hamosh of Johns Hopkins University, who treats patients with OTC deficiency. "After really rocky beginnings, people took the time to do the biology" and craft a better therapy.

Jesse's father, Paul Gelsinger, who is not a scientist but has followed the trial, agrees. "I think it's great that Ultragenyx had the courage to take on OTC. … I also think it's wonderful that they have achieved efficacy, even limited," says Gelsinger, whose son would have been 40 years old this year.

People born with OTC deficiency lack an enzyme needed to turn excess nitrogen from protein into urea. This leads to the buildup of ammonia, which can cause coma, brain damage, and death. Because the *OTC* gene is on the X chromosome, the disease is often fatal in infant boys. But girls, who have a second, working copy of the gene, and boys with mutations that give them a partially functioning OTC enzyme can reduce ammonia overload with a low-protein diet and drugs.

Jesse Gelsinger had that milder adult form. At age 18, he joined a trial at the University of Pennsylvania (UPenn) because he wanted to help babies with OTC deficiency. He died 4 days after being injected with an adenovirus modified to serve as a "vector" for a working *OTC* gene, ferrying it into liver cells. But in Jesse's case, the adenovirus, a type of cold virus now used at much lower doses in some COVID-19 vaccines, caused a massive immune reaction and organ failure (*Science*, 18 February 2005, p. 1028).

Federal regulators found the study's leader, UPenn gene therapist James Wilson, had violated regulations, including disregarding serious side effects in other trial subjects. UPenn paid a $500,000 fine. Other gene therapy trials were halted and companies pulled out. Wilson's lab pivoted to a safer vector, adenoassociated virus (AAV). AAV vectors have led to a slow rebirth of the field; they have been used in more than 250 trials and two U.S.-approved gene therapies.

Wilson returned to treating OTC deficiency in mice, this time with AAV, because he felt "the unmet need was so huge." But he says he was "nervous" about the outcome of Ultragenyx's early stage trial, launched 4 years ago. And Paul Gelsinger worried about whether the trial's highest planned dose would be sufficiently below the AAV levels toxic in animals. Gelsinger met with CEO and President Emil Kakkis, who reassured him with a plan to monitor patients closely.

The trial, which has tested three AAV doses in 11 of a planned 12 patients, uncovered no serious safety problems, although some patients had a rise in liver enzymes that, as in other AAV trials, were treated with steroids, co-investigator Cary Harding of Oregon Health & Science University reported at the ASGCT meeting. And within 1 year, two men and one woman were producing normal urea levels and no longer needed a special diet or drugs. Three "partial responders" have reduced medications and dietary restrictions by at least half.

Canadian Josh McQuillin, 32, had a complete response after being treated 3 years ago. "It was life-changing," he says. "I was getting by before, but now I'm just like a normal person." He can eat steak and sushi and no longer has to worry about staying close to a hospital, allowing him to travel freely and go back-country camping.

The results are "absolutely" a milestone, Harding says. Jesse's death "was a huge setback, although it did obviously push people to develop a lot of new things, [like] AAV."

Ultragenyx plans to launch a phase 3 trial later this year. For babies with severe OTC deficiency, however, the therapy would only be a temporary fix—perhaps buying time to get a liver transplant—because as the infants grow, their dividing liver cells will gradually lose the DNA for normal OTC. Wilson's lab is working on using the CRISPR gene-editing tool to repair the *OTC* gene in mice, which could be a lasting fix.

For now, observers like ethicist Laurie Zoloth of the University of Chicago Divinity School welcome the trial's modest success. "This is a good, if tentative next step in the use of gene therapy," she says, "making good on the long-awaited and fragile promise." ■

Bills giving NSF big budget boost gain traction

Two panels shrink size of proposed technology directorate as Senate debate begins

By **Jeffrey Mervis**

Two congressional panels have endorsed a vision for a rapid doubling of the National Science Foundation's (NSF's) budget as part of a broader strategy for outinnovating China and the rest of the world. Science advocates hailed the move as an important step in a 20-year effort to move NSF toward parity with the National Institutes of Health, the giant among federal research agencies. But the panels scaled back one aspect of the original proposal, by Senate Majority Leader Chuck Schumer (D–NY): creating a new technology directorate at NSF that would dwarf the rest of the agency.

In separate votes last week on related bills—one pending in the U.S. Senate, the other before the House of Representatives—lawmakers called for boosting NSF's existing programs from $8.5 billion to roughly $13 billion over 5 years. "Great news," says one higher education lobbyist. "But there's still a lot of work that needs to be done." Legislators must negotiate other, more contentious provisions in the sprawling Senate bill. And the bills only authorize spending; even if they become law, Congress will have to appropriate the additional money.

First introduced in May 2020, Schumer's bill, the Endless Frontier Act (S. 1260), proposed a $100 billion technology directorate at NSF to accelerate development of 10 key technologies, including artificial intelligence, advanced materials, and quantum information science. The money would go to create university technology and innovation centers that work closely with industry, fund test beds for promising technologies, promote entrepreneurship at campuses across the country, and invest heavily in education and training.

Although the research community welcomed the idea of additional funding for NSF, some worried a huge new technology directorate might divert NSF from its core mission of supporting fundamental research across all disciplines without regard to how quickly—or even whether—it fuels economic growth and contributes to national security. Some legislators, meanwhile, fretted that NSF's directorate might duplicate research funded by other federal agencies or that U.S. competitors, notably China, might find a way to illegally acquire some of the fruits of that research.

On 11 May a bipartisan group of lawmakers wrote to Schumer and Minority Leader Mitch McConnell (R–KY) advocating for giving the Department of Energy's (DOE's) network of 17 national laboratories a bigger role in any funding boost. The letter added, "DOE and its labs are also better placed and experienced to prevent the theft of defense and other commercial technologies and know-how by competitors, including China."

The Senate commerce committee took the concerns to heart the following day. The new version, approved by a vote of 24 to four, now authorizes DOE to receive $16.9 billion in additional funding over 5 years, compared with a total of $26.6 billion for NSF's technology directorate. NSF's overall budget would grow to $21.3 billion by 2026, with the technology directorate getting $8.4 billion that year.

Two ways to spread the wealth

Bills that aim to help the United States compete with China have different targets for boosting research funding over 5 years ($ billions).

	SENATE BILL (S. 1260)	HOUSE BILL (H.R. 2225)
National Science Foundation (total)	$81	$73
Existing activities	$54.4	$60
New directorate	$26.6	$13
Energy Department	$16.9	$0
Commerce Department	$11.6	$0

Senator Todd Young (R–IN), the chief advocate for the Endless Frontier Act during the hearing, was not happy. "This is a poison pill," he said of the provision shifting funds to DOE. "It would underfund the technology directorate … [and] also seems somewhat parochial." But Leland Cogliani, a lobbyist for Lewis-Burke Associates who tracks energy issues, says the change had broad appeal. Republicans, for example, "didn't want to grow the overall size of the bill," he says, "and other senators didn't want to harm NSF core programs. They also wanted to achieve some degree of parity between DOE and NSF."

The Senate committee also responded to long-standing complaints that NSF funding is concentrated in a handful of states. It attached language backed by the panel's top Republican, Senator Roger Wicker (MS), requiring both NSF and DOE to allocate 20% of any new funds to institutions in states, such as his, that struggle to win federal research grants. It also adds geography to the categories used to define the diversity of grantees, which traditionally include race, ethnicity, gender, and disability status. "This amendment is a game changer for geographic diversity. … It is one of the changes that I am most excited about," Wicker exclaimed.

The next day, the research subcommittee of the House science committee agreed unanimously to authorize a 116% hike in NSF's overall budget over 5 years. Funding for its traditional programs would rise to $13.2 billion, close to the $12.9 billion in Senate bill. However, the new NSF directorate—called Science and Engineering Solutions in the House bill—would be significantly smaller than the Senate's version, starting at $1 billion in 2022 and growing to $5.1 billion in 2026. "This bill pushes NSF to be its own best self, not an entirely new agency," explained Representative Eddie Bernice Johnson (D–TX), who chairs the full committee.

The committee's top Republican, Representative Frank Lucas (OK), agreed. "The funding path is practical, sustainable, and in balance with the rest of the foundation."

The narrower House bill faces a relatively smooth path to passage. However, the Senate bill, now 1420 pages, hit the floor this week with new and controversial sections aimed at dealing with China's ascendent economic and military strength. "We fear the bill may become overloaded with extraneous and complicated provisions that will undermine its primary goals," says Barbara Snyder, president of the 66-member Association of American Universities, suggesting that AAU and other higher education groups might withdraw their support if their concerns aren't addressed.

The White House will also be an important player. President Joe Biden has expressed support for investing $50 billion over several years in a technology directorate at NSF. But to date his requested 20% boost for NSF in 2022 doesn't specify any initial funding for the directorate. ■

DATA: U.S. SENATE; U.S. HOUSE OF REPRESENTATIVES

PHYSICS

Romania left out of high-powered laser project

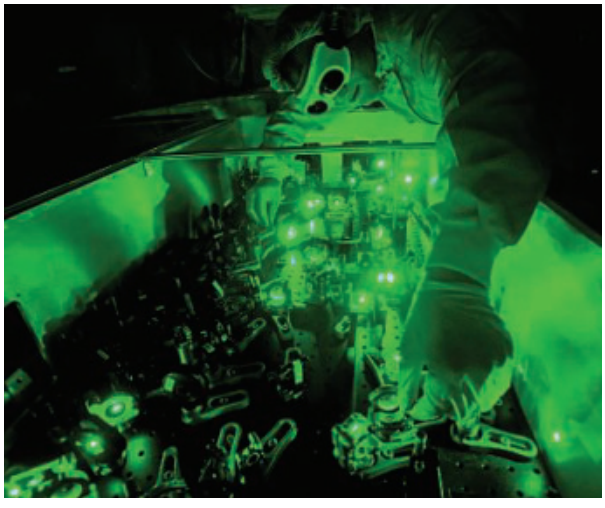
Legal dispute mars international launch of Extreme Light Infrastructure in Eastern Europe

By **Edwin Cartlidge**

The €950 million Extreme Light Infrastructure (ELI), taking shape in the Czech Republic, Hungary, and Romania, will give scientists some of the most powerful lasers on the planet, potentially leading to breakthroughs in everything from cancer therapy to the treatment of nuclear waste—while boosting research in some of Europe's poorer regions. It took another step forward on 30 April when the European Commission approved the European Research Infrastructure Consortium (ERIC) to shift control from a loose confederation of national initiatives to a single international umbrella.

But Romania has been left in the rain: It was omitted from ERIC, following a dispute over a gamma ray source central to its facility. And two rich members of ELI, France and the United Kingdom, have pulled out, leaving a smaller, less financially secure club.

ELI was first proposed by Gérard Mourou, a physicist at the École Polytechnique near Paris who won a Nobel Prize for ways to compress laser beams into short pulses of astonishing power. The three Eastern European nations were chosen as hosts in 2009 because they could draw on EU "structural funds"—normally used by poorer EU members for infrastructure such as roads and bridges.



Czech researchers test lasers in Europe's Extreme Light Infrastructure.

The project is well along. At ELI-Beamlines near Prague, researchers have begun first experiments with lasers that will reach up to 10 petawatts in power, yielding x-rays and ions for use in materials science, astrophysics, and biomedicine. In the south of Hungary, ELI Attosecond Light Pulse Source (ELI-ALPS) will chop lasers into short pulses to explore how electrons move in atoms and molecules. And ELI Nuclear Physics (ELI-NP), on the outskirts of Bucharest, Romania, is meant to generate intense beams of gamma rays, which, when combined with light from two 10-petawatt lasers, will probe atomic nuclei and the quantum vacuum (*Science*, 26 January 2018, p. 382).

EuroGammaS, a consortium of public research institutes and industry, delivered much of the gamma ray source to ELI-NP in 2018 but said the lab floor was uneven and refused to install the components. ELI-NP managers insisted the floor was OK and fined EuroGammaS for its delay—which the consortium contested in court in October 2018. A month later, ELI-NP canceled its €67 million contract with EuroGammaS and later hired a U.S. company, Lyncean Technologies, to build it. EuroGammaS returned to court to reinstate its contract.

ELI Director General Allen Weeks points out that some EuroGammaS members, such as Italy's National Institute for Nuclear Physics (INFN), are also part of ELI—creating an unprecedented internal conflict. "I can't remember member institutions ever taking others to court." Fearing the spat would cause other members to walk away, Weeks says, ELI's governing assembly decided in March 2019 to push ahead with an ERIC for just ELI-Beamlines and ELI-ALPS.

That wasn't enough to keep France in the consortium, however. Its departure in the summer of 2019 was a particular disappointment, Weeks says. "People really expected that France would not only be in, but leading somehow." The United Kingdom followed in November 2020. ERIC now has just four members: the Czech Republic, Hungary, Italy, and Lithuania (with Germany and Bulgaria joining as observers). Ultimately, it will need to attract other members to contribute to operational costs. "It's not sustainable for the host countries to provide 100% funding, that is clear," says ELI-Beamlines project director Roman Hvězda.

Despite the ill will over the affair, which the Romanian Academy described in May 2020 as "concerted actions to discredit Romania," Weeks hopes the country will eventually become a member. But other ERIC nations have conditions; in June 2020 they released a statement saying ELI-NP's management needs to demonstrate "good faith cooperation and capability to run an international facility in a transparent and verifiable way."

Some researchers in Romania are disillusioned. George Epurescu, a laser physicist at the National Institute for Laser, Plasma and Radiation Physics, is critical of Victor Zamfir, former head of ELI-NP. Epurescu accuses him of using the delay with the gamma source as a way to acquire more power over the center and its finances. Zamfir, who was removed from ELI-NP in August 2020 by Romania's research minister, did not respond to questions from *Science*.

The ongoing turbulence raises doubts that ELI-NP will open on schedule by the end of 2023, as its EU funding stipulates. In a 2020 statement, European Commissioner for Cohesion and Reforms Elisa Ferreira said the European Union may impose a "financial correction" if the lab cannot meet the deadline. Epurescu says that will be difficult given a shortage of trained laser physicists in the country.

Others have concerns about Lyncean's ability to deliver the gamma ray source. Unlike EuroGammaS, it has yet to publish any peer-reviewed papers on the source, says Luca Serafini, an INFN nuclear physicist who was part of EuroGammaS. "It is not in the scientific mainstream." Benjamin Hornberger, product manager at Lyncean, says the company is confident it can deliver the source by early 2023, although delays from the pandemic have led to a "tight project schedule."

It would be a big disappointment if ELI-NP lacks the gamma source that is its raison d'être. But Weeks reckons that even without it, the center could do worthwhile research. In the end, he says, "It is too big to fail." ■

Edwin Cartlidge is a journalist based in Rome.

PHOTO: © VIT SIMANEK/CTK PHOTO/ALAMY LIVE NEWS



Passengers at Hankou railway station in Wuhan on 22 January 2020, the day before the Chinese government locked down the city.

PHOTO: XIAO YIJIU/XINHUA/EYEVINE/REDUX

COVID-19

China overhauls its public health bureaucracy

Early stumbles in pandemic response prompt new top-level agency to better handle future threats

By **Dennis Normile**

The Chinese government, roundly criticized at home and abroad for its initial response to the COVID-19 pandemic, appears to have taken some lessons from that crisis. On 13 May, it announced an overhaul of its public health bureaucracy, centered on the creation of a new national agency that will report directly to China's State Council. On paper, at least, the new structure should help bypass the layers of bureaucracy that stymied the timely flow of information from local authorities in Wuhan and Hebei province to top national officials in the early days of the coronavirus outbreak.

The new National Administration of Disease Prevention and Control (NADPC) will be tasked with safeguarding and promoting public health, establishing an epidemic monitoring and early warning system, and guiding disease control research, according to the official Xinhua News Agency. It will absorb the existing Chinese Center for Disease Control and Prevention (China CDC) and will be headed by Wang Heshang, an official at the National Health Commission (NHC) who was dispatched to Hubei last year to direct the governmental response to the outbreak.

"The development is clearly important," says Keiji Fukuda, an epidemiologist at the University of Hong Kong who previously held several positions at the World Health Organization (WHO). Although Xinhua's announcement did not link NADPC's creation to the pandemic failures, "In essence, it is a response to China's internal assessment of what it needs to do differently to perform better," Fukuda says. "What is not clear is how this will actually work in practice."

Through stringent quarantines, contact tracing, and lockdowns, China crushed its COVID-19 epidemic months after it erupted in January 2020. But the country stumbled badly in the early days, as a report issued earlier this month by the international Independent Panel for Pandemic Preparedness and Response has confirmed. Health care workers were warning about a serious, unusual pneumonia spreading among hospital staff in Wuhan as early as 30 December 2019, but local authorities ordered institutions not to disclose information to the public. Whistleblowers were silenced. The first report that scientists had fingered a novel coronavirus came not from authorities, but in a story in *The Wall Street Journal*. It wasn't until 20 January 2020 that an NHC delegation led by noted respiratory diseases expert Zhong Nanshan acknowledged that human-to-human transmission was occurring and that health care workers were being infected.

"The structure of the Chinese political system creates incentives for lower level officials to conceal and manipulate information," aided by censorship and the lack of independent media, says Jennifer Pan, a political scientist at Stanford University.

As a result, China missed a chance to better control the outbreak and failed to warn other countries early. When the national government finally got up to speed, it fired local officials deemed responsible. Chinese health experts also began to discuss a new high-level agency that would combine the administrative functions of the existing NHC with the research functions of China CDC, says Yanzhong Huang, a global health specialist at the Council on Foreign Relations in New York City. In a speech last week, Sun Chunlan, a vice premier and member of the Communist Party Politburo, emphasized that the new agency should strengthen its leadership over lower level disease control agencies, according to Xinhua.

It's not the first time China has tried to make its public health bureaucracy more effective. In 2002, it converted the Chinese Academy of Preventive Medicine into China CDC, modeled on the U.S. Centers for Disease Control and Prevention. Yet in 2003, the country badly botched the outbreak of severe acute respiratory syndrome, another coronavirus disease, by failing to respond quickly and initially withholding information from the public and WHO.

Additional reforms after that episode did not overcome the structural issues, Pan says. China CDC remained "bedeviled by a lack of funding and autonomy," Huang adds. Local officials blocked reports of unusual disease cases from reaching the agency, which was not authorized to issue alerts about looming public health emergencies, he says.

The Xinhua report does not mention what will happen to China CDC, but the agency's head, George Gao, confirmed to *Science* that it will be under the new agency, without giving further details. NADPC is still technically affiliated with NHC, and its mission and authority "remain not very clear," Huang says. But if NADPC gets sufficient resources and authority, he says, China might be better prepared for the next disease crisis. ■



A shredded electric vehicle battery can yield recyclable metals, but it is often cheaper for batterymakers to use new materials.

A DEAD BATTERY DILEMMA

With millions of electric vehicles set to hit the road, scientists are seeking better battery recycling methods

By **Ian Morse**

PHOTO: ARGONNE NATIONAL LABORATORY

The battery pack of a Tesla Model S is a feat of intricate engineering. Thousands of cylindrical cells with components sourced from around the world transform lithium and electrons into enough energy to propel the car hundreds of kilometers, again and again, without tailpipe emissions. But when the battery comes to the end of its life, its green benefits fade. If it ends up in a landfill, its cells can release problematic toxins, including heavy metals. And recycling the battery can be a hazardous business, warns materials scientist Dana Thompson of the University of Leicester. Cut too deep into a Tesla cell, or in the wrong place, and it can short-circuit, combust, and release toxic fumes.

That's just one of the many problems confronting researchers, including Thompson, who are trying to tackle an emerging problem: how to recycle the millions of electric vehicle (EV) batteries that manufacturers expect to produce over the next few decades. Current EV batteries "are really not designed to be recycled," says Thompson, a research fellow at the Faraday Institution, a research center focused on battery issues in the United Kingdom.

That wasn't much of a problem when EVs were rare. But now the technology is taking off. Several carmakers have said they plan to phase out combustion engines within a few decades, and industry analysts predict at least 145 million EVs will be on the road by 2030, up from just 11 million last year. "People are starting to realize this is an issue," Thompson says.

Governments are inching toward requiring some level of recycling. In 2018, China imposed new rules aimed at promoting the reuse of EV battery components. The European Union is expected to finalize its first requirements this year. In the United States, the federal government has yet to advance recycling mandates, but several states, including California—the nation's largest car market—are exploring setting their own rules.

Complying won't be easy. Batteries differ widely in chemistry and construction, which makes it difficult to create efficient recycling systems. And the cells are often held together with tough glues that make them difficult to take apart. That has contributed to an economic obstacle: It's often cheaper for batterymakers to buy freshly mined metals than to use recycled materials.

Better recycling methods would not only prevent pollution, researchers note, but also help governments boost their economic and national security by increasing supplies of key battery metals that are controlled by one or a few nations. "On the one side, [disposing of EV batteries] is a waste management problem. And on the other side, it's an opportunity for producing a sustainable secondary stream of critical materials," says Gavin Harper, a University of Birmingham researcher who studies EV policy issues.

To jump-start recycling, governments and industry are putting money into an array of research initiatives. The U.S. Department of Energy (DOE) has pumped some $15 million into a ReCell Center to coordinate studies by scientists in academia, industry, and at government laboratories. The United Kingdom has backed the ReLiB project, a multi-institution effort. As the EV industry ramps up, the need for progress is becoming urgent, says Linda Gaines, who works on battery recycling at DOE's Argonne National Laboratory. "The sooner we can get everything moving," she says, "the better."



Materials scientist Dana Thompson develops solvents for extracting valuable metals from spent car batteries.

PHOTO: FARADAY INSTITUTION

EV BATTERIES are constructed a bit like nested dolls. Typically, a main pack holds several modules, each of which is constructed from numerous smaller cells (see graphic, p. 782). Inside each cell, lithium atoms move through an electrolyte between a graphite anode and a cathode sheet composed of a metal oxide. Batteries are usually defined by the metals in the cathode. There are three main types: nickel-cobalt-aluminum, iron-phosphate, and nickel-manganese-cobalt.

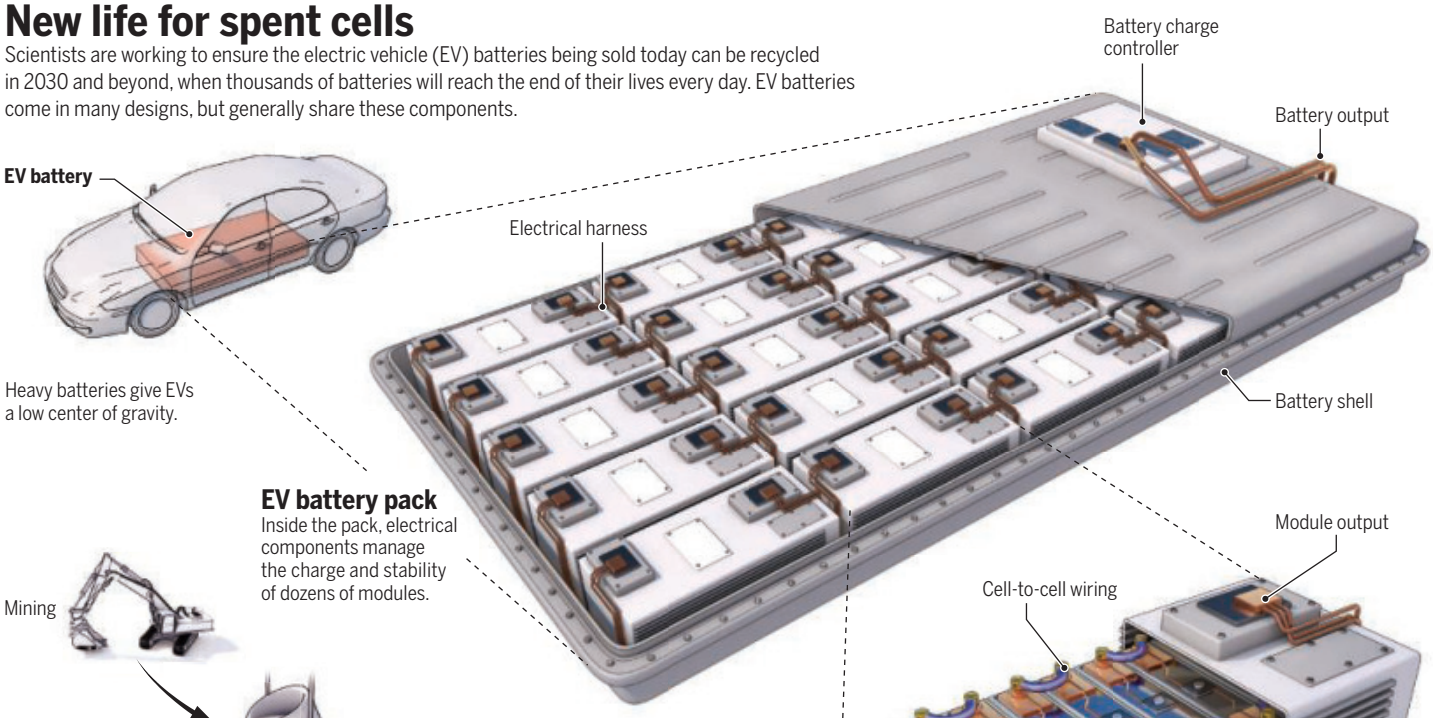
Now, recyclers primarily target metals in the cathode, such as cobalt and nickel, that fetch high prices. (Lithium and graphite are too cheap for recycling to be economical.) But because of the small quantities, the metals are like needles in a haystack: hard to find and recover.

To extract those needles, recyclers rely on two techniques, known as pyrometallurgy and hydrometallurgy. The more common is pyrometallurgy, in which recyclers first mechanically shred the cell and then burn it, leaving a charred mass of plastic, metals, and glues. At that point, they can use several methods to extract the metals, including further burning. "Pyromet is essentially treating the battery as if it were an ore" straight from a mine, Gaines says. Hydrometallurgy, in contrast, involves dunking battery materials in pools of acid, producing a metal-laden soup. Sometimes the two methods are combined.

Each has advantages and downsides. Pyrometallurgy, for example, doesn't require the recycler to know the battery's design or composition, or even whether it is completely discharged, in order to move ahead safely. But it is energy intensive. Hydrometallurgy can extract materials not easily obtained through burning, but it can involve chemicals that pose health risks. And recovering the desired elements from the chemical soup can be difficult, although researchers are experimenting with compounds that promise to dissolve certain battery metals but leave others in a solid form, making them easier to recover. For example, Thompson has identified one candidate, a mixture of acids and bases

New life for spent cells

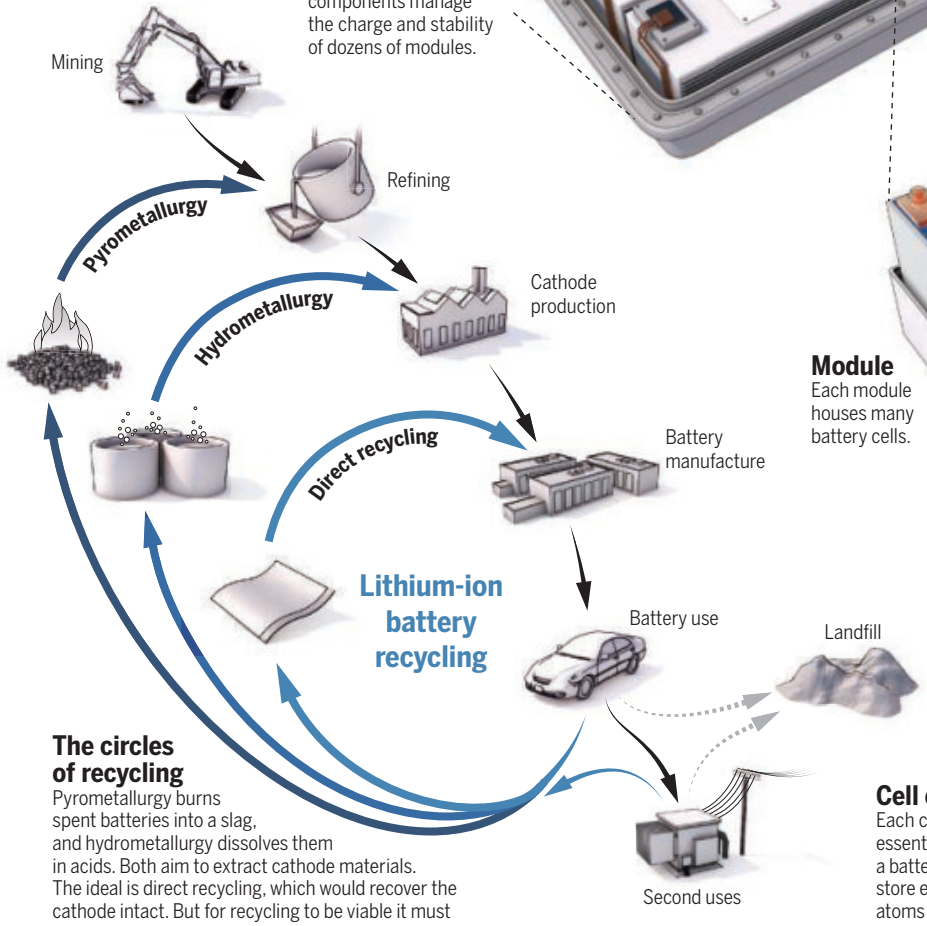
Scientists are working to ensure the electric vehicle (EV) batteries being sold today can be recycled in 2030 and beyond, when thousands of batteries will reach the end of their lives every day. EV batteries come in many designs, but generally share these components.



EV battery pack
Inside the pack, electrical components manage the charge and stability of dozens of modules.

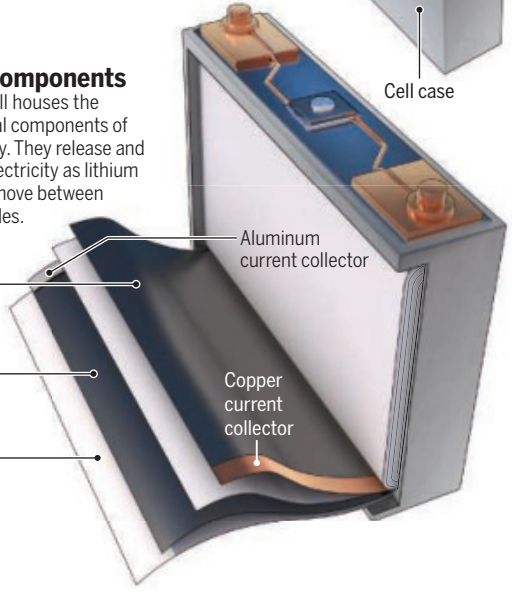
Module
Each module houses many battery cells.

Cell
EV batteries can have hundreds or even thousands of cells. Designs vary, and include rectangular prismatic cells (below, right) and cylindrical cells (below, left).

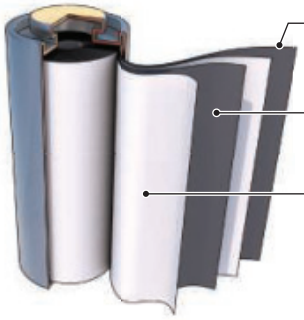


The circles of recycling
Pyrometallurgy burns spent batteries into a slag, and hydrometallurgy dissolves them in acids. Both aim to extract cathode materials. The ideal is direct recycling, which would recover the cathode intact. But for recycling to be viable it must be cost competitive with mined materials.

Cell components
Each cell houses the essential components of a battery. They release and store electricity as lithium atoms move between electrodes.



Cylindrical cell
A tough steel casing makes these cells difficult to open. Often durable glue combines thousands of cells into packs.



Cathode
The cathode typically holds the most valuable recyclable material, made up of many metals.

Anode
Negative electrodes are composed of graphite, carbon, or silicon-based components.

Electrolyte and separator
Lithium travels through a separator sheet soaked in electrolyte.

GRAPHIC: C. BICKEL/*SCIENCE*

called a deep eutectic solvent, that dissolves everything but nickel.

Both processes produce extensive waste and emit greenhouse gases, studies have found. And the business model can be shaky: Most operations depend on selling recovered cobalt to stay in business, but batterymakers are trying to shift away from that relatively expensive metal. If that happens, recyclers could be left trying to sell piles of "dirt," says materials scientist Rebecca Ciez of Purdue University.

THE IDEAL is direct recycling, which would keep the cathode mixture intact. That's attractive to batterymakers because recycled cathodes wouldn't require heavy processing, Gaines notes (although manufacturers might still have to revitalize cathodes by adding small amounts of lithium). "So if you're thinking circular economy, [direct recycling] is a smaller circle than pyromet or hydromet."

In direct recycling, workers would first vacuum away the electrolyte and shred battery cells. Then, they would remove binders with heat or solvents, and use a flotation technique to separate anode and cathode materials. At this point, the cathode material resembles baby powder.

So far, direct recycling experiments have only focused on single cells and yielded just tens of grams of cathode powders. But researchers at the U.S. National Renewable Energy Laboratory have built economic models showing the technique could, if scaled up under the right conditions, be viable in the future.

To realize direct recycling, however, batterymakers, recyclers, and researchers need to sort out a host of issues. One is making sure manufacturers label their batteries, so recyclers know what kind of cell they are dealing with—and whether the cathode metals have any value. Given the rapidly changing battery market, Gaines notes, cathodes manufactured today might not be able to find a future buyer. Recyclers would be "recovering a dinosaur. No one will want the product."

Another challenge is efficiently cracking open EV batteries. Nissan's rectangular Leaf battery module can take 2 hours to dismantle. Tesla's cells are unique not only for their cylindrical shape, but also for the almost indestructible polyurethane cement that holds them together.

Engineers might be able to build robots that could speed battery disassembly, but sticky issues remain even after you get inside the cell, researchers note. That's because more glues are used to hold the anodes, cathodes, and other components in place. One solvent that recyclers use to dissolve cathode binders is so toxic that the European Union has introduced restrictions on its use, and the U.S. Environmental Protection Agency determined last year that it poses an "unreasonable risk" to workers.

"In terms of economics, you've got to disassemble … [and] if you want to disassemble, then you've got to get rid of glues," says Andrew Abbott, a chemist at the University of Leicester and Thompson's adviser.



A technician in Germany makes sure a burned lithium-ion battery is discharged before further recycling.

PHOTO: WOLFGANG RATTAY/REUTERS

TO EASE THE PROCESS, Thompson and other researchers are urging EV- and batterymakers to start designing their products with recycling in mind. The ideal battery, Abbott says, would be like a Christmas cracker, a U.K. holiday gift that pops open when the recipient pulls at each end, revealing candy or a message. As an example, he points to the Blade Battery, a lithium ferrophosphate battery released last year by BYD, a Chinese EV-maker. Its pack does away with the module component, instead storing flat cells directly inside. The cells can be removed easily by hand, without fighting with wires and glues.

The Blade Battery emerged after China in 2018 began to make EV manufacturers responsible for ensuring batteries are recycled. The country now recycles more lithium-ion batteries than the rest of the world combined, using mostly pyro- and hydrometallurgical methods.

Nations moving to adopt similar policies face some thorny questions. One, Thompson says, is who should bear primary responsibility for making recycling happen. "Is it my responsibility because I bought [an EV] or is it the manufacturer's responsibility because they made it and they're selling it?"

In the European Union, one answer could come later this year, when officials release the continent's first rule. And next year a panel of experts created by the state of California is expected to weigh in with recommendations that could have a big influence over any U.S. policy.

Recycling researchers, meanwhile, say effective battery recycling will require more than just technological advances. The high cost of transporting combustible items long distances or across borders can discourage recycling. As a result, placing recycling centers in the right places could have a "massive impact," Harper says. "But there's going to be a real challenge in systems integration and bringing all these different bits of research together."

There's little time to waste, Abbott says. "What you don't want is 10 years' worth of production of a cell that is absolutely impossible to pull apart," he says. "It's not happening yet—but people are shouting and worried it will happen." ■

Ian Morse is a journalist in Seattle.

INSIGHTS

PERSPECTIVES



Thousands of geese, ducks, and other birds were found dead from avian influenza virus on the west coast of Schleswig-Holstein, Germany, in November 2020.

PHOTO: CHRISTIAN CHARISIUS/PICTURE-ALLIANCE/DPA/AP IMAGES

PUBLIC HEALTH

Emerging H5N8 avian influenza viruses

The global spread of H5N8 avian influenza viruses is a public health concern

By **Weifeng Shi**[1,2] *and* **George F. Gao**[3,4]

The first confirmed outbreak of highly pathogenic avian influenza virus (HPAIV) in birds was documented in Scotland in 1959 with the influenza A H5N1 subtype, although there have been numerous suspected HPAIV outbreaks documented globally since 1878. H5N1 and its genetic reassortants (including H5N2, H5N5, H5N6, and H5N8) have been found to cause thousands of outbreaks worldwide (*1*, *2*) in both farmed poultry and wild birds, with massive mortality. The H5Ny HPAIVs are lethal to most farmed poultry, and culling is often used to prevent further spread. Several of the H5Ny AIVs have zoonotic and pandemic potential because they have been demonstrated to cross the species barrier, transmitting to mammals, including humans. Eurasia and Africa are experiencing a new wave of highly pathogenic H5Ny AIV outbreaks. The zoonotic potential of AIVs warrants continuous, vigilant monitoring to avert further spillovers that could result in disastrous pandemics.

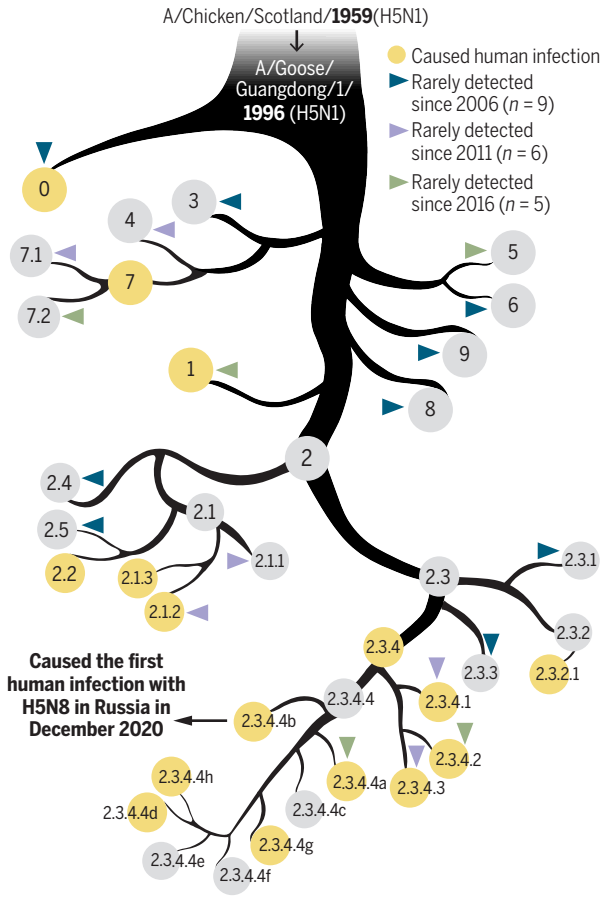
Among the four types (A to D) of influenza viruses, type A tends to be zoonotic, and the natural hosts are regarded to be water birds. Influenza A virus is further divided into different subtypes according to the antigenicity of two viral glycoproteins: hemagglutinin (*HA*, of which there are 18 subtypes, H1 to H18) and neuraminidase (*NA*, of which there are 11 subtypes, N1 to N11); most *HA-NA* combinations in AIVs have been identified. AIVs evolve mainly through two major mechanisms: genetic drift from point mutation(s) and genetic exchange through reassortment of the segmented genomes. Both mechanisms can endow AIVs with new genetic characteristics (sometimes referred to as variants), which may affect transmissibility, pathogenicity, and even antigenicity.

Within a subtype, influenza viruses can be further classified into various clades and subclades generally on the basis of the similarity of the *HA* gene sequences. Scientists have proposed a unified nomenclature system to describe the constant evolution of the H5Ny AIVs on the basis of the phylogenetic characterization and sequence homology of their *HA* gene sequences. In this system, new clades and subclades can be designated when their average percentage pairwise nucleotide distances exceed 1.5% from known clades. These are defined as second-, third-, or fourth-order clades and assigned a numerical "address" that links them to their original clade. For example, within the distinct clade 2.1 of H5, third-order clades meeting the clade definition are designated as clades 2.1.1 and 2.1.2, and so on (see the figure).

The first described strain of the H5Ny HPAIV is referred to as A/Goose/Guangdong/1/1996 (H5N1), and it was identified in China in 1996 (*1*). Since then, the *HA* gene of the H5 subtype has evolved into various clades and subclades (*3*, *4*), with the clade 2.3.4 gradually becoming dominant across the world since 2010. The H5N8 AIV clade 2.3.4 was first isolated from a domestic duck at a wet market in Jiangsu, China, in 2010. In early 2014, H5N8 AIVs of this clade caused outbreaks in domestic and wild birds in South Korea as well as in Japan. A routine surveillance study subsequently revealed that the South Korea–like H5N8 had already existed in domestic birds in Zhejiang, China, as early as November 2013. Clade 2.3.4 H5N8 AIVs were also identified in Russia and several other European countries and in the United States in late 2014. Additionally, an H5N2 virus that contained gene segments related to H5N8 was found in Canada in late 2014. A Bayesian phylogenetic analysis revealed that the introduction of H5Ny AIVs into North America from the Eurasian continent likely occurred through long-distance migratory birds entering by way of the Bering Strait flyway in August 2014 (*5*). In 2016, clade 2.3.4.4 H5N8 AIVs reemerged in China, Mongolia, Russia, Europe, and India. Therefore, clade 2.3.4 H5 AIVs, particularly the H5N8 subtype, have clearly displayed a propensity for rapid global spread in migratory birds.

H5 avian influenza viruses

The H5 subtype of avian influenza viruses can be phylogenetically subclassified into clades and subclades according to their sequence similarity to the hemagglutinin (*HA*) gene (numbers in circles). Several of the H5 clades have caused human infections, and in particular, clade 2.3.4.4b was circulating across Eurasia and Africa during 2020 and caused human infections in Russia.



The majority of the classified H5Ny clades and subclades have been reported to cause human infections, particularly the clade 2.3.4, with H5N1 (*6*) and H5N6 (*7*) subtypes implicated. To date, there have been a total of 862 laboratory-confirmed human cases of infection with H5N1 reported to the World Health Organization (WHO), including 455 deaths (*8*). These cases were from 17 countries, with ~76% from Egypt and Indonesia. No sustained human-to-human transmission of H5N1 or H5N6 AIVs has been documented, despite the report of probable cases arising through close contact. However, gain-of-function studies have shown that H5N1 variants with a few specific mutations in the *HA* gene and seven other gene segments from the H1N1 human influenza virus (which caused a global pandemic in 2009) were able to transmit among laboratory animals through respiratory droplets, which is indicative of the pandemic potential of H5Ny AIVs (*9*, *10*).

The constant evolution of H5Ny AIVs and their potential reassortment with AIVs of other subtypes clearly warrant close attention. According to nationwide AIV surveillance in China since 2014 (*7*, *11*), H5N6 had supplanted H5N1 as the dominant circulating AIV subtype (particularly in duck species) in southern China over the 2014–2016 period. Conversely, H9N2 was the dominant subtype in birds sampled from northern China (*7*), which has also caused numerous human infections. The seroprevalence of antibodies specific to H9N2 among healthy poultry workers in some regions of China exceeded 10%. However, the AIV positivity rate in live poultry markets (LPMs) substantially decreased during 2016–2019 in most regions compared with data collected between 2014 and 2016 (26.90% versus 12.73%, respectively) (*7*, *11*). Since its emergence in early 2013, H7N9 AIVs have caused 1568 laboratory-confirmed human cases, including 616 deaths. However, the positivity rate of H7N9 also substantially decreased between 2016 and 2019, and notably, H9N2 has replaced H5N6 and H7N9 as the dominant AIV subtype in both chickens and ducks across China. Furthermore, new reassortants and viral variants continued to emerge, including H7N3, H9N9, H9N6, and H5N6 subtypes. Almost all of the H9 AIVs and many H7N9 and H6N2 strains encode HAs that preferentially bind to the human α2,6–linked sialic acid cell receptor (*11*), suggesting an increased propensity for human infections. These results highlight the dynamic and complex AIV circulation patterns that are important for optimal selection of vaccine candidates and maximizing vaccine efficacy in birds.

Owing to the COVID-19 pandemic, prevention and control measures—including reduced mobility, increased use of masks, and enhanced social distancing and disinfection—have sharply reduced the global

GRAPHIC: N. CARY/*SCIENCE*

[1]School of Public Health, Shandong First Medical University and Shandong Academy of Medical Sciences, Ji'nan 250000, China. [2]Key Laboratory of Etiology and Epidemiology of Emerging Infectious Diseases in Universities of Shandong, Shandong First Medical University and Shandong Academy of Medical Sciences, Taian 271000, China. [3]National Institute for Viral Disease Control and Prevention, Chinese Center for Disease Control and Prevention, Beijing 102206, China. [4]CAS Key Laboratory of Pathogenic Microbiology and Immunology, Institute of Microbiology, Chinese Academy of Sciences (CAS), Beijing 100101, China. Email: shiwf@ioz.ac.cn; gaof@im.ac.cn

incidence of the seasonal human influenza A and B viruses (*12*). The influenza surveillance data, however, may be underestimated and should be interpreted with a degree of caution because the ongoing COVID-19 pandemic has influenced to varying extents health-seeking behaviors, laboratory staffing and routines in sentinel hospitals or centers for disease control and prevention, as well as testing priorities and capacities (*12*). Nonetheless, highly pathogenic H5Ny AIVs have caused frequent outbreaks in birds in several countries across the Eurasian and African continents since late 2019, especially during the winter season (*2*).

Highly pathogenic H5Ny AIVs—including H5N1, H5N2, H5N5, and H5N8 subtypes—resulted in ongoing outbreaks in both poultry and wild birds in Chinese Taipei throughout 2020. Highly pathogenic H5N8 AIV also caused continuous outbreaks in poultry in South Africa in 2020. Moreover, H5N8 caused numerous outbreaks in central and eastern Europe from January to early June 2020. In the autumn and winter of 2020, Eurasia experienced a sudden recurrence of H5N8 AIV, above other subtypes: In August 2020, H5N8 caused outbreaks in Russia in both poultry and wild fowl, and the affected regions extended to Kazakhstan in mid-September; in October 2020, a new wave of outbreaks of H5N8 in poultry and wild birds was reported in several European countries, including Denmark, Germany, Ireland, the Netherlands, and the United Kingdom. Meanwhile, in the Middle East (Israel) and East Asia (Japan and South Korea), H5N8 outbreaks arose in poultry and/or wild birds. To date, more than 20 million poultry have been slaughtered in South Korea and Japan, and phylogenetic analysis revealed that the causative agent belonged to clade 2.3.4.4b (*13*), a previously identified minor clade of H5Ny AIV (*4*, *13*).

The affected geographic regions have been expanding continuously, and at least 46 countries have reported highly pathogenic H5N8 AIV outbreaks. In addition, the HA protein of these H5N8 AIVs harbors several amino acid substitutions of concern, including Thr^{160}→Ala (T160A, H3 numbering), which has been reported to enhance the binding capacity to α-2,6 sialic acid receptors that are favored by human influenza viruses (*14*). The first human cases of H5N8 influenza virus infection were reported in Russia in December 2020: Seven poultry farm workers tested positive when they participated in a response operation to contain an H5N8 AIV outbreak (*15*). Phylogenetic analysis revealed that the H5N8 virus sequenced from the human cases also belonged to clade 2.3.4.4b of the H5 phylogeny. Therefore, the global spread of AIVs, particularly the H5N8 subtype, has become a major concern to poultry farming and wildlife security but, critically, also to global public health.

Because of the long-distance migration of wild birds, the innate capacity for reassortment of AIVs, the increased human-type receptor binding capability, and the constant antigenic variation of HPAIVs, it is imperative that the global spread and potential risk of H5N8 AIVs to poultry farming, avian wildlife, and global public health are not ignored. Therefore, surveillance of HPAIVs in poultry farms, LPMs, and wild birds should be restored to the level before the COVID-19 pandemic or higher. Further assessment of the transmissibility, pathogenicity, and antigenicity of 2.3.4.4b H5N8 is also required. If there is distinct antigenic variation, vaccines should be updated with the emergent HPAIVs. In addition, decreasing small-scale family-based poultry farming, increasing large-scale high-standard modern poultry farming, and enhanced management of LPMs will help reduce the spread of HPAIVs and potential human infections. Education and outreach are also important, including enhanced personal protection measures during the influenza season, keeping away from wild birds, and avoiding hunting and eating wild birds. ■

REFERENCES AND NOTES

1. X. Xu, N. J. Subbarao, N. J. Cox, Y. Guo, *Virology* **261**, 15 (1999).
2. The World Organisation for Animal Health (OIE), "Update on avian influenza in animals (types H5 and H7)" (2020); www.oie.int/en/animal-health-in-the-world/update-on-avian-influenza.
3. World Health Organization (WHO), "Evolution of the Asian H5 hemagglutinin" (2011); www.who.int/influenza/gisrs_laboratory/201101_h5n1evoconceptualdiagram.pdf?ua=1.
4. Y. Li *et al.*, *Emerg. Infect. Dis.* **26**, 2956 (2020).
5. The Global Consortium for H5N8 and Related Influenza Viruses, *Science* **354**, 213 (2016).
6. K. Y. Yuen *et al.*, *Lancet* **351**, 467 (1998).
7. Y. Bi *et al.*, *Cell Host Microbe* **20**, 810 (2016).
8. WHO, "Cumulative number of confirmed human cases for avian influenza A(H5N1) reported to WHO, 2003-2020" (2020); www.who.int/influenza/human_animal_interface/2020_DEC_tableH5N1.pdf?ua=1.
9. M. Imai *et al.*, *Nature* **486**, 420 (2012).
10. Y. Zhang *et al.*, *Science* **340**, 1459 (2013).
11. Y. Bi *et al.*, *Nat. Commun.* **11**, 5909 (2020).
12. World Health Organization, "Influenza update – 388" (2021); www.who.int/influenza/surveillance_monitoring/updates/latest_update_GIP_surveillance/en.
13. N. Isoda *et al.*, *Viruses* **12**, 1439 (2020).
14. R. Yamaji *et al.*, *Rev. Med. Virol.* **30**, e2099 (2020).
15. WHO, "Human infection with avian influenza A (H5N8) – the Russian Federation" (2021); www.who.int/csr/don/26-feb-2021-influenza-a-russian-federation/en.

ACKNOWLEDGMENTS

This work was supported by National Science and Technology Major Project (2018ZX10101004) and the Academic Promotion Programme of Shandong First Medical University (2019QL006). W.S. is supported by the Taishan Scholars Program of Shandong Province.

10.1126/science.abg6302

ECOLOGY

The growing challenge of vegetation change

Analysis of past change puts risks of plant carbon management in a long-term context

By **Jonathan T. Overpeck**[1] *and* **David D. Breshears**[2]

A substantial portion of the planet has been on fire. Climate change has been implicated in sweeping wildfires in the western United States, Australia, the boreal forest stretching around the globe, Amazonia, and elsewhere (*1*). Other forests have experienced extensive tree loss, again largely because of hotter and drier climate extremes (*2*, *3*). Forest disturbance driven by aridity, heat, fire, disease, pests, and wind creates opportunity for vegetation change. At the same time, climate change shifts conditions to favor different plant species across the landscape. The risk of future vegetation and ecosystem change will continue to grow unless climate change is strongly slowed (*4*). On page 860 of this issue, Mottl *et al.* (*5*) reveal that the drivers of global vegetation change are more substantial than thought, as are the implications for managing carbon with plants.

Many aspects of responding to climate change assessments have become more challenging because observations have shown worse than expected change, and also because our scientific understanding has revealed the fuller complexity of the dynamics behind Earth system change. The Arctic is warming and melting faster than expected, and the rate of global coral death has also exceeded expectations. Sea-level rise forecasts have become worse, while a growing appreciation for the role of increasing temperature in hydroclimatic change

[1]School for Environment and Sustainability, University of Michigan, Ann Arbor, MI, USA. [2]School of Natural Resources and the Environment, University of Arizona, Tucson, AZ, USA. Email: overpeck@umich.edu; daveb@email.arizona.edu

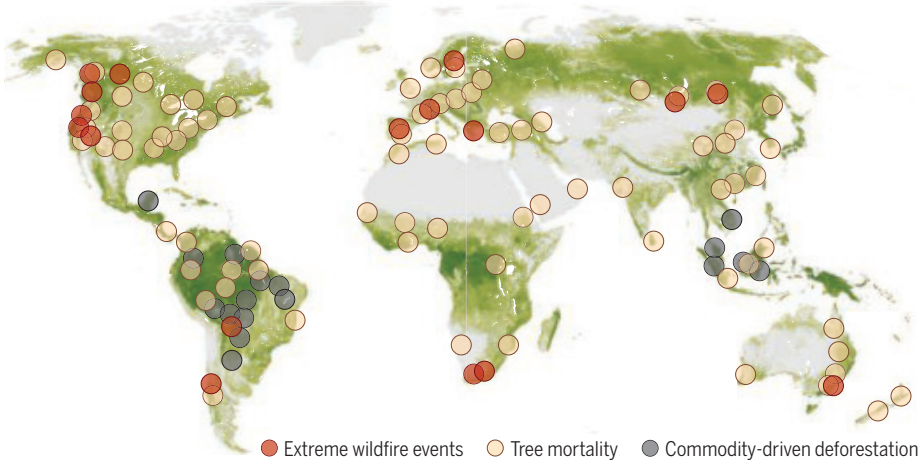
means that the implications of aridification and drought are becoming more dire in many parts of the world (*6*, *7*).

Paleoclimatologists have long known that the largest amount of global climate change since the last Ice Age was concentrated in the period of deglaciation between 16,000 and 10,000 years ago (*4*), and have assumed with good reason that this global climate change drove the largest vegetation change of the post Ice Age period. Mottl *et al.* combined new statistical methods and an impressively large global fossil pollen compilation to show that this assertion is not entirely correct. Instead, it appears that vegetation change across the planet began to accelerate markedly within the last several thousand years as agriculture intensified, and may have exceeded rates observed during the deglaciation. It is known with confidence, however, that the rates of climate change during this more recent period were substantially lower than over the deglacial period. Thus, the new findings point to humans as a potent force, even in preindustrial times, capable of driving large vegetation change at the scale of the planet.

The findings of Mottl *et al.* confirm that the Anthropocene began prior to the Industrial Revolution as humans began to exert a large impact on vegetation, terrestrial ecosystems, biodiversity, and biogeochemical cycles around the globe (*8*). In particular, the study suggests that managing future vegetation change and associated terrestrial ecosystem services could be more difficult than thought. Clear signs of this challenge are evident (see the figure). In addition to expanding wildfires and tree loss (due to drought, heat, and associated pests and pathogens), human-driven deforestation continues to expand globally (*9*). Especially troubling is the ongoing human assault on tropical forests, which hold vast amounts of biodiversity and sequestered carbon and also are critical to atmospheric water recycling at low latitudes (*10*). Humans continue the inexorable pace of deforestation to grow more crops and animals for food, fiber, and energy. Additional climate-driven change is also a sure bet. Even in a world where climate change is soon halted, global temperature rise will likely reach between 1.5° and 2°C above preindustrial levels. This means that global vegetation will likely face climate change effects that are substantially worse than already experienced.

Rapid tree loss around the world

Global tree decline is attributed to commodity-driven deforestation (*9*), loss by wildfire (*1*), and drought- and heat-related mortality (often associated with pests and pathogens). The latter two are affected by increasing atmospheric moisture demand that drives forest stress. Forested areas are shown with tree heights ranging from 5 m (lightest green) to greater than 60 m (darkest green).



GRAPHIC: K. FRANKLIN/*SCIENCE*

Two categories of partial solution exist. One strategy is to stop emissions of greenhouse gases as much, and as fast, as possible. If this is accomplished, climate-driven vegetation change will be more limited, but still a greater challenge to manage than it is today. Another partial solution is to rethink how we manage vegetation, and to manage proactively for the changes that we can anticipate. Given that plant species respond individually to climate change, and that many climatic conditions of the future may be new (*11*), it will likely prove more effective to manage vegetation, particularly forests, for the ecosystem services they provide, rather than attempt to maintain them as they were in the 20th century (*12*). Although complete success is impossible, an important goal must be to reduce the risk of severe wildfires that are destroying lives and communities, injecting increasing amounts of toxic smoke to the air, and releasing growing amounts of carbon and soot to the atmosphere, further accelerating climate change (*1*, *13*).

Managing vegetation for anticipated change will cost more money, but where needed, funding can be generated by the ecosystem services that management protects (*12, 14*). For example, money is already spent to reduce wildfire risk, fight wildfires, and preserve functioning ecosystems for water supply, biodiversity, hunting, fishing, and other forms of recreation. Money is also spent to conserve biodiversity, "wildness," and cultural values. However, adding the management of vegetation for carbon sequestration will require more resources to support those who do the management—most likely those who live in rural and Indigenous communities who need the ecosystem services the most. Nonetheless, this management enterprise could bring about a stronger economy by paying more directly for those desired ecosystem services.

Decision-makers need to enable new science, policy, and finance mechanisms that are optimized for handling the ecosystem disturbance and vegetation change that are unstoppable, and also to ensure that the trees and forests that are planted or preserved for the carbon they sequester survive in the face of climate change and other human threats. Failure to meet this challenge will mean that large terrestrial stores of carbon will be lost to the atmosphere, accelerating climate change and the impacts on vegetation that threaten many more of the ecosystem services on which humans depend. It also means that the dream of large-scale tree-planting as a substitute for direct reductions of atmospheric carbon dioxide emissions may be seriously compromised. The upcoming United Nations Climate Change Conference (*15*) will need to face this challenge head on. ■

REFERENCES AND NOTES

1. A. Duane, M. Castellnou, L. Brotons, *Clim. Change* **165**, 43 (2021).
2. H. Hartmann *et al.*, *New Phytol.* **218**, 15 (2018).
3. K. X. Ruthrof *et al.*, *Sci. Rep.* **8**, 13094 (2018).
4. C. Nolan *et al.*, *Science* **361**, 920 (2018).
5. O. Mottl *et al.*, *Science* **372**, 860 (2021).
6. J. Garner *et al.*, *Earths Futur.* **6**, 1603 (2018).
7. A. Park Williams *et al.*, *Nat. Clim. Chang.* **3**, 292 (2013).
8. W. F. Ruddiman, *Annu. Rev. Earth Planet. Sci.* **41**, ٦ 45 (2013).
9. P. G. Curtis, C. M. Slay, N. L. Harris, A. Tyukavina, M. C. Hansen, *Science* **361**, 1108 (2018).
10. Y. Malhi *et al.*, *Science* **319**, 169 (2008).
11. J. W. Williams, S. T. Jackson, J. E. Kutzbach, *Proc. Natl. Acad. Sci. U.S.A.* **104**, 5738 (2007).
12. W. R. L. Anderegg *et al.*, *Science* **368**, eaaz7005 (2020).
13. S. L. Stephens *et al.*, *Bioscience* **68**, 77 (2018).
14. W. R. Turner *et al.*, *Bioscience* **57**, 868 (2007).
15. United Nations Climate Change Conference, Conference of Parties (COP) 26, 1 to 12 November 2021, Glasgow, UK.

10.1126/science.abi9902

REDOX FLOW BATTERIES

Tanking up energy through atypical charging

Designed ketone molecules can undergo two-electron charge storage in aqueous solutions

By **Bo Hu** *and* **T. Leo Liu**

Aqueous redox flow batteries could provide viable grid-scale electrochemical energy storage for renewable energy because of their high-power performance, scalability, and safe operation (*1*, *2*). Redox-active organic molecules serve as the energy storage materials (*2*, *3*), but only very few organic molecules, such as viologen (*4*, *5*) and anthraquinone molecules (*6*), have demonstrated promising energy storage performance (*2*). Efforts continue to develop other families of organic molecules for flow battery applications that would have dense charge capacities and be chemically robust. On page 836 of this issue, Feng *et al.* (*7*) report a class of ingeniously designed 9-fluorenone (FL) molecules as high-performance, potentially low-cost organic anode electrolytes (anolytes) in aqueous organic redox flow batteries (see the figure, top). These FL anolytes not only display exceptional energy storage performance but also exhibit an unprecedented two-electron storage mechanism.

The past decade has witnessed the rapid development of aqueous organic redox flow batteries using sustainable and tunable redox-active organic molecules as charge storage materials (*2*, *8*, *9*). Previous studies investigated the possibility of using organic ketones as anolyte materials but with limited success (*10*, *11*), and Rodriguez *et al.* (*11*) reported the one-electron, reversible FL/FL$^{\bullet-}$ redox couple in alkaline solutions. However, the poor battery performance of FL molecules was not suitable for durable energy storage, and there was no clear understanding of FL's chemical stability (*11*).

Feng *et al.* report the molecular engineering of FL molecules to achieve substantially improved stability and charge capacity for flow battery applications. The strategy adopted in their research is to introduce electron-withdrawing groups (EWGs), such as sulfonate and carboxylate groups, into the aromatic rings of FL to increase the acid dissociation constant K_a of its reduction product, FL-OH. This design aims to stabilize the charged FL species, such as FL$^{\bullet-}$ radical anions and FL^{2-} dianions, for battery cycling by avoiding the irreversible protonation of these anions and allowing the redox reactions to occur in the potential window available in water (see the figure, bottom). Their density functional theory calculations of a series of FL-OH derivatives also suggest that EWGs effectively increase the K_a of both O-H and benzylic C-H protons. Upon functionalization of FL with EWGs, the first electron reversibility of FL at ~–0.7 V versus the normal hydrogen electrode is notably improved in alkaline solutions. Nevertheless, the second electron redox event at ~–1.13 V is still irreversible, as revealed in cyclic voltammetry studies, but is accessible for energy storage, as explained below.

For flow battery demonstration, the authors chose 2-carboxylate-7-sulfonate fluorenone (4C7SFL). A solution of 1.36 M 4C7SFL in NaOH was used as an anolyte with a mixture of $K_4Fe(CN)_6/K_3Fe(CN)_6$ as a cathode electrolyte (catholyte). At room temperature, the 4C7SFL/ferrocyanide flow batteries delivered a high energy efficiency of 78.8% at 60 mA cm^{-2}. The battery was cycled at 20 mA cm^{-2} for more than 4 months and had a small capacity decay of 2.62%—equivalent to a capacity decay of 0.02% per day. The exceptional chemical stability of 4C7SFL was confirmed by postcycling spectroscopic studies that revealed only a small amount of a desulfonated product. Notably, the 4C7SFL anolyte actually exhibited two-electron storage capacity (equivalent to 1.8 moles of electrons per 1.0 mole of 4C7SFL) in the battery studies, despite the control of the charge and discharge processes at the FL/FL$^{\bullet-}$ redox couple.

At first glance, it would seem impossible that an irreversible redox process such as the second-electron reduction of 4C7SFL could be used for energy storage under these conditions. Feng *et al.* propose that the two-electron storage property of 4C7SFL originates from the disproportionation of a FL$^{\bullet-}$ radical anion, rather than the electrochemical reduction of FL$^{\bullet-}$ to FL^{2-}. During the charging process, electrochemically generated FL$^{\bullet-}$ disproportionates to FL-OH, a two-electron reduced product, and FL. The regenerated FL undergoes reduction again until an equilibrium is reached under battery-charging conditions.

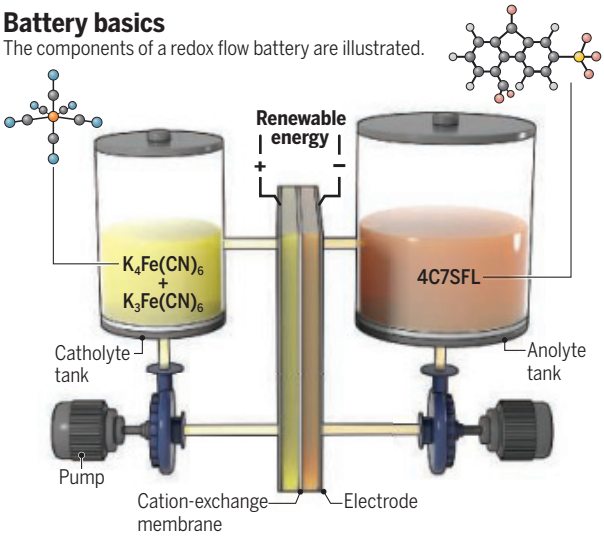
This hypothesis is supported by nuclear magnetic resonance spectroscopy studies that detected the

Extra electrons without catalysts

Feng *et al.* demonstrated an aqueous organic redox flow battery based on reversible hydrogenation of functionalized 9-fluorenone (2-carboxylate-7-sulfonate fluorenone, or 4C7SFL). This molecule enabled two-electron storage without the use of a catalyst.

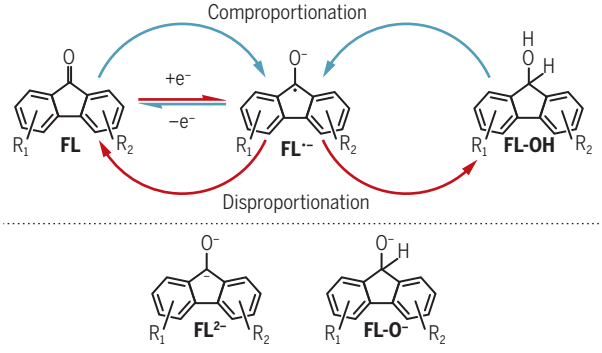
Battery basics

The components of a redox flow battery are illustrated.



Charging and discharging molecules

Charging (red arrows) and discharging (blue arrows) mechanism of 9-fluorenone (FL) (top) and possibly involved species (bottom) are shown.



GRAPHIC: V. ALTOUNIAN/*SCIENCE*

Department of Chemistry and Biochemistry, Utah State University, Logan, UT, USA.
Email: leo.liu@usu.edu

FL-OH product, 4C7SFL-OH, even at a 25% state of charge. The authors also studied the comproportionation reaction by combining 4C7SFL and 4C7SFL-OH, and they detected a small amount of the $[4C7SFL]^{\bullet-}$ radical by electron paramagnetic resonance spectroscopy. The $FL^{\bullet-}$ generated from the comproportionation can be used for electrochemical discharge. These studies suggest that an equilibrium exists between $FL^{\bullet-}$, FL, and FL-OH, and also favors the disproportionation.

The formation and cleavage of the benzylic C–H bond of FL in the disproportionation and comproportionation reactions are likely regulated by subtle proton-coupled electron transfer processes that are subject to further study. The singly protonated species, $FL\text{-}O^-$, may be the final charged state and involves the chemical reactions under the strong alkaline condition. In addition, the reduction of ketones to alcohols typically involves a catalyst (*12*), so the reversible, uncatalyzed hydrogenation of FL represents an unusual two-electron storage mechanism for flow battery applications and is mechanistically different from the direct electrochemical two-electron reduction of viologen and anthraquinone anolytes (*2*).

The work by Feng *et al.* expands the selection of stable organic anolytes and serves as a good example of rational molecular engineering to develop durable electrolyte materials. However, a large excess of the $K_4Fe(CN)_6/K_3Fe(CN)_6$ catholyte was needed in the flow battery tests because of the long-term instability of ferro- and ferricyanide in alkaline solutions (*13*). Thus, developing catholyte molecules with durabilities and capacities comparable to those of fluorenone, viologen, and anthraquinone anolyte molecules is urgently needed to fully unleash the energy storage potential of aqueous organic redox flow batteries. ■

REFERENCES AND NOTES

1. B. Dunn, H. Kamath, J.-M. Tarascon, *Science* **334**, 928 (2011).
2. J. Luo, B. Hu, M. Hu, Y. Zhao, T. L. Liu, *ACS Energy Lett.* **4**, 2220 (2019).
3. M. Park, J. Ryu, W. Wang, J. Cho, *Nat. Rev. Mater.* **2**, 16080 (2016).
4. B. Hu, C. DeBruler, Z. Rhodes, T. L. Liu, *J. Am. Chem. Soc.* **139**, 1207 (2017).
5. J. Luo *et al.*, *Joule* **3**, 149 (2019).
6. Y. Ji *et al.*, *Adv. Energy Mater.* **9**, 1900039 (2019).
7. R. Feng *et al.*, *Science* **372**, 836 (2021).
8. J. Winsberg, T. Hagemann, T. Janoschka, M. D. Hager, U. S. Schubert, *Angew. Chem. Int. Ed.* **56**, 686 (2017).
9. Y. Ding, C. Zhang, L. Zhang, Y. Zhou, G. Yu, *Chem. Soc. Rev.* **47**, 69 (2018).
10. P. Leung *et al.*, *Appl. Energy* **197**, 318 (2017).
11. J. Rodriguez Jr., C. Niemet, L. D. Pozzo, *ECS Trans.* **89**, 49 (2019).
12. O. Eisenstein, R. H. Crabtree, *New J. Chem.* **37**, 21 (2013).
13. J. Luo *et al.*, *Nano Energy* **42**, 215 (2017).

ACKNOWLEDGMENTS

The authors acknowledge funding support from the National Science Foundation (Career Award, grant 1847674) and a Utah State University faculty start-up.

10.1126/science.abi5911

PHOTO: CÉCILE POUZET (FRAIB/CNRS)

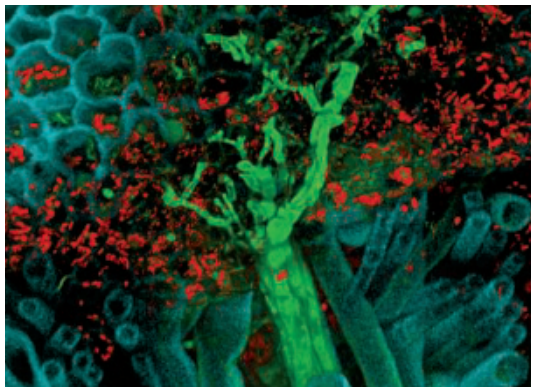
SYMBIOSIS

Plant lipids enticed fungi to mutualism

Evolution of lipid transfer from plants to fungi allowed plants to colonize land

By **Harro J. Bouwmeester**

The migration of plants from water to newly emerged land some 450 million years ago required plants to acquire a number of crucial new traits. Fossil records provide compelling evidence that one of these traits is the symbiosis (or mutualism) between these early land plants and arbuscular mycorrhizal (AM) fungi. On page 864 of this issue, Rich *et al.* (*1*) show that the primitive land plant *Marchantia paleacea* produces lipids that are transferred to the fungus and that this process is essential for a functional symbiosis (see the image). This localized lipid biosynthesis also occurs in higher plants that engage in symbiosis with AM fungi (*2*, *3*), but not in algae, suggesting that this process evolved 450 million years ago, allowing plants to colonize land, and is conserved across the plant kingdom.



The confocal microscopy image shows a symbiotic fungus (*Rhizophagus irregularis*) colonizing the liverwort *Marchantia paleacea* (plant cell walls, cyan; chloroplasts, red; fungus, green).

The symbiosis of plants with AM fungi is so crucial for plant growth on land that about 80% of land plants engage in it (*4*). The plant allows AM fungi to enter its roots and form nutrient exchange structures called arbuscules in its cells (see the figure). Outside the root, the fungal hyphae grow into the soil, up to 30 cm from the plant root, where they can take up water, phosphorus, nitrogen, and other elements that the plant cannot reach (*4*). For a long time, it was assumed that plants, in return for the resources supplied by the fungus, provided carbohydrates from photosynthesis to the fungus. Only recently, it was discovered that in addition to carbohydrates, plants also supply lipids to the fungus (*2*, *3*). To investigate how old this mechanism is, Rich *et al.* used an elegant approach: a comparison of RNA sequencing gene expression data on the AM fungal interaction in the primitive *M. paleacea* with data of AM fungal interactions in higher plants. With this comparison, the authors show that orthologs of many of the known higher-plant symbiotic genes are also expressed in *M. paleacea* upon AM fungal colonization, confirming conservation across 450 million years of plant diversification [also see (*5*)]. Rich *et al.* report that this includes genes that have been shown in higher plants to be responsible for lipid exchange from the plant to the fungus, such as the lipid biosynthesis–related *REQUIRED FOR ARBUSCULAR MYCORRHIZATION 2* (*RAM2*) and the lipid transporter *STUNTED ARBUSCULE 1* and *2* (*STR1* and *STR2*) (see the figure). With a number of experiments, they subsequently show that *M. paleacea* is indeed producing lipids and that they are essential for the symbiosis with AM fungi.

Lipid biosynthesis and transfer are not the only evolutionarily conserved processes that occur in *M. paleacea* upon colonization by AM fungi. Rich *et al.* also report orthogroups of genes involved in strigolactone biosynthesis that show a conserved response across the plant kingdom, including in *M. paleacea*. Strigolactones are rhizosphere signaling molecules that have been shown to play a key role in the colonization of roots by AM fungi (*6*) and are regularly claimed to have been instrumental for terrestrialization (*7*) (see the figure). Rich *et al.* do not go into detail on these genes, but it can be safely assumed that they refer to *CAROTENOID CLEAVAGE DIOXYGENASE 8a* and *8b* (*CCD8a* and *CCD8b*). The enzyme

Plant Hormone Biology Group, Swammerdam Institute for Life Sciences, University of Amsterdam, Science Park 904, 1098 XH Amsterdam, Netherlands. Email: h.j.bouwmeester@uva.nl

CCD8 catalyzes the second dedicated step in strigolactone biosynthesis (*8*). Of the two homologs, only *CCD8a* expression is notably up-regulated upon AMF colonization. In higher plants, this pattern is less clear; *CCD8* expression is up-regulated in rice, petunia, and *Medicago truncatula* but not in sunflower and poplar. Rich *et al.* list other carotenoid biosynthesis–related and cytochrome P450 genes that are potentially involved in strigolactone biosynthesis. Some of these are also up-regulated under AM fungi colonization in *M. paleacea*, but a consistent pattern in both *M. paleacea* and the higher plants is lacking. Recent evidence suggests that strigolactone biosynthesis is up-regulated upon AM fungal colonization (*9*), whereas other studies show that AM fungal colonization results in reduced exudation of strigolactones (*10*).

Intriguingly, Rich *et al.* also describe an ABC transporter (Marpal_utg000130g0170881), which has orthologs in all the higher plants included in this study, with up-regulated expression under AM fungal colonization across the plant kingdom. The only unambiguously identified strigolactone transporter so far is the petunia ABC transporter *PLEIOTROPIC DRUG RESISTANCE 1* (*PDR1*), with expression that is up-regulated under AM fungal colonization and was shown to be required for AM fungal symbiosis (*11*). It would be very exciting if this *M. paleacea* ABC transporter turns out to be a strigolactone transporter as well.

Rich *et al.* then focus on the processes that maintain the symbiotic relationship after it has been established, in particular, the transcriptional regulation of lipid biosynthesis. They identify two transcription factors that seem to be highly conserved across the plant kingdom and coincide with terrestrialization: *WRINKLED* (*WRI*) and *REQUIRED FOR ARBUSCULE DEVELOPMENT 1* (*RAD1*). Overexpression of *WRI* in *M. paleacea* resulted in increased expression of fatty acid biosynthesis–related genes, whereas inactivation of WRI resulted in severely compromised AM fungi colonization.

Higher plants contain multiple paralogs of *WRI*, of which several function, apparently redundantly, in symbiosis (*12*). *M. paleacea* contains only one copy of *WRI*, and extensive orthology searches led Rich *et al.* to conclude that *WRI* (and *RAD1*) are absent from the nonsymbiotic algae. The likelihood that recruitment of *WRI* and *RAD1* occurred specifically for this purpose is further strengthened by the observation that fatty acid and lipid biosynthesis also occur in algae (*13*) but are not used for symbiosis. In all, the findings of Rich *et al.* show that these transcription factors specifically evolved to facilitate symbiosis, which was required for terrestrialization.

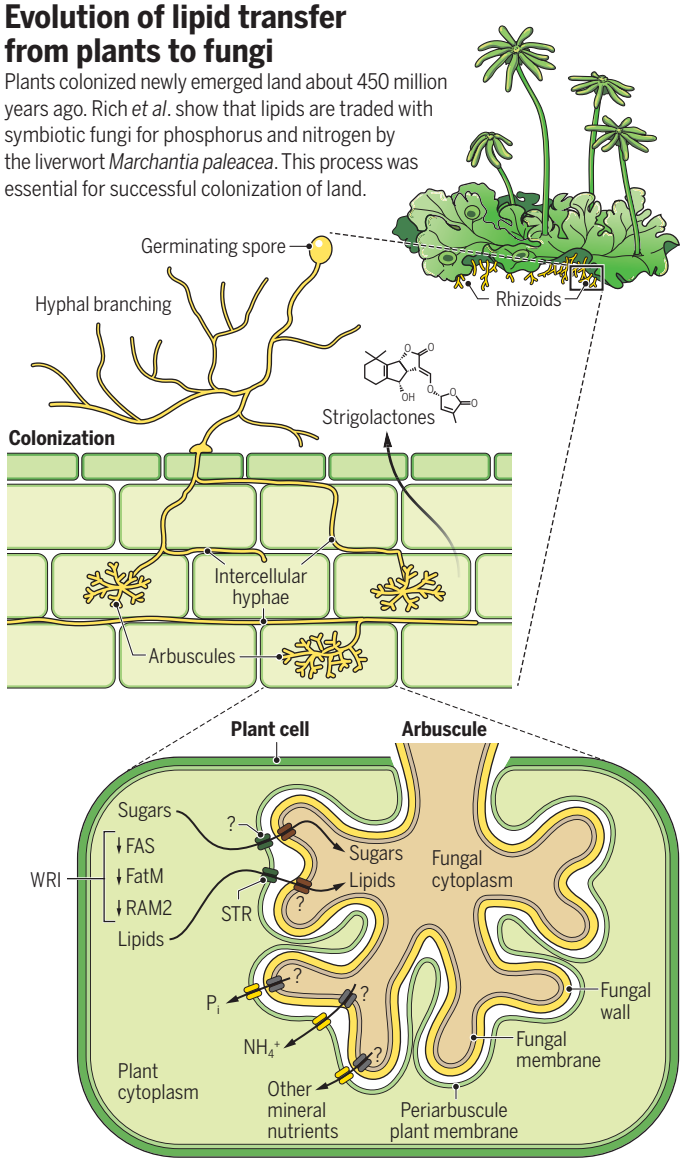
The presence of a single copy of *WRI* in *M. paleacea* suggests that the multiple paralogs of *WRI* in higher plants (*12*) have evolved from a single ancestor. One of these orthologs, *WRINKLED1*, is involved in the regulation of lipid biosynthesis in seeds (*14*). Evidently, duplication and neofunctionalization of the ancestral *WRI* in higher plants not only resulted in the apparent specialization of its function in symbiosis but also resulted in the loss of its symbiotic function to allow for the large accumulation of lipids in the seeds of seed plants.

With their study, Rich *et al.* highlight the importance of the mutual exchange of resources between plants and AM fungi as a driver of the symbiosis. They show that plants have evolved transcriptional regulators, such as *WRI*, to allow for the production of lipids for the AM fungi in the cells where the AM symbiotic organ, the arbuscule, has formed. The further radiation of *WRI* during the evolution of higher plants confirms the importance of this process for symbiosis with AM fungi.

It will be of interest to see why multiplication of *WRI* arose in higher plants and what the specific roles and fitness benefits of these paralogs might be. The datasets generated by Rich *et al.* could also provide information about other symbiotic genes that may have evolved to allow terrestrialization. This could, for example, further illuminate the presumptive role of strigolactones in the terrestrialization process. ■

Evolution of lipid transfer from plants to fungi

Plants colonized newly emerged land about 450 million years ago. Rich *et al.* show that lipids are traded with symbiotic fungi for phosphorus and nitrogen by the liverwort *Marchantia paleacea*. This process was essential for successful colonization of land.



FAS, type I fatty acid synthase; FatM, acyl-ACP (acyl carrier protein) thioesterase required for arbuscular mycorrhizal symbiosis; P_i, inorganic phosphorus; RAM2, REQUIRED FOR ARBUSCULE MYCORRHIZATION 2; STR, STUNTED ARBUSCULE; WRI, WRINKLED.

GRAPHIC: KELLIE HOLOSKI/*SCIENCE*

REFERENCES AND NOTES

1. M. K. Rich *et al.*, *Science* **372**, 864 (2021).
2. Y. Jiang *et al.*, *Science* **356**, 1172 (2017).
3. L. H. Luginbuehl *et al.*, *Science* **356**, 1175 (2017).
4. S. E. Smith, F. A. Smith, *Annu. Rev. Plant Biol.* **62**, 227 (2011).
5. G. V. Radhakrishnan *et al.*, *Nat. Plants* **6**, 280 (2020).
6. K. Akiyama, K. Matsuzaki, H. Hayashi, *Nature* **435**, 824 (2005).
7. M. T. Waters *et al.*, *Annu. Rev. Plant Biol.* **68**, 291 (2017).
8. Y. Wang, H. J. Bouwmeester, *J. Exp. Bot.* **69**, 2219 (2018).
9. J. Choi *et al.*, *Nat. Commun.* **11**, 2114 (2020).
10. J. A. López-Ráez *et al.*, *J. Plant Physiol.* **168**, 294 (2011).
11. T. Kretzschmar *et al.*, *Nature* **483**, 341 (2012).
12. L. Xue *et al.*, *Proc. Natl. Acad. Sci. U.S.A.* **115**, E9239 (2018).
13. H. H. Chen, J. G. Jiang, *J. Agric. Food Chem.* **65**, 8099 (2017).
14. S. A. Baud, S. Wuillème, A. To, C. Rochat, L. Lepiniec, *Plant J.* **60**, 933 (2009).

ACKNOWLEDGMENTS

H.J.B. is funded by the Dutch Research Council (NWO/OCW) for the MiCRop Consortium program "Harnessing the second genome of plants" (grant 024.004.014) and by the European Research Council through ERC Advanced grant CHEMCOMRHIZO (670211).

10.1126/science.abi8016

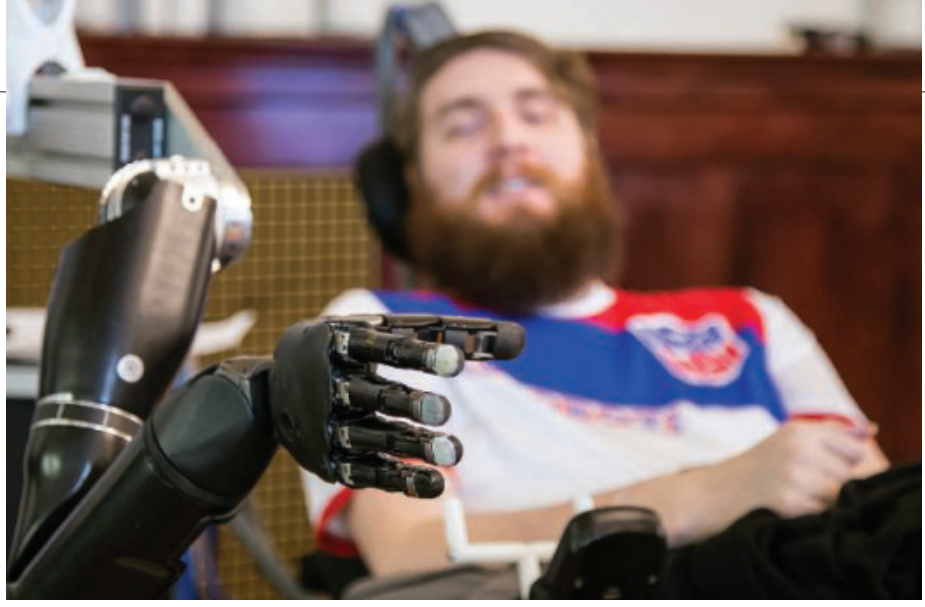


PHOTO: UPMC/PITT HEALTH SCIENCES

A brain-machine interface, which gives sensory feedback from a robotic hand directly to the brain, boosts the speed and success rate of grasping.

NEUROSCIENCE

Putting touch into action

Bidirectional brain-machine interfaces boost movement restoration in a paralyzed user

By **A. Aldo Faisal**[1,2,3,4,5]

Human tactile senses maintain contact with the environment and are essential for the ability to manipulate objects dexterously (*1*). People suffering from upper spinal cord injuries, nerve injuries, and other forms of arm paralysis lose the ability not only to move their hand but also to feel with their fingers. Over the past decades, brain-machine interfacing has achieved the ability to read out action intentions from the human brain and restore movement by enabling paralyzed patients to control robotic arms (*2*) or to electrically stimulate muscles so paralyzed arms can move again (*3*). It is commonly assumed that this needs to be complemented with restoring sensory feedback. On page 831 of this issue, Flesher *et al.* (*4*) demonstrate a substantial practical benefit for a paralyzed patient whose ability to manipulate objects through a brain-controlled robotic arm was substantially increased through artificial tactile feedback.

There are two main ways by which lost sensory feedback to the brain could be restored. The first is sensory substitution, where unaffected regions of the body or other senses are hijacked to convey tactile information—for example, by artificially stimulating a patch of skin where natural sensory feedback is still intact or by audio or visual cues as a proxy (*5*) to signal where and how a robotic hand touched an object. Sensory substitution techniques are low-cost, noninvasive, and easy to set up on a day-to-day basis. However, they require some learning, they do not give feedback that feels natural, and they repurpose sensory capacity, which crowds the patient's intact senses and may reduce their ability to perceive or communicate with the environment.

The second option is to restore sensory feedback by directly interfacing with the nervous system. This can be at the peripheral level, for example, on residual nerves in arm stumps of hand amputees (*6*) or in the central nervous system, as is necessary in patients with high-level spinal cord injuries. "Writing" sensory information into the brain is not trivial: It usually requires neurosurgery, implantation of neural interfaces, and then finding a way to communicate with the brain so that the information is perceived meaningfully. Although it has been possible for more than 80 years to evoke tactile sensations by stimulating hundreds of neurons with a small electrical current (microstimulation), generating appropriate and controlled sensory feedback is more challenging.

The microstimulation approach first required a better understanding of how tactile information is processed and represented in the nervous system and better neural interfaces. Decades of research in human volunteers and electrophysiological studies in nonhuman primates unlocked the foundations of tactile processing in the nervous system and how to stimulate the somatosensory cortex (*7*, *8*). Critically, appropriate intracortical microstimulation (ICMS) with electrodes implanted in human somatosensory cortex was shown to create tactile sensations that appeared to originate from specific locations on the hand. Moreover, these ICMS experiments could induce tactile sensations that felt like natural sensations of pressure, sensation could be graded in strength, and the mapping between ICMS and reported sensation could remain stable for months (*9*).

Flesher *et al.* now demonstrate the practical implementation of a bidirectional brain-machine interface (which "reads" and "writes" information to the brain). Their system decoded the brain activity of a tetraplegic patient to translate their intentions into control commands for a robotic arm and hand. At the same time, sensors on the robotic hand recorded the mechanical forces it experienced, transmitting these to the somatosensory cortex through ICMS. Specifically, the robotic arm and hand used torque sensing at the metacarpophalangeal joint at the base of the four robotic fingers to measure the forces they were experiencing when manipulating objects. Then it translated these into electrical stimuli that the authors had previously established would trigger tactile sensations linked to each of the four fingers. The sensations were localized to the same finger, and the strength of the sensations varied with the strength of the forces that the fingers experienced. Although the tactile feedback was limited in how natural it may have felt, it had a strong impact on performance, enabling the patient to perform the task much faster.

The time taken to successfully grasp an object was halved and grasping was less prone to error, suggesting that the feedback provided gave the individual confidence about when the object was reliably in their hand. The movement time after picking up the object and transferring it to its target also improved, suggesting that the stimulation may have wider effects, including potentially stimulating motor circuits. The patient's performance improved rapidly and did not require training, suggesting that ICMS acted differently from sensory substitution such that little learning was involved. A direct comparison of task performance using ICMS-based sensory feedback versus sensory substitution in performing the same task would answer the important question of whether

[1]Brain & Behaviour Lab, Imperial College, London, UK. [2]Department of Bioengineering, Imperial College, London, UK. [3]Department of Computing, Imperial College, London, UK. [4]UK Research and Innovation (UKRI) Centre for Doctoral Training in AI for Healthcare, Imperial College, London, UK. [5]Medical Research Council (MRC) London Institute of Medical Sciences, London, UK. Email: a.faisal@imperial.ac.uk

any modality of sensory feedback would be equally effective.

The results of Flesher *et al.* open up many avenues of inquiry, including the possibility of advancing robotics and the development of tactile artificial skins (*10*) into clinical use, and transhumanist questions about augmenting human capabilities with nonbiological sensors. This proof-of-principle study raises an important challenge: Although a rich body of work in neuroscience developed high-level computational theories of how sensory feedback should control movement (*11*), much of the circuit-level understanding is limited and focused on decoding of the action. Yet, brains operate best when the loop between perception and action is closed, as demonstrated so effectively in this study. Moreover, sensors that inform how a robotic hand is configured (hand pose) are at least as important as tactile sensors, yet, in neuroscience, much of the research has focused on touch instead of the sense of bodily pose (proprioception). Integrating both senses—touch and proprioception—are going to be important for future bidirectional brain-machine interfaces and may help future patients to experience full restoration of their motor capabilities.

Although neurotechnology has progressed in great leaps over the past decade, the uptake and long-term use of these devices was not commensurate. For example, many bionic hand prostheses are often abandoned within months by patients, which has been attributed to users perceiving them as inconvenient foreign objects that are not a part of their body (*12*). Restoration of sensory feedback through nervous system interfacing, as demonstrated by Flesher *et al.*, is hopefully going to resolve these issues, not only because such technology substantially improves a patient's motor capabilities but also because it may restore sensory ownership over their technologically extended body (*13*). ■

REFERENCES AND NOTES

1. R. L. Sainburg *et al.*, *J. Neurophysiol.* **73**, 820 (1995).
2. L. R. Hochberg *et al.*, *Nature* **485**, 372 (2012).
3. C. Ethier *et al.*, *Nature* **485**, 368 (2012).
4. S. N. Flesher *et al.*, *Science* **372**, 831 (2021).
5. P. Bach-y-Rita, S. W Kercel, *Trends Cogn. Sci.* **7**, 541 (2003).
6. S. Raspopovic *et al.*, *Sci. Transl. Med.* **6**, 222ra19 (2014).
7. S. J. Bensmaia, L. E. Miller, *Nat. Rev. Neurosci.* **15**, 313 (2014).
8. T. Callier *et al.*, *J. Neural Eng.* **12**, 056010 (2015).
9. S. N. Flesher *et al.*, *Sci. Transl. Med.* **8**, 361ra141 (2016).
10. R. Dahiya, *Proc. IEEE* **107**, 247 (2019).
11. J. Diedrichsen, R. Shadmehr, R. B. Ivry, *Trends Cogn. Sci.* **14**, 31 (2010).
12. E. A. Biddiss, T. T. Chau, *Prosthet. Orthot. Int.* **31**, 236 (2007).
13. T. Makin, F. de Vignemont, A. A. Faisal, *Nat. Biomed. Eng.* **1**, 0014 (2017).

ACKNOWLEDGMENTS

A.A.F. acknowledges his UKRI Turing AI Fellowship (EP/V025449/1).

10.1126/science.abi7262

PHYSIOLOGY

Putting a brake on hunger

Targeting activation of the melanocortin-4 receptor for weight loss in obesity

By **Sadaf Farooqi**

G protein–coupled receptors (GPCRs) interact with heterotrimeric guanine nucleotide-binding (G) proteins to modulate many physiological processes. Their structural properties make them highly druggable targets; 30% of currently prescribed medications target GPCRs. The melanocortin-4 receptor (MC4R) is a brain-expressed GPCR that plays a critical role in the regulation of body weight and for this reason has been the subject of intense focus as a target for weight loss therapy. On page 808 of this issue, Israeli *et al.* (*1*) present the structure of MC4R in complex with its main effector G protein ($G\alpha_s$) and a weight loss drug that targets MC4R, setmelanotide. These findings provide mechanistic insights into how MC4R is activated and could inform the rational design of new weight loss therapies to tackle the substantial health burden faced by people with obesity.

Obesity (an excess of adipose tissue that adversely affects health) is a global public health problem because of the associated comorbidities of type 2 diabetes, cardiovascular disease, and cancer. Morbidity and mortality are greatest in people with severe obesity [defined as a body mass index (BMI) >40 kg/m^2], for whom new medical treatments are urgently needed. Weight loss of 5 to 10% of baseline weight is sufficient to substantially reduce the risk of complications in severely obese individuals.

One of the major challenges in developing anti-obesity medications is that the brain pathways that regulate weight overlap with those that modulate mood, anxiety, and behavior. Neurons in one particular region, the hypothalamus, are pivotal to weight regulation (*2*). Hypothalamic neuronal circuits receive inputs from, and project to, multiple parts of the brain, allowing them to respond to innate biological signals and environmental cues (such as sight, smell, and taste) to modulate hunger (drive to eat) and satiety (fullness after a meal) to maintain body weight. Because receptors that mediate the effects of neurotransmitters and neuropeptides such as dopamine, serotonin, and norepinephrine are widely expressed on these hypothalamic neurons, it has been challenging to target specific appetite-regulating molecules without affecting other centrally driven physiological systems. For this reason, many anti-obesity medications have been withdrawn because of concerns about the safety of long-term use.

A key hypothalamic pathway involved in the regulation of weight comprises neurons that respond to leptin, the major hormonal signal of nutritional state (*3*), which defends against starvation. Leptin-responsive neurons express pro-opiomelanocortin (POMC) (which is post-translationally processed to yield melanocortin peptides) and agouti-related protein (AgRP); these peptides function as neurotransmitters. POMC- and AgRP-expressing neurons synapse with second-order neurons expressing MC4R, which in turn connect to preganglionic sympathetic neurons that regulate blood pressure. In the fasted state, a fall in circulating leptin concentrations stimulates AgRP$^+$ neurons while inhibiting POMC$^+$ neurons, the net effect being to reduce activation of MC4R (the brake in the circuit), driving hunger and food intake to restore energy homeostasis. In the fed state, increased leptin concentrations stimulate POMC$^+$ neurons while inhibiting AgRP$^+$ neurons, resulting in increased activation of MC4R, which puts a brake on hunger and eating.

Targeted deletion of *Mc4r* in mice causes weight gain (*4*), and in humans, heterozygous loss-of-function *MC4R* mutations that reduce $G\alpha_s$-mediated cyclic adenosine monophosphate (cAMP) production have been identified in cohorts of obese children and adults in many populations (*5*, *6*). Common variants near to the *MC4R* locus are associated with increased BMI in the population (*7*), and gain-of-function *MC4R* variants are associated with protection from obesity and type 2 diabetes (*8*). Cumulatively, a substantial amount of genetic evidence supports the critical role of this GPCR in the regulation of food intake and body weight (see the figure). Unsurprisingly, therefore, the development of MC4R agonists for weight loss therapy has been a major focus of drug development for 20 years (*9*).

Wellcome-MRC Institute of Metabolic Science, Box 289, Addenbrooke's Hospital, Cambridge, UK. Email: isf20@cam.ac.uk

The study by Israeli *et al.* may provide answers to a number of questions in the field. The development of cryo–electron microscopy (cryo-EM) and related methods has led to the characterization of structures for many GPCRs in the inactive state or bound to inverse agonists and antagonists, including recently for MC4R (*10*). However, structural determination of agonist-bound GPCRs in the fully active state, coupled to a heterotrimeric G protein, has been more challenging. Outstanding questions include the structural basis of the interaction between MC4R and other effectors. MC4R mutations can affect the recruitment of β-arrestins, which are scaffolding proteins that drive endocytosis, signaling, and gene transcription through mitogen-activated protein kinase (MAPK) pathway activation; MC4R mutations can also affect receptor recycling and homodimerization (*11*). Several accessory proteins regulate MC4R activity; specifically, understanding how melanocortin-2 receptor accessory protein 2 (MRAP2) interacts with MC4R to regulate weight remains an important question because mice lacking *Mrap2* develop severe obesity (*12*). Structures of MC4R may guide predictions of how genetic variants in other melanocortin receptors affect their function. MC1R, expressed on melanocytes in skin and hair, is highly polymorphic; variants are associated with red hair, fair skin, freckles, and melanoma risk. Additionally, MC3Rs expressed on $AgRP^+$ neurons modulate the activity of $MC4R^+$ neurons in response to caloric restriction or to a calorie-rich diet and are implicated in weight gain.

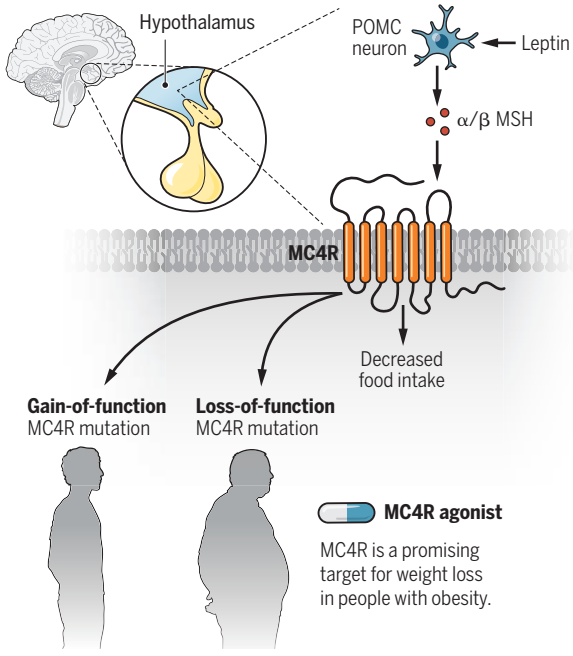
The structure reported by Israeli *et al.* may clarify the mechanisms by which germline inactivating mutations in the gene encoding $G\alpha_s$ (*GNAS*) cause an imprinted monogenic disorder that is characterized by developmental delay and obesity with or without hormone resistance. Brain-specific deletion of the maternal *Gnas* allele impairs the ability of an MC4R agonist to reduce body weight, suggesting that MC4Rs are involved in obesity in *GNAS* deficiency. As such, modeling of *GNAS* mutations may provide new insights into whether human *GNAS* mutations may directly impair downstream MC4R signaling.

Structural models can provide valuable information to inform drug development and may illuminate the mechanisms that underlie variation in response within a class of drugs. First-generation MC4R agonists increased blood pressure in clinical trials, effects that halted their development; MC4R deficiency in mice and humans leads to reduced blood pressure because of impaired sympathetic tone, suggesting that the coupling of changes in weight and blood pressure is mediated by central melanocortin signaling (*13*). Yet, for reasons that are not understood, setmelanotide reduces body weight without increasing blood pressure. As a result of its efficacy and safety profile (main side effect being hyperpigmentation due to agonism at MC1R), it has recently been approved by the U.S. Food and Drug Administration (FDA) for chronic weight management in POMC and leptin receptor deficiency (*14*). Understanding the molecular basis for the unexpected divergence between first- and second-generation MC4R agonists could aid the design of new drugs targeting MC4R and indeed other GPCRs because activation domains are often highly conserved between receptors. Another potential therapeutic strategy may be informed by phenotypic studies of obese people with loss-of-function *MC4R* mutations who have an increase in lean body mass (*6*). These findings, which align with findings in mice (*4*), suggest that therapeutic antagonism of MC4R could potentially be useful in conditions characterized by weight loss and suppression of appetite, such as cancer cachexia.

As highlighted by Israeli *et al.*, there is considerable interest in whether some obese people with pathogenic *MC4R* mutations will respond to setmelanotide. Potential mechanisms by which the agonist could lead to weight loss in those with nonfunctioning MC4Rs include action as a pharmacological chaperone to rescue plasma membrane expression of mutant forms of MC4R that exhibit impaired trafficking. Alternatively, because most people are carriers of heterozygous *MC4R* mutations, setmelanotide may increase signaling through normal (wild type) MC4R. The MC4R structure provided by Israeli *et al.* may allow more precise modeling of the effects of specific obesity-associated *MC4R* mutations and structural prediction of their responsiveness to setmelanotide. Given the prevalence of MC4R deficiency, which could be up to 0.3% of people according to data from a UK birth cohort (*15*), the potential to treat a substantial number of people with severe obesity has major implications for their clinical care. This work advances the much-anticipated potential of precision medicine for the treatment of people with severe obesity. ■

A drug target for obesity

In the hypothalamus, leptin-responsive neurons express pro-opiomelanocortin (POMC), which is processed to yield α- and β-melanocyte stimulating hormone (MSH), which activate melanocortin-4 receptor (MC4R). MC4R activation decreases hunger and food intake and also regulates blood pressure. Loss-of-function MC4R mutations are associated with increased body mass index, whereas gain-of-function mutations are associated with protection from obesity.



GRAPHIC: KELLIE HOLOSKI/*SCIENCE*

REFERENCES AND NOTES

1. H. Israeli *et al.*, *Science* **372**, 808 (2021).
2. L. Gautron *et al.*, *Cell* **161**, 133 (2015).
3. J. M. Friedman, *Nat. Metab.* **1**, 754 (2019).
4. D. Huszar *et al.*, *Cell* **88**, 131 (1997).
5. C. Vaisse *et al.*, *J. Clin. Invest.* **106**, 253 (2000).
6. I. S. Farooqi *et al.*, *N. Engl. J. Med.* **348**, 1085 (2003).
7. R. J. Loos *et al.*, *Nat. Genet.* **40**, 768 (2008).
8. L. A. Lotta *et al.*, *Cell* **177**, 597 (2019).
9. G. S. H. Yeo *et al.*, *Mol. Metab.* **48**, 101206 (2021).
10. J. Yu *et al.*, *Science* **368**, 428 (2020).
11. B. Brouwers *et al.*, *Cell Rep.* **34**, 108862 (2021).
12. M. Asai *et al.*, *Science* **341**, 275 (2013).
13. J. R. Greenfield *et al.*, *N. Engl. J. Med.* **360**, 44 (2009).
14. K. Clément *et al.*, *Lancet Diabetes Endocrinol.* **8**, 960 (2020).
15. K. H. Wade *et al.*, *medRxiv* 10.1101/2020.10.30.20220467 (2020).

ACKNOWLEDGMENTS

I.S.F. was supported by the Wellcome Trust (207462/Z/17/Z), the National Institute for Health Research Cambridge Biomedical Research Centre, Fondation Botnar, and the Bernard Wolfe Health Neuroscience Endowment and wishes to thank members of her research team for their contributions. I.S.F has consulted for a number of companies seeking to target MC4R and design weight loss treatments.

10.1126/science.abi8942

POLICY FORUM

CHILDREN AND FAMILIES

The impact of early childhood interventions on mothers

Failure to measure the impacts on women's time and other maternal outcomes implicitly sets their value at zero

By **David K. Evans[1], Pamela Jakiela[2], Heather A. Knauer[3]**

Over 250 million children in low- and middle-income countries (LMICs) are at risk of failing to meet their developmental potential, primarily because of a lack of adequate nutrition and stimulation in early childhood (*1*). Well-designed early childhood development (ECD) interventions can have substantial impacts on children's physical, cognitive, and socioemotional development, as well as their eventual schooling attainment, wages, and other outcomes (*1*–*3*). Although the potential indirect effects of interventions on mothers and other household members are generally acknowledged, few studies explicitly quantify outcomes related to labor market activities, health, or well-being of household members other than young children. This may lead policymakers to overinvest in programs that impose substantial costs on women and to underinvest in those that improve women's well-being. Systematically ignoring impacts on specific subgroups—particularly vulnerable groups such as women in LMICs—risks exacerbating inequalities in the name of evidence-based policy.

Many ECD interventions have important implications for mothers and other caregivers. Center-based care may give mothers more time for outside labor force opportunities, whereas parent education and home visiting programs impose on mothers' time. Parent education programs may improve maternal mental health by equipping mothers with skills to better handle stressful situations, but they may also change parents' beliefs about the extent to which they are taking adequate care of their children. Child-targeted cash transfer programs may reduce stress by loosening household budget constraints.

[1]Center for Global Development, Washington, DC, USA. [2]Department of Economics, Williams College, Williamstown, MA, USA. [3]School of Social Work, University of Michigan, Ann Arbor, MI, USA. Email: pj5@williams.edu

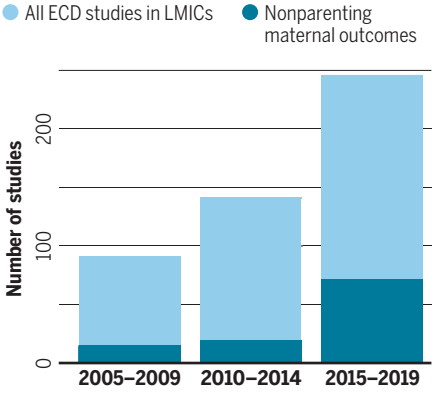
Research examining the costs and benefits of different approaches to ECD and childcare rarely highlights the value of women's time or measures the costs and benefits of programs that change women's time use. Even if the primary objective of an ECD intervention is to improve outcomes for children, failing to measure the impact on women's time and other maternal outcomes implicitly sets their value at zero.

THE PAUCITY OF EVIDENCE

We examined 3716 studies from databases that cover medical, psychological, economic, and other social science research, and we supplemented the results of this systematic review with 27 additional papers that met our inclusion criteria. We identified a total of 478 studies published between 2005 and 2019 that evaluated ECD-related interventions in LMICs using an experimental or quasi-experimental research design [see supplementary materials (SM) for details on all analyses].

A growing, but still too narrow, body of evidence

The number of quantitative studies measuring the impact of early childhood development (ECD) interventions in low- and middle-income countries (LMICs) (light blue), and the number of those studies that report nonparenting outcomes for mothers (blue), have both grown over time.



GRAPHIC: N. DESAI/*SCIENCE*

Of those studies, the overwhelming majority (91%) include either outcomes for children aged 0 to 5 years or parenting outcomes relevant for young children. However, only 22% (105 studies) report any mother-specific outcomes that are not exclusively focused on parenting practices. Though both the number of ECD studies and the proportion reporting impacts on mothers have grown over time, the latter proportion remains quite small (see the first figure). Only 19 studies (4%) examined maternal labor market outcomes, and only six (1%) report outcomes related to other aspects of women's empowerment. Studies documenting impacts on women's health are slightly more common (though still relatively rare): 55 studies (12%) report impacts on maternal mental health, while 47 studies (10%) report impacts on women's physical health.

A further 23 studies (5%) report any household-level outcomes beyond parenting practices (e.g., food security or sanitation practices). Only 12 studies (3%) report any father-specific outcomes—including father-specific measures of parenting practices—and only seven (1%) report impacts on older siblings in middle childhood or adolescence. In total, only 119 studies (25%) report outcomes related to the labor market activities, health, or well-being of household members other than young children.

This pattern of selective reporting might make sense if ECD interventions do not affect older household members: If all relevant costs and benefits of programs are captured in child and parenting outcomes, then there is no reason to report impacts on other household members. However, ECD interventions like childcare have obvious, direct implications for household labor supply, whereas many other interventions rely on parents to mediate impacts by changing their behavior (for example, by attending parent education classes or engaging in more stimulating activities with young children). Thus, there is a strong theoretical basis for measuring and reporting impacts on mothers, in particular—even when these impacts are null or imprecise. Moreover, among those studies that measure effects on mothers and other caregivers, many report statistically significant impacts.

IMPACTS ON WOMEN'S LABOR FORCE PARTICIPATION

Women—particularly mothers but also grandmothers, older sisters, and other relatives—do most of the childcare in most societies (*4*, *5*), and the theoretical and empirical relationship between parenting effort, access to childcare, and female labor force participation is well documented in

both low-income and high-income settings (*6*–*8*). Nevertheless, only 4% of the impact evaluations in our sample report impacts on women's labor force participation, income, or time use. Fortunately, there is substantial overlap across studies in terms of both the interventions being evaluated and the outcomes reported, making it possible to draw tentative conclusions from the existing evidence base (see the second figure)—though caution is clearly warranted, particularly in regard to sample selection if null results are less likely to be reported.

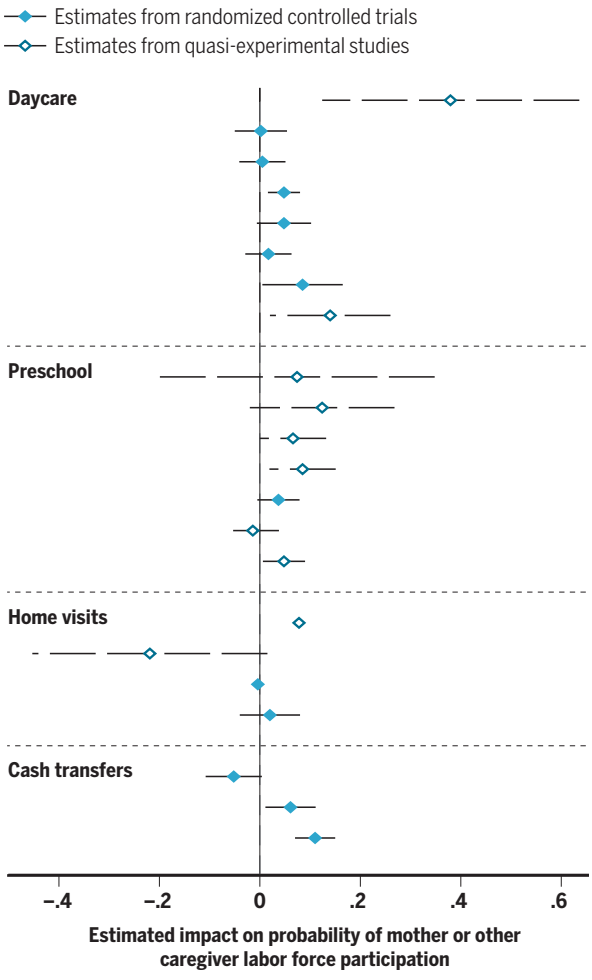
All four studies that measure the impact of access to daycare on women's employment (in Brazil, Ecuador, Kenya, and Nicaragua) report some positive impacts—from a 5 percentage point increase in the employment of a child's primary caregiver in Brazil (though in that setting the child's primary caregiver is often a grandmother or adult sister rather than the child's mother) to a 31 percentage point increase in maternal employment in Ecuador. Differences in the size of effects across settings may depend on differences in job opportunities and other contextual factors (see SM for details on all studies analyzed for this article).

Existing evidence also suggests that access to daycare has a positive impact on women's income and overall household income. In Kenya, access to daycare increased mothers' income. In Brazil, access to daycare increased household income and had a marginally significant impact on the income of a child's primary caregiver, though it did not increase maternal income significantly. In Ecuador, childcare centers had a significant positive impact on both mother's income and the income of the household head. All four studies estimating the impact of preschool on women's labor force participation also report some weakly positive impacts, though the evidence is less robust than in the case of access to daycare.

Thus, the existing evidence base suggests that expanding access to daycare and preschool is likely to increase women's employment and household income in many settings—but less than half of the evaluations of such interventions in our sample report impacts on these outcomes. Many evaluations may be ignoring important program impacts. Moreover, whereas interventions such as daycare that reduce women's carework burden tend to increase female labor force participation, ECD programs that encourage parents to increase their parenting effort might have the opposite effect. A home visiting intervention in Ecuador decreased maternal labor force participation, although a similar program in South Africa did not. Though interventions involving home visits are increasingly common, impacts on mothers' time use and labor supply are almost never measured—making it impossible to know whether these programs alter women's domestic burden. Studies that do not measure the impacts of ECD interventions on women's time use and labor supply cannot fully account for the costs and benefits of such policy interventions.

Targeting children, affecting mothers: labor force participation

Estimated impacts (and 95% confidence intervals) on mother or other caregiver labor force participation are shown from studies of different interventions in low- and middle-income countries. Although too few studies measure these outcomes, those that do suggest that daycare and preschool interventions tend to have either no impact or a positive impact on women's labor force participation. For details on sources and estimates, see the supplementary materials.



GRAPHIC: N. DESAI/*SCIENCE*

IMPACTS ON MATERNAL MENTAL HEALTH

ECD interventions have the potential to affect maternal mental health in several ways. Because women do most of the childcare in LMIC contexts, any intervention targeting young children has the potential to bring mothers into contact with the implementing partners (e.g., child development specialists or government health care workers) and other mothers participating in the intervention. These interactions may reduce feelings of isolation and strengthen social support networks. This is particularly true of home visiting interventions and parent education classes, which work by engaging primary caregivers in regular interactions with individuals outside their own household. At the same time, these interventions impose on mothers' time, which could increase stress or reduce time available for income generation.

Interventions like cash transfers are often targeted to women, sometimes with the explicit objective of increasing mothers' autonomy and decision-making power, whereas daycare and other interventions that influence women's labor force participation may improve women's bargaining power and strengthen their social networks outside the home.

Existing empirical evidence supports the hypothesis that many ECD interventions in LMICs have positive impacts on mothers' mental health and well-being. In our sample of 478 impact evaluations of ECD interventions, 55 (12%) report impacts on any outcomes related to maternal mental health—and 27 of those report positive (in the sense of improving women's well-being), statistically significant impacts. Only three find negative, statistically significant impacts.

Group-based parent education interventions reduced maternal depression in Bangladesh, Guatemala, Pakistan, South Africa, Uganda, and Zambia; and home visits from child development professionals reduced maternal depression in Bangladesh, Jamaica, Iran, and Pakistan. In other settings, similar interventions improved maternal self-confidence and parental efficacy—even when impacts on overall mental health were not statistically significant. Evaluations of these interventions were also more likely to report impacts on maternal mental health: 80% of studies reporting impacts on maternal

mental health are evaluations of either home visiting programs or group-based parent education, even though these types of interventions do not account for 80% of all studies in our sample. Studies of cash transfers rarely report impacts on maternal mental health, and those that do have typically not found statistically significant positive impacts—though cash transfers have been shown to improve overall well-being in other contexts (*9*)—and evaluations of other ECD interventions (including daycare and preschool programs) that report impacts on maternal mental health are exceedingly rare.

Group-based parent education programs and interventions involving home visits are both common, and it is impossible to tell whether the papers that report maternal mental health outcomes are representative of the overall distribution of impacts. Caution is warranted—it should not be concluded that these programs automatically improve women's mental health. However, the number of impact evaluations of home visits and group-based parenting classes that find positive impacts on maternal mental health is higher than would be expected if these results were spurious. Evaluations that do not capture potential impacts on maternal mental health cannot fully evaluate program costs and benefits.

OTHER MEASURES OF EMPOWERMENT

Although female labor force participation and mental health are both entwined with women's empowerment, only six studies evaluate the impacts of ECD interventions on women's autonomy or decision-making power within the household—but five of the six find some evidence of positive impacts. In contrast to the cases discussed above, there is no evidence that studies of one specific class of intervention are more likely to report impacts on empowerment: The six studies that measure empowerment include evaluations of a program to treat postpartum depression, an intervention intended to promote fathers' involvement in child-rearing, a cash transfer program targeting parents of young children, and a program providing vouchers for daycare.

This range of interventions—all of which appear to increase women's financial autonomy or involvement in household decision-making—highlights the connections between women's childcare responsibilities, their sense of social support, their financial independence and agency, and their mental well-being. Evaluations that ignore these impacts cannot trace out the mechanisms that explain why interventions work in some contexts and not in others.

IMPLICATIONS

Households—and especially mothers—invest substantial time and energy in their young children, and ECD interventions often have large impacts on child-rearing practices. Research that ignores impacts on caregivers can only provide a partial characterization of program effects. Relatively few evaluations of ECD interventions in LMICs report impacts on mothers, and even fewer report impacts for other caregivers such as fathers or older siblings. Beyond interventions intended to boost child outcomes, other studies demonstrate the adverse impacts of negative experiences like early childhood illnesses on parents and older siblings (*10*).

The expected link between ECD interventions and women's outcomes varies across interventions. Providing daycare or preschool has obvious implications for women's labor force participation. Purely medical interventions for young children—which we have excluded from our review—have less obvious implications, as do some health and nutrition interventions such as vitamin supplements. However, many studies fall between those two extremes. Specifically, interventions such as parenting education intended to change mothers' behavior are increasingly common. When an intervention's theory of change involves changing the behavioral practices of mothers (or other caregivers), it makes sense to ask how mothers will be affected by treatment. Yet, many researchers who study ECD interventions are primarily interested in improving outcomes for children, and this may predispose them to focus on child rather than mother outcomes.

"There can be no evidence-based policy regarding caregiving interventions without evidence on the caregivers."

There can be no evidence-based policy regarding caregiving interventions without evidence on the caregivers. Our findings point to the urgent need to routinely incorporate measures of caregivers' productivity and well-being into evaluations of ECD interventions. They also suggest the importance of evaluating ECD programs against multiple objectives. A program that delivers gains for both mothers and children may be more cost-effective than a program that delivers similar gains for children alone.

This has real-world policy implications. A 2015 study published by the Inter-American Development Bank found much higher benefit-cost ratios for home visiting programs relative to daycare programs, but only factored benefits to children into the calculations (*11*). Incorporating benefits to women shifts those calculations, even if it does not overturn them (*12, 13*). These kinds of calculations can influence national investment programs.

Ultimately, the evidence from those few studies that do measure impacts of ECD interventions on women suggests that many programs that are good for children also yield benefits for women's financial well-being, mental health, and overall empowerment. The case for ECD interventions may be even stronger than previously believed and may open the door to financing these programs from a wider range of sources. More of this measurement may shift emphasis from ECD interventions that are best for children to those that are best for children and for their caregivers. Policy-makers can only identify these trade-offs and interdependencies if they have information about all the gains that programs deliver. ■

REFERENCES AND NOTES

1. M. M. Black *et al.*, *Lancet* **389**, 77 (2017).
2. P. L. Engle *et al.*, *Lancet* **378**, 1339 (2011).
3. P. Gertler *et al.*, *Science* **344**, 998 (2014).
4. S. B. Hrdy, *Mothers and Others: The Evolutionary Origins of Mutual Understanding* (Belknap, 2009).
5. D. F. Lancy, *The Anthropology of Childhood: Cherubs, Chattel, Changelings* (Cambridge Univ. Press, Cambridge, ed. 2, 2014); www.cambridge.org/core/books/anthropology-of-childhood/B34D307F81527FC3C91AE9D0B02D48D7.
6. J. J. Heckman, "Effects of Child-Care Programs on Women's Work Effort" (c3687, National Bureau of Economic Research, 1974); www.nber.org/books-and-chapters/marriage-family-human-capital-and-fertility/effects-child-care-programs-womens-work-effort.
7. E. U. Cascio, *J. Hum. Resour.* **44**, 140 (2009).
8. D. Del Boca, "Child care arrangements and labor supply" (2015); https://publications.iadb.org/en/publication/12189/child-care-arrangements-and-labor-supply.
9. J. Haushofer, J. Shapiro, *Q. J. Econ.* **131**, 1973 (2016).
10. M. Alsan, A. Xing, P. Wise, G. L. Darmstadt, E. Bendavid, *Pediatrics* **140**, e20163175 (2017).
11. S. Berlinski, N. Schady, Eds., *The Early Years: Child Well-Being and the Role of Public Policy* (2015); https://publications.iadb.org/publications/english/document/The_Early_Years_Child_Well-being_and_the_Role_of_Public_Policy.pdf.
12. M. Díaz *et al.*, *Cashing in on Education: Women, Childcare, and Prosperity in Latin America and the Caribbean* (2016); https://publications.iadb.org/en/cashing-education-women-childcare-and-prosperity-latin-america-and-caribbean.
13. J. Sandefur, "Is daycare a bad investment for Latin America?" (2017); www.cgdev.org/blog/is-daycare-bad-investment-latin-america.

ACKNOWLEDGMENTS

We thank Echidna Giving, the Hewlett Foundation, and the Bill & Melinda Gates Foundation for financing this project. Authors are listed alphabetically. A. Mendez Acosta provided extensive research assistance. E. Galasso, M. O'Donnell, and O. Ozier provided helpful comments. All errors are our own.

SUPPLEMENTARY MATERIALS

science.sciencemag.org/content/372/6544/794/suppl/DC1

10.1126/science.abg0132

Your Legacy to Science

AN ESTATE GIFT TO THE
AMERICAN ASSOCIATION FOR THE ADVANCEMENT OF SCIENCE





Since 1848, our founding year, the American Association for the Advancement of Science (AAAS) has been deeply committed to advancing science, engineering and innovation around the world for the benefit of all people.

By making AAAS a beneficiary of your will, trust, retirement plan or life insurance policy, you become a member of our 1848 Society, joining Thomas Edison, Alexander Graham Bell and the many distinguished individuals whose vision led to the creation of AAAS and our world-renowned journal, *Science*, so many years ago.

Unlike many of its peers, *Science* is not for-profit. Your estate gift would provide long-term financial stability and durable annual income that will support operations and competitive innovation for years to come. **This support is vital.**

"As a teacher and instructor, I bear responsibility for the younger generations. If you have extra resources, concentrate them on organizations, like AAAS, that are doing work for all."

—Prof. Elisabeth Ervin-Blankenheim, 1848 Society member

If you intend to include AAAS in your estate plans, provide this information to your lawyer or financial adviser:

Legal Name: American Association for the Advancement of Science
Federal Tax ID Number: 53-0196568
Address: 1200 New York Avenue, NW, Washington, DC 20005

If you would like more information on making an estate gift to AAAS, cut out and return the form below or send an email to philanthropy@aaas.org. Additional details are also available online at **www.aaas.org/1848Society**.

1848 SOCIETY
AAAS

cut here

Yes, I would like more information about joining the AAAS 1848 Society.

PLEASE CONTACT ME AT:

Name: _____

Address: _____

City: _____ State: _____ Zip code: _____ Country: _____

Email: _____ Phone: _____

RETURN THIS FORM TO:
AAAS Office of Philanthropy and Strategic Partnerships • 1200 New York Avenue, NW • Washington, DC 20005 USA



Frank Rosenblatt and Charles Wightman manipulate a perceptron prototype in 1958.

BOOKS *et al.*

NEURAL NETWORKS

What AI can learn from the biological brain

Brain development could hold lessons for building better artificial neural networks

By **Kamila Maria Jóźwik**

Despite their overlapping interests, it is rare for developmental neurobiologists to consult artificial intelligence (AI) experts in the course of their research and vice versa. But in his new book, *The Self-Assembling Brain*, neurobiologist Peter Robin Hiesinger argues that doing so would likely be of great benefit to both parties. In 10 chapters, he describes a series of imagined conversations between four hypothetical individuals—a developmental geneticist, a neuroscientist, a robotics engineer, and an AI researcher—that offer readers insight into the information that is needed both to understand the workings of the brain and to create an artificial system that mimics the brain. These fictional conversations are followed by "seminars" in which the author discusses specific topics in greater detail.

Hiesinger elegantly moves through a variety of topics, ranging from biological development to AI and ending with a discussion of the advances that deep neural networks have brought to the field of brain-machine interfaces. At each stage, he discusses the commonalities and differences that define developmental science and AI research.

I appreciated, in particular, Hiesinger's efforts to link information on different levels of abstraction, such as when he describes why linking genetic information to human behavior is complicated and reveals the caveats of attempting to do so. He uses this discussion to prompt the reader to ponder at what level we need to work to build an artificial brain, a topic on which he elaborates later.

In the seminar "From Algorithmic Growth to Artificial Intelligence," Hiesinger describes differences that exist in the training of artificial neural networks (ANNs) and the early development of brains, raising questions about the way we train ANNs. The network architecture and training rules are fixed during ANN training, and the network learns by exposure to large datasets. During human development, however, the brain changes as it grows, and the learning rules change too.

The hypothetical dialogues that open each chapter successfully capture various disciplinary perspectives and illustrate tensions between the fields represented. In one passage, for example, Minda, the developmental geneticist, argues that genes contain all of the information necessary to build an artificial brain, whereas Pramesh, the AI researcher, maintains that this level of description does not translate into a principle he could program into an artificial system.

Such conversations acknowledge the limitations of the respective approaches taken in different fields, identify different naming conventions for related concepts, and convey the enthusiasm many researchers feel when learning about other fields. However, I wish that the views that were expressed had given readers a better sense of how new interdisciplinary research collaborations might be established.

The book's last discussion and the accompanying seminar will be of particular interest to researchers who work at the interface between neuroscience and AI. Here, Hiesinger argues that in order to achieve AI comparable to human intelligence, we cannot take any shortcuts and must include information present on every biological level—a position that may be seen as controversial by both neuroscientists and AI researchers. He acknowledges, however, that the path to reaching artificial general intelligence may not necessitate humanlike intelligence.



The Self-Assembling Brain: How Neural Networks Grow Smarter
Peter Robin Hiesinger
Princeton University Press, 2021. 384 pp.

One shortcoming of this otherwise entertaining book is that it tries to cover many concepts but often fails to provide sufficient detail for the reader to fully grasp a specific issue. However, given that Hiesinger aims to engage a variety of people from different backgrounds, some context must inevitably be sacrificed to keep the narrative moving. Overall, this book accurately illustrates current debates occurring in this space and is likely to inspire future discussions at the intersection of neuroscience and AI. ■

The reviewer is at the Department of Psychology, University of Cambridge, Cambridge CB2 3EB, UK, and the Center for Brains, Minds and Machines, Massachusetts Institute of Technology, Cambridge, MA 02139, USA. Email: kmjozwik@mit.edu

10.1126/science.abi4889

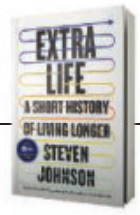
PHOTO: COURTESY OF DIVISION OF RARE BOOK AND MANUSCRIPT COLLECTIONS/CORNELL UNIVERSITY LIBRARY

PUBLIC HEALTH

Long live humankind

Data collection and analysis earn top spots among factors that have drastically increased life expectancy

Extra Life
Steven Johnson
Riverhead, 2021. 320 pp.



Extra Life
Duncan Singh, Helen Sage, Tristan Quinn, David Alvarado, Jason Sussberg, directors
Nutopia, 2021. Airing 11 May to 1 June 2021 on PBS. Check local listings.

By **Alyson A. van Raalte**

The average person in the longest-living populations has gained an extra 50 years of life in just a handful of generations. Such an extraordinary achievement should be headline news. Instead, our preference for attending to acute, dramatic events leaves little space for the acknowledgment of this remarkable, incremental accomplishment. In *Extra Life*, science writer Steven Johnson sets out to remedy this.

After centuries of stagnation, life expectancy began to climb in earnest in northwestern Europe starting around the middle of the 19th century. The reason for this has for decades been the source of heated debates among scholars. Johnson discusses the most important of these factors, which include vaccination, the collection of vital statistics, pasteurization, drug regulation and testing, antibiotics, car and industrial safety, and agricultural innovations such as synthetic fertilizer.

There are two main ways that this book is set apart from others that have previously touched on this subject. First, Johnson introduces the reader to a lively cast of characters involved in the most important innovations that have contributed to our longer life spans. These include both the discoverers themselves and their "amplifiers"—those with high social capital who were vital in promoting the innovation in question. Second, he gives almost equal weight to the usual proximate causes of mortality decline—for example, vaccination, antibiotics, improved nutrition, safe drinking water—and to "less tangible innovations," such as the collection and analysis of data.

As a result, well-trodden stories about Edward Jenner discovering vaccination or Robert Koch and Louis Pasteur isolating bacterial strains are balanced with anecdotes about lesser-known statistical innovators. For example, readers are introduced to John Graunt, founder of the life table, which allowed ages at death to be compared across populations with different age structures, and to John Snow, who developed spatial epidemiological techniques to trace the waterborne source of the 1854 cholera pandemic in London. Readers also learn about the work of Austin Bradford Hill and Richard Doll, who introduced the randomized controlled trial in medicine, and William Foege, who put forward the ring vaccination approach to snuff out epidemic outbreaks.



A scientist tests sewage for COVID-19 at the East Bay Municipal Lab in Oakland, California, in a scene from *Extra Life*.

Why aren't these individuals also household names? In Johnson's view: "You can't put the randomized controlled trial on display in a science museum."

The book magnificently transports the reader to some truly horrific historical episodes that would send the most ardent of libertarians knocking on the doors of government regulators. My personal favorite was Johnson's description of the swill milk scandal of mid-19th century New York—so named after the practice of feeding cows the waste products from nearby distilleries, which had the unfortunate side effect of turning the milk blue (a problem solved by adulterating the milk with chalk, flour, and eggs).

If there is one main takeaway from the book, it is that the public sector has made many positive contributions to public health over the long course of history, spurring innovation and creating effective institutions and regulatory bodies that have saved countless lives. The World Health Organization is singled out in particular for its successful eradication of smallpox during the heated Cold War political era.

The book's weakest sections, surprisingly, are those describing the very trend central to its theme. It is no secret that life expectancy is one of the most poorly understood statistics in the world, and Johnson misses an opportunity to educate readers on why we use life expectancy, what it measures, and, importantly, what it does not.

He gets caught in some of the usual traps—jumping between period (calendar year) and cohort (birth year) mortality statistics as though they are interchangeable. Johnson is certainly not the first to make this mistake, but it would not have hurt to remind readers that the COVID-19–induced shock to life expectancy will not reduce our own future survival prospects once the pandemic has run its course.

Extra Life is accompanied by an excellent four-part documentary series of the same name from Nutopia, which debuted on PBS on 11 May. While complementary, the book and documentary series have somewhat different stories to tell. The COVID-19 pandemic comes across as a tangential backdrop to the story being told in the book—a devastating hiccup in the overall arc of progress. The series, on the other hand, uses the pandemic as a lens through which to take stock of the medical, data, and social innovations of the past century. This includes a greater focus on the social determinants of health, including racism, as well as on the origins of many of our most effective behavioral innovations in fighting infectious disease.

Precisely because of the moment we find ourselves in, *Extra Life* could not be timelier. Both the book and the series strike an uplifting tone, reminding readers of what humanity has accomplished by working together toward the common good. ■

The reviewer is at the Max Planck Institute for Demographic Research, 18057 Rostock, Germany. Email: vanraalte@demogr.mpg.de

10.1126/science.abi4718

PHOTO: COURTESY OF MARIO FURLONI/NUTOPIA

The Most ADVANCED Patch Clamp System Available Today

Visit
www.dpatch.com
to learn more



SUTTER INSTRUMENT

+1.415.883.0128
info@sutter.com
www.sutter.com



Share
Your Robotics Research with the **World**.

Shaping the future of robotics with high impact research!

As a multidisciplinary online-only journal, *Science Robotics* publishes original, peer-reviewed, research articles that advance the field of robotics. The journal provides a central forum for communication of new ideas, general principles, and original developments in research and applications of robotics for all environments.

Submit your research today.
Learn more at: **robotics.sciencemag.org**

Twitter: @SciRobotics
Facebook: @ScienceRobotics

Science Robotics
AAAS



LETTERS

Three otter species in China, including the Asian small-clawed otter (*Aonyx cinereus*), are now endangered.

PHOTO: JURGEN AND CHRISTINE SOHNS/MINDEN PICTURES

Edited by **Jennifer Sills**

Stop the decline of China's wild otters

China is home to three species of otters: the Eurasian otter (*Lutra lutra*), the Asian small-clawed otter (*Aonyx cinereus*), and the smooth-coated otter (*Lutrogale perspicillata*) (*1*). Otters are the flagship species of (*2*, *3*), and important indicators of health for (*4*), freshwater ecosystems. Although once widely distributed throughout China, wild otter populations declined in the late 20th century (*5*, *6*), and all three species have now been listed as Endangered on the Red List of China's Vertebrates (*7*). Sightings of wild otters in China are rare, and the smooth-coated otter has not been recorded in the wild for more than 10 years (*6*, *8*). To prevent the extinction of these otter species, China must do more to protect them.

From the 1950s to 1980s, many Chinese wild otters were killed because their pelts and other body parts were used in medicine (*8*). In 1989, all three otter species were ranked as class II on China's National Key Protected Species List (*9*), but their populations continued to decline (*6*). The continued catastrophic decline of otter populations likely resulted from overexploitation, habitat loss, water pollution, and food shortages (*6*, *10*). Because otters sometimes hunt in aquaculture fishponds, they are also at risk of conflict with those in the aquaculture industry who consider them to be pests (*11*).

To protect Chinese wild otters, a nationwide survey should be conducted to identify their habitat sites and the status of current populations (*3*, *5*). The Chinese government should then implement strict measures to protect the habitats identified by the survey. Policies should aim to prevent water pollution and should ban fishing, as did the recent policy protecting the Yangtze river (*12*). More research, including assessments of habitat water quality, habitat and food selection mechanisms, population dynamics, and genetic diversity, should be carried out to inform conservation measures. Ecological education should make the local residents, especially those working in aquaculture, aware of the value of wild otters. If China can continue to improve the otters' habitat, the species will be more likely to avoid human contact, giving these vulnerable populations a chance to recover.

Qinguo Wei, Xiaoyang Wu, Xiaodong Gao, Honghai Zhang*
College of Life Sciences, Qufu Normal University, Qufu, China.
*Corresponding author.
Email: zhanghonghai67@126.com

REFERENCES AND NOTES

1. A. T. Smith, Y. Xie, *Mammals of China* (Princeton University Press, 2013), pp. 318–320.
2. S. Stevens, J. Organ, T. L. Serfass, *IUCN Otter Specialist Group Bulletin* **28(a)**, 150 (2011).
3. C. Cianfrani *et al.*, *Biol. Conserv.* **144**, 2068 (2011).
4. H. Kruuk, *Otters: Ecology, Behaviour and Conservation* (Oxford University Press, 2006), pp. 212–215.
5. S. Perkins, *Science*, 10.1126/science.aal0633 (2017).
6. L. Zhang *et al.*, *Biol. Conserv.* **228**, 259 (2018).
7. Z. Jiang *et al.*, *Biodivers. Sci.* **24**, 500 (2016) [in Chinese].
8. F. Li, B. P. L. Chan, *Oryx* **52**, 619 (2017).
9. The Ministry of Forestry, "The National Key Protected Species List," *Wild Life* **2**, 11 (1989) [in Chinese].
10. N. Duplaix, M. Savage, *The Global Otter Conservation Strategy* (IUCN/SSC Otter Specialist Group, 2018). pp. 5–29.
11. Z. Liu, *China Three Gorges Trib.* **262**, 37 (2013) [in Chinese].
12. Z. Mei, P. Cheng, K. Wang, Q. Wei, D. Wang, *Science* **367**, 1314 (2020).

10.1126/science.abj2530

The Chinhai spiny newt needs a safer habitat

The Chinhai spiny newt (*Echinotriton chinhaiensis*), an amphibian endemic to China, is listed as Critically Endangered on the International Union for Conservation of Nature (IUCN) Red List (*1*). Since it was first recognized in 1932 (*2*), several comprehensive field surveys have confirmed

that the estimated population of 369 individuals (*3*–*5*) is limited to an area of less than one square hectare in Ningbo, Zhejiang Province, China (*6*). Without urgent action, this endangered species could become extinct.

The Chinhai spiny newt faces a range of threats, the most critical of which is habitat loss (*7*). From late March to early May, female newts lay eggs on the shores of small still-water pools (*8*), where the eggs are vulnerable to drought, fungal infection, and predation (*4*, *8*). Only 20% of the hatched newborns enter the water for a metamorphosis of approximately two months, during which mortality of the newts is as high as 84% (*8*). After metamorphosis, the newts leave the water and live in the surrounding habitats, which are engulfed by intense human activities, such as deforestation and urban expansion (*5*). Given their low mobility, the newts are limited to their existing range.

Although the Chinhai spiny newt has been listed as a first-class Key National Protected Wild Animal Species (*9*), there are few coordinated plans for its conservation at the national or provincial level. In 2009, the municipal government established a nature reserve for the purpose of protecting the newts, but it was ineffective because of insufficient financial and institutional support (*6*). Their breeding pools remain behind the concrete walls of the reserve, but construction continues in the surrounding area that serves as the habitat for adults. To protect the species, stricter measures should be taken to protect the remaining population and habitat. The nature reserve should be better funded and expanded to protect the wild newt populations and their current and potential habitats. Artificial breeding of the newts could allow for reintroductions to suitable habitats outside of the current range. Effective conservation efforts and successful future reintroduction to the wild will require further research to understand the newt's life history in the wild.

Aichun Xu[1], Zhigang Jiang[2,3], Chunlin Li[4]*
[1]College of Life Science, China Jiliang University, Hangzhou 310018, China. [2]Key Laboratory of Animal Ecology and Conservation Biology, Institute of Zoology, Chinese Academy of Sciences, Beijing 100101, China. [3]University of Chinese Academy of Sciences, Beijing 100049, China. [4]School of Resources and Environmental Engineering, Anhui University, Hefei 230601, China.
*Corresponding author.
Email: lichunlin1985@163.com

REFERENCES AND NOTES

1. F. Xie, H. Gu, "*Echinotriton chinhaiensis*" (IUCN Red List of Threatened Species, 2004).
2. M. L. Y. Chang, *Zool. Ser.* **8**, 201 (1932).
3. F. Xie *et al.*, in *Principles of Animal Behavior and Species Conservation Methods*, Z. Jiang, Ed. (China Science Press, Beijing, 2003), pp. 293–320.
4. C. Cai, L. Fei, *Acta Herpetol. Sinica* **3**, 71 (1984).
5. L. Fei, *Chin. J. Zool.* **27**, 39 (1992).
6. J. Zhang, thesis, China Jiliang University (2019).
7. C. Liu *et al.*, *Sichuan J. Zool.* **29**, 24 (2010).
8. F. Xie, L. Fei, C. Ye, Z. Wang, C. Cai, *Curr. Zool.* **48**, 554 (2002).
9. State Forestry and Grassland Administration, Announcement of the Ministry of Agriculture and Rural Affairs of the State Forestry and Grassland Administration (No. 3 of 2021) (List of National Key Protected Wild Animals) (2021); www.forestry.gov.cn/main/3457/20210205/122612568723707.html [in Chinese].

10.1126/science.abi9279

Green strategies for sustainable packaging

Packaging constitutes roughly 46% of global plastic waste (*1*). In the European Union, packaging waste increased by 9.4% (6.7 million metric tons) in the decade after 2008, reaching 77.7 million metric tons in 2018 (*2*). Globally, the total value of packaging was USD917 billion in 2019; it will likely increase to USD1.05 trillion by 2024 (*3*). Countries such as the UK and China are making an effort to curtail packaging waste, but to make real progress, governments must require the packaging industry to embrace more sustainable methods.

The UK generates more than 11 million metric tons of packaging waste each year despite a recycling and recovery rate of 70% (*4*). To reduce its packaging-related pollution and boost recycling and recovery, the country launched a plastic packaging tax, under which manufacturers and importers are charged USD277 per ton when using packaging with less than 30% recycled plastic (*5*). The UK is also considering strategies to make packaging producers responsible for the full cost of designing, producing, and discarding the packaging they place on the market (*6*) and a system in which consumers would pay a fee at the time of sale that would be reimbursed when they return reusable packaging to a designated location (*7*).

In 2018, China's express delivery sector generated 8.8 million metric tons of packaging waste, and in 2020 the country shipped more than 80 billion plastic-wrapped parcels—the most in the world (*8*, *9*). In March, the Chinese Ministry of Transport implemented a green packaging regulation to reduce over-wrapping and increase the use of green materials and recycling bins for packaging (*10*). Companies that do not comply with the regulations by using single-use plastic could be charged up to USD15,450 per violation.

Regulations like those in the UK and China are a step toward making producers responsible for their use of packaging products and encouraging more recycling-friendly plastic packaging (*11*). However, few companies have kept pace with previous legislation related to sustainability. A survey showed that 60% of global packaging companies reported no policies on key sustainable packaging–related topics (*12*). Legislation must be structured to make green strategies and sustainable products essential for packaging companies to maintain competitiveness and financial profitability. All countries, including the UK and China, should require the packaging industry to meet environmental, social, and governance standards for sustainability. Regulations should be written to include regular evaluations of companies' performance and hold those in violation accountable with fines or fees that are high enough to incentivize compliance.

Siming You[1]*, Wangliang Li[2], Wei-Cheng Yan[3], Christian Sonne[4]
[1]University of Glasgow, Glasgow, UK. [2]Institute of Process Engineering, Chinese Academy of Sciences, Beijing, China. [3]Jiangsu University, Zhenjiang, China. [4]Aarhus University, Roskilde, Denmark.
*Corresponding author:
Email: siming.you@glasgow.ac.uk

REFERENCES AND NOTES

1. I. Tiseo, "Distribution of plastic waste generation worldwide in 2018, by sector," *Statista* (2020).
2. "Packaging waste by waste management operations," *Eurostat* (2021).
3. "The future of global packaging to 2024," *Smithers* (2019).
4. UK Department for Environment, Food & Rural Affairs, "UK statistics on waste" (2020).
5. UK HM Revenue & Customs, "Introduction of a new plastic packaging tax" (2020).
6. UK Department for Environment, Food & Rural Affairs, "Packaging and packaging waste: Introducing extended producer responsibility" (2021).
7. UK Department for Environment, Food & Rural Affairs, "Introducing a deposit return scheme in England, Wales and Northern Ireland" (2021).
8. P. Kang *et al.*, *Nat. Commun.* **12**, 1 (2021).
9. The State Council, People's Republic of China, "Country's express delivery business volume exceeds 80 billion pieces in 2020" (2020); www.gov.cn/xinwen/2020-12/21/content_5571848.htm [in Chinese].
10. The State Council, People's Republic of China, "Regulations of mail and delivery packaging" (2021); www.gov.cn/zhengce/zhengceku/2021-02/25/content_5588767.htm [in Chinese].
11. S. A. Bassi *et al.*, *Resour. Conserv. Recycl.* **162**, 105030 (2020).
12. G. Thoumi *et al.*, "Unwrapping investor risk: Global plastic containers and packaging sector," *Planet Tracker* (2021).

10.1126/science.abj1042

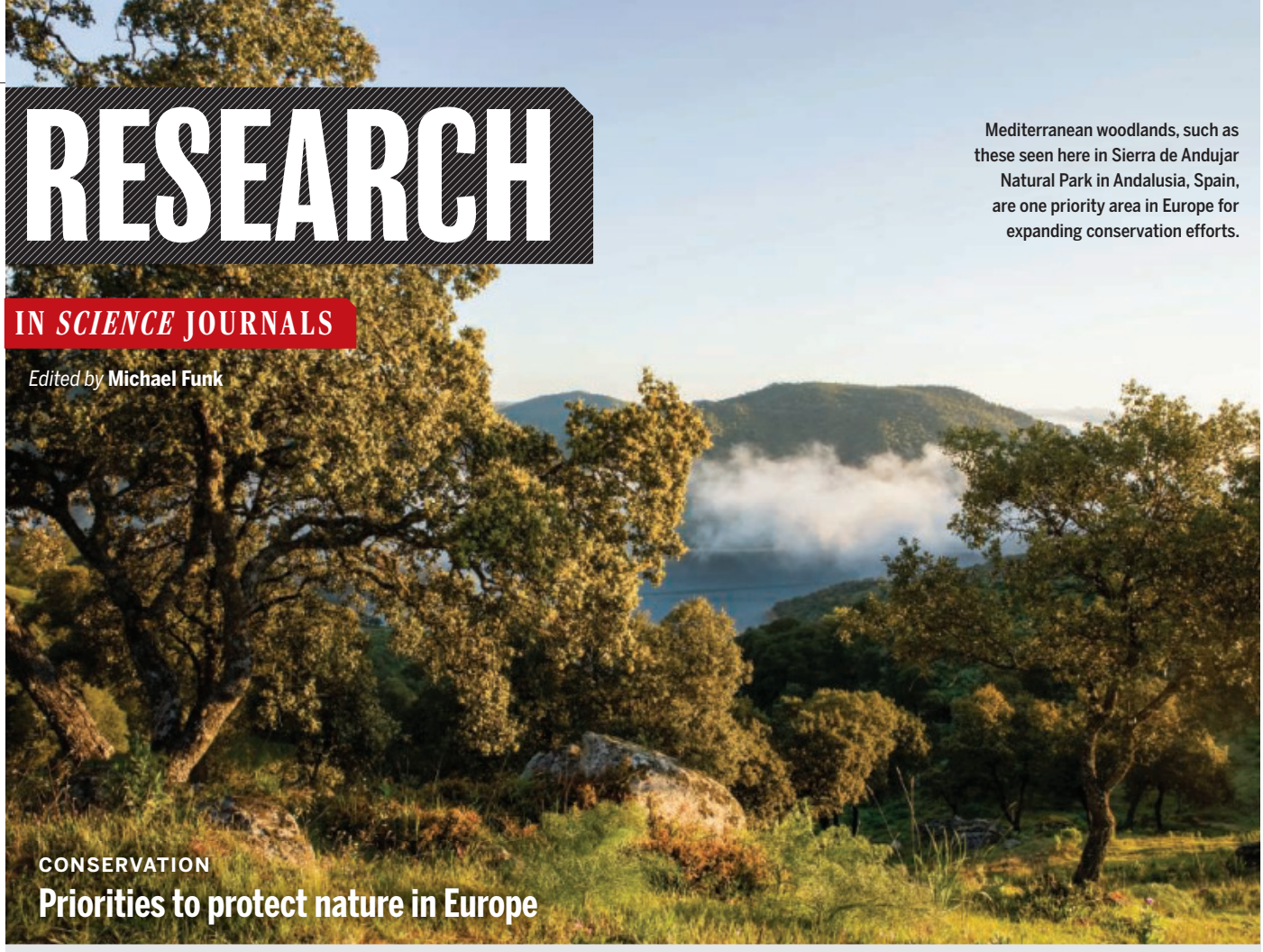
ERRATA

Erratum for the Report "Electrophotocatalytic diamination of vicinal C–H bonds," by T. Shen and T. H. Lambert, *Science* **372**, eabj3275 (2021). Published online 14 May 2021; 10.1126/science.abj3275

RESEARCH

IN *SCIENCE* JOURNALS

Edited by **Michael Funk**



Mediterranean woodlands, such as these seen here in Sierra de Andujar Natural Park in Andalusia, Spain, are one priority area in Europe for expanding conservation efforts.

PHOTO: SEBASTIAN KENNERKNECHT/MINDEN PICTURES

CONSERVATION

Priorities to protect nature in Europe

There is consensus among conservation scientists that protected areas should be expanded to safeguard biodiversity and ecosystem services, but it is often difficult to prioritize areas for protection. Considering factors that motivate conservation across Europe, an analysis by O'Connor *et al.* includes the value of species, represented by distribution of >800 vertebrate species; the cultural value of landscapes, represented by activities such as nature tourism; and the value of ecosystem services such as carbon sequestration and flood protection. Although these three main features often do not coincide in the landscape, the authors found that a focus on biodiversity in spatial conservation planning is the most effective means of capturing a range of nature's values. —AMS

Science, abc4896, this issue p. 856

CORONAVIRUS

Unmitigated spread in Brazil

Despite an extensive network of primary care availability, Brazil has suffered profoundly during the severe acute respiratory syndrome coronavirus 2 (SARS-CoV-2) pandemic. Using daily data from state health offices, Castro *et al.* analyzed the pattern of spread of COVID-19 cases and deaths in the country from February to October 2020. Clusters of deaths before cases became apparent indicated unmitigated spread. SARS-CoV-2 circulated undetected in Brazil for more than a month as it spread north from São Paulo. In Manaus, transmission reached unprecedented levels after a momentary respite in mid-2020. Faria *et al.* tracked the evolution of a new, more aggressive lineage called P.1, which has 17 mutations, including three (K417T, E484K, and N501Y) in the spike protein. After a period of accelerated evolution, this variant emerged in Brazil during November 2020. Coupled with the emergence of P.1, disease spread was accelerated by stark local inequalities and political upheaval, which compromised a prompt federal response. —CA

Science, abh1558 and abh2644, this issue p. 821 and p. 815

ELECTRON MICROSCOPY

Locating atoms with higher precision

Two major problems that limit the resolution and interpretation of electron microscopy images are lens aberrations and multiple scattering. Chen *et al.* overcame these issues with ptychography, a technique that uses coherent scattering and multiple overlapping illumination spots to reconstruct an image from far-field diffraction patterns. This method works at a resolution that is limited, not by optics, but rather by the scattering strength of the sample, so it can work better with thicker samples. The authors achieved ultimate lateral resolution better than the thermal vibration of atoms in a $PrScO_3$ sample and showed that it is theoretically possible to identify single dopant atoms. —MSL

Science, abg2533, this issue p. 826

TRANSLATION

Quantifying translation in space and time

During development, precise control of gene expression establishes reproducible patterns, leading to the formation of organs at the right time and place. The emergence of developmental

patterns has been primarily studied at the transcriptional level, but the fate of these transcripts has received little attention. Dufourt *et al.* used the SunTag labeling method to image the dynamics of translation of individual messenger RNA (mRNA) molecules in living fruit fly embryos. This work revealed "translation factories"—clusters of mRNA and translation machinery—and heterogeneities in the efficiency of translation between identical mRNAs. —BAP

Science, abc3483, this issue p. 840

QUANTUM GASES

Finding the breaking point

A superfluid can flow without viscosity but only if the speed of the flow is lower than the so-called critical velocity. Sobirey *et al.* measured the critical velocity of a system of ultracold fermionic atoms confined to two dimensions. The researchers trapped a gas of lithium-6 atoms in a box-shaped potential and then moved another, periodic potential through the trap. The response of the gas to this perturbation showed a sudden increase when the speed of the periodic potential reached the critical velocity. —JS

Science, abc8793, this issue p. 844

NANOMATERIALS

Biphenylene carbon sheets

Although graphene forms two-dimensional carbon sheets, other arrangements of carbon rings could also assemble as flat sheers. Fan *et al.* synthesized an ultraflat biphenylene carbon sheet consisting of sp^2-hybridized carbon atoms forming four-, six-, and eight-membered rings on a gold surface. An adsorbed halogenated terphenyl molecule undergoes a two-step interpolymer dehydrofluorination polymerization that creates the four- and eight-membered rings through carbon–carbon bond formation. Scanning tunneling spectroscopy revealed that this carbon allotrope is metallic. —PDS

Science, abg4509, this issue p. 852

NEUROSCIENCE

Strengthening synapses with leptin

Early-life malnutrition is associated with neurodevelopmental disorders. Sahin *et al.* found that leptin, a hormone produced by adipocytes that induces the feeling of satiety, is critical for the development of inhibitory γ-amino butyric acid (GABA)-ergic synapses in the brain. In cultured hippocampal neurons from rat pups, leptin enhanced protein interactions that led to increased levels of $GABA_A$ receptors at synapses. The findings reveal how leptin facilitates neuronal connectivity in the developing hippocampus and may provide clues for understanding and treating neurodevelopmental disorders. —LKF

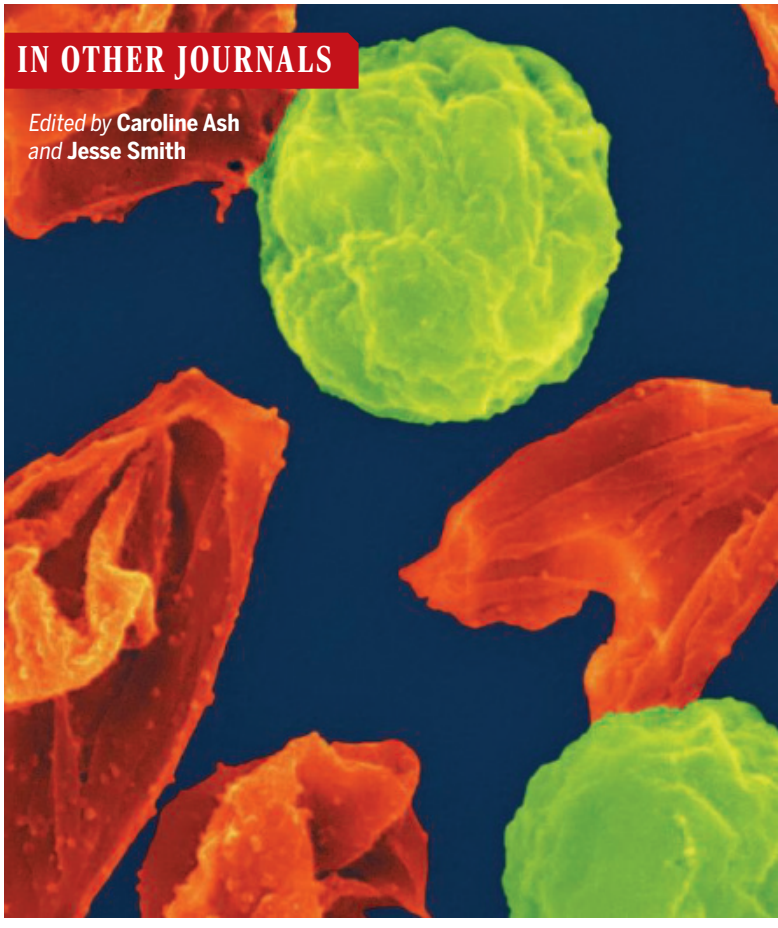
Sci. Signal. **14**, eabe4111 (2021).

SPECTROSCOPY

Nonlinear spectroscopy goes extreme

Nonlinear optical spectroscopies play an indispensable role in our understanding and analysis of matter but have been mostly restricted to the infrared-ultraviolet region in the laboratory. Extending these spectroscopic tools to shorter wavelengths typically requires a major facility with equipment such as a free-electron laser. Helk *et al.* demonstrate second-harmonic generation (SHG) in the extreme ultraviolet (XUV) region using a femtosecond tabletop laser. They show that the observed XUV-SHG emission from titanium is specific to the inversion symmetry broken surface and likely enhanced by core-level atomic transitions. These findings open the door to more routine studies of symmetry and dynamics in complex materials and interfaces with atomic specificity. —XYZ

Sci. Adv. 10.1126/sciadv.abe2265 (2021).



IN OTHER JOURNALS

Edited by **Caroline Ash** *and* **Jesse Smith**

IMAGE: DENNIS KUNKEL MICROSCOPY/SCIENCE SOURCE

NEUROSCIENCE

Imagery and recall of faces

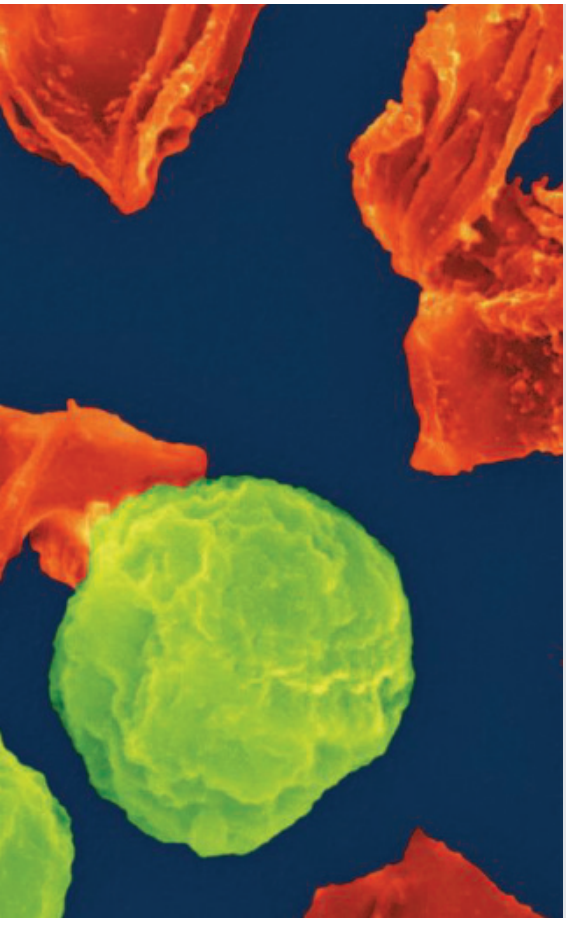
In the ventral temporal cortex (VTC) of the primate brain, there are special visual areas for the recognition of faces. The role of VTC neurons in nonsensory visual processing such as imagery and recall is poorly understood. Khuvis *et al.* recorded from electrodes implanted in the VTC of patients being monitored for surgery to treat epilepsy while they viewed faces and later recalled them. Recorded neurons showed diverse response patterns while maintaining specialization for nonliving and living stimuli. Likewise, neural responses to the presentation of individual faces were robustly discriminated. These responses were reproduced when subjects recalled and visualized previously presented faces in the absence of sensory stimuli. —PRS

J. Neurosci. **41**, 3386 (2021).

3D PRINTING

Reprocessible, rubbery, printable polymers

Three-dimensional (3D) printing is a valuable tool for rapidly prototyping complex parts from a range of materials. A challenge in printing most elastomers (rubber-like, highly stretchable polymers) is that they are mechanically soft and thus require external support during the printing process. Nian *et al.* developed a series of bottlebrush polymers composed of polydimethylsiloxane and poly(benzyl methacrylate) that have a high overall molecular weight because of their high density of short side chains but form few entanglements in the melt state. The polymers can be 3D printed without a support structure but are 100 times softer than other printed elastomers. At the same time, the printed structures can be stretched up to 600% and are



HOST DEFENSE

Variable malaria susceptibility

The development of effective malaria vaccines has been hampered by substantial geographic variability in immunity to the pathogen, *Plasmodium falciparum*. These differences likely result from the combined effects of genetics and environment. de Jong *et al.* experimentally infected both malaria-naïve Europeans and Africans known to have variable susceptibilities to malaria with *P. falciparum*. Using mass cytometry, RNA sequencing, and machine learning, the authors developed profiles for circulating immune cells both before and after inoculation. Before infection, an enhanced activation state of both innate and adaptive immune cells correlated with protection. After infection, African patients with controlled parasitemia responded more rapidly, with enhanced levels of distinct subsets of immune cells, including $CD4^+$ T cells, innate-like T cells, and plasmacytoid dendritic cells. —STS

Nat. Immunol. **22**, 654 (2021).

In humans, there is a distinct geographical signature in the subsets of immune cells responding to malaria parasites, shown in green in this scanning electron micrograph.

stable up to 180°C but can be reprocessed with the aid of solvents. —MSL

Chem. Mater. **33**, 2436 (2021).

ORGANIC CHEMISTRY

Better boron placement

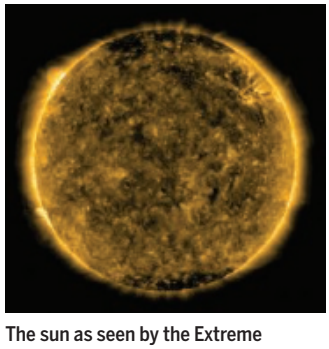
Over the past two decades, iridium-catalyzed borylation has proven to be a versatile method for substituting carbon–hydrogen (C–H) bonds that are otherwise relatively inert. Hoque *et al.* now report a pyridyl thiophene ligand for this reaction that induces the catalyst to target carbonyl-adjacent aryl C–H bonds or nitrogen-adjacent alkyl C–H bonds specifically. Heteroarenes were borylated next to their nitrogen, oxygen, or sulfur substituent. The iridium–ligand complex (bound datively at the pyridine nitrogen but metallated at a thiophene carbon) was conveniently compatible with open-air conditions. —JSY

J. Am. Chem. Soc. **143**, 5022 (2021).

SOLAR PHYSICS

Megakelvin campfires on the Sun

The Sun's corona (diffuse upper atmosphere) has a temperature of several million kelvin, far hotter than the photosphere (visible surface). The origin of the required coronal heating is unknown, with numerous proposals under investigation. Berghmans *et al.* observed the Sun in extreme ultraviolet light using the Solar Orbiter spacecraft. They identified hundreds of small, bright flashes near the base of the corona, which they call "campfires." These campfires lasted 10 to 200 seconds and reached one million kelvin. Similar features have previously been seen above active regions, but the authors show in this study that they also occur on the quiet Sun in sufficient numbers to plausibly provide the coronal heating. The driving mechanism remains unknown. —KTS



The sun as seen by the Extreme Ultraviolet Imager of the Solar Orbiter satellite on 30 May 2020

Astron. Astrophys. 10.1051/0004-6361/202140380 (2021).

NEURODEGENERATION

Phagocytosis promotes plaque

Many of the human genes associated with increased risk for Alzheimer's disease (AD) are exclusively expressed in the brain by microglia. Microglia express the tumor-associated macrophage (TAM) receptor tyrosine kinases Axl and Mer, which have been linked to AD. Huang *et al.* performed molecular, genetic, cell biological, and in vivo two-photon imaging analyses of AD mouse models crossed into Axl- and Mertk-knockout mouse mutants. Induced expression of Axl and Mer in plaque-associated microglia led to the recruitment of the TAM ligand Gas6 and to the formation of dense accumulations of phagocytosed amyloid within the microglia. An AD mouse model lacking Axl and Mer did not phagocytose amyloid as normal. Despite this, the mice developed fewer plaques than AD mice with normal microglia. Thus, TAM receptor signaling is required for microglial recognition of amyloid plaques, and, counterintuitively, TAM-driven microglial phagocytosis promotes plaque deposition and growth. —SMH

Nat. Immunol. **22**, 586 (2021).

CANCER

Unexpected benefits of microbiota

Cachexia is a condition of muscle wasting seen in cancer that contributes to mortality. On the basis of previously reported connections between gut microbiota and cachexia, de Clercq *et al.* transplanted fecal microbiota from healthy obese donors to patients with cancer cachexia and compared their outcomes with those of patients receiving autologous microbiota. Unexpectedly, the allogeneic transplantations had no effect on cachexia but they did improve patients' responses to chemotherapy and overall survival. The findings are intriguing but also raise numerous questions about the specific effects of the microbiota: There were no nonobese donor controls, so it is possible that any allogeneic microbiota transplantation might be beneficial. —YN

Clin. Cancer Res. 10.1158/1078-0432.CCR-20-4918 (2021).

PHOTO: ESA/SOLAR ORBITER/EUI

REVIEW SUMMARY

HUMAN EVOLUTION

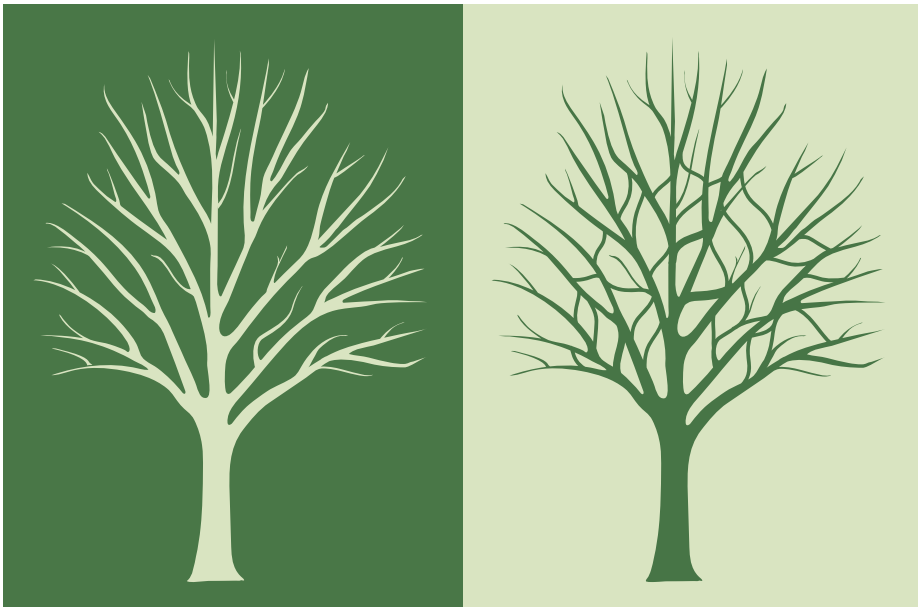
Modern theories of human evolution foreshadowed by Darwin's *Descent of Man*

Peter J. Richerson, Sergey Gavrilets*, Frans B. M. de Waal

BACKGROUND: Charles Darwin's *The Descent of Man*, published on 24 February 1871, laid the grounds for scientific studies into human origins and evolution. We look at the advances in our understanding of these processes through the lenses of modern speciation theory. Applying this theory to specific cases requires one to identify and understand the nature of (i) the ancestor and various preexisting adaptations and traits that it possessed that allowed or simplified the speciation process, (ii) evolutionary forces responsible for major differences between the emergent species and its close relatives, and (iii) the most salient adaptations characteristic of the new species and its evolutionary history (such as genetic, morphological, behavioral, spatial, and temporal).

ADVANCES: Modern research shows that we share many developmental, physiological, morphological, cognitive, and psychological characteristics as well as about 96% of our DNA with the anthropoid apes. We now know that since our last common ancestor with the other apes 6 million to 8 million years ago, human evolution followed the path common for other species with diversification into closely related species and some subsequent hybridization between them. Since Darwin, a long series of unbridgeable gaps have been proposed between humans and other animals. They focused on tool-making, cultural learning and imitation, empathy, prosociality and cooperation, planning and foresight, episodic memory, metacognition, and theory of mind. However, new insights from neurobiology, genetics, primatology, and behavioral biology only reinforce Darwin's view that most differences between humans and higher animals are "of degree and not of kind." What makes us different is that our ancestors evolved greatly enhanced abilities for (and reliance on) cooperation, social learning, and cumulative culture—traits emphasized already by Darwin. Cooperation allowed for environmental risk buffering, cost reduction, and the access to new resources and benefits through the "economy of scale." Learning and cumulative culture allowed for the accumulation and rapid spread of beneficial innovations between individuals and groups. The enhanced abilities to learn from and cooperate with others became a universal tool, removing the need to evolve specific biological organs for specific environmental challenges. These human traits likely evolved as a response to increasing high-frequency climate changes on the millennial and submillennial scales during the Pleistocene. Once the abilities for cumulative culture and extended cooperation were in place, a suite of subsequent evolutionary changes became possible and likely unavoidable. In particular, human social systems evolved to support mothers through the recruitment of males and nonreproductive females. The most distinctive feature of our species, language, appeared arguably driven by selection for simplifying cooperation. Reliance on social learning and conformity led to the emergence of new factors constraining and driving human behavior, such as morality, social norms, and social institutions. These forces often act against the immediate biological or material interests of individuals, promoting instead the interests of the society as a whole or of its powerful segments. Continuous engagement in cooperation has led to the evolution of strong coalitionary psychology, which can bring us together whenever we perceive that our identity group faces outside threats. Coalitionary psychology also has an undesirable byproduct: often negative or even hostile reaction to others who differ from us in their looks, behaviors, beliefs, caste, or class.

OUTLOOK: Our society faces challenges, including climate change; various types of inequality; economic crises; political, cultural, and religious conflicts; and pandemics. Similar challenges have repeatedly arisen and were dealt with in the past with varying success. What makes the current situation different is not only the scale of societal threats but also that modern science can provide guidance on how to respond to them. Adequately answering these challenges requires understanding humans' social behavior and the roles of cooperation, social learning, and culture for human decision-making. Evolutionary perspective is already helping to synthesize the contributions of social sciences, including anthropology, psychology, economics, political science, and history. The impact of *Descent* on the social sciences and on the development and implementation of different policies by practitioners and policymakers to improve our society will only grow. ■



Depictions of organic evolution versus cultural evolution. (Left) Organic evolution and (right) cultural evolution, as described in Alfred L. Kroeber's 1923 textbook *Anthropology: Cultural Patterns and Processes*. Biological inheritance is rigid from parents to offspring in eukaryotes, and species mostly do not exchange genes. Culture is potentially acquired from anyone in a person's social network, and ideas spread rather readily from culture to culture.

IMAGE: N. CARY/*SCIENCE*

The list of author affiliations is available in the full article online.
*Corresponding author. Email: gavrila@utk.edu
Cite this article as P. J. Richerson *et al.*, *Science* **372**, eaba3776 (2021). DOI: 10.1126/science.aba3776

READ THE FULL ARTICLE AT
https://doi.org/10.1126/science.aba3776

RESEARCH ARTICLE SUMMARY

NEUROSCIENCE

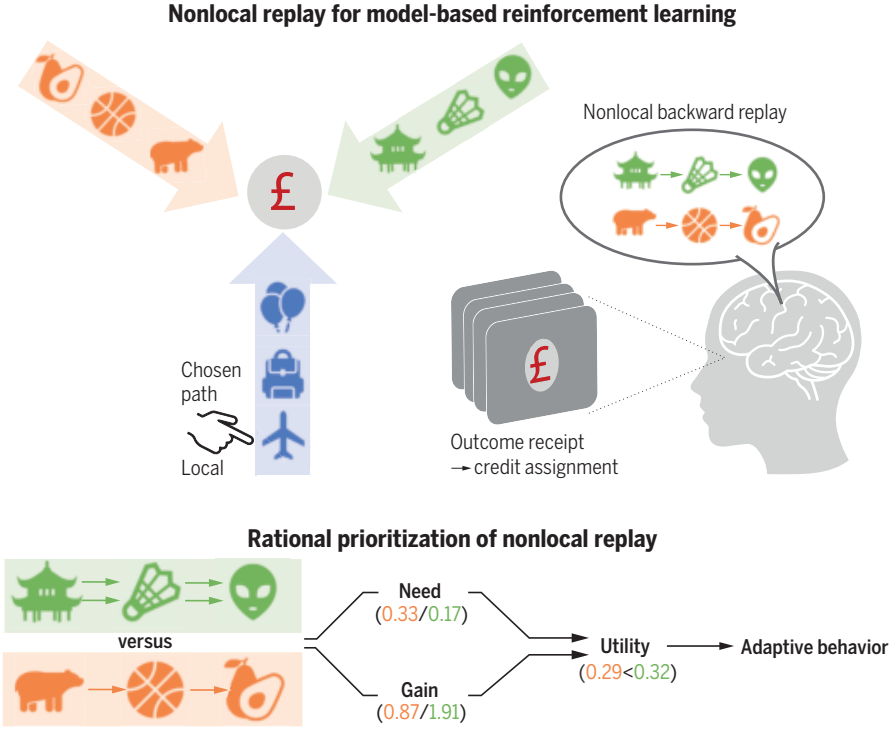
Experience replay is associated with efficient nonlocal learning

Yunzhe Liu*†, Marcelo G. Mattar†, Timothy E. J. Behrens, Nathaniel D. Daw‡, Raymond J. Dolan‡

INTRODUCTION: Adaptive decision-making requires assimilation of reward information to guide subsequent choices. However, actions and outcomes are often separated by time and space, rendering this difficult. In reinforcement learning, this problem can be solved using "model-based" inference, in which an agent leverages a learned model of the environment to link local reward to nonlocal actions; this process is known as experience replay.

A potential neural substrate for this process is hippocampal "replay." In rodents, cells in the hippocampus fire in an organized manner that recapitulates past or potential future trajectories during rest. A similar phenomenon has also been observed in humans during a post-task rest period. However, a direct connection between replay and nonlocal (i.e., model-based) learning has yet to be established.

RATIONALE: The question of how to achieve model-based learning in the service of adaptive behavior is central to understanding intelligence in both biological and artificial agents. We addressed this question by exploiting a normative model of replay based on reinforcement learning theory. This model makes specific predictions regarding how replay relates to nonlocal learning and about which information is more or less useful if replayed. To measure replay in humans, we used machine learning techniques in conjunction with magnetoencephalography (MEG) recordings of whole-brain neural activity. These techniques enabled us to ask whether and how neural replay contributes to nondirect learning in humans. In so doing, we address an outstanding question in reinforcement learning theory: how the brain forms links between disjoint actions and goals and uses these to inform better decisions in the future.



Experience replay is associated with efficient nonlocal learning. Top left: The key element of the experimental design is a separation of local versus nonlocal learning. The chosen path (indicated by hand) reflects local experience; the other two paths leading to the same outcome state (the red £), but not directly experienced, are the nonlocal paths. Arrow direction indicates the order of actual experience; color indicates the arm identity. There are three arms, and outcomes are shared across the three arms. Top right: Nonlocal backward replay after reward receipt. There are two nonlocal experiences per trial. We found neural replay of these paths after reward receipt, consistent with a credit assignment account in reinforcement learning—an assignment of local reward information to nonlocal actions. Bottom: Consistent with reinforcement learning theory, replay was prioritized according to utility (need × gain) and was related to more efficient nonlocal learning. In the example, this is illustrated as stronger replay (double arrows) for the green path, because of its higher utility (0.32 versus 0.29) relative to the orange path.

RESULTS: We designed a novel decision-making task to separate local from nonlocal learning—that is, learning from direct experience as opposed to indirect learning based on inference. Specifically, we developed a three-arm task, wherein each arm comprised two paths leading to distinct end states. Crucially, the two end states, reachable from each arm, are shared across all three arms. This design feature allows post-choice reward feedback to inform future choices not only in the chosen arm (local learning) but also in either of the other two arms (nonlocal learning).

This work revealed the existence of backward neural replay of nonlocal experiences after reward receipt, with a 160-ms state-to-state time lag. In line with normative theory, such replay predominantly represents the path most useful for future behavior. This backward replay encoded nonlocal experience alone and was physiologically distinct from a faster forward replay (30-ms time lag), which was associated with power increase in a ripple band.

Using computational modeling, we showed that the strength of this backward replay relates to efficient trial-by-trial within-subject learning of the same nonlocal experience, as well as a better overall task performance across subjects. This is consistent with our theoretical predictions and provides strong support for a reinforcement learning–based account of neural replay in decision-making.

CONCLUSION: Backward replay accompanies efficient nonlocal learning in humans and is prioritized according to its utility. These results connect several findings in human and rodent neuroscience and implicate experience replay in model-based reinforcement learning. ■

The list of author affiliations is available in the full article online.
†These authors contributed equally to this work.
‡These authors contributed equally to this work.
*Corresponding author. Email: yunzhe.liu@bnu.edu.cn
Cite this article as Y. Liu *et al.*, *Science* **372**, eabf1357 (2021). DOI: 10.1126/science.abf1357

READ THE FULL ARTICLE AT
https://doi.org/10.1126/science.abf1357

RESEARCH ARTICLES

STRUCTURAL BIOLOGY

Structure reveals the activation mechanism of the MC4 receptor to initiate satiation signaling

Hadar Israeli[1,2]†, Oksana Degtjarik[1]†, Fabrizio Fierro[3,4], Vidicha Chunilal[5], Amandeep Kaur Gill[5], Nicolas J. Roth[5], Joaquin Botta[5]‡, Vadivel Prabahar[1], Yoav Peleg[6], Li F. Chan[5], Danny Ben-Zvi[2]*, Peter J. McCormick[5]*, Masha Y. Niv[3,4]*, Moran Shalev-Benami[1]*

Obesity is a global epidemic that causes morbidity and impaired quality of life. The melanocortin receptor 4 (MC4R) is at the crux of appetite, energy homeostasis, and body-weight control in the central nervous system and is a prime target for anti-obesity drugs. Here, we present the cryo–electron microscopy (cryo-EM) structure of the human MC4R-G_s signaling complex bound to the agonist setmelanotide, a cyclic peptide recently approved for the treatment of obesity. The work reveals the mechanism of MC4R activation, highlighting a molecular switch that initiates satiation signaling. In addition, our findings indicate that calcium (Ca^{2+}) is required for agonist, but not antagonist, efficacy. These results fill a gap in the understanding of MC4R activation and could guide the design of future weight-management drugs.

Obesity is a global epidemic, with more than 40% of the adult population considered overweight or obese (*1*). Obesity is a major risk factor for chronic diseases—including type 2 diabetes, coronary artery disease, and cancer—and constitutes an important cause of morbidity and impaired quality of life (*2*). Over the years, various weight loss–targeting drugs have been developed, yet most of these were ultimately removed from the market because of questionable efficacy, lack of target specificity, or severe adverse effects. This highlights the need for a better understanding of the molecular mechanisms governing weight regulation and its related pathologies.

Melanocortin 4 receptor (MC4R) is a member of the melanocortin receptor family (MCRs), a class A G protein–coupled receptor (GPCR) subgroup consisting of five subtypes (MC1R to MC5R) that mediate multiple physiological effects in humans (*3*). MC4R is abundant throughout the mammalian central nervous system (CNS) and is expressed, in particular, within the paraventricular nucleus of the hypothalamus, a region critical for energy homeostasis (*4*–*6*). MC4R has been shown to play a key role in modulating satiety in pharmacological and genetic studies in animal models and patients (*7*–*9*). Loss-of-function mutations in MC4R have been implicated in ~6 to 8% of early-onset severe obesity cases and are considered the most common form of monogenic obesity (*7*, *10*), whereas gain-of-function mutations have been linked to low body mass index (BMI) (*9*). Beyond its critical role in the regulation of food intake and energy expenditure, MC4R also functions in other CNS regions with clinical implications in pain sensation, sexual function, anhedonia, and blood pressure regulation (*11*–*13*).

MC4R is an unusual GPCR because it has both an endogenous agonist and an endogenous antagonist (*14*, *15*). Specifically, MC4R is activated by alpha-melanocyte-stimulating hormone (α-MSH), a proopiomelanocortin (POMC)–derived peptide that mediates anorexigenic effects and is antagonized through binding of the agouti-related peptide (AgRP), which promotes appetite (*14*). A recent crystal structure of MC4R bound to a potent antagonist provided a snapshot of the inactive receptor conformation (*16*), but the molecular architecture of an active complex with cognate signaling partners remained unknown. We determined the structure of the active human MC4R bound to the cyclic peptide agonist setmelanotide and in complex with the G_s heterotrimer at 3-Å resolution by cryo–electron microscopy (cryo-EM). Setmelanotide (Imcivree) is a promising weight-control drug shown to induce weight loss in patients suffering from POMC deficiency (*17*, *18*), leptin receptor deficiency (*19*), and other forms of severe genetic obesity and was recently registered by the U.S. Food and Drug Administration for the treatment of these conditions (*20*–*23*).

[1]Department of Chemical and Structural Biology, Weizmann Institute of Science, Rehovot 7610001, Israel. [2]Department of Developmental Biology and Cancer Research, The Institute for Medical Research Israel-Canada, The Hebrew University–Hadassah Medical School, Jerusalem, Israel. [3]The Faculty of Agriculture, Food and Environment, The Hebrew University, Rehovot, Israel. [4]The Fritz Haber Center for Molecular Dynamics, The Hebrew University, Jerusalem, Israel. [5]Centre for Endocrinology, William Harvey Research Institute, Barts and the London School of Medicine, Queen Mary, University of London, Charterhouse Square, London, UK. [6]Structural Proteomics Unit (SPU), Life Sciences Core Facilities (LSCF), Weizmann Institute of Science, Rehovot 7610001, Israel.
†These authors contributed equally to this work.
‡Present address: Sosei-Heptares, Cambridge, UK.
***Corresponding author. Email: moransb@weizmann.ac.il (M.S.-B.); p.mccormick@qmul.ac.uk (P.J.M.); masha.niv@mail.huji.ac.il (M.Y.N.); danny.ben-zvi@mail.huji.ac.il (D.B.-Z.)**

The molecular architecture of the native MC4R signaling complex

The setmelanotide-MC4R-G_s complex was assembled by supplying agonist to cells coexpressing heterotrimeric G_s and full-length MC4R and was stabilized using the single-chain variable fragment scFv16 (*24*). ScFv16 was originally developed for the stabilization of the G_{i1} heterotrimer and has been used to determine several $G_{i/o}$ and G_q GPCR complex structures (*25*–*29*). We replaced the αN helix of $G\alpha_s$ (residues 1 to 38) with that of $G\alpha_{i1}$ (residues 1 to 31) to enable complex recognition by scFv16 ($G\alpha_{s\text{-}iN}$) (*24*). This strategy yielded a stable G_s heterotrimer that coupled to activated MC4R (fig. S1).

We used single-particle cryo-EM analysis to obtain a three-dimensional reconstruction of the MC4R-G_s complex at a nominal resolution of 3 Å (Fig. 1, figs. S1 and S2, and tables S1 and S2). The map revealed the architectures of all complex components, as well as the mode of receptor association with the G_s heterotrimer and the orientation of setmelanotide within the orthosteric binding pocket (Fig. 1, C and D). Most notably, MC4R differs from previously reported class A GPCR–G protein complexes in the extracellular region, which is relatively open, containing an exposed cavity of 1082 $Å^3$ (Fig. 2, B and C; and fig. S3A). This feature can be attributed to a short extracellular loop 2 (ECL2) that lacks secondary structural elements compared with other class A members (fig. S3B) (*30*). As noted previously (*16*), MC4R lacks a disulfide bond found in other class A GPCRs that connects ECL2 with transmembrane helix 3 (TM3) (*31*). Instead, the MC4R extracellular region has two other disulfide bonds, which link the N terminus to TM7 and ECL3 to TM6, both of which are clearly visualized in our EM density ($C40^{N\text{-}term}$-$C279^{7.30}$ and $C271^{6.61}$-$C277^{ECL3}$; C indicates Cys, and superscript numbers correspond to the Ballesteros-Weinstein nomenclature; fig. S2G). Overall, our structure enables the analysis of the full-length, active MC4R coupled with its cognate cellular effectors and supplies residue-resolution information on the main signaling pathway leading to satiety.

Description of setmelanotide in the MC4R binding pocket

Setmelanotide is a potent mimetic of α-MSH, the endogenous hormone agonist that acts on MC4R to signal satiety and increase energy expenditure (Fig. 2A). Unlike α-MSH, setmelanotide is linked by a disulfide bond

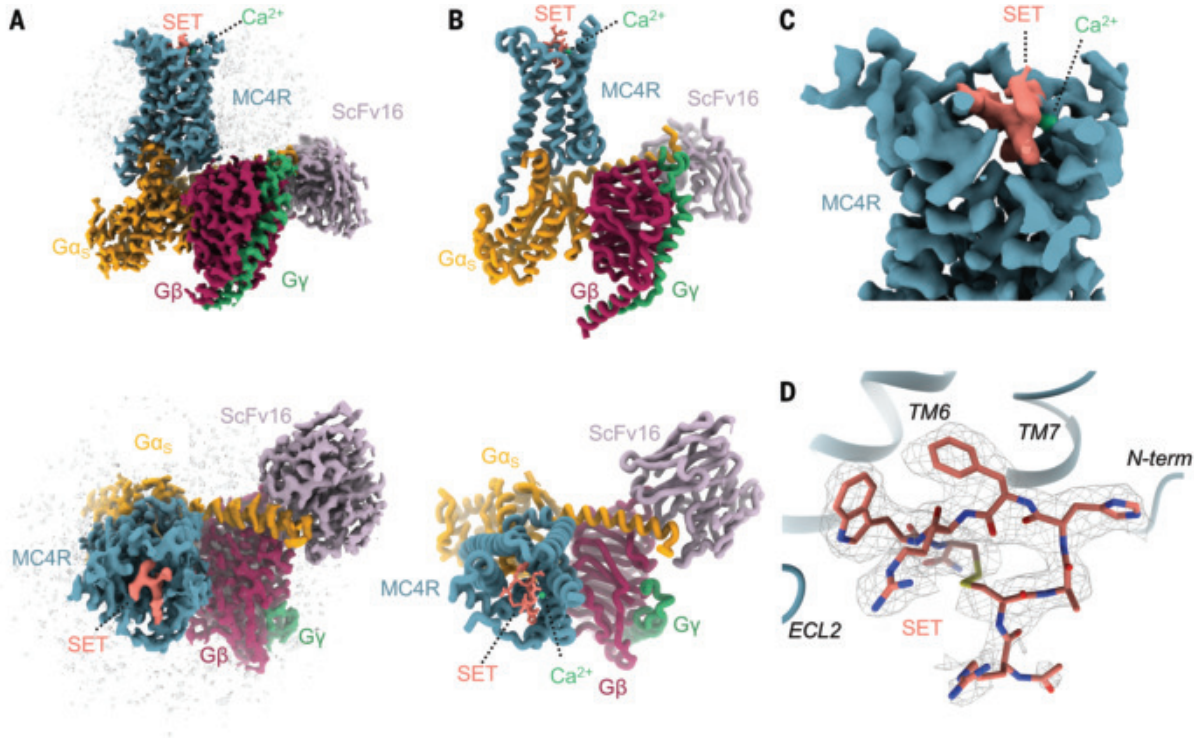


Fig. 1. An overall description of MC4R architecture. (**A**) Cryo-EM map of the MC4R-G_s signaling complex embedded within an LMNG:GDN (lauryl maltose neopentylglycol:glyco-diosgenin) micelle. MC4R is in blue, setmelanotide (SET) is in pink, and $G\alpha_s$, Gβ, and Gγ are in yellow, magenta, and green, respectively. ScFv16 is in light purple. The bottom map is rotated 90° along the *x* axis. The map contour level is 0.027. (**B**) Cartoon model corresponding to map positions presented in (A). (**C**) A view of the MC4R cryo-EM map with setmelanotide in the orthosteric binding pocket. Setmelanotide is in pink, and the density for Ca^{2+} is presented in light green. The map contour level is 0.027. (**D**) Setmelanotide in density. The map contour level is 0.02.

between cysteines near its termini. Setmelanotide contains the highly conserved HFRW (His-Phe-Arg-Trp) motif that is shared between all POMC-derived peptides and contributes directly to the activation of receptors of the MCR family (*32*). However, the phenylalanine in setmelanotide is in the D configuration, whereas it is in the L conformation in α-MSH (Fig. 2A).

In the cryo-EM structure, setmelanotide engages MC4R through extensive electrostatic and hydrophobic interactions with residues in the transmembrane domain (Fig. 3A). These interactions are mostly attributed to the HFRW motif and include hydrogen bonds with S188, π-π stacking interaction with F51, C–H···O contacts (*33*) with F184, Y268, and F284, and hydrophobic contacts with T101, I129, L133, I185, I194, and F261 (Fig. 3A) (S, Ser; F, Phe; Y, Tyr; T, Thr; I, Ile; L, Leu). Most of these residues are highly conserved among the MCR family and account for the cross reactivity with POMC-derived peptides. Interactions outside the HFRW motif include contacts between Cys_8 in setmelanotide and Y268 and F284 in the receptor, only the last of which is conserved in members of the MCR family (Fig. 3B and fig. S4). Additional contacts are from Arg_1 and Ala_3 to D122 and I104 (D, Asp), respectively, both of which are conserved in MCR family members. Arg_1 in setmelanotide substitutes for a serine in α-MSH and likely contributes to the increased potency of the drug compared with the endogenous hormone (Fig. 2, A and D).

A notable feature of setmelanotide binding is a Ca^{2+} ion coordinated by both the agonist and the receptor. A Ca^{2+} ion was observed in a similar position in the complex of MC4R with the synthetic antagonist SHU9119 [Fig. 3C and (*16*)]. In both structures, the receptor contributes the side chains of the acidic residues ($D122^{3.25}$, $D126^{3.29}$, and $E100^{2.60}$; E, Glu) to Ca^{2+} coordination, and both setmelanotide and SHU9119 have a direct interaction to the ion using the D-Phe_5 backbone oxygen (D-naphthyl alanine, D-Nal_4, in SHU9119; Fig. 3C). One difference in the coordination of the Ca^{2+} between the antagonist and agonist structures is that SHU9119 contributes the backbone carbonyl of Asp_2 in a backbone-ligand interaction, whereas setmelanotide uses a water-mediated interaction between the backbone carbonyl of D-Ala_3 and the ion (Fig. 3C and fig. S2F). Molecular dynamics simulations suggest that the backbone carbonyl of Cys_2 may alternate with the backbone carbonyl of D-Ala_3 in creating the water-mediated interaction (fig. S5, A and B).

Ca^{+2} functions as a cofactor required for receptor activation but not inhibition

Molecular dynamics simulations support Ca^{2+} binding by MC4R even in the absence of a ligand, suggesting that Ca^{2+} may have a ligand-independent role or may prime the pocket for ligand binding (Fig. 3D and fig. S5, C and D). Although the simulations suggest that Ca^{2+} does not depend on other ligands for binding, MC4R agonists require Ca^{2+} to achieve full efficacy. The median effective concentration (EC_{50}) for both α-MSH and setmelanotide decreased by about two orders of magnitude in the presence of physiological Ca^{2+} concentrations (1 mM) in our cellular assays (Fig. 4, A and B; and fig. S6). Indeed, an estimation of the affinity constant for allosteric modulation (K_B) for Ca^{2+} (0.06μM; fig. S6M) supports Ca^{2+} binding at physiologic levels to MC4R. Notably, other divalent ions did not have similar effects, nor did we detect allosteric effects on Ca^{2+} binding caused by the presence of other ions (fig. S6, A to J). These results are in accordance with several

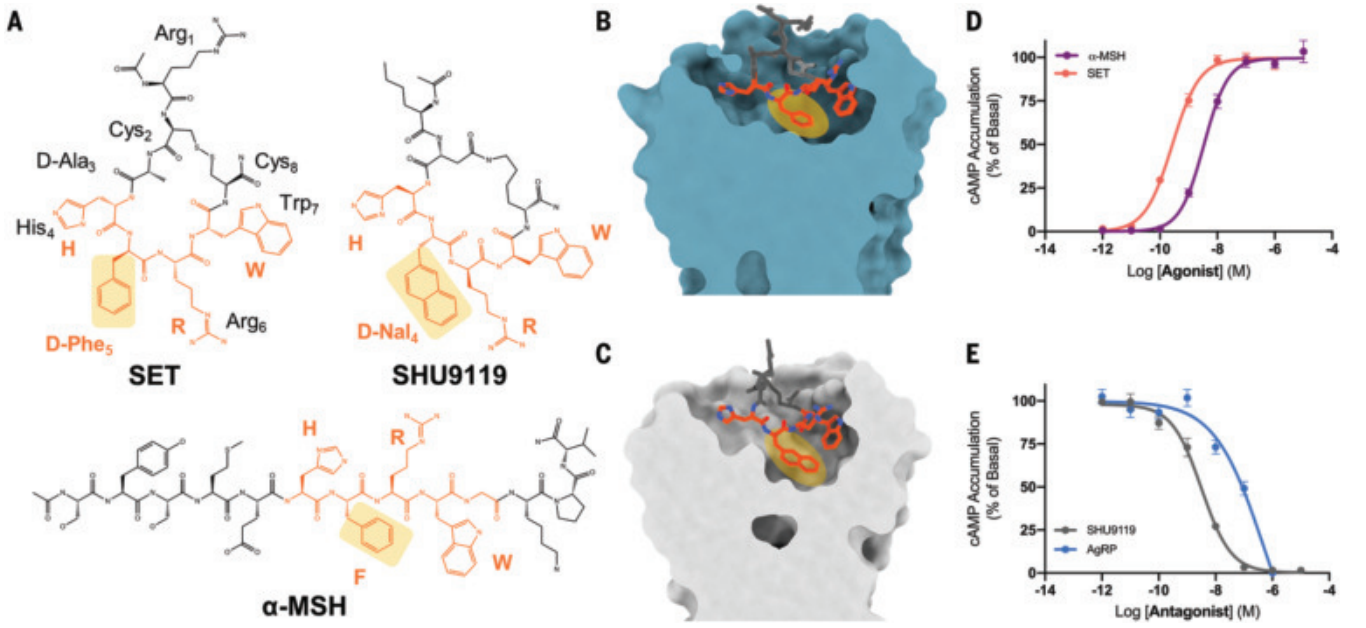


Fig. 2. Agonists and antagonists for MC4R. (**A**) Chemical structures of MC4R agonists α-MSH and setmelanotide (SET) and the antagonist SHU9119. The conserved HFRW motif is in orange. Phenylalanine substitutions in SET (D-Phe_5) and in SHU9119 (D-Nal_4) are highlighted in yellow. (**B** and **C**) A view of setmelanotide (B) and SHU9119 (PDB 6W25) (C) at the MC4R orthosteric binding pocket. The HFRW motif is in orange with D-Phe_5 (SET) and D-Nal_4 (SHU9119) highlighted in yellow. The active receptor is in blue (B), and the inactive receptor is in gray (C). When comparing the active and inactive receptor states, the D-Nal_4 moiety of the antagonist SHU9119 penetrates more deeply into the pocket. (**D**) Dose response curves for the agonists α-MSH (purple) and setmelanotide (pink) measured as cAMP production normalized by percentage of basal activity of the wild-type receptor. Data are represented as mean ± SEM from three independent experiments done in triplicate, indicating EC_{50} values of 3.79 ± 0.87 and 0.29 ± 0.04 nM for α-MSH and setmelanotide, respectively. (**E**) Competition assays of inverse agonists AgRP (blue) and SHU9119 (gray) with α-MSH, calculated as the decrease in cAMP production in the presence of an increasing dose of the antagonists. Experiments were conducted in the presence of 1 μM α-MSH. Data are represented as mean ± SEM from three independent experiments done in triplicate. pIC_{50} values (the negative log of the mean inhibitory concentration when converted to molar) are 6.67 ± 0.18 and 8.51 ± 0.05 nM for AgRP and SHU9119, respectively.

previous reports that α-MSH, as well as synthetic agonists, depends on the presence of Ca^{2+} for signaling, with no notable change in response to other ions (*16*, *34*). We also found that the nonpeptide synthetic MC4R agonist THIQ depends on Ca^{2+} for enhanced activity and binding (fig. S7).

By contrast, we found that physiological Ca^{2+} concentrations do not contribute to SHU9119- or AgRP-induced antagonistic activity. Signaling assays revealed that physiological Ca^{2+} concentrations do not substantially affect the ability of SHU9119 to compete with α-MSH and that AgRP activity is indeed hampered by the presence of Ca^{2+} (Fig. 4, C and D). This suggests that Ca^{2+} plays a role in modulating receptor susceptibility to endogenous agonists and antagonists.

Notably, one of the residues that was found to coordinate Ca^{2+} positioning within the binding pocket and modulate ligand accommodation in the receptor, $D122^{3.25}$, corresponds to a conserved cysteine residue in other class A members, which composes a disulfide bridge missing in MCRs (fig. S8, A to C). These data highlight the possibility that Ca^{2+} serves as a surrogate to the function of the bridge and contributes to the structural integrity of the canonical binding pocket. Given the opposite effect of Ca^{2+} on the endogenous agonist and antagonist, we suggest that Ca^{2+} can provide MC4R sufficient flexibility to modulate the binding pocket to differentially accommodate agonists and antagonists.

Mutation of residues involved in Ca^{2+} coordination reduces receptor activation

Mutational studies were conducted to further explore the function of Ca^{2+} coordination in receptor activity and to assess the implications for human disease. Two of the Ca^{2+}-coordinating residues, D122N (N, Asn) and D126Y, are naturally occurring mutations associated with obesity (*18*, *35*). An E100A (A, Ala) mutation was introduced to probe the function of the third Ca^{2+}-coordinating side chain. The D122N mutant displayed a two-log increase in EC_{50} and a ~50% decrease in efficacy for α-MSH and setmelanotide under physiological Ca^{2+} concentrations. For the E100A mutant, the impairment was not the same for the natural and artificial agonists. Whereas α-MSH signaling was almost completely abolished by the E100A mutation, setmelanotide was still able to signal, but at half maximum and with a two-log increase in EC_{50} (Fig. 4, E and F). The D126Y mutant resulted in the complete abolishment of receptor function. The more pronounced effect of the D126 substitution can be explained by the fact that D122 and E100 each contribute a single bond to Ca^{2+} coordination, whereas D126 contributes two (Fig. 3C). Both the D122N and E100A mutants remained dependent on Ca^{2+} for signaling for both setmelanotide and α-MSH, suggesting that altering the aspartates at these positions did not eliminate Ca^{2+} coordination (fig. S8, E and F). Flow cytometry analysis indicated similar profiles of surface expression levels for wild-type and mutant receptors, indicating that the observed activity changes were not due to poor cell surface availability (fig. S8D). These results are in agreement with previously reported work in which mutations at positions 122 and 126 in MC4R resulted in impaired ligand binding properties (*18*, *35*–*38*). The differential activation profile of the D122N variant by setmelanotide compared with α-MSH

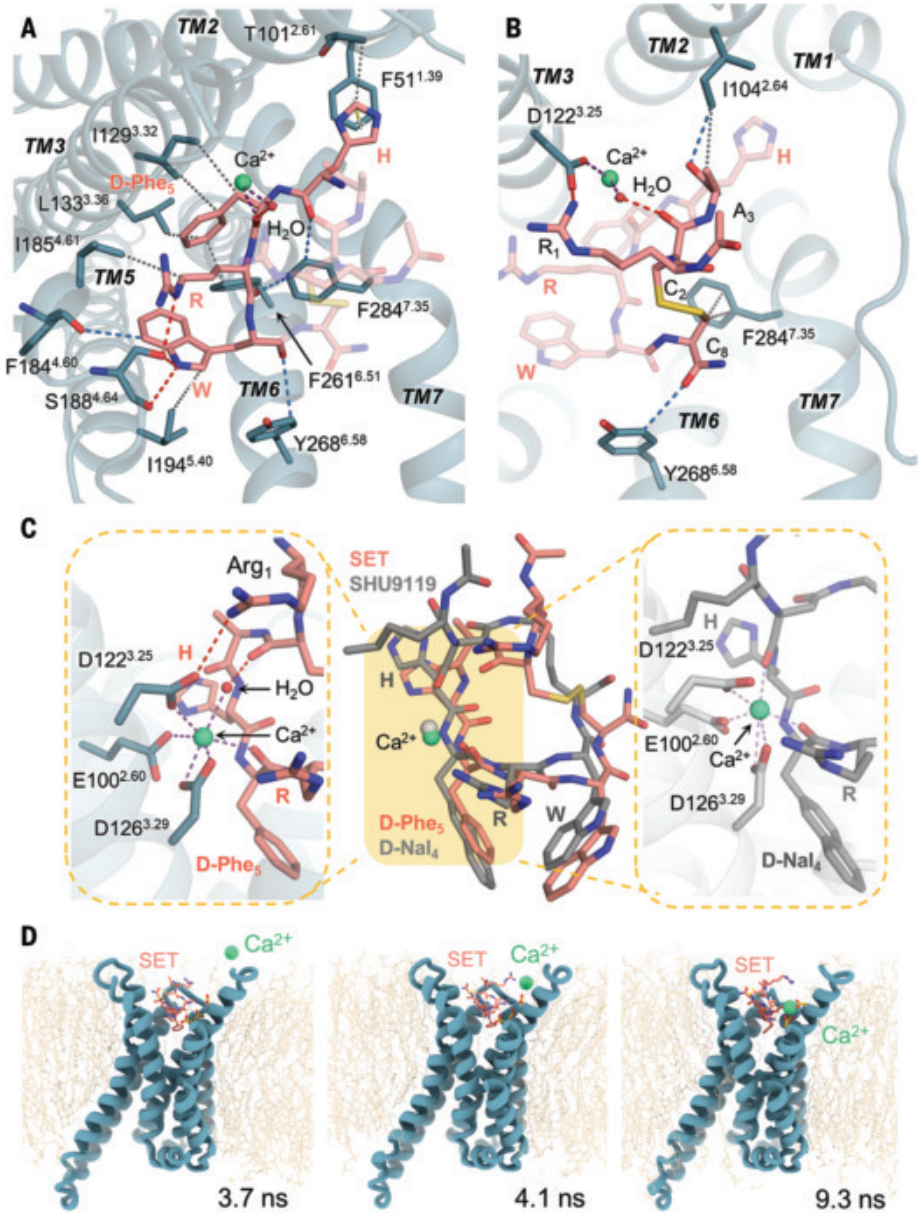


Fig. 3. Ligand accommodation within the MC4R binding pocket. (**A** and **B**) Setmelanotide interactions in the MC4R binding pocket. The receptor is presented in light blue, setmelanotide (SET) is in pink, and Ca^{2+} is in green. Dashed lines are colored according to the type of interactions, with hydrogen bonds in red, hydrophobic interactions in gray, CH–O in blue, and Ca^{2+} coordination in purple. π-π stacking is indicated in yellow and marked by an asterisk. Interactions with the HFRW motif are shown in (A), and interactions with nonconserved residues are shown in (B). (**C**) A comparison of the Ca^{2+} coordination in the presence of setmelanotide (agonist, pink, left) and SHU9119 (antagonist, gray, right; PDB 6W25). Superposition of the agonist and antagonist is shown in the middle, with the Ca^{2+} ion appearing in green for the active structure and gray for the inactive structure. The receptor is presented as a cartoon with the active conformation in light blue (left) and the inactive conformation in gray (right). (**D**) Snapshots of the molecular dynamics equilibration steps after 3.7, 4.1, and 9.3 ns (molecular dynamics run with setmelanotide, replica 1) showing the Ca^{2+} ion (green sphere) entering the ion binding pocket (yellow licorice side chains, showing residues $D122^{3.25}$, $D126^{3.29}$, and $E100^{2.60}$) of the MC4R receptor (light blue cartoon). Setmelanotide is shown in pink, and the membrane lipids are in cream. In the starting configuration of all the simulations, Ca^{2+} was positioned in the intra- and extracellular water layers, leaving the Ca^{2+} binding site free. Out of a total cumulative simulation time of 2 μs, Ca^{2+} was found in the MC4R-bound position for ~1.8 μs and, once binding was established, the ion remained inside the binding pocket throughout the simulations performed (fig. S5, C and D).

highlights setmelanotide as a potential therapeutic path for individuals harboring a D122N mutation. Discussion of common mutations in MC4R is further provided in fig. S9.

Identification of a mechanical activation switch in MC4R

By comparing the inactive and active states of MC4R, the outward displacement of TM6 is clearly evident (Fig. 5A and fig. S3C). This structural rearrangement is a hallmark of GPCR activation, allowing the C-terminal α5 helix of the $G\alpha_s$ subunit to engage the receptor core and initiate signaling. In MC4R, binding of the agonist setmelanotide partly resembles the binding of the antagonist SHU9119 (*16*) (Figs. 2 and 3), raising the question of how the structural change and GPCR activation are induced selectively by the agonist. A noticeable difference between the binding modes of the antagonist and the agonist is that the D-Nal_4 group of SHU9119, which is bulkier than the D-Phe_5 in setmelanotide, penetrates the binding pocket more deeply and interacts with $L133^{3.36}$ (Figs. 2, B and C, and 5B). $L133^{3.36}$ is a key modulator in class A GPCR activation because it directly interacts with $W258^{6.48}$, which plays a crucial role in TM6 displacement during receptor transition to the active state (*31*). In the inactive state, $L133^{3.36}$ engages the aromatic face of $W258^{6.48}$ (W, Trp), with the two methyl groups facing the π-electrons and maintaining CH-π contacts (Fig. 5B). In the active conformation, $L133^{3.36}$ is oriented with the two methyl groups facing away from $W258^{6.48}$. As a result, $W258^{6.48}$ is free to accommodate an alternate state that allows for the conformational rearrangement of TM6 that is required for G protein coupling (Fig. 5, A and B). This conformational change resembles the classic toggle switch in other GPCRs, where, in the inactive state, $F^{3.36}$ stacks upon $W^{6.48}$ to maintain the inactive receptor, whereas in the active conformation, $F^{3.36}$ rotates and allows the release of $W^{6.48}$ [e.g., CB1R (*26*, *39*), CB2R (*40*), and CCR5 (*41*); Fig. 5C]. Comparison of the agonist- and antagonist-bound structures suggests that whereas SHU9119 sterically hinders the displacement of $L133^{3.36}$ toward the active state, the phenyl residue in setmelanotide stabilizes the active state conformation (Fig. 5B).

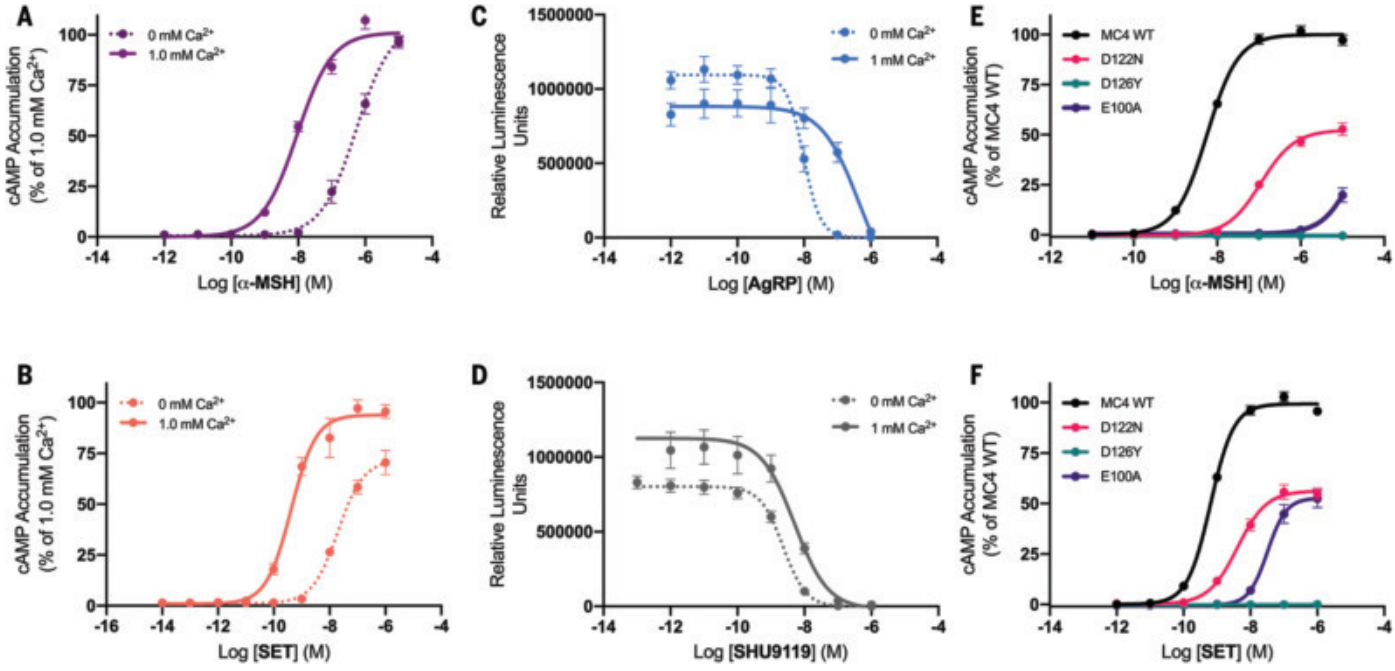


Fig. 4. Ca^{2+} acts as a cofactor for MC4R activation. (**A** and **B**) Dose response curves for the agonists α-MSH (A) and setmelanotide (B) in the absence and presence of 1 mM Ca^{2+}. The absence of Ca^{2+} is indicated with a dashed line. Data are represented as mean ± SEM from three independent experiments done in triplicate. (**C** and **D**) Competition assays of antagonists AgRP (C) and SHU9119 (D) with α-MSH in the absence and presence of 1 mM Ca^{2+}. Assays are calculated as the decrease in cAMP production in the presence of an increasing dose of the antagonists. Experiments were conducted in the presence of 1 μM α-MSH. Data are represented as mean ± SEM from three independent experiments done in triplicate. (**E** and **F**) Mutations in residues involving Ca^{2+} coordination considerably reduce receptor's activation through α-MSH (E) and setmelanotide (F). Dose response curves for the agonists indicate an increase in cAMP production and are represented as mean ± SEM from three independent experiments done in triplicate. Cell cytometry analysis indicating surface expression of wild type (WT) and mutants is in fig. S8D. Mutant dependence on Ca^{2+} is shown in fig. S8, E and F.

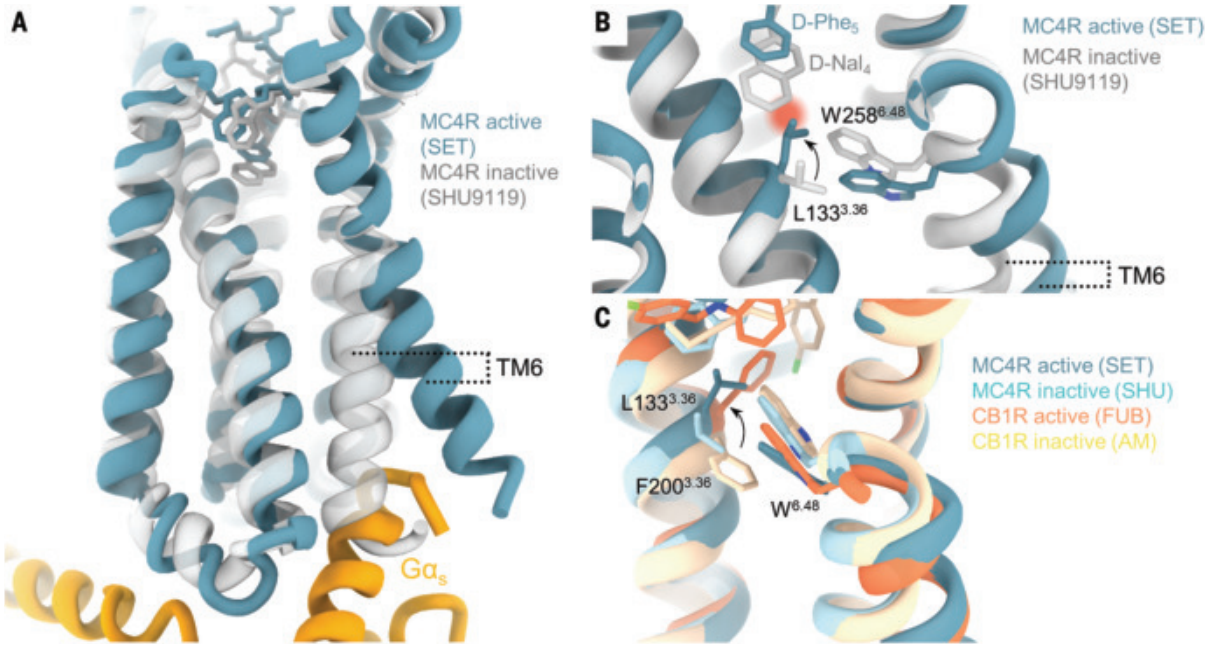


Fig. 5. MC4R activation switch. (**A**) Superposition of the MC4R active complex (blue) with an antagonist-bound receptor (SHU9119, PDB 6W25, gray). Setmelanotide (SET, blue) and SHU9119 (gray) bound at the MC4R canonical pocket differentially interact with $L133^{3.36}$, which composes the switch that controls receptor conformation. The outward movement of TM6 is indicated by black dashed lines. $G\alpha_s$ is in yellow. (**B**) The bulky D-Nal_4 moiety in SHU9119 stabilizes the inactive switch conformation (gray), by which $L133^{3.36}$ is stacked upon $W258^{6.48}$. The D-Phe_5 moiety in setmelanotide contributes to an alternative rotamer, releasing $W258^{6.48}$, which enables the outward movement of TM6 to allow the accommodation of $G\alpha_s$ and receptor activation (blue). The arrow indicates switch alternation from the inactive to the active state. (**C**) Superposition of the MC4R activation switch (active, blue; inactive, light cyan) with a classical "toggle twin switch" of CB1R [PDB 6N4B and 5TGZ, for active (orange) and inactive (light yellow) conformations, respectively]. The comparison of the two switches indicates a similar conformation of the two switches despite the difference in the identity of the switch residues. In MC4R, the switch is composed of $L133^{3.36}$ and $W258^{6.48}$, whereas the classical switch in CB1R is composed of $F200^{3.36}$ and $W356^{6.48}$.

A challenge in targeting MC4R is to avoid undesired side effects due to cross-reactivity with other members of the MCR family (e.g., MC3R and MC1R). Thus, identifying distinct features in the activation mechanism of MC4R is important. MC1R is a close homolog of MC4R, and cross-reactivity with MC1R is often observed when agonists and antagonists designed for MC4R are used clinically (*18*, *22*). Further evidence can be seen in patients treated with afamelanotide, an MC1R agonist used for the treatment of erythropoietic protoporphyria; these patients often suffer from decreased appetite due to cross-reactivity with MC4R (*42*). A puzzling observation is that MC4R antagonists such as SHU9119 act as agonists for MC1R (*43*). Residues in the orthosteric binding pocket of MC4R and MC1R are almost identical, but L133$^{3.36}$ of the MC4R activation switch is replaced by a methionine, M128$^{3.36}$, in MC1R (fig. S4). We introduced an L133M mutation into MC4R and confirmed that SHU9119 acts as an agonist for this mutant (fig. S8, G to I). By contrast, we found that AgRP did not activate the mutant receptor, suggesting differences in the binding mode for the endogenous antagonist compared with the synthetic derivative (fig. S8G). Comparing the MC4R structure to structures harboring a 3.36 methionine (e.g., the μ-opioid receptor MOR1), shows that the rotameric state of L133$^{3.36}$ in an inactive MC4R overlaps with the active state of M151$^{3.36}$ in MOR1 (fig. S8J). Furthermore, superposition of the structure of MC4R bound to SHU9119 with an inactive structure of MOR1 indicates a clash between the naphthyl group in SHU9119 and M151$^{3.36}$ (fig. S8K). These observations suggest why SHU9119 contributes to agonistic activity in the mutant. These experiments also demonstrate the potential for a selectivity window to reduce the cross-reactivity with MC1R that contains a methionine at position 3.36. A full analysis of conserved and synonymous residues in the binding pocket of MCR family members is provided in fig. S4.

Exploring MC4R canonical and noncanonical signaling pathways

The conventional $G\alpha_s$ signaling of MC4R is crucial in inducing anorexogenic signaling in the hypothalamus to result in negative energy balance (*44*–*46*). However, MC4R can activate other signaling mediators to trigger downstream signaling effects. These include coupling to $G\alpha_i$, $G\alpha_q$, and $G\alpha_{15}$; interaction with β-arrestins (*47*, *48*); and through G protein–independent coupling to the inwardly rectifying potassium channel Kir7.1 (*49*). Our work presents the structural mechanistic properties of MC4R activation by setmelanotide and captures the MC4R-G_s bound state that allows for the delineation of the coupling interface. The MC4R-$G\alpha_s$ interface is mostly composed of interactions between residues in TM3, TM5, and TM6 at the receptor and the C-terminal helix (α5 helix) of $G\alpha_s$ (Fig. 6A and fig. S10). These interactions also include a class A conserved π-cation stacking between Y370$^{H5.23}$ in G_s and R147$^{3.50}$ (R, Arg) in MC4R, where R$^{3.50}$ composes part of the DRY (Asp-Arg-Tyr) motif that plays an important role in G protein coupling (*50*–*54*). All residues in MC4R that are involved in G_s interactions are strictly conserved among all MCR family members, reflecting their shared coupling to G_s (fig. S4A) (*55*). In addition, MC4R mutations in residues involved in G_s recruitment have been associated with impaired signaling through the G_s pathway and have also been identified in obese individuals (*56*, *57*). Notable examples are A219V (V, Val) and T150I, which demonstrate impaired cyclic adenosine monophosphate (cAMP) production without

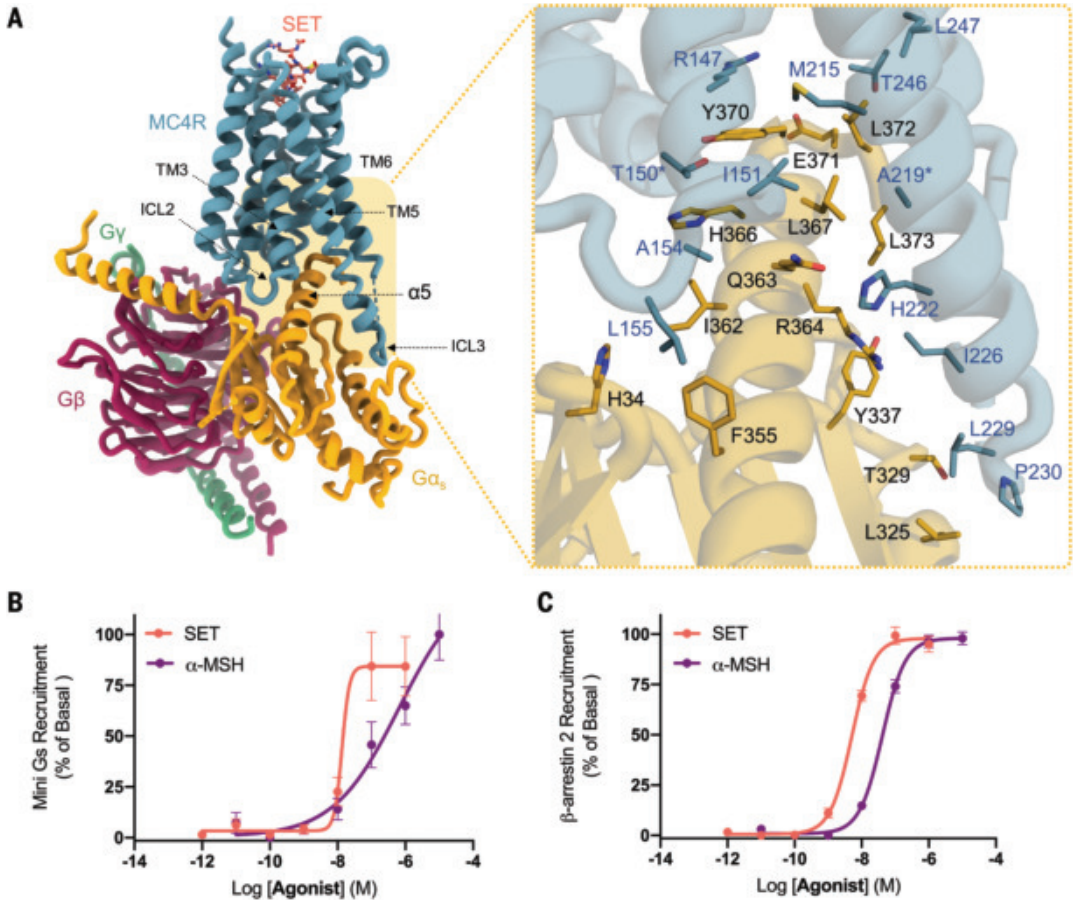


Fig. 6. MC4R G protein coupling and biased signaling. (**A**) Analysis of residues in MC4R involved in G_s recruitment. Residues in MC4R that are discussed in the main text are highlighted with an asterisk. A full description of the interactions is provided in fig. S10. P, Pro; Q, Gln. (**B**) Mini-G_s recruitment upon setmelanotide and α-MSH binding. Recruitment was monitored by nanoluciferase complementation using an MC4R-LgBit and a mini-G_s smBit. (**C**) β-arrestin 2 recruitment to MC4R. β-arrestin 2 was monitored by nanoluciferase complementation using an MC4R-LgBiT and β-arrestin 2–SmBiT in human embryonic kidney (HEK) 293 cells and plotted as a change in luciferase over time. For both (B) and (C), the *y* axis is presented as the percentage of basal as plotted in dose response curves for the agonists indicated and are represented as mean ± SEM from three independent experiments done in triplicate. Analysis in the absence and presence of Ca^{2+} is provided in fig. S6, K and L.

change in binding affinity to α-MSH compared with the wild-type receptor (*9*, *35*, *58*–*61*). $A219^{5.65}$ is close to the tip of $G\alpha_s$ helix α5. Substitution of alanine with a bulkier valine might create a clash that would disturb MC4R-$G\alpha_s$ binding. Residues that interact with $A219^{5.65}$ ($L367^{H5.20}$, $L372^{H5.25}$, and $L373^{H5.26}$) are also conserved in G_q and G_{15}, which are both reported to bind MC4R (*47*, *62*); thus, mutations at this position might also interfere with signaling through alternative pathways for this receptor. $T150^{3.53}$ is located at the tip of TM3 and contributes two hydrogen bonds to the binding interface through direct interactions with H366 (H, His) and Y370. Substitution of threonine by hydrophobic isoleucine would abolish one of the hydrogen bonds, thus impairing recruitment of the Gα subunit.

A recent genetic variant study showed that mutations in MC4R observed in patients with low BMI were associated with MC4R gain of function through biased β-arrestin 2 recruitment to the receptor. These studies highlight the importance of targeting preferred pathways by drugs to treat obesity (*9*). Analysis of mutations associated with gain of function or loss of function of MC4R is provided in fig. S9. When comparing the abilities of setmelanotide and α-MSH to recruit $G\alpha_s$ or β-arrestin 2, we saw no bias toward these two pathways (Fig. 6, B and C). Thus, our studies suggest that for the wild-type receptor, both setmelanotide and α-MSH will act similarly to activate these pathways.

This work provides a major leap in our understanding of the molecular basis of MC4R activation and inhibition, ligand specificity, and the contribution of genetic variations to MC4R-related pathologies. Looking forward, this work will set the stage for future efforts to develop new therapeutic strategies to fight obesity and possibly other weight-regulation disorders.

REFERENCES AND NOTES

1. World Health Organization, Obesity and overweight; www.who.int/news-room/fact-sheets/detail/obesity-and-overweight.
2. M. Blüher, *Nat. Rev. Endocrinol.* **15**, 288–298 (2019).
3. K. L. J. Ellacott, R. D. Cone, *Recent Prog. Horm. Res.* **59**, 395–408 (2004).
4. K. G. Mountjoy, M. T. Mortrud, M. J. Low, R. B. Simerly, R. D. Cone, *Mol. Endocrinol.* **8**, 1298–1308 (1994).
5. J. Rossi *et al.*, *Cell Metab.* **13**, 195–204 (2011).
6. B. P. Shah *et al.*, *Proc. Natl. Acad. Sci. U.S.A.* **111**, 13193–13198 (2014).
7. I. S. Farooqi *et al.*, *N. Engl. J. Med.* **348**, 1085–1095 (2003).
8. A. S. Garfield *et al.*, *Nat. Neurosci.* **18**, 863–871 (2015).
9. L. A. Lotta *et al.*, *Cell* **177**, 597–607.e9 (2019).
10. K. K. Alharbi *et al.*, *Hum. Mutat.* **28**, 294–302 (2007).
11. L. H. T. Van der Ploeg *et al.*, *Proc. Natl. Acad. Sci. U.S.A.* **99**, 11381–11386 (2002).
12. M. Beltramo *et al.*, *Brain Res. Mol. Brain Res.* **118**, 111–118 (2003).
13. B. K. Lim, K. W. Huang, B. A. Grueter, P. E. Rothwell, R. C. Malenka, *Nature* **487**, 183–189 (2012).
14. M. M. Ollmann *et al.*, *Science* **278**, 135–138 (1997).
15. I. Suzuki *et al.*, *J. Invest. Dermatol.* **108**, 838–842 (1997).
16. J. Yu *et al.*, *Science* **368**, 428–433 (2020).
17. P. Kühnen *et al.*, *N. Engl. J. Med.* **375**, 240–246 (2016).
18. T. H. Collet *et al.*, *Mol. Metab.* **6**, 1321–1329 (2017).
19. K. Clément *et al.*, *Nat. Med.* **24**, 551–555 (2018).
20. K. Clément *et al.*, *Lancet Diabetes Endocrinol.* **8**, 960–970 (2020).
21. U.S. Food and Drug Administration, "FDA approves first treatment for weight management for people with certain rare genetic conditions," 27 November 2020; www.fda.gov/drugs/drug-safety-and-availability/fda-approves-first-treatment-weight-management-people-certain-rare-genetic-conditions.
22. R. Haws *et al.*, *Diabetes Obes. Metab.* **22**, 2133–2140 (2020).
23. A. Markham, *Drugs* **81**, 397–403 (2021).
24. S. Maeda *et al.*, *Nat. Commun.* **9**, 3712 (2018).
25. A. Koehl *et al.*, *Nature* **558**, 547–552 (2018).
26. K. Krishna Kumar *et al.*, *Cell* **176**, 448–458.e12 (2019).
27. S. Maeda, Q. Qu, M. J. Robertson, G. Skiniotis, B. K. Kobilka, *Science* **364**, 552–557 (2019).
28. K. Kim *et al.*, *Cell* **182**, 1574–1588.e19 (2020).
29. J. Yin *et al.*, *Nature* **584**, 125–129 (2020).
30. B. Holst, T. W. Schwartz, *Ann. N. Y. Acad. Sci.* **994**, 1–11 (2003).
31. A. J. Venkatakrishnan *et al.*, *Nature* **494**, 185–194 (2013).
32. J. P. L. Gonçalves, D. Palmer, M. Meldal, *Trends Pharmacol. Sci.* **39**, 402–423 (2018).
33. L. Jiang, L. Lai, *J. Biol. Chem.* **277**, 37732–37740 (2002).
34. R. Link *et al.*, *J. Neurochem.* **153**, 346–361 (2020).
35. F. Stutzmann *et al.*, *Diabetes* **57**, 2511–2518 (2008).
36. Z. Q. Wang, Y. X. Tao, *Biochim. Biophys. Acta* **1812**, 1190–1199 (2011).
37. B. A. Fleck *et al.*, *Biochemistry* **44**, 14494–14508 (2005).
38. Y. K. Yang *et al.*, *Biochemistry* **39**, 14900–14911 (2000).
39. S. D. McAllister *et al.*, *J. Biol. Chem.* **279**, 48024–48037 (2004).
40. X. Li *et al.*, *Cell* **176**, 459–467.e13 (2019).
41. Q. Tan *et al.*, *Science* **341**, 1387–1390 (2013).
42. E. I. Minder, J. Barman-Aksoezen, X. Schneider-Yin, *Clin. Pharmacokinet.* **56**, 815–823 (2017).
43. Y. Yang *et al.*, *J. Biol. Chem.* **277**, 20328–20335 (2002).
44. Y. Minokoshi *et al.*, *Nature* **428**, 569–574 (2004).
45. K. G. Mountjoy, L. S. Robbins, M. T. Mortrud, R. D. Cone, *Science* **257**, 1248–1251 (1992).
46. I. Gantz *et al.*, *J. Biol. Chem.* **268**, 15174–15179 (1993).
47. C. Avet *et al.*, SSRN 3586569 [Preprint]. 15 May 2020; https://doi.org/10.2139/ssrn.3586569.
48. A. Inoue *et al.*, *Cell* **177**, 1933–1947.e25 (2019).
49. M. Ghamari-Langroudi *et al.*, *Nature* **520**, 94–98 (2015).
50. J. Ballesteros *et al.*, *J. Biol. Chem.* **273**, 10445–10453 (1998).
51. B. Carpenter, R. Nehmé, T. Warne, A. G. W. Leslie, C. G. Tate, *Nature* **536**, 104–107 (2016).
52. X. Lin *et al.*, *Nature* **579**, 152–157 (2020).
53. G. E. Rovati, V. Capra, R. R. Neubig, *Mol. Pharmacol.* **71**, 959–964 (2007).
54. L.-K. Yang, Y.-X. Tao, *Int. J. Mol. Sci.* **21**, 7611 (2020).
55. A. R. Rodrigues, H. Almeida, A. M. Gouveia, *Cell. Mol. Life Sci.* **72**, 1331–1345 (2015).
56. Z. C. Fan, Y. X. Tao, *J. Cell. Mol. Med.* **13**, 3268–3282 (2009).
57. Y. X. Tao, D. L. Segaloff, *J. Clin. Endocrinol. Metab.* **90**, 5632–5638 (2005).
58. L. H. Larsen *et al.*, *J. Clin. Endocrinol. Metab.* **90**, 219–224 (2005).
59. Z. Xiang, B. Proneth, M. L. Dirain, S. A. Litherland, C. Haskell-Luevano, *Biochemistry* **49**, 4583–4600 (2010).
60. Z. Xiang *et al.*, *Biochemistry* **45**, 7277–7288 (2006).
61. C. Lubrano-Berthelier *et al.*, *J. Clin. Endocrinol. Metab.* **91**, 1811–1818 (2006).
62. Y. Q. Li *et al.*, *J. Clin. Invest.* **126**, 40–49 (2016).

ACKNOWLEDGMENTS

We thank N. Elad for technical support with microscope operation. We thank D. Fass and A. Horovitz for their helpful discussions and insights. **Funding:** This work was funded by the Abisch-Frenkel Foundation and the Minerva Stiftung Foundation (M.S.-B). M.S.-B. holds the Tauro Career Development Chair in Biomedical Research. M.S.-B. is supported by the Zuckerman STEM Leadership Program, the Ilse Katz Institute for Material Sciences and Magnetic Resonance Research, the Helen and Milton A. Kimmelman Center for Biomolecular Structure and Assembly, the Joseph and Wolf Lebovic Lab, the Dov and Ziva Rabinovich Endowed Fund for Structural Biology, the Harmstieg New Scientist Fund, and the Pearl Welinsky Merlo Foundation and by P. and T. Gardner. H.I. is the recipient of a Glassman fellowship. M.Y.N. is supported by Israel Science Foundation (ISF) grant #1129/19. F.F. is the recipient of the S. A. Schonbrunn Fellowship Fund. L.F.C. was supported by a Medical Research Council (MRC) UK/Academy of Medical Sciences Clinician Scientist Grant (G0802796). D.B.-Z. is supported by the Zuckerman STEM Leadership Program. P.J.M. was supported by the BBSRC (BB/R006946/1) and MRC (MR/S008608/1). N.J.R. is funded by an MRC doctoral training partnership, and V.C. is funded by an MRC-Barts Charity iCase award (MRC0227). M.S.-B., M.Y.N., and P.J.M. are members of the EU-funded ERNEST COST action CA18133. **Author contributions:** H.I. prepared the MC4R-G_s complex with the help of O.D. and under the supervision of M.S.-B.; V.P. purified ScFv16; O.D. prepared grids, obtained cryo-EM data, processed data, and modeled the structure under the supervision of M.S.-B.; Y.P. and M.S.-B. cloned MC4R constructs, mutants, and G_s chimera and optimized conditions for protein expression; F.F. performed and analyzed molecular dynamics simulations and docking under the supervision of M.Y.N.; J.B., A.K.G., and V.C. performed the cAMP accumulation assays, and N.J.R. analyzed the surface expression of receptors by means of flow cytometry analysis under the supervision of P.J.M. and L.F.C.; M.S.-B., P.J.M., M.Y.N., and D.B.-Z. conceptualized the study; and M.S.-B. and P.J.M. wrote the manuscript with the help of H.I., O.D., and F.F. All authors provided input for the final manuscript version. **Competing interests:** The authors declare no competing interests. **Data and materials availability:** The cryo-EM density map has been deposited in the Electron Microscopy Data Bank (EMDB) under accession code EMD-11927, and model coordinates have been deposited in the Protein Data Bank (PDB) under accession no. 7AUE. All other data are available in the manuscript or supplementary materials. Materials are available from M.S.-B. and P.J.M. upon request.

SUPPLEMENTARY MATERIALS

science.sciencemag.org/content/372/6544/808/suppl/DC1
Materials and Methods
Figs. S1 to S10
Tables S1 to S5
References (*63*–*88*)
MDAR Reproducibility Checklist

19 November 2020; accepted 8 April 2021
Published online 15 April 2021
10.1126/science.abf7958

CORONAVIRUS

Genomics and epidemiology of the P.1 SARS-CoV-2 lineage in Manaus, Brazil

Nuno R. Faria[1,2,3,4]*†, Thomas A. Mellan[1,2]†, Charles Whittaker[1,2]†, Ingra M. Claro[3,5]†, Darlan da S. Candido[3,4]†, Swapnil Mishra[1,2]†, Myuki A. E. Crispim[6,7], Flavia C. S. Sales[3,5], Iwona Hawryluk[1,2], John T. McCrone[8], Ruben J. G. Hulswit[9], Lucas A. M. Franco[3,5], Mariana S. Ramundo[3,5], Jaqueline G. de Jesus[3,5], Pamela S. Andrade[10], Thais M. Coletti[3,5], Giulia M. Ferreira[11], Camila A. M. Silva[3,5], Erika R. Manuli[3,5], Rafael H. M. Pereira[12], Pedro S. Peixoto[13], Moritz U. G. Kraemer[4], Nelson Gaburo Jr.[14], Cecilia da C. Camilo[14], Henrique Hoeltgebaum[15], William M. Souza[16], Esmenia C. Rocha[3,5], Leandro M. de Souza[3,5], Mariana C. de Pinho[3,5], Leonardo J. T. Araujo[17], Frederico S. V. Malta[18], Aline B. de Lima[18], Joice do P. Silva[18], Danielle A. G. Zauli[18], Alessandro C. de S. Ferreira[18], Ricardo P. Schnekenberg[19], Daniel J. Laydon[1,2], Patrick G. T. Walker[1,2], Hannah M. Schlüter[15], Ana L. P. dos Santos[20], Maria S. Vidal[20], Valentina S. Del Caro[20], Rosinaldo M. F. Filho[20], Helem M. dos Santos[20], Renato S. Aguiar[21], José L. Proença-Modena[22], Bruce Nelson[23], James A. Hay[24,25], Mélodie Monod[15], Xenia Miscouridou[15], Helen Coupland[1,2], Raphael Sonabend[1,2], Michaela Vollmer[1,2], Axel Gandy[15], Carlos A. Prete Jr.[26], Vitor H. Nascimento[26], Marc A. Suchard[27], Thomas A. Bowden[9], Sergei L. K. Pond[28], Chieh-Hsi Wu[29], Oliver Ratmann[15], Neil M. Ferguson[1,2], Christopher Dye[4], Nick J. Loman[30], Philippe Lemey[31], Andrew Rambaut[8], Nelson A. Fraiji[6,32], Maria do P. S. S. Carvalho[6,33], Oliver G. Pybus[4,34]‡, Seth Flaxman[15]‡, Samir Bhatt[1,2,35]*‡, Ester C. Sabino[3,5]*‡

Cases of severe acute respiratory syndrome coronavirus 2 (SARS-CoV-2) infection in Manaus, Brazil, resurged in late 2020 despite previously high levels of infection. Genome sequencing of viruses sampled in Manaus between November 2020 and January 2021 revealed the emergence and circulation of a novel SARS-CoV-2 variant of concern. Lineage P.1 acquired 17 mutations, including a trio in the spike protein (K417T, E484K, and N501Y) associated with increased binding to the human ACE2 (angiotensin-converting enzyme 2) receptor. Molecular clock analysis shows that P.1 emergence occurred around mid-November 2020 and was preceded by a period of faster molecular evolution. Using a two-category dynamical model that integrates genomic and mortality data, we estimate that P.1 may be 1.7- to 2.4-fold more transmissible and that previous (non-P.1) infection provides 54 to 79% of the protection against infection with P.1 that it provides against non-P.1 lineages. Enhanced global genomic surveillance of variants of concern, which may exhibit increased transmissibility and/or immune evasion, is critical to accelerate pandemic responsiveness.

Brazil has experienced high mortality during the COVID-19 pandemic, recording >300,000 deaths and >13 million reported cases, as of March 2021. Severe acute respiratory syndrome coronavirus 2 (SARS-CoV-2) infection and disease burden have been highly variable across the country, with the state of Amazonas in north Brazil being the worst-affected region (*1*). Serological surveillance of blood donors in Manaus, the capital city of Amazonas and the largest city in the Amazon region, has suggested >67% cumulative attack rates by October 2020 (*2*). Similar but slightly lower seroprevalences have also been reported for cities in neighboring regions (*3*, *4*). However, the level of previous infection in Manaus was clearly not sufficient to prevent a rapid resurgence in SARS-CoV-2 transmission and mortality there during late 2020 and early 2021 (*5*), which has placed substantial pressure on the city's health care system.

Here, we show that the second wave of infection in Manaus was associated with the emergence and rapid spread of a new SARS-CoV-2 lineage of concern, named lineage P.1. The lineage carries a distinctive constellation of mutations (table S1), including several that have been previously determined to be of virological importance (*6*–*10*) and that are located in the spike protein receptor binding domain (RBD), the region of the virus involved in recognition of the angiotensin-converting enzyme-2 (ACE2) cell surface receptor (*11*). Using genomic data, structure-based mapping of mutations of interest onto the spike protein, and dynamical epidemiology modeling of genomic and mortality data, we investigated the emergence of the P.1 lineage and explored epidemiological explanations for the resurgence of COVID-19 in Manaus.

Identification and nomenclature of the P.1 lineage in Manaus

In late 2020, two SARS-CoV-2 lineages of concern were discovered through genomic surveillance, both characterized by sets of notable mutations: lineage B.1.351, first reported in South Africa (*12*), and lineage B.1.1.7, detected in the UK (*13*). Both variants have transmitted rapidly in the countries where they were discovered and spread to other regions (*14*, *15*). Analyses indicate that B.1.1.7 has higher transmissibility and causes more severe illness as compared with those of previously circulating lineages in the UK (*1*, *16*, *17*).

After a rapid increase in hospitalizations in Manaus caused by severe acute respiratory infection (SARI) in December 2020 (Fig. 1A), we focused ongoing SARS-CoV-2 genomic surveillance (*2*, *18*–*22*) on recently collected samples from the city (supplementary materials, materials and methods, and table S2). Before this, only seven SARS-CoV-2 genome sequences from Amazonas were publicly available (SARS-CoV-2 was first detected in Manaus

[1]MRC Centre for Global Infectious Disease Analysis, School of Public Health, Imperial College London, London, UK. [2]The Abdul Latif Jameel Institute for Disease and Emergency Analytics (J-IDEA), School of Public Health, Imperial College London, London, UK. [3]Instituto de Medicina Tropical, Faculdade de Medicina da Universidade de São Paulo, São Paulo, Brazil. [4]Department of Zoology, University of Oxford, Oxford, UK. [5]Departamento de Moléstias Infecciosas e Parasitárias, Faculdade de Medicina da Universidade de São Paulo, São Paulo, Brazil. [6]Fundação Hospitalar de Hematologia e Hemoterapia, Manaus, Brazil. [7]Diretoria de Ensino e Pesquisa, Fundação Hospitalar de Hematologia e Hemoterapia, Manaus, Brazil. [8]Institute of Evolutionary Biology, University of Edinburgh, Edinburgh, UK. [9]Division of Structural Biology, Wellcome Centre for Human Genetics, University of Oxford, Oxford, UK. [10]Departamento de Epidemiologia, Faculdade de Saúde Pública da Universidade de São Paulo, Sao Paulo, Brazil. [11]Laboratório de Virologia, Instituto de Ciências Biomédicas, Universidade Federal de Uberlândia, Uberlândia, Brazil. [12]Institute for Applied Economic Research–Ipea, Brasília, Brazil. [13]Institute of Mathematics and Statistics, University of São Paulo, São Paulo, Brazil. [14]DB Diagnósticos do Brasil, São Paulo, Brazil. [15]Department of Mathematics, Imperial College London, London, UK. [16]Virology Research Centre, Ribeirão Preto Medical School, University of São Paulo, Ribeirão Preto, SP, Brazil. [17]Laboratory of Quantitative Pathology, Center of Pathology, Adolfo Lutz Institute, São Paulo, Brazil. [18]Instituto Hermes Pardini, Belo Horizonte, Brazil. [19]Nuffield Department of Clinical Neurosciences, University of Oxford, Oxford, UK. [20]CDL Laboratório Santos e Vidal, Manaus, Brazil. [21]Departamento de Genética, Ecologia e Evolução, Instituto de Ciências Biológicas, Universidade Federal de Minas Gerais, Belo Horizonte, Brazil. [22]Laboratory of Emerging Viruses, Department of Genetics, Evolution, Microbiology, and Immunology, Institute of Biology, University of Campinas (UNICAMP), São Paulo, Brazil. [23]Instituto Nacional de Pesquisas da Amazônia, Manaus, Brazil. [24]Department of Epidemiology, Harvard T. H. Chan School of Public Health, Boston, MA, USA. [25]Center for Communicable Disease Dynamics, Harvard T. H. Chan School of Public Health, Boston, MA, USA. [26]Departamento de Engenharia de Sistemas Eletrônicos, Escola Politécnica da Universidade de São Paulo, São Paulo, Brazil. [27]Department of Biomathematics, Department of Biostatistics, and Department of Human Genetics, University of California, Los Angeles, CA, USA. [28]Institute for Genomics and Evolutionary Medicine, Temple University, Philadelphia, PA, USA. [29]Mathematical Sciences, University of Southampton, Southampton, UK. [30]Institute for Microbiology and Infection, University of Birmingham, Birmingham, UK. [31]Department of Microbiology, Immunology and Transplantation, Rega Institute, KU Leuven, Leuven, Belgium. [32]Diretoria Clínica, Fundação Hospitalar de Hematologia e Hemoterapia do Amazonas, Manaus, Brazil. [33]Diretoria da Presidência, Fundação Hospitalar de Hematologia e Hemoterapia do Amazonas, Manaus, Brazil. [34]Department of Pathobiology and Population Sciences, The Royal Veterinary College, London, UK. [35]Section of Epidemiology, Department of Public Health, University of Copenhagen, Copenhagen, Denmark.
†These authors contributed equally to this work. ‡These authors contributed equally to this work.
*Corresponding author. Email: n.faria@imperial.ac.uk (N.R.F.); samir.bhatt@sund.ku.dk (S.B.); sabinoec@usp.br (E.S.C.)

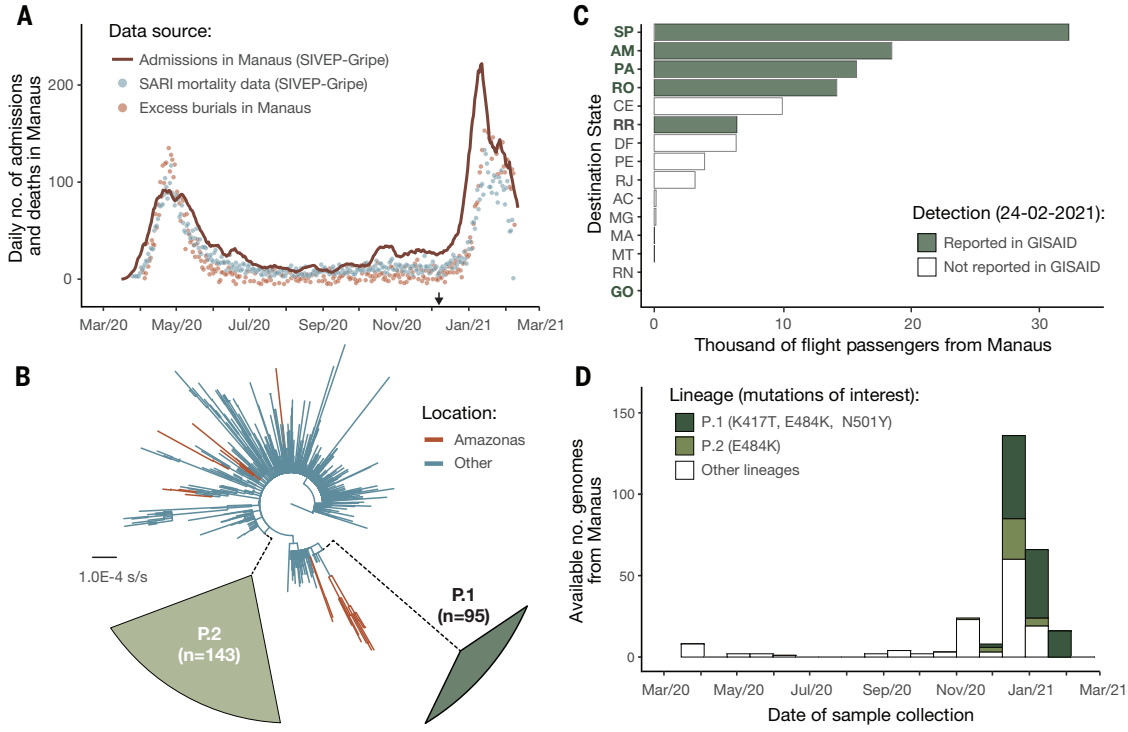


Fig. 1. SARS-CoV-2 epidemiological, diagnostic, genomic, and mobility data from Manaus. (**A**) Dark solid line shows the 7-day rolling average of the COVID-19 confirmed and suspected daily time series of hospitalizations in Manaus. Admissions in Manaus are from Fundação de Vigilância em Saúde do Amazonas (*66*). Green dots indicate daily severe acute respiratory mortality records from the SIVEP-Gripe (Sistema de Informação de Vigilância Epidemiológica da Gripe) database (*67*). Red dots indicate excess burial records based on data from Manaus Mayor's office for comparison (supplementary materials, materials and methods). The arrow indicates 6 December 2020, the date of the first P.1 case identified in Manaus by our study. (**B**) Maximum likelihood tree (n = 962 viral genomes) with B.1.1.28, P.1, and P.2 sequences, with collapsed views of P.1 and P.2 clusters and highlighting other sequences from Amazonas state, Brazil. Ancestral branches leading to P.1 and P.2 are shown as dashed lines. A more detailed phylogeny is available in fig. S3. Scale bar is shown in units of nucleotide substitutions per site (s/s). (**C**) Number of air travel passengers from Manaus to all states in Brazil was obtained from National Civil Aviation Agency of Brazil (www.gov.br/anac). The ISO 3166-2:BR codes of the states with genomic reports of P.1 [GISAID (*68*), as of 24 February 2021], are shown in bold. An updated list of GISAID genomes and reports of P.1 worldwide is available at https://cov-lineages.org/global_report_P.1.html. (**D**) Number of genome sequences from Manaus belonging to lineages of interest (supplementary materials, materials and methods). Spike mutations of interest are denoted.

on 13 March 2020) (*19*, *23*). We sequenced SARS-CoV-2 genomes from 184 samples from patients seeking COVID-19 testing in two diagnostic laboratories in Manaus between November and December 2020, using the ARTIC V3 multiplexed amplicon scheme (*24*) and the MinION sequencing platform. Because partial genome sequences can provide useful epidemiological information, particularly regarding virus genetic diversity and lineage composition (*25*), we harnessed information from partial (n = 41 viral sequences, 25 to 75% genome coverage), as well as near-complete (n = 95 viral sequences, 75 to 95%) and complete (n = 48 viral sequences, ≥95%) sequences from Manaus (figs. S1 to S4), together with other available and published genomes from Brazil for context. Viral lineages were classified by using the Pangolin (*26*) software tool (http://pangolin.cog-uk.io), nextclade (https://clades.nextstrain.org), and standard phylogenetic analysis using complete reference genomes.

Our early data indicated the presence of a novel SARS-CoV-2 lineage in Manaus that contained 17 amino acid changes (including 10 in the spike protein), three deletions, four synonymous mutations, and a four–base-pair nucleotide insertion compared with the most closely related available sequence (GISAID ID: EPI_ISL_722052) (Fig. 1B; lineage-defining mutations can be found in table S1) (*27*). This lineage was given a new designation, P.1, on the basis that (i) it is phylogenetically and genetically distinct from ancestral viruses, (ii) associated with rapid spread in a new area, and (iii) carries a constellation of mutations that may have phenotypic relevance (*26*). Phylogenetic analysis indicated that P.1—and another lineage, P.2 (*19*)—were descendants of lineage B.1.1.28 that was first detected in Brazil in early March 2020 (Fig. 1B). Our preliminary results were shared with local teams on 10 January 2021 and published online on 12 January 2021 (*27*). Concurrently, cases of SARS-CoV-2 P.1 infection were reported in Japan in travelers from Amazonas (*28*). As of 24 February 2021, P.1 had been confirmed in six Brazilian states, which in total received >92,000 air passengers from Manaus in November 2020 (Fig. 1C). Genomic surveillance first detected lineage P.1 on 6 December 2020 (Fig. 1A), after which the frequency of P.1 relative to other lineages increased rapidly in the tested samples from Manaus (Fig. 1D; lineage frequency information can be found in fig. S5). Retrospective genome sequencing might be able to recover earlier P.1 genomes. Between 2 November 2020 and 9 January 2021, we observed 7137 SARI cases and 3144 SARI deaths in Manaus (Fig. 1A). We generated a total of 182 SARS-CoV-2 sequences from Manaus during this period. This corresponds to one genome for each 39 SARI cases in Manaus, and this ratio is >100-fold higher as compared with the average number of shared genomes per reported case during the same period in Brazil.

Dating the emergence of the P.1 lineage

We used molecular-clock phylogenetics to understand the emergence and evolution of lineage P.1 (*25*). We first regressed root-to-tip genetic distances against sequence sampling dates (*29*) for the P.1, P.2, and B.1.1.28 lineages separately (figs. S6 to S8). This exploratory analysis revealed similar evolutionary rates within each lineage but greater root-to-tip distances for P.1 compared with B.1.1.28 (fig. S8), suggesting that the emergence of P.1 was preceded by a period of faster molecular evolution. The B.1.1.7 lineage exhibits similar evolutionary characteristics (*13*), which was hypothesized to have occurred in a chronically infected or immunocompromised patient (*30*, *31*).

To date the emergence of P.1, while accounting for a faster evolutionary rate along

its ancestral branch, we used a local molecular clock model (*32*) with a flexible nonparametric demographic tree prior (*33*). Using this approach, we estimated the date of the common ancestor of the P.1 lineage to be around 15 November 2020 [median, 95% Bayesian credible interval (BCI), 6 October to 24 November 2020; mean, 9 November 2020] (fig. S9). This is only 3 to 4 weeks before the resurgence in SARS-CoV-2 confirmed cases in Manaus (Figs. 1A and 2 and fig. S9). The P.1 sequences formed a single well-supported group (posterior probability = 1.00) that clustered most closely with B.1.1.28 sequences from Manaus (Fig. 2, "AM"), suggesting that P.1 emerged there. The earliest P.1 samples were detected in Manaus (*34*). The first known travel-related cases were detected in Japan (*28*) and São Paulo (table S3) and were both linked to travel from Manaus. Furthermore, the local clock model statistically confirmed a higher evolutionary rate for the branch immediately ancestral to lineage P.1 compared with lineage B.1.1.28 as a whole [Bayes factor (BF) = 6.04].

Our data indicate multiple introductions of the P.1 lineage from Amazonas to Brazil's southeastern states (Fig. 2). We also detected seven small well-supported clusters of P.2 sequences from Amazonas (two to six sequences, posterior probability = 1.00). Virus exchange between Amazonas state and the urban metropolises in southeast Brazil largely follows patterns of national air travel mobility (Fig. 1D and fig. S10).

Infection with P.1 and sample viral loads

We analyzed all quantitative reverse transcription polymerase chain reaction (RT-PCR) SARS-CoV-2–positive results from a laboratory that has provided testing in Manaus since May 2020 (Fig. 1A and data file S1), with the aim of exploring trends in sample quantitative RT-PCR cycle threshold (Ct) values, which are inversely related to sample virus loads and transmissibility (*35*). By focusing on data from a single laboratory, we reduced instrument and process variation that can affect Ct measurements.

We analyzed a set of quantitative RT-PCR positive cases for which virus genome sequencing and lineage classification had been undertaken (n = 147 samples). Using a logistic function (Fig. 3A), we found that the fraction of samples classified as P.1 increased from 0 to 87% in around 7 weeks (table S4), quantifying the trend shown in Fig. 1C. We found a small but statistically significant association between P.1 infection and lower Ct values, for both the *E* gene (lognormal regression, P = 0.029, n = 128 samples, 65 of which were P.1) and *N* gene (P = 0.01, n = 129 samples, 65 of which were P.1), with Ct values lowered by 1.43 [0.17 to 2.60, 95% confidence interval (CI)] and 1.91 (0.49 to 3.23) cycles in the P.1 lineage on average, respectively (Fig. 3B).

Using a larger sample of 942 Ct values (including an additional 795 samples for which no lineage information was available), we investigated Ct values across three time periods characterized by increasing P.1 relative abundance. Average Ct values for both the *E* and *N* genes declined through time, as both case numbers and the fraction of P.1 infections increased, with Ct values significantly lower in period 3 as compared with period 1 (*E* gene, P = 0.12 and P < 0.001 for comparison of time periods 2 and 3 to period 1; *N* gene, P = 0.14 and P < 0.001, respectively) (Fig. 3C). Analyses of Ct values for samples from a different laboratory, also based in Manaus, showed similarly significant declines between the first and third time periods defined here (P < 0.0001 for both *E* and *N* genes) (fig. S11 and data file S3).

However, population-level Ct distributions are sensitive to changes in the average time since infection when samples are taken, so that median Ct values can decrease during epidemic growth periods and increase during epidemic decline (*36*). To account for this effect, we assessed the association between P.1 infection and Ct levels while controlling for the delay between symptom onset and sample collection. Statistical significance was lost for both data sets (E gene, P = 0.15, n = 42 samples, 22 of which were P.1; N gene, P = 0.12, n = 42 samples, 22 of which were P.1). Owing to this

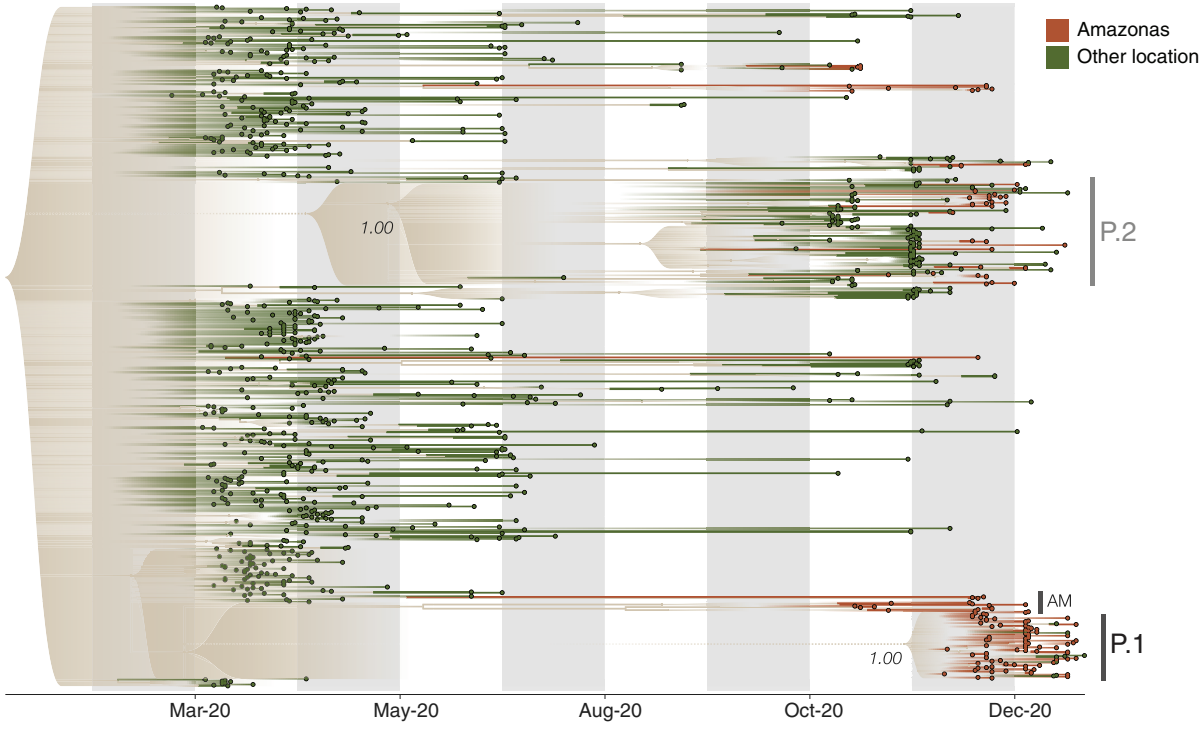


Fig. 2. Visualization of the time-calibrated maximum clade credibility tree reconstruction for B.1.1.28, P.1, and P.2 lineages in Brazil. Terminal branches and tips of Amazonas state are colored in brown, and those from other locations are colored in green (n = 962 viral genomes). Nodes with posterior probabilities of <0.5 have been collapsed into polytomies, and their range of divergence dates are illustrated as shaded expanses.

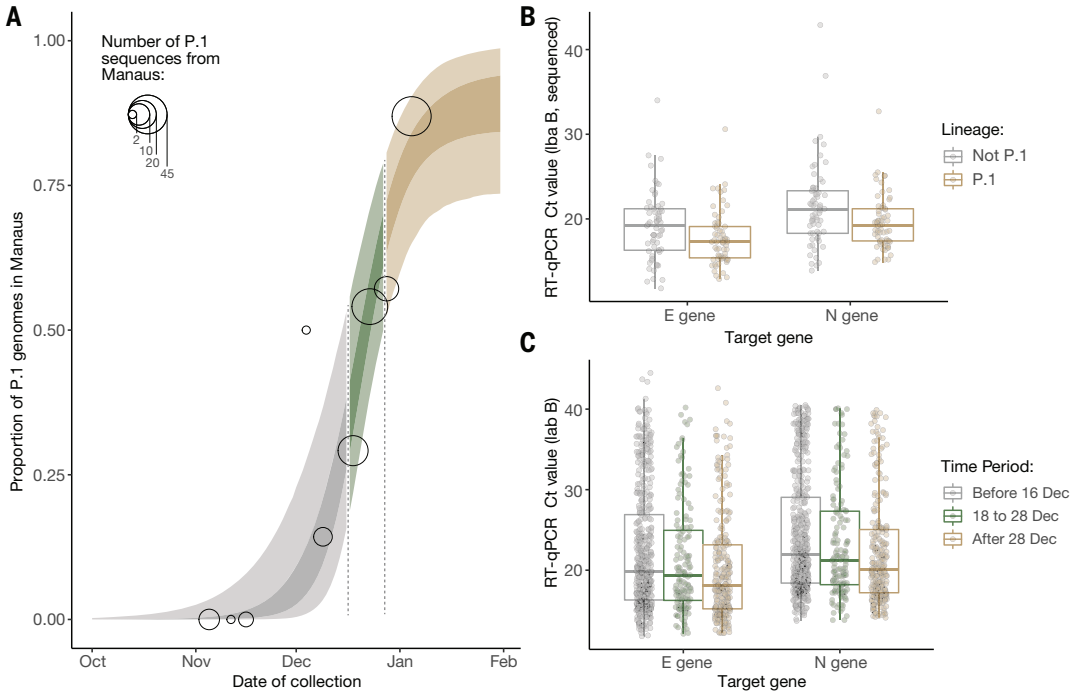


Fig. 3. Temporal variation in the proportion of sequenced genomes belonging to P.1, and trends in quantitative RT-PCR Ct values for COVID-19 infections in Manaus. (**A**) Logistic function fitting to the proportion of genomes in sequenced infections that have been classified as P.1 (black circles, size indicating number of infections sequenced), divided up into time periods when the predicted proportion of infections that are due to P.1 is <1/3 (light brown), between 1/3 and 2/3 (green), and greater than 2/3 (gray). For the model fit, the darker ribbon indicates the 50% credible interval, and the lighter ribbon indicates the 95% credible interval. For the data points, the gray thick line is the 50% exact binomial CI, and the thinner line is the 95% exact binomial CI. (**B**) Ct values for genes E and N in a sample of symptomatic cases presenting for testing at a health care facility in Manaus (laboratory A), stratified according to the period defined in (A) in which the oropharyngeal and nasal swab collections occurred. (**C**) Ct values for genes E and N in a subsample of 184 infections included in (B) that had their genomes sequenced (dataset A).

confounding factor, we cannot distinguish whether P.1 infection is associated with increased viral loads (*37*) or a longer duration of infection (*38*).

Mathematical modeling of lineage P.1 epidemiological characteristics

We next explored epidemiological scenarios that might explain the recent resurgence of transmission in Manaus (*39*). To do this, we extended a semimechanistic Bayesian model of SARS-CoV-2 transmissibility and mortality (*40*–*42*) to include two categories of virus ("P.1" and "non-P.1") and to account for infection severity, transmissibility, and propensity for reinfection to vary between the categories. It also integrates information on the timing of P.1 emergence in Manaus using our molecular clock results (Fig. 2). The model explicitly incorporates waning of immune protection after infection, parameterized on the basis of dynamics observed in recent studies (*16*, *43*), to explore the competing hypothesis that waning of prior immunity might explain the observed resurgence (*42*). We used the model to evaluate the statistical support that P.1 possesses altered epidemiological characteristics compared with local non-P.1 lineages. Epidemiological model details and sensitivity analyses (tables S5 to S10) can be found in the supplementary materials. The model is fitted to both COVID-19 mortality data [with a correction for systematic reporting delays (*44*, *45*)] and the estimated increase through time in the proportion of infections due to P.1 derived from genomic data (table S4). We assumed that within-category immunity wanes over time (50% wane within a year, although sensitivity analyses varying the rapidity of waning are presented in table S7) and that cross-immunity (the degree to which previous infection with a virus belonging to one category protects against subsequent infection with the other) is symmetric between categories.

Our results suggest that the epidemiological characteristics of P.1 are different from those of previously circulating local SARS-CoV-2 lineages, but the results also highlight substantial uncertainty in the extent and nature of this difference. Plausible values of transmissibility and cross-immunity exist in a limited area but are correlated (Fig. 4A, with the extent of immune evasion defined as 1 minus the inferred cross-immunity). This is expected because in the model, a higher degree of cross-immunity means that greater transmissibility of P.1 is required to generate a second epidemic. Within this plausible region of parameter space, P.1 can be between 1.7 and 2.4 times more transmissible (50% BCI, 2.0 median, with a 99% posterior probability of being >1) than local non-P1 lineages and can evade 21 to 46% (50% BCI, 32% median, with a 95% posterior probability of being able to evade at least 10%) of protective immunity elicited by previous infection with non-P.1 lineages, corresponding to 54 to 79% (50% BCI, 68% median) cross-immunity (Fig. 4A). The joint-posterior distribution is inconsistent with a combination of highly increased transmissibility and low cross-immunity and, conversely, also with near-complete cross-immunity but only a small increase in transmissibility (Fig. 4A). Moreover, our results further show that natural immunity waning alone is unlikely to explain the observed dynamics in Manaus, with support for P.1 possessing altered epidemiological characteristics robust to a range of values assumed for the date of the lineage's emergence and the rate of natural immunity waning (tables S5 and S7). We caution that these results are not generalizable to other settings; more detailed and direct data are needed to identify the exact degree and nature of the changes to the epidemiological characteristics of P.1 compared with previously circulating lineages.

We estimate that infections are 1.2 to 1.9 times more likely (50% BCI, median 1.5, 90% posterior probability of being >1) to result in mortality in the period after the emergence of P.1, compared with before, although posterior estimates of this relative risk are also correlated with inferred cross-immunity (Fig. 4B). More broadly, the recent epidemic in Manaus has strained the city's health care system, leading to inadequate access to medical care (*46*). We therefore cannot determine whether the estimated increase in relative mortality risk is due to P.1 infection, stresses on the Manaus

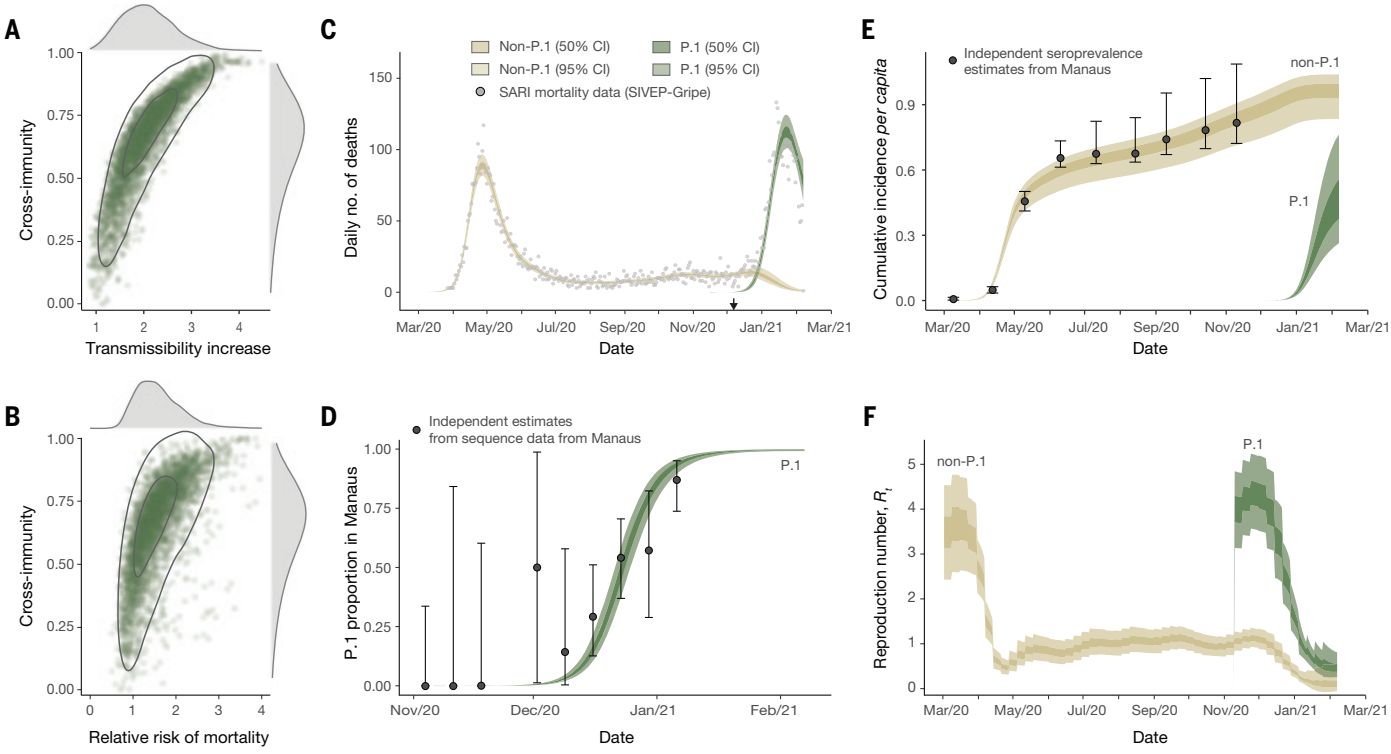


Fig. 4. Estimates of the epidemiological characteristics of P.1 inferred from a multicategory Bayesian transmission model fitted to data from Manaus, Brazil. (**A**) Joint posterior distribution of the cross-immunity and transmissibility increase inferred through fitting the model to mortality and genomic data. Gray contours indicate posterior density intervals ranging from the 95 and 50% isoclines. Marginal posterior distributions for each parameter shown along each axis. (**B**) As for (A), but showing the joint-posterior distribution of cross-immunity and the inferred relative risk of mortality in the period after emergence of P.1 compared with the period prior. (**C**) Daily incidence of COVID-19 mortality. Points indicate severe acute respiratory mortality records from the SIVEP-Gripe database (*67*, *69*). Brown and green ribbons indicate model fit for COVID-19 mortality incidence, disaggregated by mortality attributable to non-P.1 lineages (brown) and the P.1 lineage (green). (**D**) Estimate of the proportion of P.1 infections through time in Manaus. Black data points with error bars are the empirical proportion observed in genomically sequenced cases (Fig. 3A), and green ribbons (dark = 50% BCI, light = 95% BCI) are the model fit to the data. (**E**) Estimated cumulative infection incidence for the P.1 and non-P.1 categories. Black data points with error bars are reversion-corrected estimates of seroprevalence from blood donors in Manaus (*2*). Colored ribbons are the model predictions of cumulative infection incidence for non-P.1 lineages (brown) and P.1 lineages (green). These points are shown for reference only and were not used to fit the model. (**F**) Bayesian posterior estimates of trends in reproduction number R_t for the P.1 and non-P.1 categories.

health care system, or both. Detailed clinical investigations of P.1 infections are needed. Our model makes the assumption of a homogeneously mixed population and therefore ignores heterogeneities in contact patterns (differences in private versus public hospitals are provided in fig. S13). This is an important area for future research. The model fits observed time series data from Manaus on COVID-19 mortality (Fig. 4C) and the relative frequency of P.1 infections (Fig. 4D) and also captures previously estimated trends in cumulative seropositivity in the city (Fig. 4E). We estimate the reproduction number (R_t) on 7 February 2021 to be 0.1 (median, 50% BCI, 0.04 to 0.2) for non-P.1 and 0.5 (median, 50% BCI, 0.4 to 0.6) for P.1 (Fig. 4F).

Characterization and adaptation of a constellation of spike protein mutations

Lineage P.1 contains 10 lineage-defining amino acid mutations in the virus spike protein (L18F, T20N, P26S, D138Y, R190S, K417T, E484K, N501Y, H655Y, and T1027I) compared with its immediate ancestor (B.1.1.28). In addition to the possible increase in the rate of molecular evolution during the emergence of P.1, we found by use of molecular selection analyses (*47*) evidence that eight of these 10 mutations are under diversifying positive selection (table S1 and fig. S14). (Single-letter abbreviations for the amino acid residues are as follows: A, Ala; C, Cys; D, Asp; E, Glu; F, Phe; G, Gly; H, His; I, Ile; K, Lys; L, Leu; M, Met; N, Asn; P, Pro; Q, Gln; R, Arg; S, Ser; T, Thr; V, Val; W, Trp; and Y, Tyr. In the mutants, other amino acids were substituted at certain locations; for example, K417T indicates that lysine at position 417 was replaced by threonine.)

Three key mutations present in P.1—N501Y, K417T, and E484K—are in the spike protein RBD. The former two interact with human ACE2 (hACE2) (*11*), whereas E484K is located in a loop region outside the direct hACE2 interface (fig. S14). The same three residues are mutated with the B.1.351 variant of concern, and N501Y is also present in the B.1.1.7 lineage. The independent emergence of the same constellation of mutations in geographically distinct lineages indicates a process of convergent molecular adaptation. Similar to SARS-CoV-1 (*48*–*50*), mutations in the RBD may increase affinity of the virus for host ACE2 and consequently influence host cell entry and virus transmission. Recent molecular analysis of B.1.351 (*51*) indicates that the three P.1 RBD mutations may similarly enhance hACE2 engagement, providing a plausible hypothesis for an increase in transmissibility of the P.1 lineage. Moreover, E484K is associated with reduced antibody neutralization (*6*, *9*, *52*, *53*). RBD-presented epitopes account for ~90% of the neutralizing activity of sera from individuals previously infected with SARS-CoV-2 (*54*); thus, tighter binding of P.1 viruses to hACE2 may further reduce the effectiveness of neutralizing antibodies.

Conclusion

We show that P.1 most likely emerged in Manaus in mid-November, where high attack rates have been previously reported. High rates of mutation accumulation over short time periods have been reported in chronically infected or immunocompromised patients (*13*). Given a sustained generalized epidemic in Manaus, we believe that this is a potential scenario for P.1 emergence. Genomic surveillance and early data sharing by teams worldwide have led to the rapid detection and characterization of SARS-CoV-2 and new variants of concern (VOCs) (*25*), yet such surveillance is still limited in many settings. The P.1 lineage is spreading rapidly across Brazil (*55*), and this lineage has now been detected in >*36* countries (*56*). But existing virus genome sampling strategies are often inadequate for determining the true extent of VOCs in Brazil, and more detailed data are needed to address the impact of different epidemiological and evolutionary processes in their emergence. Sustainable genomic surveillance efforts to track variant frequency [for example, (*57*–*59*)] coupled with analytical tools to quantify lineage dynamics [for example, (*60*, *61*)] and anonymized epidemiological surveillance data (*62*, *63*) could enable enhanced real-time surveillance of VOCs worldwide. Studies to evaluate real-world vaccine efficacy in response to P.1 are urgently needed. Neutralization titers represent only one component of the elicited response to vaccines, and minimal reduction of neutralization titers relative to earlier circulating strains is not uncommon. Until an equitable allocation and access to effective vaccines is available to all, nonpharmaceutical interventions should continue to play an important role in reducing the emergence of new variants.

REFERENCES AND NOTES

1. P. C. Hallal *et al*., *Lancet Glob. Health* **8**, e1390–e1398 (2020).
2. L. F. Buss *et al*., *Science* **371**, 288–292 (2021).
3. C. Álvarez-Antonio *et al*., medRxiv 21249913 [Preprint] 20 January 2021. doi:10.1101/2021.01.17.21249913.
4. M. Mercado, M. Ospina, Institutoo Nacional de Salud, "Seroprevalencia de SARS-CoV-2 durante la epidemia en Colombia: estudio país" (2020); www.ins.gov.co/BibliotecaDigital/Seroprevalencia-estudio-colombia.pdf.
5. Fundação de Vigilância em Saúde do Amazonas, "Perfil clínico e demográfico dos casos de Covid-19 no estado do Amazonas: uma análise comparativa entre 2020 e 2021," No. 17 (2021); www.fvs.am.gov.br/media/publicacao/boletim_covid_17.pdf.
6. A. J. Greaney *et al*., *Cell Host Microbe* **29**, 463–476.e6 (2021).
7. T. N. Starr *et al*., *Cell* **182**, 1295–1310.e20 (2020).
8. M. A. Suchard, R. E. Weiss, J. S. Sinsheimer, *Syst. Biol.* **52**, 48–54 (2003).
9. Z. Wang *et al*., *Nature* (2021).
10. Y. Weisblum *et al*., *eLife* **9**, e61312 (2020).
11. J. Lan *et al*., *Nature* **581**, 215–220 (2020).
12. H. Tegally *et al*., *Nature* (2021).
13. A. Rambaut *et al*., on behalf of COVID-19 Genomics Consortium UK (CCoG-UK), "Preliminary genomic characterisation of an emergent SARS-CoV-2 lineage in the UK defined by a novel set of spike mutations" (2020); https://virological.org/t/preliminary-genomic-characterisation-of-an-emergent-sars-cov-2-lineage-in-the-uk-defined-by-a-novel-set-of-spike-mutations/563.
14. SAMRC Report on Weekly Deaths in South Africa (2021); www.samrc.ac.za/reports/report-weekly-deaths-south-africa?bc=254.
15. N. L. Washington *et al*., Genomic epidemiology identifies emergence and rapid transmission of SARS-CoV-2 B.1.1.7 in the United States. medRxiv 21251159 [Preprint] 7 February 2021). doi:10.1101/2021.02.06.21251159.
16. C. H. Hansen, D. Michlmayr, S. M. Gubbels, K. Mølbak, S. Ethelberg, *Lancet* **397**, 1204–1212 (2021).
17. E. Volz *et al*., *Nature* (2021).
18. D. D. S. Candido *et al*., *J. Travel Med.* **27**, taaa042 (2020).
19. D. S. Candido *et al*., *Science* **369**, 1255–1260 (2020).
20. W. M. de Souza *et al*., *Nat. Hum. Behav.* **4**, 856–865 (2020).
21. J. G. Jesus *et al*., *Rev. Inst. Med. Trop. São Paulo* **62**, e30 (2020).
22. I. M. Claro *et al*., *Emerg. Infect. Dis.* **27**, 970–972 (2021).
23. V. A. D. Nascimento *et al*., *Mem. Inst. Oswaldo Cruz* **115**, e200310 (2020).
24. J. R. Tyson *et al*., *bioRxiv* 2020.09.04.283077 (2020).
25. World Health Organization, (2021). Genomic sequencing of SARS-CoV-2: a guide to implementation for maximum impact on public health, 8 January 2021. World Health Organization (2021); https://apps.who.int/iris/handle/10665/338480.
26. A. Rambaut *et al*., *Nat. Microbiol.* **5**, 1403–1407 (2020).
27. N. R. Faria *et al*., on behalf of CADDE Genomic Network, "Genomic characterisation of an emergent SARS-CoV-2 lineage in Manaus: preliminary findings" (2021); https://virological.org/t/genomic-characterisation-of-an-emergent-sars-cov-2-lineage-in-manaus-preliminary-findings/586.
28. T. Fujino *et al*., *Emerg. Infect. Dis.* **27**, (2021).
29. A. Rambaut, T. T. Lam, L. Max Carvalho, O. G. Pybus, *Virus Evol.* **2**, vew007 (2016).
30. B. Choi *et al*., *N. Engl. J. Med.* **383**, 2291–2293 (2020).
31. V. A. Avanzato *et al*., *Cell* **183**, 1901–1912.e9 (2020).
32. A. J. Drummond, M. A. Suchard, *BMC Biol.* **8**, 114 (2010).
33. M. S. Gill *et al*., *Mol. Biol. Evol.* **30**, 713–724 (2013).
34. F. N. Naveca *et al*, *Nat. Portfolio* 10.21203/rs.3.rs-275494/v1 (2021).
35. M. Marks *et al*., *Lancet Infect. Dis.* S1473-3099(20)30985-3 (2021).
36. J. A. Hay, L. Kennedy-Shaffer, S. Kanjilal, M. Lipsitch, M. J. Mina, Estimating epidemiologic dynamics from single cross-sectional viral load distributions. medRxiv 20204222 [Preprint] 13 February 2021). doi:10.1101/2020.10.08.20204222.
37. M. Kidd *et al*., *J. Infect. Dis.* jiab082 (2021).
38. K. Stephen *et al*., Densely sampled viral trajectories suggest longer duration of acute infection with B.1.1.7 variant relative to non-B.1.1.7 SARS-CoV-2 (2021); https://nrs.harvard.edu/URN-3:HUL.INSTREPOS:37366884.
39. E. C. Sabino *et al*., *Lancet* **397**, 452–455 (2021).
40. H. J. T. Unwin *et al*., *Nat. Commun.* **11**, 6189 (2020).
41. S. Flaxman *et al*., *Nature* **584**, 257–261 (2020).
42. James Scott, Axel Gandy, Swapnil Mishra, Juliette Unwin, Seth Flaxman, Samir Bhatt, Epidemia - Modeling of epidemics using hierarchical Bayesian models; https://imperialcollegelondon.github.io/epidemia/index.html.
43. V. Hall *et al*., *bioRxiv* 21249642 [Preprint] 15 January 2021). doi:10.1101/2021.01.13.21249642.
44. S. F. McGough, M. A. Johansson, M. Lipsitch, N. A. Menzies, *PLOS Comput. Biol.* **16**, e1007735 (2020).
45. I. Hawryluk *et al*., Gaussian Process Nowcasting: Application to COVID-19 Mortality Reporting. *arXiv* **arXiv:2102.11249**, (2021).
46. Agencia Brasil, Covid-19: Amazonas já transferiu 424 pacientes para outros estados (2021); https://agenciabrasil.ebc.com.br/saude/noticia/2021-02/covid-19-amazonas-ja-transferiu-424-pacientes-para-outros-estados.
47. S. L. Pond, S. D. Frost, S. V. Muse, *Bioinformatics* **21**, 676–679 (2005).
48. X. X. Qu *et al*., *J. Biol. Chem.* **280**, 29588–29595 (2005).
49. H. D. Song *et al*., *Proc. Natl. Acad. Sci. U.S.A.* **102**, 2430–2435 (2005).
50. W. Li *et al*., *EMBO J.* **24**, 1634–1643 (2005).
51. D. Zhou *et al*., *Cell* S0092-8674(21)00226-9 (2021).
52. C. K. Wibmer *et al*., *Nat. Med.* (2021).
53. S. Cele *et al*., *Nature* (2021).
54. L. Piccoli *et al*., *Cell* **183**, 1024–1042.e21 (2020).
55. A. F. Martins *et al*., *Euro Surveill.* **26**, 2100276 (2021).
56. A. O'Toole *et al*., The COVID-19 Genomics UK (COG-UK) consortium, et al., "Tracking the international spread of SARS-CoV-2 lineages B.1.1.7 and B.1.351/501Y-V2" (2021); https://virological.org/t/tracking-the-international-spread-of-sars-cov-2-lineages-b-1-1-7-and-b-1-351-501y-v2/592.
57. TESSy. The European Surveillance System (TESSy) (2015); www.ecdc.europa.eu/en/publications-data/european-surveillance-system-tessy.
58. COG-UK, COVID-19 Genomics UK Consortium (2020); www.cogconsortium.uk.
59. SPHERES, SARS-CoV-2 Sequencing for Public Health Emergency Response, Epidemiology, and Surveillance; (2020); www.cdc.gov/coronavirus/2019-ncov/covid-data/spheres.html.
60. L. du Plessis *et al*., *Science* **371**, 708–712 (2021).
61. E. Volz *et al*., *Cell* **184**, 64–75.e11 (2021).
62. B. Xu, M. U. G. Kraemer, Open COVID-19 Data Curation Group, *Lancet Infect. Dis.* **20**, 534 (2020).
63. Global.health (2021); https://global.health.
64. GitHub Repository; https://github.com/CADDE-CENTRE.
65. S., CADDE CENTRE, C. Whittaker, CADDE-CENTRE/Novel-SARS-CoV-2-P1-Lineage-in-Brazil: Genomics and epidemiology of the P.1 SARS-CoV-2 lineage in Manaus, Brazil (peer-review version out soon). Zenodo (2021); doi:10.5281/zenodo.4676853.
66. Fundação de Vigilância em Saúde do Amazonas, Amazonas, "Dados epidemiológicos e financeiros das ações de combate à COVID-19. Publicações (2021); www.fvs.am.gov.br/publicacoes.
67. SRAG 2020 - Banco de Dados de Síndrome Respiratória Aguda Grave - incluindo dados da COVID-19 - Open Data; https://opendatasus.saude.gov.br/dataset/bd-srag-2020.
68. Y. Shu, J. McCauley, *Euro Surveill.* **22**, 30494 (2017).
69. SRAG 2021 - Banco de Dados de Síndrome Respiratória Aguda Grave - incluindo dados da COVID-19 - Open Data; https://opendatasus.saude.gov.br/dataset/bd-srag-2021.

ACKNOWLEDGMENTS

We thank L. Matkin (University of Oxford), M. Oikawa (Universidade Federal do ABC), and A. Acosta (University of Sao Paulo) for logistic support and C. Sachi (Instituto Adolfo Lutz) for agreeing with the use of unpublished sequence data available in GISAID before publication. We thank the anonymous reviewers for their considerations and suggestions. We thank the administrators of the GISAID database for supporting rapid and transparent sharing of genomic data during the COVID-19 pandemic. A full list acknowledging the authors publishing data used in this study can be found in data file S4. **Funding:** This work was supported by a Medical Research Council-São Paulo Research Foundation (FAPESP) CADDE partnership award (MR/S0195/1 and FAPESP 18/14389-0) (https://caddecentre.org); FAPESP (E.C.S.: 18/14389-0; I.M.C: 2018/17176-8 and 2019/12000-1, F.C.S.S.: 2018/25468-9; J.G.d.J.: 2018/17176-8, 2019/12000-1, 18/14389-0; T.M.C.: 2019/07544-2; C.A.M.S.: 2019/21301-5; W.M.S.: 2017/13981-0, 2019/24251-9; L.M.d.S.: 2020/04272-9; M.C.d.P.: 2019/21568-1; V.H.N.: 2018/12579-7; C.A.P.: 2019/21858-0; and P.S.P.: 16/18445-7; J.L.P.-M.: 2020/04558-0); Wellcome Trust and Royal Society (N.R.F.: Sir Henry Dale Fellowship: 204311/Z/16/Z); Wellcome Trust (Wellcome Centre for Human Genetics: 203141/Z/16/Z); Clarendon Fund and Department of Zoology, University of Oxford (D.d.S.C.); Medical Research Council (T.A.B and R.J.G.H: MR/S007555/1); European Molecular Biology Organisation (R.J.G.H.: ALTF 869-2019); CNPq (R.S.A.: 312688/2017-2, 439119/2018-9; W.M.S.: 408338/2018-0, 304714/2018-6; V.H.N.: 304714/2018-6); FAPERJ (R.S.A.: 202.922/2018); FFMUSP (M.S.R.: 206.706; C.A.P.); Imperial College COVID-19 Research Fund (H.M.S. and S.F.); CAPES (G.M.F. and C.A.P., Code 001); Wellcome Trust Collaborator Award (P.L., A.R., and N.J.L.: 206298/Z/17/Z); European Research Council (P.L and A.R.: 725422-ReservoirDOCS); European Union's Horizon 2020 project MOOD (P.L. and M.U.G.K.: 874850); U.S. National Institutes of Health (M.A.S.: U19 AI135995); Oxford Martin School (O.G.P.); Branco Weiss Fellowship (M.U.G.K); Covid-19 Research Fund (S.F.); EPSRC (S.F.: EP/V002910/1; M.M. through the EPSRC Centre for Doctoral Training in Modern Statistics and Statistical Machine Learning); BMGF (S.B.); UKRI (S.B.); Novo Nordisk Foundation (S.B.); Academy of Medical Sciences (S.B.); BRC (S.B.); MRC (S.B.); and Bill & Melinda Gates Foundation (O.R.: OPP1175094). We acknowledge support from the Rede Corona-ômica BR MCTI/FINEP affiliated to RedeVírus/MCTI (FINEP 01.20.0029.000462/20, CNPq 404096/2020-4), FAPESP project 2018/12579-7 CNPq project 304714/2018-6 (V.H.N.), EPSRC Centre for Doctoral Training in Modern Statistics and Statistical Machine Learning at Imperial and Oxford (M.M.), and the Bill & Melinda Gates Foundation (OPP1175094) (O.R.). This work received funding from the UK Medical Research Council under a concordat with the UK Department for International Development. We additionally acknowledge support from Community Jameel and the NIHR Health Protection Research Unit in Modelling Methodology. Last,

we also gratefully acknowledge support from Oxford Nanopore Technologies for a donation of sequencing reagents and NVIDIA Corporation and Advanced Micro Devices for a donation of parallel computing resources. **Author contributions:** Conceptualization: N.R.F., T.A.M., C.W., I.M.C., D.d.S.C., A.R., C.D., O.G.P., S.F., S.B., and E.C.S. Methodology: N.R.F., T.A.M., C.W., I.M.C., D.d.S.C., S.M., F.C.S.S., I.H., M.S.R., J.G.d.J., L.A.M.F., P.S.A., T.M.C., C.A.M.S., E.R.M., J.T.M., R.H.M.P., P.S.P., M.U.G.K., R.J.G.H., T.A.B., O.G.P., M.A.S., S.L.K.P., O.R., N.M.F., N.J.L., P.L., A.R., C.D., S.F., S.M., and E.C.S. Investigation: N.R.F., T.A.M., C.W., I.M.C., D.d.S.C., S.M., M.A.E.C., F.C.S.S., I.H., M.S.R., J.G.d.J., L.A.M.F., P.S.A., T.M.C., C.A.M.S., E.R.M., J.T.M., R.H.M.P., P.S.P., M.U.G.K., R.J.H.H, N.G., W.M.S., L.J.T.A., C.d.C.C., H.H., G.M.F., E.C.R., L.M.d.S., M.C.d.P., F.S.V.M., A.B.d.L., J.d.P.S., D.A.G.Z., A.C.d.S.F., R.P.S., D.J.L., P.G.T.W., H.M.S., A.L.P.d.S., M.S.V., , V.S.D.C., R.M.F.F., H.M.d.S., R.S.A., B.N., J.A.H., M.M., X.M., H.C., R.S., A.G., M.A.S., T.A.B., S.L.K.P., C.-H.W., O.R., N.M.F., C.A.P., V.H.N., N.J.L., P.L., A.R., N.A.F., M.d.P.S.S.C., C.D., O.G.P., S.F., S.B., and E.C.S. Visualization: N.R.F., T.A.M., C.W., D.d.S.C., I.M.C., J.T.M., A.R., S.L.K.P., T.A.B., C.W., and S.B. Funding acquisition: N.R.F., N.J.L., A.R., O.G.P., N.A.F., S.F., S.B., and E.C.S. Project administration: N.R.F. and E.C.S. Supervision: N.R.F., O.G.P., A.R., C.D., N.J.L., S.B., and E.C.S. Writing, original draft: N.R.F., T.A.M., C.W., I.M.C., D.d.S.C., S.F., S.B., O.G.P., C.D., and E.C.S. Writing, review and editing: All authors. **Competing interests:** S.B. declares that he advises on The Scientific Pandemic Influenza Group on Modelling (SPI-M) and advises the FCA on a legal matter regarding COVID-19 infections in England in March 2020. He is not paid for either of these advisory roles, and neither are related to the work in this paper. All other authors declare that they have no competing interests. **Data and materials availability:** All data, code, and materials used in the analysis are available in a dedicated GitHub Repository (*64*, *65*). This work is licensed under a Creative Commons Attribution 4.0 International (CC BY 4.0) license, which permits unrestricted use, distribution, and reproduction in any medium, provided the original work is properly cited. To view a copy of this license, visit https://creativecommons.org/licenses/by/4.0/. This license does not apply to figures/photos/artwork or other content included in the article that is credited to a third party; obtain authorization from the rights holder before using such material.

SUPPLEMENTARY MATERIALS

science.sciencemag.org/content/372/6544/815/suppl/DC1
Materials and Methods
Supplementary Text
Figs. S1 to S16
Tables S1 to S10
References (*70*–*102*)
Data Files S1 to S6
MDAR Reproducibility Checklist

25 February 2021; accepted 11 April 2021
Published online 14 April 2021
10.1126/science.abh2644

REPORTS

CORONAVIRUS

Spatiotemporal pattern of COVID-19 spread in Brazil

Marcia C. Castro[1]*, Sun Kim[1], Lorena Barberia[2], Ana Freitas Ribeiro[3,4], Susie Gurzenda[1], Karina Braga Ribeiro[5], Erin Abbott[6], Jeffrey Blossom[6], Beatriz Rache[7], Burton H. Singer[8]

Brazil has been severely hit by COVID-19, with rapid spatial spread of both cases and deaths. We used daily data on reported cases and deaths to understand, measure, and compare the spatiotemporal pattern of the spread across municipalities. Indicators of clustering, trajectories, speed, and intensity of the movement of COVID-19 to interior areas, combined with indices of policy measures, show that although no single narrative explains the diversity in the spread, an overall failure of implementing prompt, coordinated, and equitable responses in a context of stark local inequalities fueled disease spread. This resulted in high and unequal infection and mortality burdens. With a current surge in cases and deaths and several variants of concern in circulation, failure to mitigate the spread could further aggravate the burden.

Brazil is the only country with a population larger than 100 million that has a universal, comprehensive, free of charge health care system. Over three decades, this system contributed to reducing inequalities in access to health care and outcomes (*1*). It also facilitated the management of previous public health emergencies such as the HIV/AIDS pandemic (*2*). Despite recent cuts in the health budget (*3*), it was expected that Brazil's health system would place the country in a good position to mitigate the COVID-19 pandemic. With national coordination and through a vast network of community health agents, actions adapted to existing local inequalities (i.e., regional distribution of physicians and hospital beds) could have been implemented (*4*). However, Brazil is one of the countries most severely hit by COVID-19. As of 11 March 2021, 11,277,717 cases and 272,889 deaths have been reported. These numbers represent 9.5% and 10.4% of the worldwide cases and deaths, respectively, yet Brazil shares only 2.7% of the world's population. In late May 2020, Latin America was declared the epicenter of the COVID-19 pandemic, mainly because of Brazil. Since 7 June 2020, Brazil has ranked second in deaths worldwide.

In Brazil, the federal response has been a dangerous combination of inaction and wrongdoing, including the promotion of chloroquine as treatment despite a lack of evidence (*5*, *6*). Without a coordinated national strategy, local responses varied in form, intensity, duration, and start and end times, which to some extent were associated with political alignments (*7*, *8*). The country has seen very high attack rates (*9*) and disproportionally higher burden among the most vulnerable (*10*, *11*), illuminating local inequalities (*12*). After multiple introductions of severe acute respiratory syndrome coronavirus 2 (SARS-CoV-2), Brazil had an initial epidemic phase (15 February to 18 March 2020) with restricted circulation (*13*), preceded by undetected virus circulation (*14*). Although the initial spread was determined by existing socioeconomic inequalities, the lack of a coordinated, effective, and equitable response likely fueled the widespread spatial propagation of SARS-CoV-2 (*12*). The goal of this study was to understand, measure, and compare the pattern of spread of COVID-19 cases and deaths in Brazil at fine spatial and temporal scales. We used daily data from state health offices covering the period from epidemiological week 9 (23 to 29 February 2020) to week 41 (4 to 10 October 2020).

In all states, it took <1 month between the first case and the first death; only 11 days in Amazonas and 21 in São Paulo (table S1). Epidemiological curves for Brazil (fig. S1) hide distinct patterns of initial reporting, propagation, and containment of SARS-CoV-2 across administrative units. As states and cities imposed and relaxed restrictive measures at different times, population mobility facilitated the circulation of the virus and acted as a trigger of disease spread (*15*). Figure 1, A and B, show that cumulative cases and deaths, respectively, per 100,000 people were not uniformly distributed across municipalities. We used the space-time scan statistic (*16*) to identify areas that recorded a significantly high number of cases (Fig. 1C and table S2) or deaths (Fig. 1D and table S3) over a defined period.

Deaths clustered ~1 month before cases. This likely reflects problems in surveillance, data reporting, and low testing capacity. The first significant cluster of COVID-19 deaths started on 18 May 2020 (Fig. 1D, #5) and was centered around Recife (the capital of Pernambuco). Five other clusters of deaths occurred before the first cluster of cases was observed on 16 June 2020 (Fig. 1C, #7). Among these were clusters around Fortaleza and Rio de Janeiro (the capitals of Ceará and Rio de Janeiro, respectively) and in a large area including

[1]Department of Global Health and Population, Harvard T. H. Chan School of Public Health, Boston, MA, USA. [2]Department of Political Science, University of São Paulo (USP), Sao Paulo, SP, Brazil. [3]Universidade Nove de Julho, São Paulo, SP, Brazil. [4]Universidade Municipal de São Caetano do Sul, São Cetano do Sul, SP, Brazil. [5]Faculdade de Ciências Médicas da Santa Casa de São Paulo, Department of Collective Health, São Paulo, SP, Brazil. [6]Center for Geographical Analysis, Harvard University, Cambridge, MA, USA. [7]Instituto de Estudos para Políticas de Saúde (IEPS), São Paulo, SP, Brazil. [8]Emerging Pathogens Institute, University of Florida, Gainesville, FL, USA.
***Corresponding author. Email: mcastro@hsph.harvard.edu**

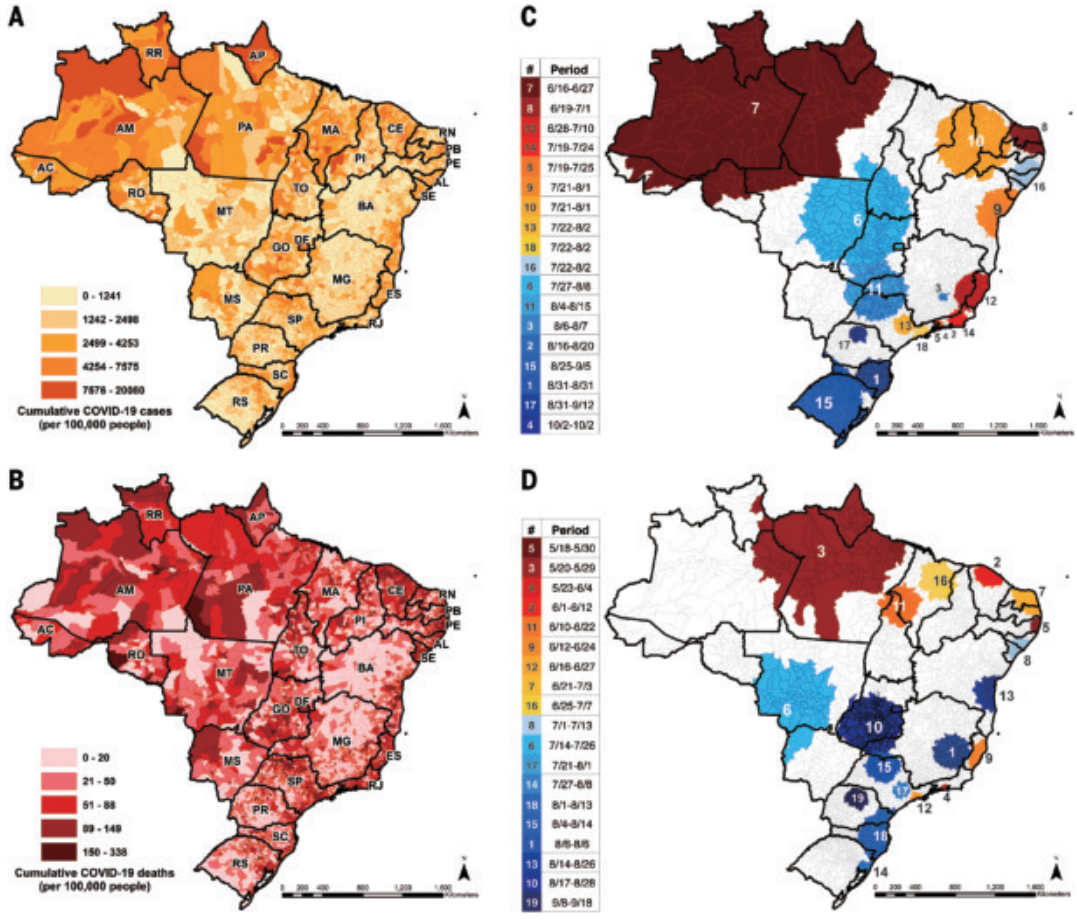


Fig. 1. Spatial distribution and clustering of reported COVID-19 cases and deaths. (**A** and **B**) Cumulative number of COVID-19 cases (A) and deaths (B) per 100,000 people by municipality. Dark lines on the maps show state boundaries. State acronyms by region are indicated as follows. North: AC, Acre; AP, Amapá; AM, Amazonas; PA, Pará; RO, Rondônia; RR, Roraima; TO, Tocantins. Northeast: AL, Alagoas; BA, Bahia; CE, Ceará; MA, Maranhão; PB, Paraíba; PE, Pernambuco; PI, Piauí; RN, Rio Grande do Norte; SE, Sergipe. Center west: DF, Distrito Federal; GO, Goiás; MT, Mato Grosso; MS, Mato Grosso do Sul. Southeast: ES, Espírito Santo; MG, Minas Gerais; RJ, Rio de Janeiro; SP, São Paulo. South: PR, Paraná; RS, Rio Grande do Sul; SC, Santa Catarina. (**C** and **D**) Spatiotemporal clustering of cases (C) and deaths (D) across Brazilian municipalities. Color and number codes in the clusters and the table on the left are the same, and the table indicates the interval during which each cluster was statistically significant. The color gradient (dark red to dark blue) indicates the temporal change based on the initial date of the cluster, and the cluster number indicates the rank of the relative risk for each cluster (tables S2 and S3). Clusters were assessed with the space-time scan statistic (see the supplementary materials).

Amazonas, Pará, and Amapá, states that have a disproportionally lower hospital capacity. Amazonas (the capital of which is Manaus) has the highest mortality per 100,000 people in the country, more than double the rate for Brazil. By October 2020, ~76% of its population was estimated to have been infected (*9*, *17*). Except for one cluster in August 2020 (Fig. 1D, #1), the duration of death clusters did not decrease over time, ranging from 10 to 13 days. This is different from what was observed in South Korea, where successful containment reduced the duration and the geographic extent of clusters over time (*18*). A similar pattern was observed for COVID-19 cases (Fig. 1C). In the central and southern areas, clusters occurred later (August and September 2020), corroborating a regional pattern of propagation of SARS-CoV-2 (*19*).

To understand and compare how COVID-19 cases and deaths spread across Brazil, we calculated the geographic center of the epidemic. Trajectories of the center by epidemiological week show that after the introduction in São Paulo, both cases (Fig. 2A and movie S1) and deaths (Fig. 2B and movie S2) progressively moved north until week 20 (starting 10 May 2020), when the epidemic started to recede in Amazonas and Ceará but gained force in Rio de Janeiro and São Paulo. Comparing trajectories in each state (fig. S2), we calculated a ratio of the distance that the center moved each week to the distance between the capital city and the most distant municipality (tables S4 and S5). In eight states, the median weekly ratio for deaths was larger than cases (Fig. 2C), suggesting a faster movement of the focus of deaths.

On average, it took 17.3 and 32.3 days to reach 50 cases and deaths, respectively. However, in four states, deaths accumulated to a 50 count first (Fig. 2D), and in Amazonas, Ceará, and Rio de Janeiro, the difference between the time it took for cases and deaths to reach a 50 count was 6, 1, and 3 days, respectively (table S1). This short interval suggests undetected (and thus unmitigated) introduction and propagation of the virus for some time. This was confirmed in Ceará (*20*), where a retrospective epidemiological investigation revealed that the virus was already circulating in January. Also, if the initial cases occurred in high-income areas, it is possible that consultations in private practices were not reported into national systems of the Ministry of Health (*20*) and remained silent to the surveillance system. In addition, testing capacity in Brazil was limited, and the first diagnostic reverse transcription polymerase chain reaction test kits started to be produced in the country only in March. Although efforts of retrospective investigation were not scaled up in the country, a comparison of standardized rates of cases and deaths per 100,000 people (Fig. 2E) shows that in 11 states, including Amazonas, Ceará, and Rio de Janeiro, the death toll was larger than incidence.

To quantitatively measure the intensity of the spread of COVID-19 cases and deaths over time, we used the locational Hoover index (HI) (*21*, *22*). HI values closer to 100 indicate concentration in few municipalities, whereas those close to zero suggest more homogeneous spreading. If containment measures were effective, then we would expect the HI to decline slowly, remaining relatively high over time. Also, if measures were effective to avoid a collapse of the hospital system, then we would expect a higher HI for deaths compared with cases. Figure 3A shows the HI for Brazil and a clear trend toward extensive spread for both

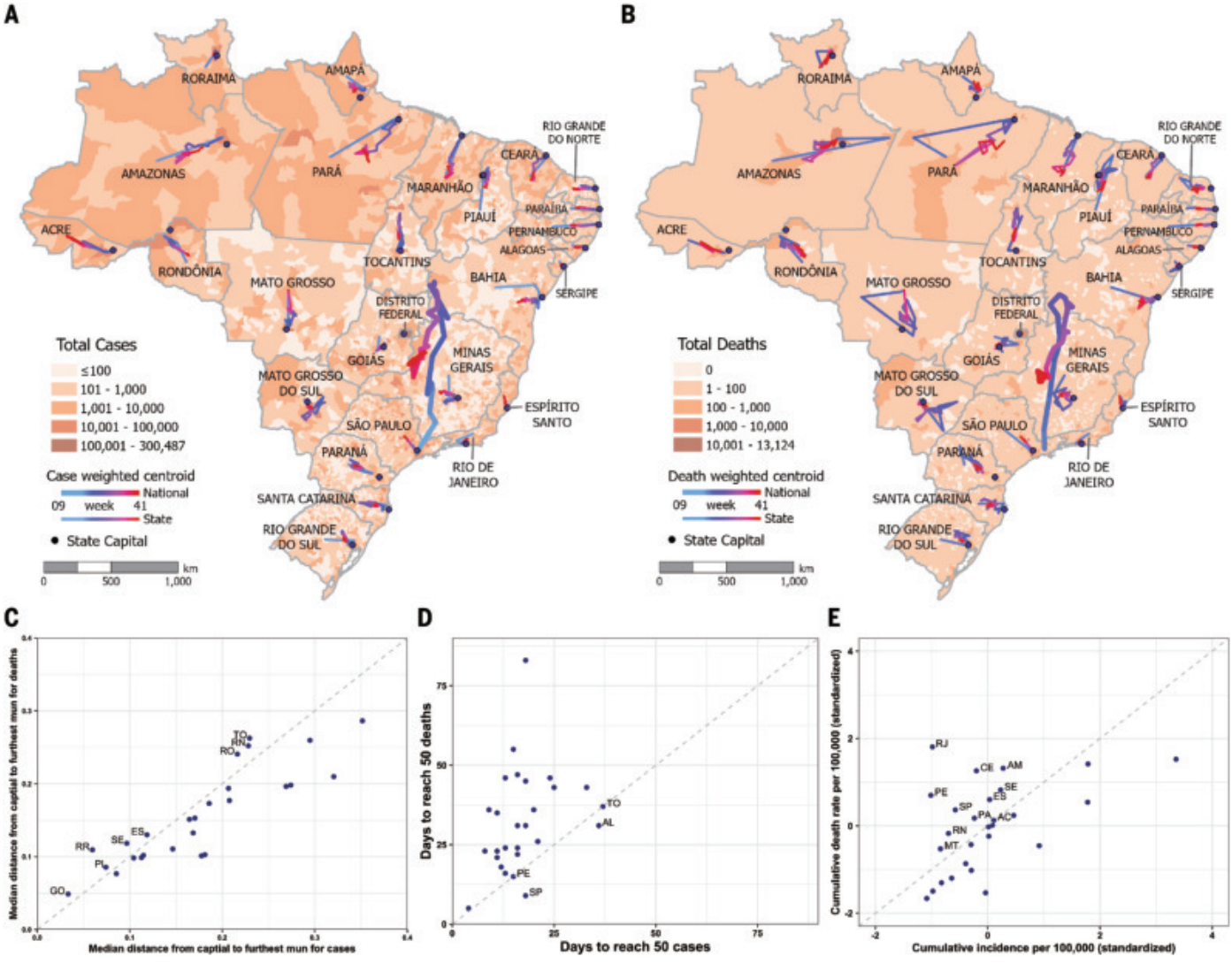


Fig. 2. Spatial and temporal spread of COVD-19 cases and deaths. (**A** and **B**) COVID-19 case-weighted (A) and death-weighted (B) geographic centers by epidemiological week. Thick lines show the geographic center for Brazil, thin lines show the trajectory of the center in each state, and the black dot indicates the state capital city (see the supplementary materials). The first case in each state was recorded in the capital city, except for Rio de Janeiro, Rondônia, Bahia, Minas Gerais, and Rio Grande do Sul, and thus the trajectory of the center starts in the interior. This was more common for deaths (14 states did not report the first death in the capital: Rio de Janeiro, Amazonas, Pará, Piauí, Rio Grande do Norte, Paraíba, Espírito Santo, Paraná, Santa Catarina, Mato Grosso do Sul, Mato Grosso, and Goiás). Figure S2 shows detailed maps for each state. (**C**) Scatterplot of the median distance that the geographical center of cases (*x*-axis) and deaths (*y*-axis) shifted weekly in each state (measured as the ratio of the distance that the geographical center of cases shifted weekly in each state to the distance between the capital city and the furthest municipality in the state). (**D**) Scatterplot of the number of days that it took for a state to reach 50 COVID-19 cases (*x*-axis) after the first case was reported and 50 deaths after the first confirmed COVID-19 death (*y*-axis). (**E**) Scatterplot of the standardized number of cases per 100,000 people (*x*-axis) and deaths per 100,000 people (*y*-axis) by state. The 45° lines in (C), (D), and (E) describe equal values for variables in the scatterplot.

cases and deaths until about week 30 (19 to 25 July 2020). The pattern, however, varied across states. In the first week with reported events, Amazonas, Roraima, and Amapá had HI <50 for both cases and deaths. This suggests either undetected circulation of the virus before initial reports (i.e., when reporting started, there was already a large fraction of the population that had been infected) or fast and multiple introductions of the virus immediately followed by rapid spatial propagation (tables S6 and S7).

Overall, the spread of COVID-19 in Brazil was fast. By week 24 (7 to 13 June 2020) and 32 (2 to 8 August 2020), all states had HI <50 for cases and deaths, respectively. In nine states, including Amazonas, Amapá, Ceará, and Rio de Janeiro, the spread of deaths was faster than that of cases over several weeks (Fig. 3B), with some overlap with the time when clusters were observed in those areas (Fig. 1, C and D). Figure 3, C and D, show the first and last weekly HI for cases and deaths by states, and there are marked contrasts in HI trajectory (tables S6 and S7). By week 41 (4 to 10 October 2020), COVID-19 deaths in Amapá (HI = 31.3) had moved to the interior faster than cases (HI = 42.9). Rio de Janeiro had the most intense interiorization of both cases (HI = 14.9) and deaths (HI = 21.9), followed by Amazonas (cases HI = 20.2, deaths HI = 30.4). Both experienced a shortage of intensive care unit (ICU) beds, but Amazonas had smaller availability (~11 ICU beds per 100,000 people versus 23 in Rio de Janeiro), all concentrated in the capital city, Manaus.

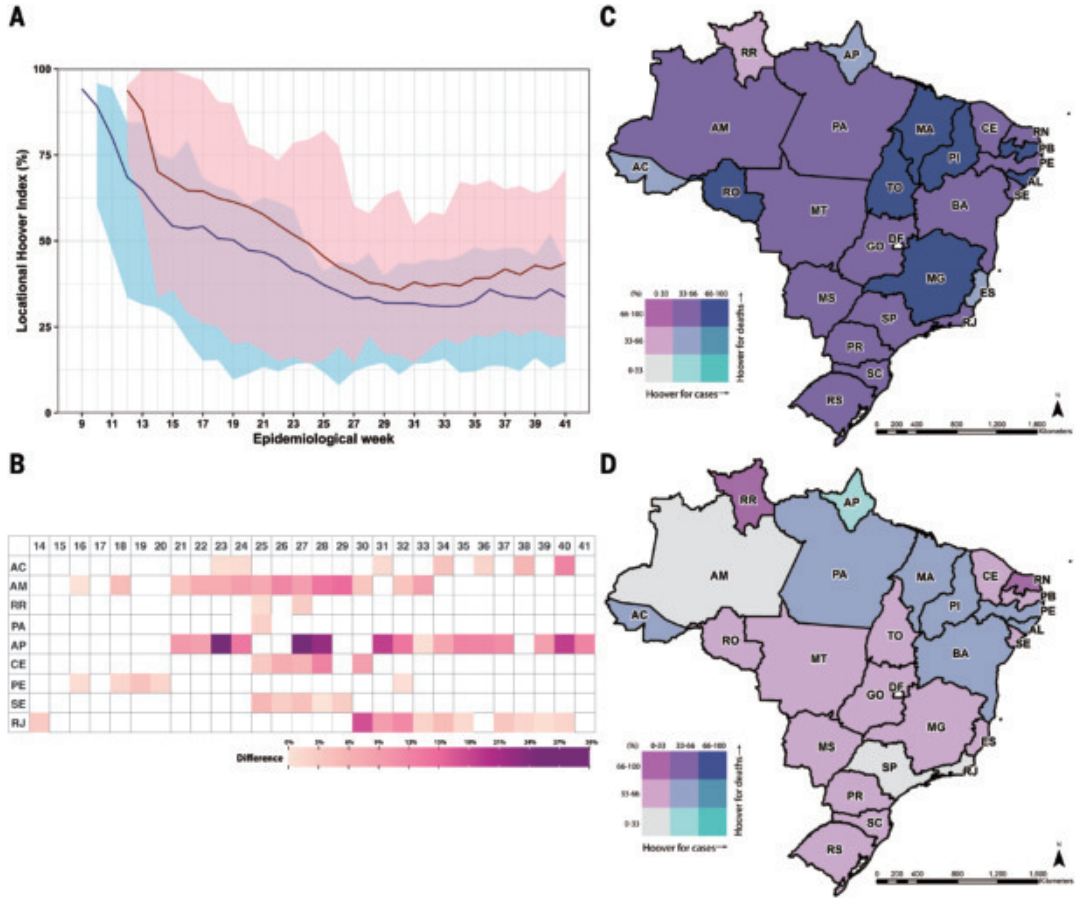


Fig. 3. Spread of COVID-19 cases and deaths. (**A**) Locational HI (see the supplementary materials) for cases (blue line) and deaths (red line) by epidemiological week. The area around each curve indicates the maximum and minimum index observed across states. (**B**) States and weeks when the locational HI for cases was bigger than that for deaths, indicating a faster spread of deaths. (**C** and **D**) Bivariate choropleth map of the locational HI for cases and deaths in epidemiological week 14 (29 March to 4 April 2020) (C) and epidemiological week 41 (4 to 10 October 2020) (D). Because SARS-CoV-2 reached states at different epidemiological weeks, (C) shows data from week 12 for RJ and SP; from week 13 for AM, PI, RN, PE, PR, SC, RS, and GO; from week 15 for AC; and from week 16 for TO. Similarly, (D) shows data for week 33 for MT and for week 39 for ES. State abbreviations are as in Fig. 1.

As the virus moved to the interior, a higher demand for scarce and distant resources intensified, not all of which were fulfilled in time to prevent fatalities (*23*). In Rio de Janeiro, political chaos compromised a prompt and effective response. Leaders were immersed in corruption accusations, the governor was removed from office and faces an impeachment trial, and the position of the Secretary of Health turned over three times between May and September, with one person who held that position arrested (*24*). By contrast, although Ceará also experienced a near collapse of the hospital system in late April to mid-May 2020 and had silent circulation of the virus >1 month before the first case was officially reported (*20*), it ranked sixth in movement of cases (HI = 31.3) but was the antepenultimate in deaths (HI = 64.5). This suggests that even with the continued spread of the virus, local actions were successful in preventing fatality. No state had HI for cases >50 by week 41, revealing an extensive pattern of disease spread toward the interior.

Overall, a higher percentage of COVID-19 cases and deaths were observed outside of capital cities in weeks 20 (10 to 16 May 2020) and 22 (24 to 30 May 2020), respectively (Fig. 4A), with varied patterns across states (table S1). Rio Grande do Sul, Santa Catarina, and Paraná, all in the southern region, had earlier and concurrent shifts in cases and deaths (in March 2020), and this was the last region to show a major surge in COVID-19. In Rio de Janeiro and Amazonas, the shift in deaths was much later than cases: 10 and 8 weeks, respectively.

To better capture policies adopted at the national and local levels and their associations with movement of COVID-19 toward the interior of states, we used three indicators, the stringency index (STR), the containment index (CTN; all policies in STR except for the use of masks), and the social distancing index (SD; based on mobile devices). Because states introduced measures at different times and these were of various durations, national indices hide much variation (Fig. 4B). We observed the expected correlations (table S8) between policy indicators and HI for cases and deaths (Fig. 4C) but a positive correlation between HI and the distance by which the national geographical center of cases shifted weekly. This suggests a pattern of progressive concentration of cases and deaths in few but widespread areas. Considering each state (fig. S3), Amapá showed a negative correlation between STR and HI for deaths, indicating that policy measures failed to prevent the movement of deaths (this was the only state where deaths moved to the interior faster than cases by week 41; Fig. 3D).

We used hierarchical clustering analysis (*25*) in an attempt to group states into categories based on measures that captured the overall COVID-19 mortality burden, intensity of transmission, speed of COVID-19 deaths toward the interior of states, and adoption of distancing measures (Fig. 4D). Categories 3 and 4 include the top 10 states in deaths per 100,000 people, as well as those that observed the first spatiotemporal clustering of deaths and fast reporting and movement of deaths. Category 2 has the highest number of contiguous states and the lowest death burden by week 41. However, all categories combine states with different levels of inequality and distinct political alignment.

In summary, our results highlight the fast spread of both cases and deaths of COVID-19 in Brazil, with distinct patterns and burden by state. They demonstrate that no single narrative explains the propagation of the virus across states in Brazil. Instead, layers of complex scenarios interweave, resulting in varied and concurrent COVID-19 epidemics across the country. First, Brazil is large and unequal, with disparities in quantity and quality of health resources (e.g., hospital beds and physicians) and income (e.g., an emergency cash transfer program started only in June 2020, and by November 2020, 41% of the households were receiving it). Second, a dense urban network

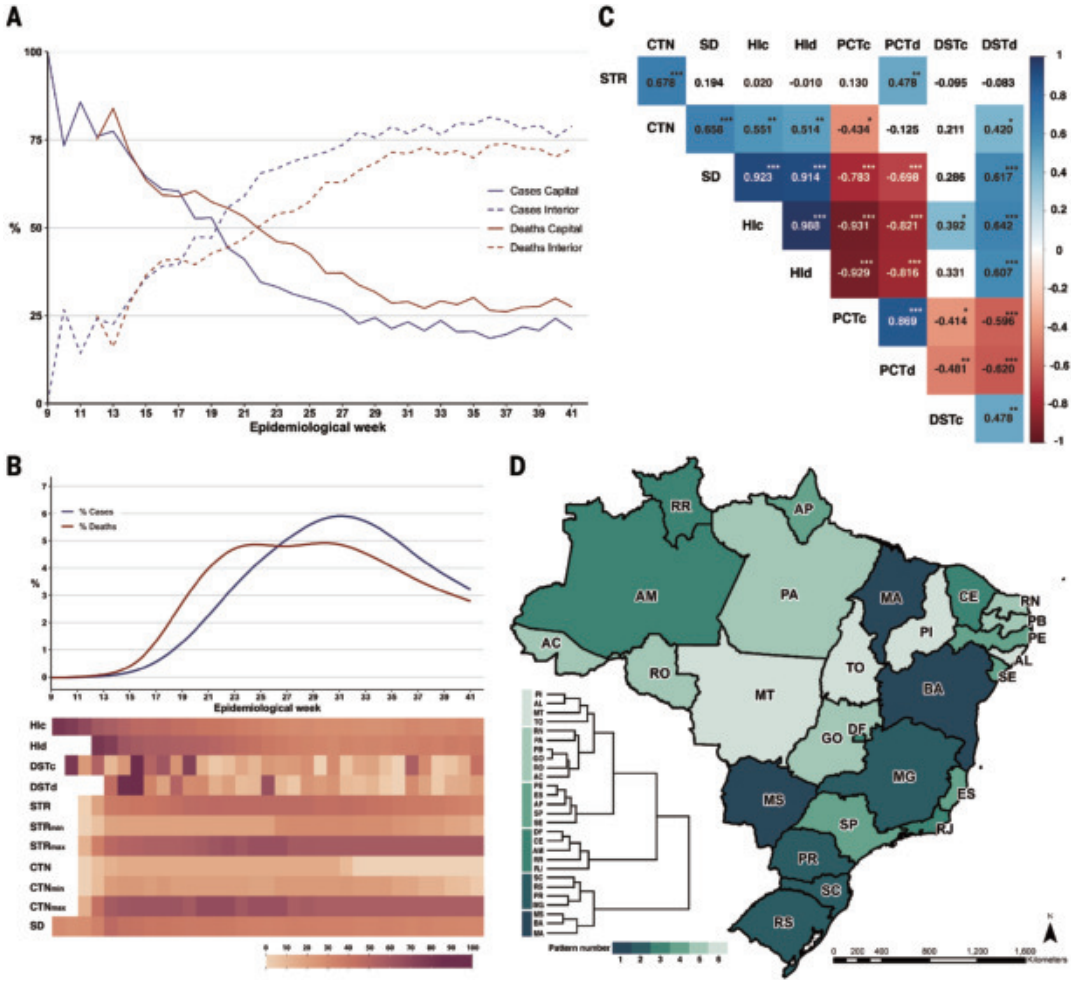


Fig. 4. Indicators of COVID-19 spread and response measures. (**A**) Percentage of cases (blue lines) and deaths (red lines) in the state capitals (solid lines) and the remaining municipalities (dashed lines) by epidemiological week. (**B**) Percentage of reported COVID-19 cases and deaths and selected variables by epidemiological week. Variables were as follows: STR, CTN, SD, HI for cases (HIc), HI for deaths (HId), percentage of cases in each epidemiological week (PCTc), percentage of deaths in each epidemiological week (PCTd), normalized distance by which the national geographical center of cases shifted in each week (DSTc), and normalized distance by which the national geographical center of deaths shifted in each week (DSTd). Distances were normalized to vary between 0 and 100. The subscript "min" indicates the minimum value of the index observed among all states in each week; the subscript "max" denotes the maximum value. (**C**) Correlation matrix (Pearson). Cells in shades of red or blue are statistically significant: $^{*}P < 0.05$, $^{**}P < 0.01$, and $^{***}P < 0.001$. (**D**) Hierarchical clustering dendrogram by state based on five variables: cumulative deaths per 100,000 people, maximum percentage of deaths in a week, maximum SD, epidemiological week when HId became <50, and maximum value of the effective reproduction number (R_t) over the study period (see the supplementary materials).

that connects and influences municipalities through transportation, services, and business (*26*) was not fully interrupted during peaks in cases or deaths. Third, political alignment between governors and the president had a role in the timing and intensity of distancing measures (*7*), and polarization politicized the pandemic with consequences to adherence to control actions (*27*). Fourth, SARS-CoV-2 was circulating undetected in Brazil for >1 month (*20*), a result of the lack of well-structured genomic surveillance (*28*). Fifth, cities imposed and relaxed measures at different moments based on distinct criteria facilitating propagation (*15*). Our findings speak to these issues but also show that some states, such as Ceará, were resilient, whereas others that had comparatively more resources, such as Rio de Janeiro, failed to contain the propagation of COVID-19.

In such a scenario, prompt and equitable responses, coordinated at the federal level, are imperative to avoid fast virus propagation and disparities in outcomes (*12*). However, the COVID-19 response in Brazil was neither prompt nor equitable. It still isn't. Brazil is currently facing the worst moment of the pandemic, with a record number of cases and deaths and near collapse of the hospital system. Vaccination has started but at a slow pace because of the limited availability of doses. A new variant of concern, which emerged in Manaus (P1) in December 2020, is estimated to be 1.4 to 2.2 times more transmissible and able to evade immunity from previous non-P1 infection (*29*). That variant is spreading across the country. It became the most prevalent in circulation in six of eight states where investigations were performed (*30*). As of 11 March 2021, Brazil had already reported deaths totaling 40% of the total COVID-19 deaths that occurred in all of 2020. In January 2021, Manaus witnessed a spike in cases and hospitalizations and a collapse of the hospital system, including a shortage of oxygen for patients (*31*). The death toll is horrific, as Manaus has already recorded 39.8% more COVID-19 deaths in 2021 than in 2020. Without immediate action, this could be a preview of what is yet to happen in other localities in Brazil. Without immediate containment, coordinated epidemiological and genomic surveillance measures, and an effort to vaccinate the largest number of people in the shortest possible time, the propagation of P1 will likely resemble the patterns described here, leading to an unimaginable loss of lives. Failure to avoid this new round of propagation will facilitate the emergence of new variants of concern, isolate Brazil as a threat to global health security, and lead to a completely avoidable humanitarian crisis.

REFERENCES AND NOTES

1. M. C. Castro *et al.*, *Lancet* **394**, 345–356 (2019).
2. A. Berkman, J. Garcia, M. Muñoz-Laboy, V. Paiva, R. Parker, *Am. J. Public Health* **95**, 1162–1172 (2005).
3. A. Massuda, T. Hone, F. A. G. Leles, M. C. de Castro, R. Atun, *BMJ Glob. Health* **3**, e000829–e000829 (2018).
4. G. Lotta, C. Wenham, J. Nunes, D. N. Pimenta, *Lancet* **396**, 365–366 (2020).
5. L. G. Barberia, E. J. Gómez, *Lancet* **396**, 367–368 (2020).
6. S. Ferigato *et al.*, *Lancet* **396**, 1636 (2020).
7. A. K. Pereira, M. S. Oliveira, T. S. Sampaio, *Rev. Adm. Pública* **54**, 678–696 (2020).
8. A. Petherick, B. Kira, R. Goldszmidt, L. Barberia, "Do Brazil's COVID-19 government response measures meet the

WHO's criteria for policy easing?" (University of Oxford, Blavatnik School of Government working paper, 2020); https://www.bsg.ox.ac.uk/research/publications/do-brazils-covid-19-government-response-measures-meet-whos-criteria-policy.
9. L. F. Buss *et al*., *Science* **371**, 288–292 (2021).
10. P. Baqui, I. Bica, V. Marra, A. Ercole, M. van der Schaar, *Lancet Glob. Health* **8**, e1018–e1026 (2020).
11. P. C. Hallal *et al*., *Lancet Glob. Health* **8**, e1390–e1398 (2020).
12. F. Ahmed, N. Ahmed, C. Pissarides, J. Stiglitz, *Lancet Public Health* **5**, e240 (2020).
13. D. S. Candido *et al*., *Science* **369**, 1255–1260 (2020).
14. W. M. de Souza *et al*., *Nat. Hum. Behav.* **4**, 856–865 (2020).
15. N. Kortessis *et al*., *Proc. Natl. Acad. Sci. U.S.A.* **117**, 30104–30106 (2020).
16. M. Kulldorff, R. Heffernan, J. Hartman, R. Assunção, F. Mostashari, *PLOS Med.* **2**, e59 (2005).
17. J. D. Y. Orellana, G. M. D. Cunha, L. Marrero, B. L. Horta, I. D. C. Leite, *Cad. Saude Publica* **36**, e00120020 (2020).
18. S. Kim, M. C. Castro, *Int. J. Infect. Dis.* **98**, 328–333 (2020).
19. O. T. Ranzani *et al*., *Lancet Respir. Med.* **9**, 407–418 (2021).
20. L. Kerr *et al*., *Cien. Saude Colet.* **25** (suppl 2), 4099–4120 (2020).
21. E. M. Hoover Jr., *J. Econ. Hist.* **1**, 199–205 (1941).
22. P. A. Rogerson, D. A. Plane, *Int. Reg. Sci. Rev.* **36**, 97–114 (2012).
23. G. S. Costa, W. Cota, S. C. Ferreira, *Phys. Rev. Res.* **2**, 043306 (2020).
24. T. McCoy, "Rio's governor suspended amid widening corruption probe involving Brazil's pandemic response," *Washington Post*, 28 August 2020; https://www.washingtonpost.com/world/the_americas/brazil-coronavirus-corruption-rio/2020/08/28/fe213756-e918-11ea-970a-64c73a1c2392_story.html.
25. G. James, D. Witten, T. Hastie, R. Tibshirani, *An Introduction to Statistical Learning with Applications in R* (Springer, 2017).
26. Instituto Brasileiro de Geografia e Estatistica, *Regiões de Influência das Cidades: 2018* (IBGE, Coordenação de Geografia, 2020).
27. C. Pereira, A. Medeiros, F. Bertholini, *Rev. Adm. Pública* **54**, 952–968 (2020).
28. The Lancet, *Lancet* **397**, 445 (2021).
29. N. R. Faria *et al*., Genomics and epidemiology of a novel SARS-CoV-2 lineage in Manaus, Brazil. medRxiv 2021.2002.2026.21252554 [Preprint]. 3 March 2021.
30. Observatório Covid-19 Fiocruz, "Fiocruz detecta mutação associada a variantes de preocupação do Sars-Cov-2 em diversos estados do país" (Observatório Covid-19 Fiocruz, 2021); https://portal.fiocruz.br/sites/portal.fiocruz.br/files/documentos/comunicado_variantes_de_preocupacao_fiocruz_2_2021-03-04.pdf.
31. T. Phillips, "Covid eruption in Brazil's largest state leaves health workers begging for help," *The Guardian*, 14 January 2021; https://www.theguardian.com/world/2021/jan/14/brazil-manaus-amazonas-covid-coronavirus.
32. Data and code for: M. C. Castro, S. Kim, L. Barberia, A. Freitas Ribeiro, S. Gurzenda, K. Braga Ribeiro, E. Abbott, J. Blossom, B. Rache, B. H. Singer, Spatiotemporal pattern of COVID-19 spread in Brazil, Zenodo (2021). https://doi.org/10.5281/zenodo.4606715.

ACKNOWLEDGMENTS

Funding: This work was supported by the Harvard T. H. Chan School of Public Health (research funds to M.C.C.). **Author contributions:** Conceptualization: M.C.C.; Data curation: M.C.C., L.B., K.B.R., S.K., S.G.; Drafting: M.C.C.; Formal analysis: M.C.C., S.K., S.G., L.B., A.F.R., E.A., J.B., B.R.; Funding: M.C.C.; Interpretation: M.C.C., B.H.S.; Methodology: M.C.C.; Review and editing: all authors; Software: S.K., J.B., E.A.; Visualization: M.C.C., J.B., S.K. **Competing interests:** The authors declare no competing interests. **Data and materials availability:** The data and code required to reproduce the results in this article can be found on Zenodo (*32*). Because data were deidentified, this study did not involve human subjects. We thank In Loco for making available their social distancing index. This work is licensed under a Creative Commons Attribution 4.0 International (CC BY 4.0) license, which permits unrestricted use, distribution, and reproduction in any medium, provided the original work is properly cited. To view a copy of this license, visit https://creativecommons.org/licenses/by/4.0/. This license does not apply to figures/photos/artwork or other content included in the article that is credited to a third party; obtain authorization from the rights holder before using such material.

SUPPLEMENTARY MATERIALS

science.sciencemag.org/content/372/6544/821/suppl/DC1
Materials and Methods
Figs. S1 to S3
Tables S1 to S14
References (*33*–*37*)
Movies S1 and S2
MDAR Reproducibility Checklist

18 February 2021; accepted 9 April 2021
Published online 14 April 2021
10.1126/science.abh1558

ELECTRON MICROSCOPY

Electron ptychography achieves atomic-resolution limits set by lattice vibrations

Zhen Chen[1]*, Yi Jiang[2], Yu-Tsun Shao[1], Megan E. Holtz[3]†, Michal Odstrčil[4]‡, Manuel Guizar-Sicairos[4], Isabelle Hanke[5], Steffen Ganschow[5], Darrell G. Schlom[3,5,6], David A. Muller[1,6]*

Transmission electron microscopes use electrons with wavelengths of a few picometers, potentially capable of imaging individual atoms in solids at a resolution ultimately set by the intrinsic size of an atom. However, owing to lens aberrations and multiple scattering of electrons in the sample, the image resolution is reduced by a factor of 3 to 10. By inversely solving the multiple scattering problem and overcoming the electron-probe aberrations using electron ptychography, we demonstrate an instrumental blurring of less than 20 picometers and a linear phase response in thick samples. The measured widths of atomic columns are limited by thermal fluctuations of the atoms. Our method is also capable of locating embedded atomic dopant atoms in all three dimensions with subnanometer precision from only a single projection measurement.

Transmission electron microscopy (TEM) plays critical roles in the study of micro- and nanostructures in many fields, including physics, chemistry, structural biology, and materials science. Progress in aberration-corrector optics for electron microscopes (*1*, *2*) has substantially improved the quality of the imaging system, pushing the spatial resolution to the sub–50-pm level (*3*, *4*). Nevertheless, in practical samples, this resolution limit is achievable only in extremely favorable conditions. One major obstacle is that multiple electron scattering is unavoidable in samples thicker than a monolayer, owing to the strong Coulomb interaction between the beam electrons and the electrostatic potentials from the atoms (*5*). Multiple scattering changes the beam shape within the sample and leads to a complicated intensity distribution at the detector plane. Nonlinear or even nonmonotonic contrast dependences on the sample thickness occur when imaging samples thicker than a few dozen atoms, which hampers direct structure determination by phase-contrast imaging. Quantitative structure-image interpretation usually relies on intensive image simulations and modeling (*6*). Direct retrieval of the sample potential requires solving the nonlinear, inverse problem of multiple scattering. Efforts have been made through different approaches, most of which are based on Bloch wave theory, by phasing different Bragg beams of crystalline samples (*7*, *8*). Unfortunately, these approaches become extremely difficult to implement for general samples with large unit cells or aperiodic structures, because a large number of unknown structure factors needs to be determined.

Ptychography is another phase-retrieval approach that dates back to Hoppe's work in the 1960s (*9*). Modern, robust setups use multiple intensity measurements—usually a series of diffraction patterns collected by scanning a small probe across the extended sample (*10*). No periodicity or symmetry constraints on the sample structure are required as a priori knowledge. This approach has been widely used in the visible-light imaging (*11*) and x-ray imaging (*12*) communities. Until recently, electron ptychography has been constrained by sample thickness and the limited detector performance in electron microscopy. Two-dimensional (2D) materials and the development of direct-electron detectors have led to a wider renewed interest (*13*–*15*). Electron ptychography for thin samples, such as 2D materials, has achieved an imaging resolution of 2.5 times the diffraction limit of the

[1]School of Applied and Engineering Physics, Cornell University, Ithaca, NY 14853, USA. [2]Advanced Photon Source, Argonne National Laboratory, Lemont, IL 60439, USA. [3]Department of Materials Science and Engineering, Cornell University, Ithaca, NY, USA. [4]Paul Scherrer Institut, 5232 Villigen PSI, Switzerland. [5]Leibniz-Institut für Kristallzüchtung, Max-Born-Str. 2, 12489 Berlin, Germany. [6]Kavli Institute at Cornell for Nanoscale Science, Ithaca, NY, USA.
***Corresponding author. Email: zhen.chen@cornell.edu (Z.C.); david.a.muller@cornell.edu (D.A.M.)**
†Present address: Department of Metallurgical and Materials Engineering, Colorado School of Mines, Golden, CO 80401, USA.
‡Present address: Carl Zeiss SMT, Carl-Zeiss-Straße 22, 73447 Oberkochen, Germany.

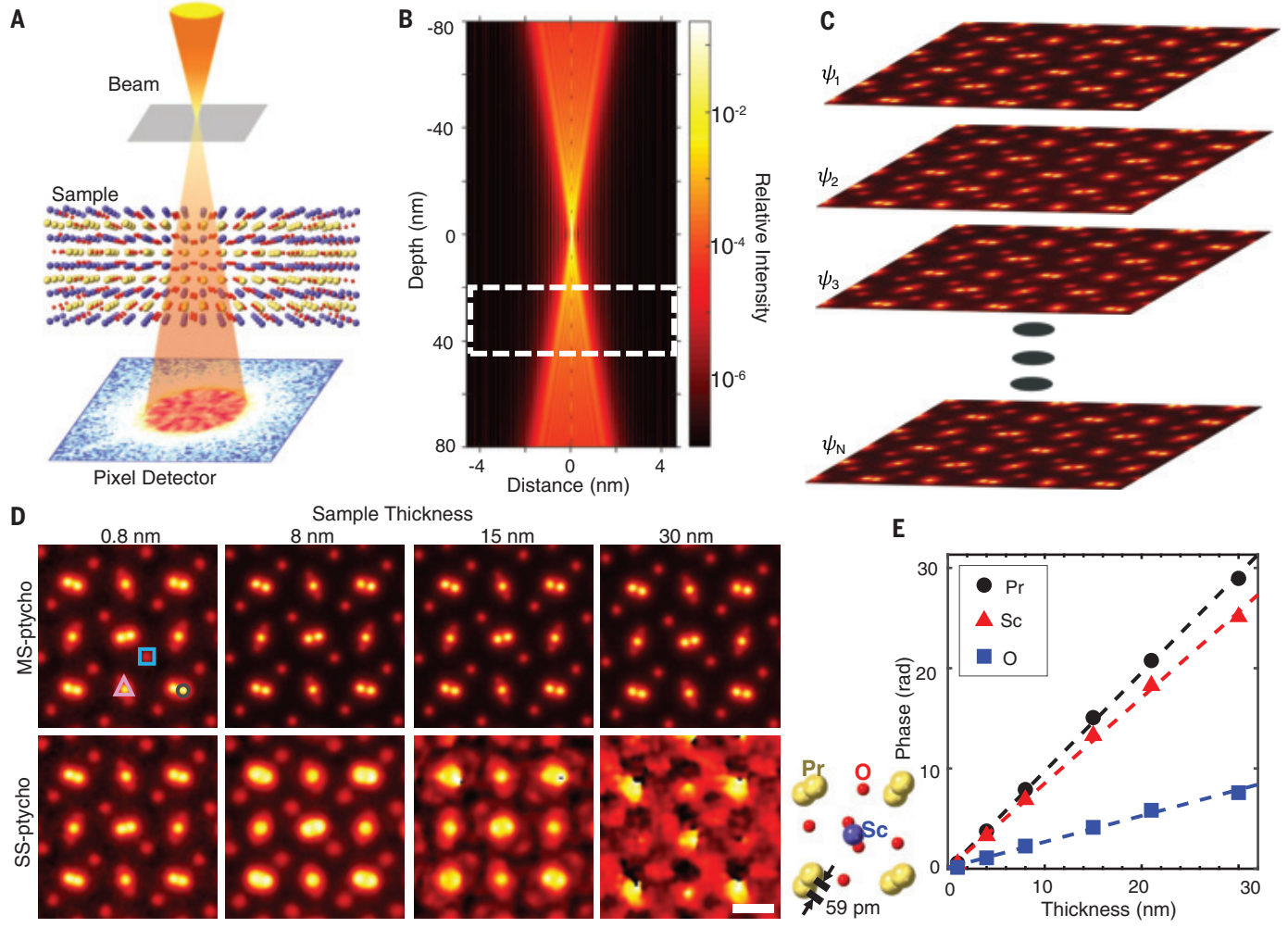


Fig. 1. Principle of multislice electron ptychography. (**A**) Experimental setup for electron ptychography. (**B**) Intensity distribution of electron probe during free-space propagation. The sample position is indicated by a dashed rectangle. (**C**) Transmission functions of multiple objects at different depth positions reconstructed via multislice electron ptychography, $\psi_i (i = 1, 2, \ldots, N)$. (**D**) Total phase images, summed from each 0.5-nm-thick slice, reconstructed via multislice electron ptychography (MS-ptycho) using simulated diffraction data for $PrScO_3$ [001] samples with different thicknesses. Corresponding phase images reconstructed by means of single-slice electron ptychography (SS-ptycho) are also shown for comparison. Scale bar, 2 Å. A structural model of $PrScO_3$ is shown at right. (**E**) Phases at Pr, Sc, and O atomic sites [denoted by a circle, triangle, and rectangle, respectively, in the top-left image of (D)] from samples with different thicknesses obtained via multislice ptychographic reconstructions. Linear fits are shown as dashed lines.

lenses, down to a 39-pm Abbe resolution (*15*). However, such super-resolution approaches can be applied reliably only to samples thinner than a few nanometers, and the resolution in thicker samples is not substantially different from that attained with conventional methods (*16*). Such thin samples are practically difficult to achieve for many bulk materials, which currently restricts applications to 2D-like systems, such as twisted bilayers (*17*). For samples thicker than the probe's depth of focus, multislice ptychography, using multiple slices to represent the sample, has been proposed (*18*). The structures of all slices can be retrieved separately. There are several successful demonstrations of multislice ptychography using either visible-light imaging (*19*) or x-ray imaging (*20*, *21*). Owing to experimental challenges, however, only a few proof-of-principle multislice electron ptychography demonstrations (*14*, *22*) have been reported and are limited in either resolution or stability.

We demonstrate multislice electron ptychographic reconstructions experimentally, recovering a linear phase response versus thickness, and push the lateral resolution close to the intrinsic atomic size, limited by thermal fluctuations of the atoms themselves. The experimental setup is shown schematically in Fig. 1A. A defocused electron probe is raster-scanned across a slablike sample, with one electron diffraction pattern recorded at each probe position by a high–dynamic range pixel array detector (fig. S1) (*23*). For thick samples, the probe function within the sample changes shape as a result of both wave propagation and strong dynamical scattering. A profile of the probe's evolution with depth into the sample is shown in Fig. 1B. In conventional ptychography, we approximate the wave function at the exit surface of the sample as a multiplication of the incident wave function with a single projected sample function (*10*, *24*). For thick samples, however, portions of the sample at different depth positions are effectively illuminated with different wave functions as a result of beam spreading by diffraction. Following the well-known Cowley-Moodie multislice solution of the electron dynamical scattering problem (*5*), the sample can be considered as many thin slices until each slice satisfies the multiplicative approximation (*10*, *12*). The entire scattering procedure is modeled as sequential scattering from each slice followed by a free-space propagation to the next slice. For the inverse problem, a similar multislice procedure can be

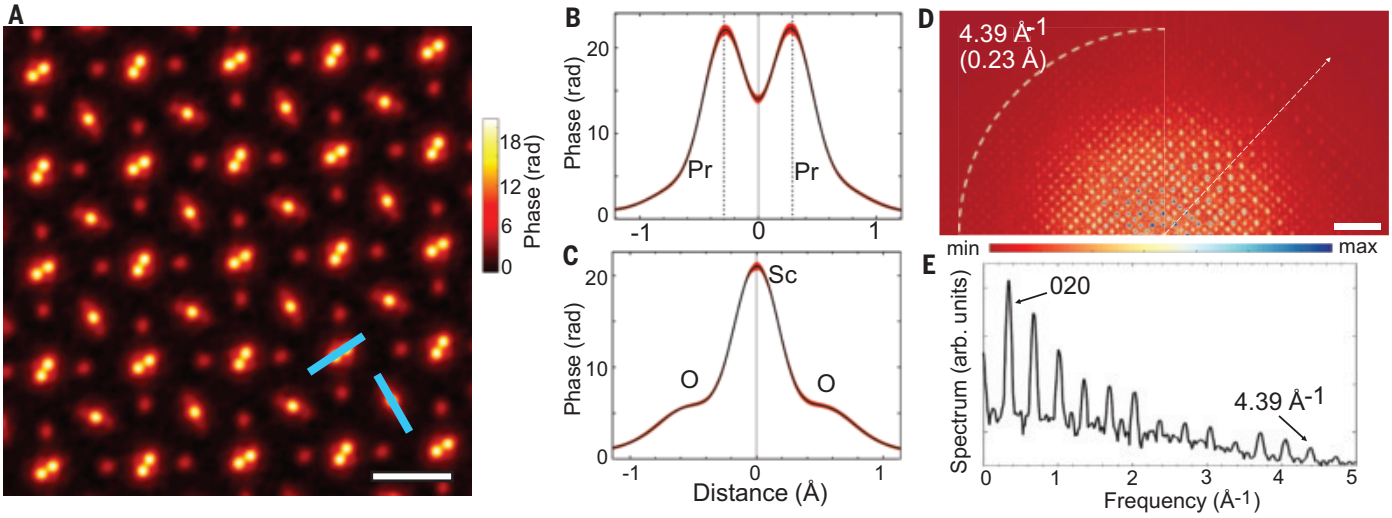


Fig. 2. Multislice electron ptychographic reconstruction of $PrScO_3$. (**A**) Total phase image, from summing all slices, of [001]-oriented $PrScO_3$ from a multislice electron ptychographic reconstruction of experimental data. Scale bar, 2 Å. (**B** and **C**) Phase profiles across Pr–Pr dumbbells and O–Sc–O directions, respectively. Red shading illustrates the variation from ~60 profiles at different atomic columns; black lines are their averages. Example positions are marked as blue lines in (A). (**D**) Intensity of Fourier transformation of the reconstructed phase image. Scale bar, 1 $Å^{-1}$. (**E**) Power spectrum along the direction marked by the dashed arrow in (D). The intensity of the power spectrum is weighted as a power of 0.2 to highlight the high-frequency information transfer. The Bragg peak of 020 is labeled in (E).

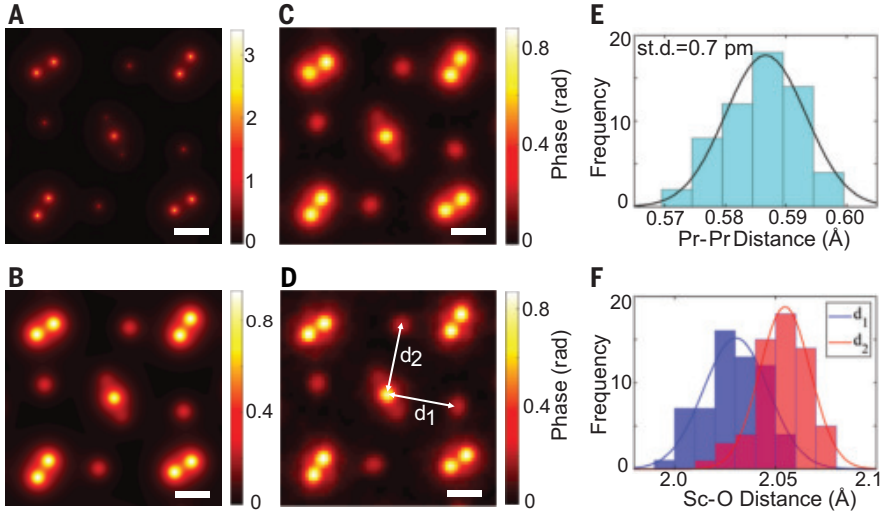


Fig. 3. Spatial resolution and measurement precision from multislice electron ptychography. (**A**) Projected electrostatic potential of $PrScO_3$ in the absence of thermal vibrations. (**B**) Projected potential after the thermal broadening at 300 K. (**C**) Cropped region of the ptychographically reconstructed potential from simulated data, including thermal fluctuations from a 21-nm-thick $PrScO_3$ sample. (**D**) Cropped region of the ptychographically reconstructed potential from experimental data. The potential in both (C) and (D) is normalized to the unit-cell thickness (8.03 Å). (**E**) Histogram of projected Pr–Pr distances from experimental measurements. The average Pr–Pr distance is 0.586 ± 0.007 Å. (**F**) Histogram of the projected Sc–O bond length from experimental measurements. d_1 and d_2 indicate different Sc–O distances along the two vertical directions, as labeled in (D). The average Sc–O distances for d_1 and d_2 are 2.030 ± 0.015 Å and 2.052 ± 0.013 Å, respectively. Scale bars in (A) to (D), 1 Å. st.d., standard deviation.

adopted on each iteration, as in multislice ptychography (*18*). In this work, there is no a priori assumption about the sample structure, and reconstructions start from random initial phases for all slices. The specimen potential for each slice is separately recovered through the phase of the transmission function, as illustrated in Fig. 1C (*23*).

We first compare the performance of multislice and single-slice electron ptychography on datasets simulated for crystalline $PrScO_3$, the same system used for our experimental measurements. For samples as thin as 8 nm, our simulation shows that multislice electron ptychography gains resolution improvement (Fig. 1D) over the single-slice approximation. For thicker samples up to 30 nm, multislice electron ptychography demonstrates stronger performance improvements, showing the 59-pm separation of Pr–Pr dumbbells, whereas single-slice electron ptychography fails to capture even the basic structure. For even-thicker samples, such as those with 50-nm thickness, reconstructions are still possible, but higher sampling densities (*21*) are required to obtain a convergent solution from multislice electron ptychography (fig. S2).

Multislice electron ptychography provides quantitative phase information, with the phase increasing linearly as more layers are added into the sample. Figure 1E shows the phase change at different atomic positions from reconstructions with different sample thicknesses. Such linearity is crucial for retrieving 3D structural information, especially for phase-contrast electron tomography, which requires a monotonic contrast dependence of sample thickness (*24*). Nevertheless, conventional methods such as scanning TEM (STEM) annular dark-field and annular bright-field imaging or high-resolution TEM (HRTEM) imaging always have a nonlinear or even non-monotonic dependence on thickness (figs. S3 and S4), and extensive simulations are required for quantitative image interpretation. Additionally, fast data acquisition and low-dose imaging capabilities that outperform conventional imaging techniques are retained in multislice ptychography, as in single-slice ptychography (figs. S10 and S11) (*17*). At present, a conventional imaging mode is still needed to align the microscope and survey the sample, as the present detector technologies and reconstruction algorithms are still too slow for live feedback.

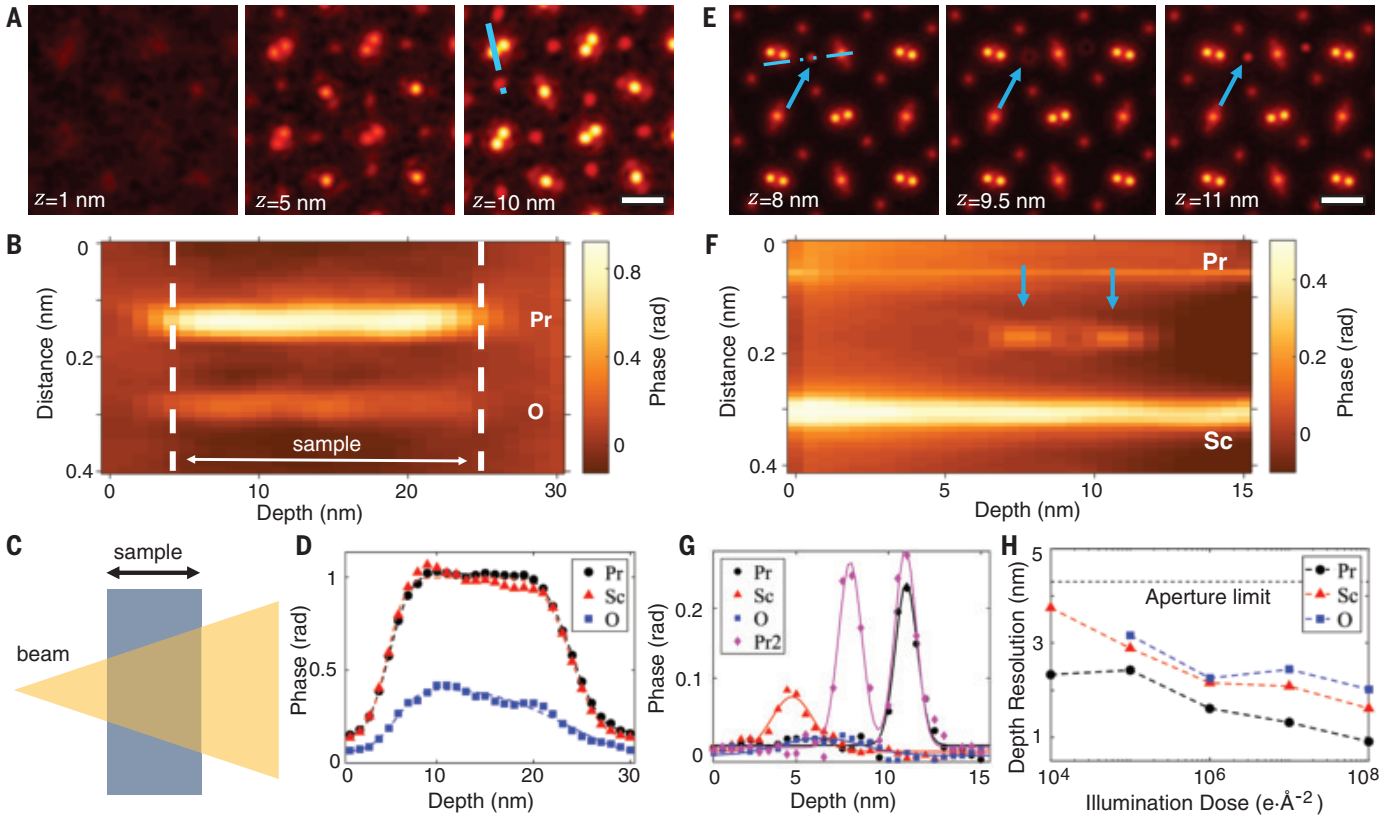


Fig. 4. Depth sectioning of multislice electron ptychography. (**A**) Ptychographically reconstructed phase of three selected slices at different depths (*z*) from experimental measurements of $PrScO_3$. The sample thickness is initially assumed as 30 nm during the reconstruction, but the retrieved sample thickness is 21 nm. (**B**) Depth profile of phase intensity along the Pr–O direction marked in (A) by the blue dash-dotted line. (**C**) Cartoon representation of the electron beam spreading into the sample. (**D**) Measured depth profile of the phase at the different atomic columns indicated in (A). FW80Ms from the error function fittings are 3.9, 3.5, and 4.2 nm of Pr, Sc, and O sites, respectively. (**E**) Simulated ptychographic reconstructions of the phase for three selected slices from a model with two interstitial Pr atom dopants located at a depth separation of 3 nm. The dash-dotted line indicates the lateral position for the depth profile in (F); arrows denote the position of the Pr dopants. (**F**) Depth variation of phase intensity across the Pr dopants. The two Pr dopants are marked with arrows. (**G**) Depth variation of the phase for different dopant positions. Solid lines are Gaussian fits. The results in (E) to (G) are for a modeled illuminated dose of 10^8 e^-·$Å^{-2}$ (e^-, electrons). (**H**) Computed depth resolution for multislice electron ptychography as a function of illuminated dose. The aperture-limited depth resolution (4.3 nm) is shown as a dashed horizontal line. Scale bars in (A) and (E), 2 Å.

We shift to experimental data collected on a 300-keV Titan Themis instrument with an electron microscope pixel array detector (EMPAD) (*25*). Full experimental details are given in the supplementary materials (*23*). Figure 2A shows one region of the phase image reconstructed by using an experimental dataset from a $PrScO_3$ sample with a thickness of 21 nm projected along the [001] zone axis, where the *c* axis of $PrScO_3$ is taken as the longest axis; this is the nonstandard *Pbnm* setting of space group 62 (*a* = 5.61 Å, *b* = 5.78 Å, and *c* = 8.03 Å) (*26*). The phase image resolves all atoms in the structure and outperforms state-of-the-art conventional electron microscopy (fig. S6) in terms of contrast and resolution: The heavy-metal atom sublattices for both Pr and Sc and the light-atom sublattice for O are resolved with a high contrast and signal-to-noise ratio. For these experimental data, both a partial coherence treatment of the electron probe (*17*, *27*) and multiple slices (*18*, *21*) are critical factors for obtaining a high-quality reconstruction (fig. S7).

The high–spatial resolution phase image of Fig. 2A is borne out by quantitative analysis. In real space, the Pr–Pr dumbbells with a separation of only 59 pm are resolved with a contrast of 63% (Fig. 2B), which is better than the 73% contrast for two point objects separated at the Rayleigh criterion. Therefore, the Rayleigh resolution of the image is much better than 59 pm. Nevertheless, the exact resolution can be determined only after considering the finite atomic size instead of assuming point objects (*28*). We can also resolve the O–Sc–O triple atom projections, even though the light O atoms are only 63 pm (*26*) from the heavier Sc atoms (Fig. 2C), and these cannot be resolved with conventional imaging techniques. The power spectrum from the Fourier transformation of the phase image (Fig. 2, D and E) shows an isotropic information transfer that is larger than 4.39 $Å^{-1}$, corresponding to 23 pm in real space.

To estimate the spatial resolution of the ptychographic reconstruction, the intrinsic width of the atoms needs to be taken into account. The static projected potential of $PrScO_3$ (i.e., at 0 K and neglecting zero-point thermal fluctuations) is very narrow (Fig. 3A). Nevertheless, the experiments were carried out at room temperature (300 K), and thermal fluctuations of atoms greatly broaden the potential (Fig. 3B). Additionally, imaging conditions, such as the finite illumination dose and maximum scattering angle of the collected diffraction patterns (*15*), will further impose a broadening factor in the reconstructed phase image (Fig. 3C). The combined effects of limited resolution and thermal fluctuations on the measured potential (Fig. 3D), each being roughly Gaussian in profile, can be added in

quadrature and approximately modeled as a convolution of one Gaussian function with the static, frozen potential (*23*). From the experimental data, the measured widths [full widths at half maximum (FWHMs)] of each atomic column estimated from more than 60 atomic columns are 44 ± 1 pm, 45 ± 1 pm, and 54 ± 2 pm from Pr, Sc, and O, respectively. By comparing the measured column widths with the Gaussian convolved potential, we can obtain the combined broadening factors (i.e., the FWHMs of the convolved Gaussian) of 28, 25, and 34 pm for Pr, Sc, and O, respectively (fig. S12 and table S1).

Thermal broadening factors of atoms can be calculated from Debye-Waller factors (DWFs) obtained from x-ray diffraction (XRD) measurements. We also measured DWFs from quantitative convergent beam electron diffraction (QCBED) (table S2 and fig. S17) (*29*). The DWFs of Pr and Sc atoms from our QCBED measurements agree well with those from XRD measurements of $PrScO_3$ single crystals (*26*). For example, after converting to the FWHM of the thermal displacement, the thermal broadening factor for Pr from both XRD (*26*) and QCBED is 23 pm, compared to the measured total broadening of 28 pm for our reconstructed image. In other words, most of the measured broadening is already accounted for by the thermal vibrations in the sample. The remaining residual broadening can be attributed primarily to the uncertainty imposed by the finite incident dose and uncorrected instabilities (*15*). We estimate the residual instrumental contribution via quadratic subtraction, which gives the residual blurring (as a Gaussian FWHM) of our ptychographic reconstruction at Pr and Sc sites of 16 ± 1 pm and 15 ± 1 pm, respectively. Notably, QCBED produces a larger DWF for oxygen site #2 (O#2) than does XRD. The resolution of O#2 is 23 ± 2 pm or 19 ± 2 pm, depending on whether the QCBED or XRD result is adopted. It is not surprising that the resolution estimated from different elements is different, because the quality of the ptychographic reconstruction at a finite illuminated dose is dependent on the scattering power of the object (*15*). Therefore, the Abbe resolution of the ptychographic reconstruction, which approximately corresponds to the FWHM of the point-spread function (*23*), is better than 15 ± 1 pm, and its Rayleigh criteria, with a factor of 1.22 correspondence, is 18 ± 1 pm. In all cases, the column width of the ptychographic reconstruction is mainly limited by the finite size of atoms, as determined by their thermal fluctuations instead of the imaging system itself. Going forward, this method should be capable of measuring directional anisotropies of thermal vibrations for individual point-defect–like structures such as nitrogen-vacancy centers in diamond, which are being explored for applications in quantum computing and quantum communications.

In addition to the resolution improvement, the precision for measuring the atomic positions is also significantly improved. Figure 3E shows repeated measurements of Pr–Pr atomic distances with a standard deviation of 0.7 pm, which indicates that we have achieved a subpicometer precision simultaneously with the 16-pm resolution. Notably, the positions of the light oxygen are also measured precisely. Because there are two different bond lengths in the distorted ScO_6 octahedra in $PrScO_3$, the Sc–O distances along two vertical directions, labeled as d_1 and d_2 in Fig. 3D, are not equal. The precision is close to 1 pm, and the histogram in Fig. 3F shows d_1 and d_2 values of 203.0 ± 1.5 pm and 205.2 ± 1.3 pm, respectively. d_1 and d_2 differ by only ~2 pm, and picometer precision is required to distinguish such a small difference. However, high precision of atomic positions from conventional imaging techniques can be realized for heavy metals only (*30*); it cannot be achieved reliably for light elements such as oxygen (*31*). High precision of atomic positions and high-resolution measurement of both heavy and light atoms are crucial for correlating structure and function in materials. Multislice ptychography does not rely on lateral periodicity, so this technique can be applied to defects and grain boundaries as well as to single crystals.

Multislice electron ptychography also allows for 3D structure determination, because it iteratively retrieves the sample structure at different layers. The depth resolution and optimal depth sampling are determined by the out-of-plane curvature of the Ewald sphere and the largest scattering vector at which usable information can be collected (*21*). First, we check the reconstructed structures at different slices from the experimental results; three example slices are shown in Fig. 4A (all slices depicted in movie S1). We find that the slices at the beginning and the end (movie S1) show very small phase shifts. In the middle slices, the phase images show strong contrast and clear structural features. Figure 4B illustrates a depth profile of the phase change cut along the Pr–O direction (marked by the dash-dotted line in Fig. 4A). This depth evolution is generated because the sample is close to a parallel-sided film and there are vacuum layers above and beneath the film (Fig. 4C). The electron beam changes shape as a function of depth into the sample, which is properly accounted for in the multislice electron ptychography algorithm, and as a result recovers a phase shift that is linearly proportional to the electrostatic potential of the sample at each different depth slice. The broadening of the depth profile from each surface of the rectangular slab is fitted by an error function (*23*) and gives a depth resolution of ~3.9 nm, estimated from the width of the error function fitted to the phase variation versus depth at Pr sites (Fig. 4D). This value is better than the aperture-limited depth resolution of 5.1 nm from conventional optical sectioning (*23*).

We also find, through simulations, that multislice electron ptychography can enable the detection and location of interstitials and single atomic dopants in all three dimensions. We constructed a structural model by introducing single dopants in a 15-nm-thick $PrScO_3$ crystalline matrix and generated diffraction data by using mutislice simulations (*23*). Dopant atoms with different atomic numbers (Z) will exhibit different visibilities in multislice electron ptychography because their potentials vary in width and magnitude. Therefore, we introduced defect atoms with a range of scattering strengths, from heavy (Pr; Z = 59) to light (O; Z = 8) and placed them at both interstitial (Fig. 4, E and F) and substitutional (fig. S14) sites and at different depth positions. Figure 4E shows the reconstructed phase images from 3 of 30 slices (movie S2) from the two Pr dopants at depths that differ by 3 nm. The depth profile across the two single dopants (Fig. 4F) shows well-localized contrast in all three dimensions. The depth resolution estimated from the full width at 80% of the maximum (FW80M) at the dopant peak in the depth profile (Pr2 in Fig. 4G) is 0.9 nm. Depth profiles from single Pr, Sc, and O dopants (Fig. 4G) are similar and show FW80M in depths of 0.9, 1.6, and 2.0 nm, respectively. This also shows that the depth resolution depends on the scattering power of the dopant, which in turn depends on the atomic number, as noted for the lateral resolution discussed earlier. A strong contrast and good depth resolution are also retained for single substitutional dopants on the atomic columns (fig. S14). Notably, the depth resolution from multislice electron ptychography exceeds the aperture-limited resolution ($\frac{\lambda}{\alpha^2}$, where λ is the wavelength and α is the probe-forming semi-angle) and has an illumination-dose dependence (Fig. 4H). Additionally, the depth resolution depends on contrast and transverse resolution and can be potentially improved by collecting electrons scattered to higher angles and using a more converging or diverging electron beam (*21*).

Because conventional imaging methods are based on projections through the entire sample, single dopants embedded in a relatively thick matrix usually show little or no contrast (fig. S16). Only dopants with large atomic numbers in a light element matrix and a very thin sample may be detectable. For example, an Sb atom in a silicon matrix can be distinguished by STEM annular dark-field imaging only in samples thinner than 5 nm (*32*). Furthermore, there is strong multiple electron scattering in crystalline samples, and the resultant rechanneling of the electron beam may

lead to incorrect column locations for dopants via conventional optical sectioning methods (*33*). These artifacts also have consequences for electron tomography, the most commonly used technique for determining 3D structures of samples, because poor or incorrect contrast from single dopants in the projection images used for electron tomography hinders their identification and correct localization. The recovered linear signal provided by our full inversion of electron multiple scattering via multislice electron ptychography addresses these deficiencies. Therefore, multislice electron ptychography provides a powerful tool for locating single dopants at more than twice the resolution in all three dimensions compared with conventional approaches. Combined with tomography, robust atomic-resolution details of defect clusters should be possible in all three dimensions.

REFERENCES AND NOTES

1. M. Haider *et al*., *Nature* **392**, 768–769 (1998).
2. P. E. Batson, N. Dellby, O. L. Krivanek, *Nature* **418**, 617–620 (2002).
3. R. Erni, M. D. Rossell, C. Kisielowski, U. Dahmen, *Phys. Rev. Lett.* **102**, 096101 (2009).
4. H. Sawada *et al*., *J. Electron Microsc.* **58**, 357–361 (2009).
5. J. M. Cowley, A. F. Moodie, *Acta Cryst.* **10**, 609–619 (1957).
6. M. J. Hÿtch, W. M. Stobbs, *Ultramicroscopy* **53**, 191–203 (1994).
7. H. G. Brown *et al*., *Phys. Rev. Lett.* **121**, 266102 (2018).
8. J. J. Donatelli, J. C. H. Spence, *Phys. Rev. Lett.* **125**, 065502 (2020).
9. W. Hoppe, *Acta Cryst. A* **25**, 495–501 (1969).
10. J. M. Rodenburg, H. M. L. Faulkner, *Appl. Phys. Lett.* **85**, 4795–4797 (2004).
11. J. M. Rodenburg, A. C. Hurst, A. G. Cullis, *Ultramicroscopy* **107**, 227–231 (2007).
12. P. Thibault *et al*., *Science* **321**, 379–382 (2008).
13. T. J. Pennycook *et al*., *Ultramicroscopy* **151**, 160–167 (2015).
14. S. Gao *et al*., *Nat. Commun.* **8**, 163 (2017).
15. Y. Jiang *et al*., *Nature* **559**, 343–349 (2018).
16. R. Close, Z. Chen, N. Shibata, S. D. Findlay, *Ultramicroscopy* **159**, 124–137 (2015).
17. Z. Chen *et al*., *Nat. Commun.* **11**, 2994 (2020).
18. A. M. Maiden, M. J. Humphry, J. M. Rodenburg, *J. Opt. Soc. Am. A* **29**, 1606–1614 (2012).
19. T. M. Godden, R. Suman, M. J. Humphry, J. M. Rodenburg, A. M. Maiden, *Opt. Express* **22**, 12513–12523 (2014).
20. A. Suzuki *et al*., *Phys. Rev. Lett.* **112**, 053903 (2014).
21. E. H. Tsai, I. Usov, A. Diaz, A. Menzel, M. Guizar-Sicairos, *Opt. Express* **24**, 29089–29108 (2016).
22. M. Schloz *et al*., *Opt. Express* **28**, 28306–28323 (2020).
23. Materials and methods are available as supplementary materials.
24. P. A. Midgley, M. Weyland, *Ultramicroscopy* **96**, 413–431 (2003).
25. M. W. Tate *et al*., *Microsc. Microanal.* **22**, 237–249 (2016).
26. T. M. Gesing, R. Uecker, J. C. Buhl, *Z. Kristallogr. New Cryst. Struct.* **224**, 365–366 (2009).
27. P. Thibault, A. Menzel, *Nature* **494**, 68–71 (2013).
28. M. A. O'Keefe, *Ultramicroscopy* **108**, 196–209 (2008).
29. J. M. Zuo, *Ultramicroscopy* **41**, 211–223 (1992).
30. A. B. Yankovich *et al*., *Nat. Commun.* **5**, 4155 (2014).
31. D. Zhou *et al*., *Ultramicroscopy* **160**, 110–117 (2016).
32. P. M. Voyles, D. A. Muller, J. L. Grazul, P. H. Citrin, H. J. L. Gossmann, *Nature* **416**, 826–829 (2002).
33. H. L. Xin, V. Intaraprasonk, D. A. Muller, *Appl. Phys. Lett.* **92**, 013125 (2008).
34. Z. Chen *et al*., Data Set: Electron ptychography achieves atomic-resolution limits set by lattice vibrations, PARADIM (2021), https://doi.org/10.34863/ssmm-2j11.
35. Z. Chen, Y. Jiang, D. A. Muller, M. Odstrcil, PtychoShelves_EM, source code for multislice electron ptychography, version 2, Zenodo (2021); https://doi.org/10.5281/zenodo.4659690.

ACKNOWLEDGMENTS

D.A.M. thanks M. Humphry of Phasefocus for helpful discussions on multislice 3D ptychography. **Funding:** This research was supported by the National Science Foundation under grant DMR-1539918 (PARADIM Materials Innovation Platform in-house program). Electron microscopy performed at the Cornell Center for Materials Research was supported by the National Science Foundation under grant DMR-1719875. **Author contributions:** Z.C. and D.A.M. initiated and conceived the research; Z.C. performed the experiments and data analyses under the supervision of D.A.M.; Z.C. and Y.J. implemented the mixed-state multislice ptychography algorithms based on the initial ptychography codes from M.O. and M.G.-S.; Y.-T.S. performed the Debye-Waller factors measurements; M.E.H. prepared the sample under the supervision of D.G.S., who also provided advice on XRD structural refinements; I.H. grew the $PrScO_3$ single crystal by the Czochralski method, under the supervision of S.G.; and Z.C. wrote the manuscript, with revisions from D.A.M. and input from all authors. **Competing interests:** Cornell University has licensed the EMPAD hardware to Thermo Fisher Scientific. **Data and materials availability:** Raw experimental data of the results presented in the main text and supplementary materials are available from PARADIM, a National Science Foundation Materials Innovation Platform (*34*). The source code for multislice electron ptychography is available in the Zenodo repository (*35*).

SUPPLEMENTARY MATERIALS

science.sciencemag.org/content/372/6544/826/suppl/DC1
Materials and Methods
Figs. S1 to S17
Tables S1 and S2
References (*36*–*58*)
Movies S1 and S2

21 December 2020; accepted 13 April 2021
10.1126/science.abg2533

NEUROSCIENCE

A brain-computer interface that evokes tactile sensations improves robotic arm control

Sharlene N. Flesher[1,2,3], John E. Downey[1,2,3,4], Jeffrey M. Weiss[1,5], Christopher L. Hughes[1,2,3], Angelica J. Herrera[1,2,3], Elizabeth C. Tyler-Kabara[6], Michael L. Boninger[1,2,5,7,8], Jennifer L. Collinger[1,2,3,5,8]†*, Robert A. Gaunt[1,2,3,5]†*

Prosthetic arms controlled by a brain-computer interface can enable people with tetraplegia to perform functional movements. However, vision provides limited feedback because information about grasping objects is best relayed through tactile feedback. We supplemented vision with tactile percepts evoked using a bidirectional brain-computer interface that records neural activity from the motor cortex and generates tactile sensations through intracortical microstimulation of the somatosensory cortex. This enabled a person with tetraplegia to substantially improve performance with a robotic limb; trial times on a clinical upper-limb assessment were reduced by half, from a median time of 20.9 to 10.2 seconds. Faster times were primarily due to less time spent attempting to grasp objects, revealing that mimicking known biological control principles results in task performance that is closer to able-bodied human abilities.

There are about 169,000 people in the United States living with tetraplegia due to spinal cord injury (SCI) (*1*). Of those with cervical SCI, nearly half desire improved arm and hand function over all other rehabilitation priorities (*2*, *3*). Brain-computer interfaces (BCIs) that measure movement-related neural activity with implanted electrodes can restore some of this lost arm and hand function (*4*–*6*) because the cortex remains capable of generating neural activity that controls arm and hand motion. BCIs can therefore bypass the injured spinal cord to control prosthetic limbs (*4*–*6*), functional electrical stimulation systems (*7*, *8*), or other devices (*9*, *10*).

We previously developed a BCI-controlled robotic arm that enables reaching and grasping movements (*6*) in up to 10 continuously and simultaneously controlled dimensions (*5*). This high-dimensional continuous control has enabled participants to complete clinical assessments of upper-limb function such as the Action Research Arm Test (ARAT) (*11*). However, this BCI control relied on vision alone and lacks a critical sensory dimension. When able-bodied people interact with the environment, tactile feedback from the skin is essential to effectively explore and manipulate objects; without tactile somatosensory feedback, even simple manipulation tasks become clumsy and slow (*12*, *13*).

[1]Rehab Neural Engineering Labs, University of Pittsburgh, Pittsburgh, PA, USA. [2]Department of Bioengineering, University of Pittsburgh, Pittsburgh, PA, USA. [3]Center for the Neural Basis of Cognition, Pittsburgh, PA, USA. [4]Department of Organismal Biology, University of Chicago, Chicago, IL, USA. [5]Department of Physical Medicine and Rehabilitation, University of Pittsburgh, Pittsburgh, PA, USA. [6]Department of Neurosurgery, University of Texas at Austin, Austin, TX, USA. [7]McGowan Institute for Regenerative Medicine, University of Pittsburgh, Pittsburgh, PA, USA. [8]VA Center of Excellence, Department of Veterans Affairs, Pittsburgh, PA, USA.
†These authors contributed equally to this work.
***Corresponding author. Email: rag53@pitt.edu (R.A.G.); collinger@pitt.edu (J.L.C.)**

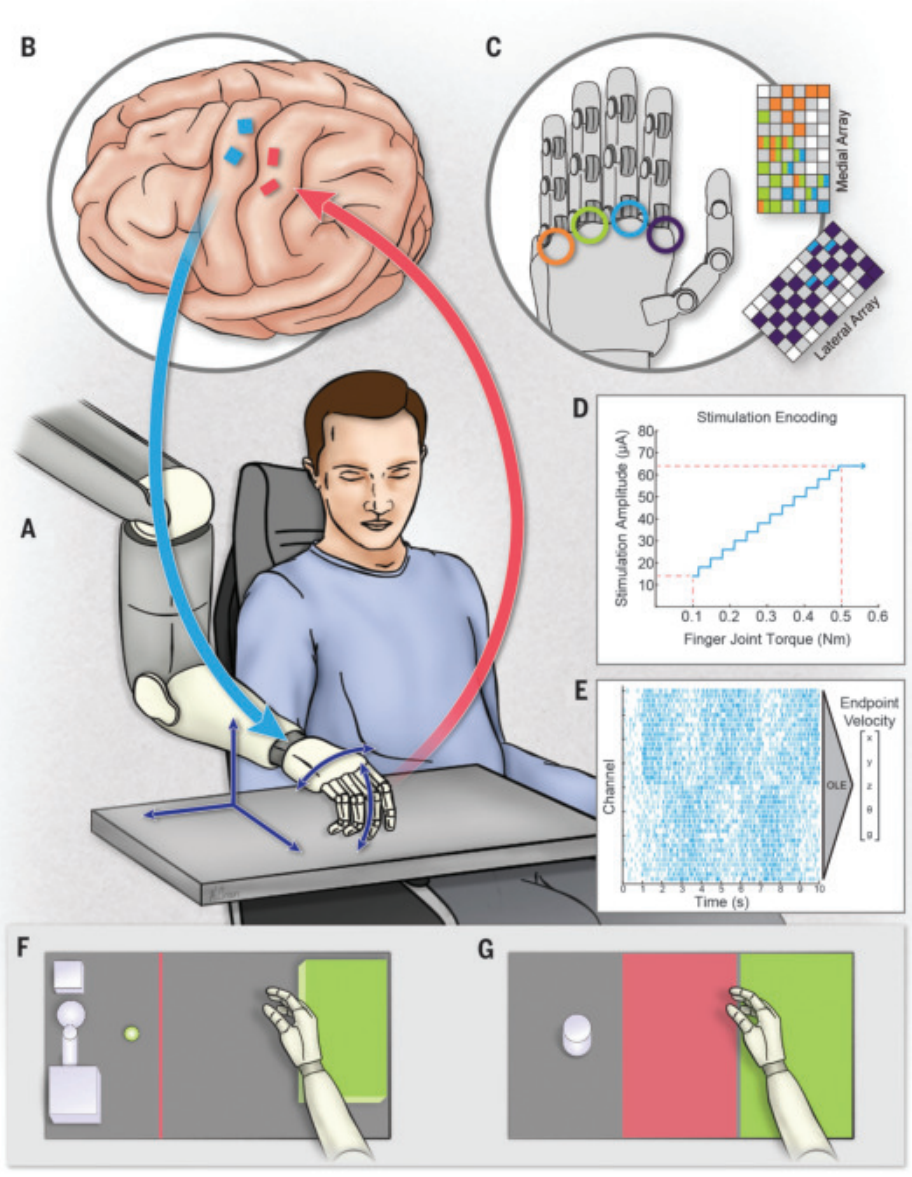


Fig. 1. Overview of the bidirectional BCI system. (**A**) The participant used the intracortical BCI to control a robotic prosthesis in real time, controlling all five dimensions (dark blue arrows) continuously from the start to the end of the trial. (**B**) Four microelectrode arrays were implanted in the left hemisphere. Arrays in the motor cortex (blue) recorded neural activity to control the prosthesis. Arrays in the somatosensory cortex (red) delivered stimulation pulses, evoking sensory percepts referred to the hand. (**C**) Torque measurements from the robotic hand controlled the stimulation of individual electrodes. Colored grids [adapted from (*19*)] represent electrodes and locations on the hand where stimulation evoked a percept. Index finger torque was used to drive stimulation of the index finger sensation, and middle finger torque was used to drive stimulation of electrodes associated with the middle, ring, and pinky finger. (**D**) Stimulation current amplitude was modulated by torque using a linear transformation. (**E**) Example raster plot of neural data recorded from the motor cortex and decoded into endpoint velocities using an optimal linear estimator (OLE). (**F**) Overhead view of the ARAT. Different objects (not all shown) were positioned at the presentation location (green dot), grasped, and then placed on the platform (green box) as quickly as possible. (**G**) Overhead view of the object-transfer task, showing the object (gray), transit (red), and target (green) zones. [Image credit: K. Green]

Neural prosthetics that restore some somatosensation for amputees are becoming more common (*14*–*17*). However, these peripheral stimulation approaches cannot translate to individuals with tetraplegia; stimulation below the level of the lesion is unable to relay information to the somatosensory cortex for processing and perception. Although stimulation in the somatosensory cortex has long been known to evoke detectable sensations (*18*), it is only in recent studies of humans with chronically implanted microelectrode arrays that the perceptual characteristics of microstimulation have been elucidated (*19*, *20*). The potential benefits of a bidirectional BCI—a system in which tactile sensations are evoked through cortical stimulation while neural recordings during attempted movement are decoded to control a robotic prosthesis—have remained unexplored in humans.

Here, we show that a bidirectional BCI (Fig. 1, A and B) that evokes tactile percepts substantially improves performance on functional tasks. These artificial tactile percepts were driven in real time by sensors in a robotic hand that responded to object contact and grasp force (Fig. 1, C and D; and figs. S1 and S2), were evoked through intracortical microstimulation (ICMS) of area 1 of the somatosensory cortex, and were experienced as originating from the participant's own palm and fingers (fig. S1). This result demonstrates that a neural interface that mimics principles of sensorimotor control can be intuitively used by a person with extensive motor impairments.

The male participant in this study was 28 years old at the time of device implant and had tetraplegia due to a C5 motor/C6 sensory ASIA B spinal cord injury sustained 10 years before providing informed consent (*19*). This study was conducted under an investigational device exemption from the U.S. Food and Drug Administration and is registered at clinicaltrials.gov (NCT01894802). Two microelectrode arrays with 88 wired electrodes were implanted in the hand and arm region of the motor cortex (Fig. 1B) to decode movement intent (Fig. 1E and supplementary materials). Two additional microelectrode arrays with 32 wired electrodes were implanted in area 1 (Fig. 1B), which is a cutaneous region of the somatosensory cortex (*21*). Stimulation evoked sensations in the palm and fingers of the participant's right hand, which he described as having cutaneous qualities (Fig. 1, C and D; and fig. S1)

(*19*). We used an observation-based paradigm (*6*) to train a new 5 degrees-of-freedom velocity decoder each day (3 degrees-of-freedom hand endpoint, wrist rotation, and hand grasp). Stimulation was never delivered during calibration (fig. S3), and the participant had an unobstructed view of the robotic hand for all trials. Before these experiments, the participant had practiced the tasks for about 2 years.

We compared performance with and without ICMS on a modified version of the ARAT (*11*, *22*) (Fig. 1F and movies S1 to S3). The ARAT variant that we used involved picking up one of eight objects and placing each one

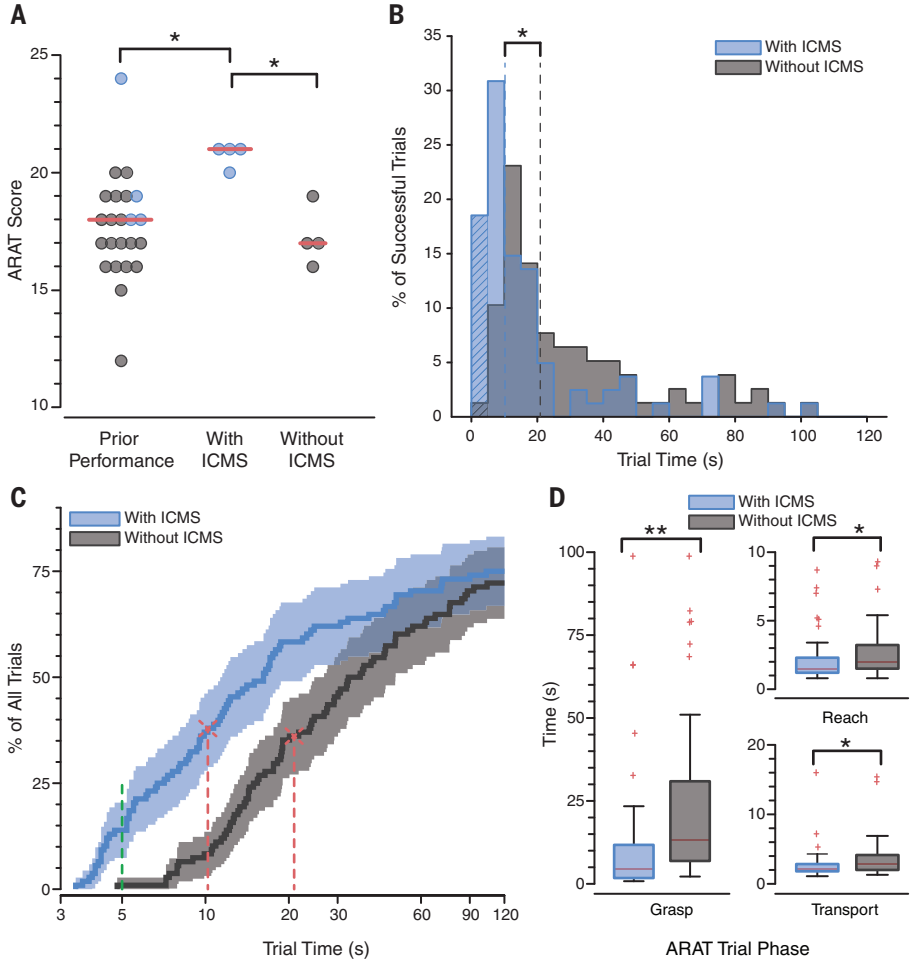


Fig. 2. Effect of ICMS on ARAT performance. (**A**) ARAT scores when ICMS feedback was provided were significantly better than prior ARAT scores (*p = 0.005), which occasionally used ICMS feedback (blue dots), and data from the current experiment without ICMS feedback (*p = 0.029). Red lines indicate median scores. (**B**) Histogram of successful trial times completed with (blue) and without (gray) ICMS tactile feedback. Median trial times (dashed lines) were significantly faster with ICMS (*p < 0.0001). Hatched bars represent trials completed in less than 5 s. (**C**) Empirical cumulative distribution of individual trial times, including failed trials, shown on a log-normalized axis. Vertical red dashed lines indicate when 50% of successful trials were completed. Data to the left of the vertical green dashed line represent trials completed in less than 5 s. Shading indicates the 95% confidence bounds, calculated with Greenwood's formula. (**D**) Amount of time spent in each phase of the ARAT task. Red lines are medians, box outlines are interquartile ranges, and whiskers are the range of the data excluding outliers (red plus signs). All task phases were faster when ICMS feedback was provided (*p < 0.001 and **p < 0.0001; table S2). For (A) to (D), significance was assessed with a Wilcoxon rank sum test.

Table 1. Performance metrics for each task per experiment day. ARAT scores were computed as the sum of the best score per object, with a maximum score of 27. Each of the nine objects was attempted three times, so that the maximum number of trials attempted per session was 27. The median and interquartile (IQR) trial times for successful ARAT trials are shown for each session. The median and IQR trials times for all successful trials were calculated by pooling trial times across all four sessions per feedback condition and calculating the median and IQR from the aggregate distribution. The total number of object transfers is the sum of all five 2-min trials per day.

Feedback condition	Session	ARAT score (out of 27)	ARAT trials completed (out of 27)	Median and IQR trial times for successful ARAT trials (s)	Object transfer (transfers per day)
With ICMS feedback	1	21	19	11.9 (6.6–27.7)	97
	2	21	22	12.0 (5.6–38.9)	74
	3	21	21	8.8 (6.0–17.2)	93
	4	20	19	8.1 (4.6–11.9)	88
	Summary	Median: 21	Median: 20	Median of all trials: 10.2 (5.5–18.1)	Total: 352
Without ICMS feedback	1	19	23	14.0 (11.1–30.9)	88
	2	16	19	27.6 (18.8–37.2)	55
	3	17	23	18.7 (12.3–41.7)	74
	4	17	13	40.5 (15.5–48.4)	98
	Summary	Median: 17	Median: 21	Median of all trials: 20.9 (13.1–40.5)	Total: 315

on a platform as quickly as possible. We also included a ninth task from the ARAT set: picking up a cup of water, pouring its contents into another cup, and setting the cup back down, upright, on the table. Each object was attempted three times in each session. The trials were timed and scored from 0 to 3 (see supplementary materials), and the highest scores for each object were summed together to produce the ARAT score; the maximum score was 27. In the first four sessions with ICMS-induced sensations driven by robotic touch, the participant achieved a median ARAT score of 21. This was significantly higher than the median score of 17 achieved during the next four sessions without ICMS-evoked tactile sensations (p = 0.029, Wilcoxon rank sum test; Table 1 and Fig. 2A) as well as 23 sessions conducted during the 23 months before these experiments (p = 0.005, Wilcoxon rank sum test; Table 1 and Fig. 2A). The scores in the four experimental sessions without ICMS were no different than the prior 23 sessions (p = 0.65, Wilcoxon rank sum test). Previous ARAT sessions included four exploratory trials with ICMS-driven tactile feedback (Fig. 2A); however, stimulation parameters were variable, and trials with and without ICMS were intermixed, rather than occurring in a blocked design (fig. S3), making the feedback unreliable.

ARAT scores improved because individual trials were completed much faster when ICMS feedback was delivered (Fig. 2, B and C; and movie S2). In the ARAT scoring system, successfully transferring an object in less than 5 s (a score of 3) is considered able-bodied performance (*22*). Without tactile sensations, this score was achieved only once during all 108 trials. When tactile sensations were provided, a score of 3 was achieved 15 times. Further, 14% of the trials with tactile feedback were completed more quickly than the fastest trial without ICMS (Fig. 2C). Times for successfully completed trials decreased by 51.2%, from a median of 20.9 to 10.2 s, when tactile feedback was provided (p < 0.0001, Wilcoxon rank sum test; Table 1; Fig. 2, B and C; and movie S3). These faster completion times were the cause of the 3.5-point improvement in the ARAT score that occurred when ICMS was provided and can be interpreted to mean that ICMS-induced tactile sensations allowed 3.5 more objects, out of nine possible objects, to be transported to the platform in a normal time (<5 s). Although the performance gains were not the same for every object, completion times improved significantly for more than half of the ARAT objects, and the median completion times were lower in all cases (fig. S4 and table S1). The objects with the largest improvements were rated by the participant as being the easiest to manipulate within the constraints of the robotic hand. Some of the smaller objects were difficult to pick up, given the grasping kinematics of the fingers; the tips of the fingers often made contact with the object rather than the pads of the distal phalanx, making grasp less stable. Further, the participant only had control over one grasp dimension that opened and closed all of the fingers as a group. There was no change in the total number of successfully completed trials with or without ICMS (p = 0.83, Wilcoxon rank sum test; Table 1).

The median time spent attempting to grasp an object—defined as the period of time between object contact and object liftoff—decreased by 66% from 13.3 s without ICMS to 4.6 s with ICMS (p < 0.0001, Wilcoxon rank sum test; Fig. 2D and table S2) and accounted for 88% of the total improvement. The median time spent in the reaching and transport phases (see supplementary materials) both decreased by 25% with ICMS. Once the participant had successfully grasped an object, he rarely dropped it. This occurred just four times with ICMS and five times without. All the drops resulted from an unstable grasp rather than the participant opening the hand.

We also tested the effect of providing ICMS-induced tactile feedback on functional performance using an object-transfer task (Fig. 1G and movie S4). In this task, the participant was asked to pick up an object from the left side of the workspace (object zone), carry it across the table (transit zone), and drop it on the right side (target zone) as many times as possible in 2 min. Four sessions without ICMS and four sessions with ICMS were conducted (fig. S3), and this task was repeated five times per session. The time spent in the object zone (Fig. 1G) decreased by 30.3%, from 3.3 ± 1.2 s per transfer without ICMS to 2.3 ± 0.4 s per transfer with ICMS (p = 0.002, Student's t test; Fig. 3A). With ICMS, the participant moved the prosthetic hand significantly less in the object zone (32.4 ± 5.9 cm per transfer with

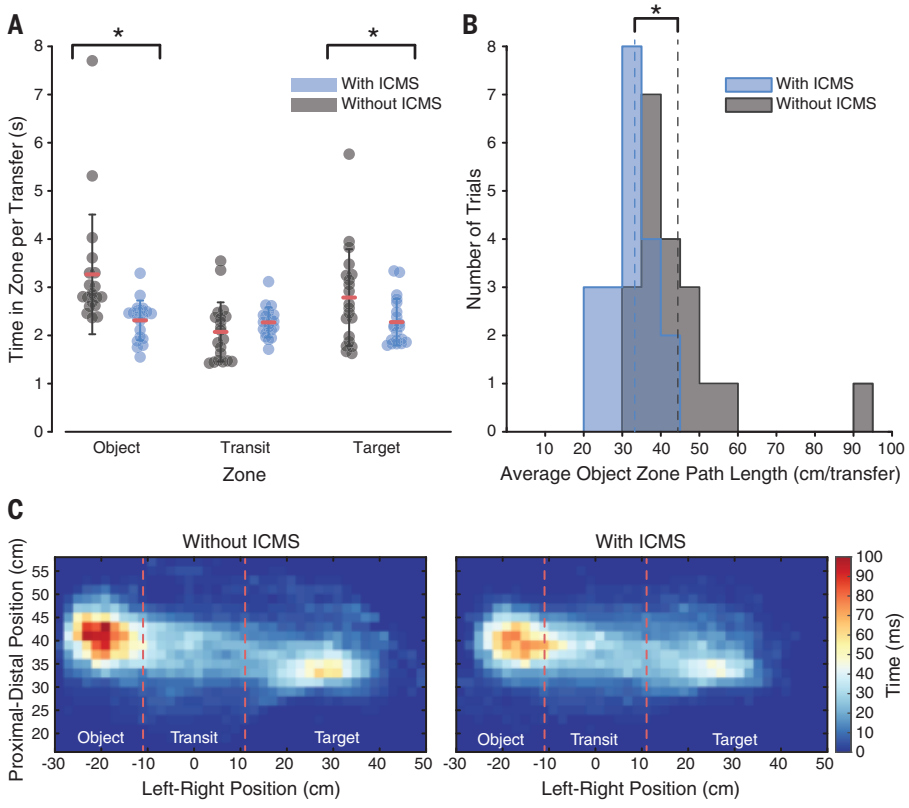


Fig. 3. Effect of ICMS on object-transfer performance. (**A**) Amount of time spent in each task zone, per transfer, by feedback condition (n = 20 trials per feedback condition). Data for all trials are shown, with the mean value indicated by the red lines and the whiskers indicating one standard deviation. The amount of time spent in the object and target zones decreased significantly with ICMS feedback (*p = 0.002 and 0.048, respectively; Student's t test). (**B**) Distribution of average path lengths in the object zone per trial for the two feedback conditions, computed as the total path length divided by the number of transfers. Mean path length decreased with ICMS feedback (*p = 0.0007, Student's t test). (**C**) Spatial map of the average amount of time spent in each location in the workspace per transfer. Each individual square represents a 2-cm–by–2-cm region of the workspace. The color indicates the average amount of time spent in each location per transfer. Without stimulation, more time was spent near the object in the object zone, as shown by the darker red colors in the object zone. Red dashed lines indicate zone boundaries.

ICMS, 44.2 ± 13.1 cm per transfer without ICMS, $p = 0.0007$, Student's t test; Fig. 3B) and spent less time in the immediate vicinity of the object (Fig. 3C). The time spent in the target zone also decreased, whereas the time spent in the transit zone was unaffected (Fig. 3A and table S3). Overall, 352 transfers were completed with ICMS and 315 transfers were completed without ICMS (Table 1), and the number of transfers increased from 15.8 ± 3.8 transfers per 2-min trial to 17.8 ± 2.4 transfers per trial with ICMS, though this difference was not statistically significant ($p = 0.050$, Student's t test).

Because differences in neural decoder performance could lead to differences in the ability to control the arm, it is possible that the improvements on days with artificial tactile feedback were simply due to the decoder. We therefore used a random target sequence task (*6*) each day to measure how well the participant could independently control each degree of freedom. This task was always performed without ICMS (fig. S3). On days when functional tasks were completed with ICMS, fewer target sequence trials were successfully completed (table S4). The median endpoint translation velocity of the robot during the sequence task was also slightly slower (table S4), suggesting that the decoder performance itself—and thus the participant's ability to control the robotic arm—was not biased toward better performance on days with ICMS.

Creating artificial tactile feedback using a bidirectional BCI substantially improved functional performance during reaching and grasping tasks compared with a motor-only BCI with visual feedback. In contrast to many studies where the effects of artificial sensations on task performance are measured without visual or auditory feedback (*14*, *15*, *23*–*27*), our aim was to determine whether a bidirectional BCI would improve performance on tasks that were already possible with existing sensory modalities, namely vision. This bidirectional BCI taps into cortical sensorimotor systems that remain intact after injury, allowing a person with chronic tetraplegia to, in some cases, perform functional tasks at able-bodied speeds.

This better performance was driven primarily by reducing the time spent attempting to grasp objects. Indeed, in the ARAT task, the grasp time decreased by more than half with ICMS, accounting for 88% of the overall time reduction. Without tactile sensations, the participant spent more time placing the hand in a position that would ensure a stable grasp. Small performance gains also occurred during the reaching phase when ICMS was not delivered. This improvement suggests that the participant approached the task with increased confidence and speed when he knew that ICMS-evoked tactile sensations would signal object contact. Similar effects were observed during the object-transfer task; shorter path lengths near the object indicate fewer corrective movements and increased confidence.

As with any single-subject study, it is not guaranteed that these findings will generalize to future experiments and participants. However, there are several reasons to believe that these results indicate the potential of restoring somatosensory percepts using ICMS in a bidirectional BCI. First, using the same fundamental neural decoding and control methods, two participants have achieved similar scores on functional tasks with vision alone (*5*, *6*, *28*). With the current participant, these scores were only exceeded when ICMS-evoked tactile feedback was provided (Fig. 2A), suggesting that without artificial tactile feedback, control is impaired, much as it is when tactile sensations are absent in people with otherwise normal motor control capabilities (*13*, *29*). Second, performance improvements were driven primarily by reductions in the time taken to successfully grasp an object (Figs. 2D and 3A). State transitions, such as object contact (*30*) during grasping, are explicitly encoded by tactile feedback in the intact nervous system. That the percepts signaled these state transitions with high temporal accuracy and enabled the participant to grasp objects more quickly suggests that ICMS delivered to area 1 of the somatosensory cortex improves task performance in a way that is congruent to the way natural cutaneous feedback improves grasp performance. In a similar way, behaviorally relevant state transitions also occur during object release (*30*), potentially explaining the slightly improved times during the transport phase in the ARAT task and the time spent in the target zone in the object-transfer task. Finally, when ICMS-induced percepts were provided after 2 years of consistent ARAT scores, performance improved significantly, and when they were removed, performance returned to pre-ICMS levels (Fig. 2A). These observations suggest that the improvements were primarily due to the addition of reliable sensory information, rather than the result of additional practice. This immediate performance improvement also demonstrates that ICMS in the somatosensory cortex was not akin to sensory substitution cues that could have been provided by electrical or mechanical stimulation of intact skin or audio or visual cues, because the relationship between these cues and behavior must be learned (*31*). This learning requirement and other factors related to attentional load have limited the impact of sensory substitution in real-world scenarios (*32*). The immediate improvements that we observed with ICMS in area 1 also demonstrate the benefits of providing intuitive feedback. By contrast, ICMS feedback in a relevant area of the cortex, but in an unintuitive way, requires considerable learning time (thousands of trials) to use effectively (*33*).

In this study, we chose one sensory encoding scheme that leveraged two capabilities of ICMS—variable intensity and multiple focal percepts (*19*)—to provide proportional feedback that evoked sensations localized to individual fingers (figs. S1 and S2). Future work should examine how the stimulation encoding design (e.g., proportional versus on-off) may affect performance across a wide range of tasks. For example, the participant rarely dropped any of the objects once they were successfully grasped. However, many of the objects were rigid, and there was no penalty for grasping the objects too firmly. Tasks that involve fragile objects or more precise control of hand posture and grasp force could be more dependent on specific sensory encoding schemes.

Ultimately, ICMS-induced tactile percepts improved task performance to levels never previously observed, decreased the time spent reaching and grasping in ways that were analogous to the role of natural tactile sensations during grasp state transitions, and do not appear to be the result of practice. That artificial tactile sensations substantially improved performance demonstrates that engineered approaches that mimic known sensorimotor circuits—albeit imperfectly at present—will have a major impact on the future performance of BCIs. This is particularly important for individuals with conditions such as SCI where the peripheral nervous system is no longer intact.

REFERENCES AND NOTES

1. National Spinal Cord Injury Statistical Center, "Facts and figures at a glance" (University of Alabama at Birmingham, 2018).
2. K. D. Anderson, *J. Neurotrauma* **21**, 1371–1383 (2004).
3. J. L. Collinger *et al.*, *J. Rehabil. Res. Dev.* **50**, 145–160 (2013).
4. L. R. Hochberg *et al.*, *Nature* **485**, 372–375 (2012).
5. B. Wodlinger *et al.*, *J. Neural Eng.* **12**, 016011 (2015).
6. J. L. Collinger *et al.*, *Lancet* **381**, 557–564 (2013).
7. C. E. Bouton *et al.*, *Nature* **533**, 247–250 (2016).
8. A. B. Ajiboye *et al.*, *Lancet* **389**, 1821–1830 (2017).
9. L. R. Hochberg *et al.*, *Nature* **442**, 164–171 (2006).
10. C. Pandarinath *et al.*, *eLife* **6**, e18554 (2017).
11. R. C. Lyle, *Int. J. Rehabil. Res.* **4**, 483–492 (1981).
12. J. Monzée, Y. Lamarre, A. M. Smith, *J. Neurophysiol.* **89**, 672–683 (2003).
13. J. C. Rothwell *et al.*, *Brain* **105**, 515–542 (1982).
14. S. Raspopovic *et al.*, *Sci. Transl. Med.* **6**, 222ra19 (2014).
15. S. Wendelken *et al.*, *J. Neuroeng. Rehabil.* **14**, 121 (2017).
16. G. S. Dhillon, S. M. Lawrence, D. T. Hutchinson, K. W. Horch, *J. Hand Surg. Am.* **29**, 605–615 (2004).
17. E. L. Graczyk, L. Resnik, M. A. Schiefer, M. S. Schmitt, D. J. Tyler, *Sci. Rep.* **8**, 9866 (2018).
18. W. Penfield, E. Boldrey, *Brain* **60**, 389–443 (1937).
19. S. N. Flesher *et al.*, *Sci. Transl. Med.* **8**, 361ra141 (2016).
20. M. Armenta Salas *et al.*, *eLife* **7**, e32904 (2018).
21. B. P. Delhaye, K. H. Long, S. J. Bensmaia, *Compr. Physiol.* **8**, 1575–1602 (2018).
22. N. Yozbatiran, L. Der-Yeghiaian, S. C. Cramer, *Neurorehabil. Neural Repair* **22**, 78–90 (2008).
23. M. Schiefer, D. Tan, S. M. Sidek, D. J. Tyler, *J. Neural Eng.* **13**, 016001 (2016).
24. E. L. Graczyk *et al.*, *Sci. Transl. Med.* **8**, 362ra142 (2016).
25. C. Klaes *et al.*, *J. Neural Eng.* **11**, 056024 (2014).

26. J. E. O'Doherty *et al*., *Nature* **479**, 228–231 (2011).
27. B. Lee *et al*., *Front. Syst. Neurosci.* **12**, 24 (2018).
28. J. E. Downey *et al*., *Sci. Rep.* **7**, 16947 (2017).
29. R. S. Johansson, R. Riso, C. Häger, L. Bäckström, *Exp. Brain Res.* **89**, 181–191 (1992).
30. R. S. Johansson, J. R. Flanagan, *Nat. Rev. Neurosci.* **10**, 345–359 (2009).
31. H. C. Stronks, A. C. Nau, M. R. Ibbotson, N. Barnes, *Brain Res.* **1624**, 140–152 (2015).
32. J. M. Loomis, R. L. Klatzky, N. A. Giudice, in *Assistive Technology for Blindness and Low Vision*, R. Manduchi, S. Kurniawan, Eds. (CRC Press, 2012).
33. M. C. Dadarlat, J. E. O'Doherty, P. N. Sabes, *Nat. Neurosci.* **18**, 138–144 (2015).

ACKNOWLEDGMENTS

We thank N. Copeland for his continuing and extraordinary commitment to this study as well as insightful discussions with the study team; D. Harrington for regulatory management of the study; A. Jorge for help with data collection; P. Gibson and B. Clarkson for video data processing; the University of Pittsburgh Clinical and Translational Science Institute and the Office of Investigator-Sponsored Investigational New Drugs and Investigational Device Exemption support for assistance with protocol development and regulatory reporting and compliance; the volunteer members of the Data Safety and Monitoring Board for their continued monitoring of this study; H. Jourdan for financial and organizational support; Blackrock Microsystems (Salt Lake City, UT, USA), especially R. Franklin, for technical support related to this project; and K. Shenoy for helpful discussions and insights regarding data interpretation. **Funding:** This material is based upon work supported by the Defense Advanced Research Projects Agency (DARPA) and Space and Naval Warfare Systems Center Pacific (SSC Pacific) under contract no. N66001-16-C-4051 and the Revolutionizing Prosthetics program (contract no. N66001-10-C-4056). S.N.F. was supported by an NSF Graduate Research Fellowship under grant number DGE-1247842. The views, opinions, and/or findings contained in this article are those of the authors and should not be interpreted as representing the official views or policies of DARPA, SSC Pacific, or the US government. **Author contributions:** Conceptualization: S.N.F., J.E.D., M.L.B., J.L.C., R.A.G.; Investigation: S.N.F., J.E.D., J.M.W., C.L.H., A.J.H., J.L.C., R.A.G.; Software: S.N.F., J.E.D., J.M.W.; Formal analysis: S.N.F., J.L.C., R.A.G.; Visualization: S.N.F., R.A.G.; Supervision: M.L.B., J.L.C., R.A.G.; Writing – original draft: S.N.F., J.L.C., R.A.G.; Writing – review and editing: S.N.F., J.E.D., J.M.W., C.L.H., A.J.H., E.C.T.-K., M.L.B., J.L.C., R.A.G. **Competing interests:** The authors declare no competing interests. **Data and materials availability:** All data are available in the manuscript or the supplementary materials.

SUPPLEMENTARY MATERIALS

science.sciencemag.org/content/372/6544/831/suppl/DC1
Materials and Methods
Figs. S1 to S4
Tables S1 to S4
References (*34*–*40*)
MDAR Reproducibility Checklist
Movies S1 to S4
Data S1

29 May 2020; accepted 25 March 2021
10.1126/science.abd0380

FLOW BATTERIES

Reversible ketone hydrogenation and dehydrogenation for aqueous organic redox flow batteries

Ruozhu Feng, Xin Zhang*, Vijayakumar Murugesan, Aaron Hollas, Ying Chen, Yuyan Shao, Eric Walter, Nadeesha P. N. Wellala, Litao Yan, Kevin M. Rosso, Wei Wang*

Aqueous redox flow batteries with organic active materials offer an environmentally benign, tunable, and safe route to large-scale energy storage. Development has been limited to a small palette of organics that are aqueous soluble and tend to display the necessary redox reversibility within the water stability window. We show how molecular engineering of fluorenone enables the alcohol electro-oxidation needed for reversible ketone hydrogenation and dehydrogenation at room temperature without the use of a catalyst. Flow batteries based on these fluorenone derivative anolytes operate efficiently and exhibit stable long-term cycling at ambient and mildly increased temperatures in a nondemanding environment. These results expand the palette to include reversible ketone to alcohol conversion but also suggest the potential for identifying other atypical organic redox couple candidates.

The prospect of using organic materials in aqueous redox flow batteries (RFBs) has become increasingly attractive because of their synthetic tunability, natural abundance, and inherent safety (*1*–*3*). The ability to carry out reversible redox reactions is a prerequisite for the materials to be used in an electrochemical energy storage device, which has so far limited the available organic core structures to a rather small library based on quinone, diimine, pyridinium, and nitroxyl functionalities (*2*, *4*–*7*), which have been tuned for their solubilities, stabilities, and redox potentials. However, a much larger number of organic structures exhibit some amount of irreversible redox activity within the potential window of water. For example, although ketones are readily reduced to alcohols through two-electron electro-hydrogenation (Fig. 1A) (*8*, *9*), direct oxidation of alcohols (charged product) to carbonyl compounds presents a barrier to the use of ketones as redox-active materials for energy storage. The potential for electrochemical oxidation of the hydroxyl moiety often resides at >1 V versus $Ag/AgNO_3$ (measured in organic solvent) (*10*), a potential that is too positive for practical use as anolyte material in an aqueous battery. This reaction usually requires the presence of either stoichiometric chemical oxidants or transition-metal catalysts (*11*). For this reason, reports on the application of ketone and alcohol compounds in secondary batteries have been rare and typified as lacking success (*12*, *13*).

A few reports have detailed the use of 9-fluorenone (FL) and benzophenone derivatives as one-electron acceptors in nonaqueous RFBs (*14*, *15*). In aqueous media, however, the radical anion formed upon reduction will inevitably become protonated and initiate complete reduction to alcohol (*9*, *16*–*18*). Benzylic protonation upon two-electron reduction presents a tremendous challenge for reversible two-electron redox reaction in aqueous media. Unlike quinone molecules that undergo the well-known proton-coupled electron transfer redox mechanism (*19*), in the case of FL 2-electron reduction, once alcohol is formed and benzylic protonation has occurred, a much higher potential would be needed to perform

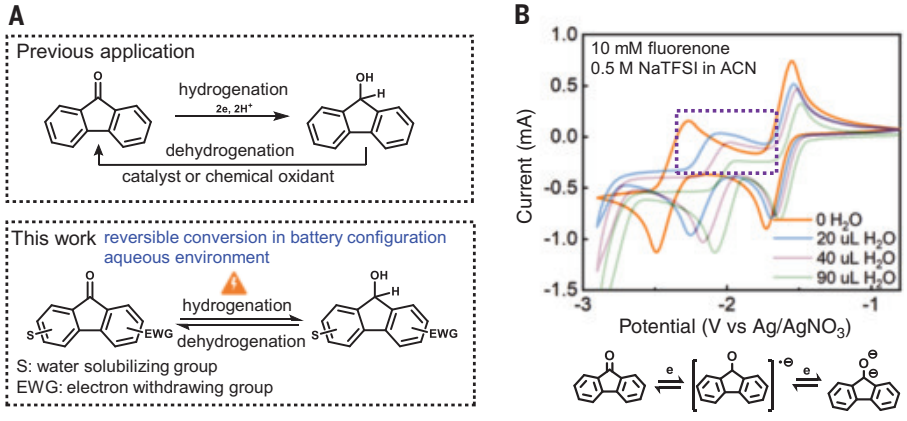


Fig. 1. Ketone–alcohol electrochemical conversion. (**A**) The generic illustration of ketone hydrogenation and alcohol dehydrogenation. (**B**) Protonation state influences on the reversibility of pristine FL electrochemistry. CV is measured in acetonitrile with 0.5 M NaTFSI, with FL concentration of 10 mM at 100 mV/s scan rate.

Pacific Northwest National Laboratory, 902 Battelle Boulevard, Richland, WA 99354, USA.
***Corresponding author. Email: xin.zhang@pnnl.gov (X.Z.); wei.wang@pnnl.gov (W.W.)**

the electrochemical reoxidation (*20*). As shown in Fig. 1B, electrochemical reduction of unsubstituted FL is facile in acetonitrile regardless of water content; however, the reoxidation peak is clearly diminished.

Using molecular structure design of FL as the example, we demonstrate reversible electrochemical conversion between ketone and alcohol at flow-battery–relevant rates and potentials on carbon-based electrodes at room temperature without a catalyst. The rigid Π-conjugated bonding structure of FL (*21*) is also shown to provide long-term stability in aqueous RFB under extended cycling and at increased temperature (50°C).

Protonation of the reduced FL species is the controlling factor yielding poor electrochemical reversibility in water. This is illustrated through density functional theory (DFT) calculations for the highest occupied molecular orbital/lowest unoccupied molecular orbital (HOMO/LUMO) energy gap and redox potential on dianionic species and fully protonated alcohol species (Fig. 2, A and B). Deprotonated anionic species are predicted to generate ~3-V negative shifts in calculated oxidation potentials, placing the predicted redox potential of the deprotonated species in a suitable potential range for an RFB anolyte. But because protonation of the reduced FL species in water would be facile and cause electrochemical irreversibility, we postulated that reducing the pK_a (acid dissociation constant) of fluorenol (FL-OH) enough to generate deprotonated fluorenolate could enable reversible electrochemical oxidation at battery operating conditions.

Owing to the extended aromatic structure of FL, the benzylic proton in FL-OH should show considerable acidity for a C–H bond (*22*), with a Bordwell pK_a of ~22 reported for 9-methoxyfluorene (*23*). This pK_a, albeit measured in dimethyl sulfoxide (DMSO), is only a few pK_a units outside of the water pK_a window (pK_a of 14) (*24*). Moreover, studies on FL-OH in mixed aqueous–organic solvents suggest that the pK_a of the benzylic C–H could be less than the pK_a of the alcohol group upon O–H deprotonation, effectively producing a $2H^+$ deprotonation step in FL-OH (*22*, *25*, *26*). Therefore, we modified FL with archetypal electron-withdrawing groups (EWGs) and electron-donating groups. (A Hammett constant comparison for functional groups is shown in fig. S1, and abbreviations for FL derivatives and their corresponding structures in the following context are summarized in tables S1 and S2). The calculated relative pK_a values for FL-OH with different electron-withdrawing or donating groups are listed in Fig. 2C (which eliminates the typical systematic error in the calculated absolute values as shown in fig. S2). It can be seen that the hydroxyl pK_a is predicted to shift to slightly

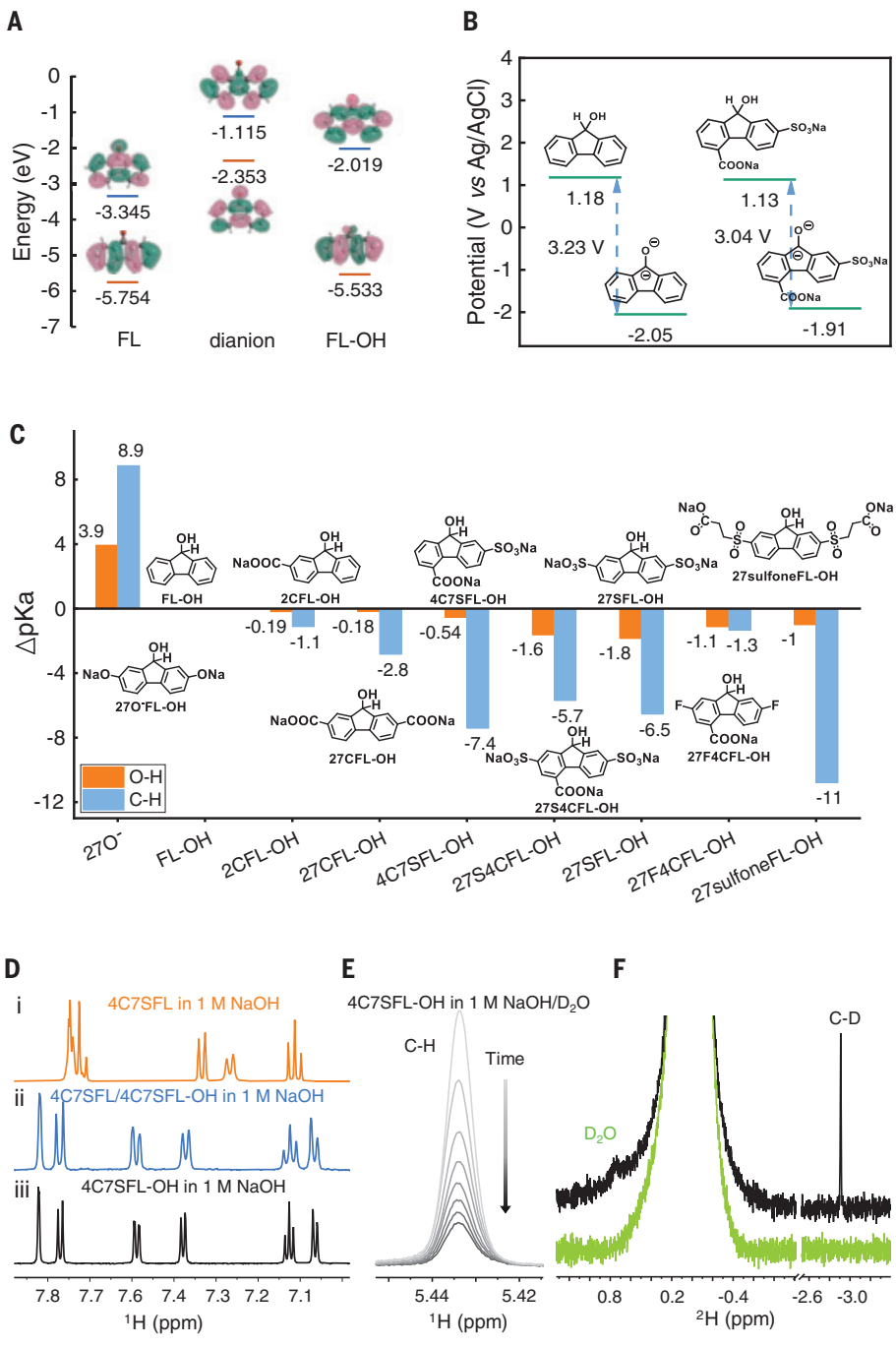


Fig. 2. Validation of hypothesis on chemical reaction equilibrium enabling discharge of FL-OH in aqueous media. (**A**) Density-functional theory calculation on LUMO and HOMO of FL, dianionic FL, and FL-OH. (**B**) Pristine and substituted dianionic FL/FL-OH calculated oxidation potential shifts. (**C**) Hydroxyl proton and benzylic proton pK_a shifts with different substitutions. The *x* axis is roughly a reflection of increasing electron-withdrawing group, but not in a linear fashion. The abbreviations follow the counterclockwise sequence of 1-8 on aromatic ring position, with O^- for deprotonated hydroxyl, C for carboxylate, S for sulfonate, F for fluorine, and sulfone for sulfonylpropionate. All anions are associated with sodium as the counterion for calculation. The C-H pK_a is calculated after deprotonation of the alcohol, where O-Na was used. A detailed summary of the alcohol structures and their full names and abbreviations is depicted in table S2. (**D**) A comparison of ^{1}H NMR spectra between trace (i) 4C7SFL in 1 M NaOH in D_2O; (ii) 1:1 ratio of 4C7SFL/4C7SFL-OH in 1 M NaOH in D_2O; (iii) 4C7SFL-OH in 1 M NaOH in D_2O. (**E**) ^{1}H NMR analysis of H-D exchange enabled by deprotonation of 4C7SFL-OH in 1 M NaOH aqueous solution. (**F**) ^{2}H NMR confirms the formation of benzylic C-D at −2.7 ppm in 4C7SFL-OH in 1 M NaOH.

smaller values with stronger EWGs, and the pK_a of the C–H bond decreases.

We verified the acidity of the benzylic C-H bond by performing nuclear magnetic resonance (NMR) experiments using chemically prepared 4-carboxylic-7-sulfonate fluorenol (4C7SFL-OH) in 1 M NaOH (Fig. 2, D and E). In D_2O, the C–H resonance appears at around 5.4 parts per million (ppm) (fig. S3 for structure characterization). With 1 M NaOH in D_2O, the peak signal diminished over time (Fig. 2E), indicating hydrogen–deuterium exchange. ^{2}H NMR (Fig. 2F) also confirmed this exchange by detecting the benzylic C-D peak. Combining NMR results in Fig. 2 confirmed the effectiveness of incorporating EWGs to enable the deprotonation process. Additionally, an exchange process also can be expected between the oxidized form of FL and reduced form of FL-OH, as indicated in Fig. 2D. With the analysis of FL/FL-OH mixture in alkaline solution (fig. S4) using electron paramagnetic resonance (EPR), the generation of the electrochemically active radical anion also can be confirmed. The incorporation of EWGs shifts the ketone reduction potential to more positive values and was readily observable in cyclic voltammetry (CV) (full CV study of the derivatives in fig. S5 and S6) of the corresponding compounds (*2*). Although this potentially could lower the battery voltage, the accompanying enhancement from the lower pK_a and reversibility proves to be a major advantage overall.

In addition to the electrochemical reversibility, the solubility is important because it dictates the energy density of the aqueous organic RFBs. We investigated the solubility of as-synthesized FLs in 2 M NaOH/KOH aqueous solution (table S3 and fig. S7). FLs with carboxylate (COO^-) and sulfonate (SO_3^-) groups were more soluble than polyethylene glycol groups (table S3). FLs with asymmetric structures have higher solubilities than symmetric structures (fig. S7), which agrees with our previous study on preferential solvation (*5*, *27*). For instance, highly symmetric 2,7-disulfonate fluorenone showed less than 50 mM solubility in both 2 M NaOH solution and 2 M KOH solution; asymmetric 2-carboxylic-7-sulfonate fluorenone exhibited solubilities of 1.1 and 0.7 M in 2 M NaOH solution and 2 M KOH solution, respectively. Highly asymmetric 4C7SFL (structural confirmation with 2D NMR analysis is provided in fig. S8) revealed the highest solubilities of 1.5 and 1.3 M in 2 M NaOH solution and 2 M KOH solution, respectively. Considering the two-electron redox reaction, the available electron concentration of 4C7SFL could reach close to 3 M.

We demonstrated the utility of these engineered FL derivatives as battery anolyte materials using 4C7SFL at high concentration. Given the long-term instability of the catholyte (potassium ferro/ferricyanide) in basic solution (*28*), excess ferro/ferricyanide was used to avoid catholyte-derived capacity loss and allow long-term cycling of the FL candidates. A flow battery consisting of a ferro/ferricyanide catholyte and 1.36 M 4C7SFL/1 equiv. NaOH anolyte (equivalent to 2.72 M electron transfer) was subjected to current density testing and extended cycling (Fig. 3) with more experimental details provided in the supplementary materials (current density test was performed in the initial 15 cycles; detailed initial 30-cycle cycling data are provided in fig. S9A). The fluctuation of capacity during operation is attributed to the temperature changes in the laboratory (fig. S10). The cell was able to provide stable cycling at 20 mA cm^{-2} for more than 120 days (1111 cycles) (Fig. 3A), with > 96% of reversible capacity delivered over 1 V during discharge throughout the

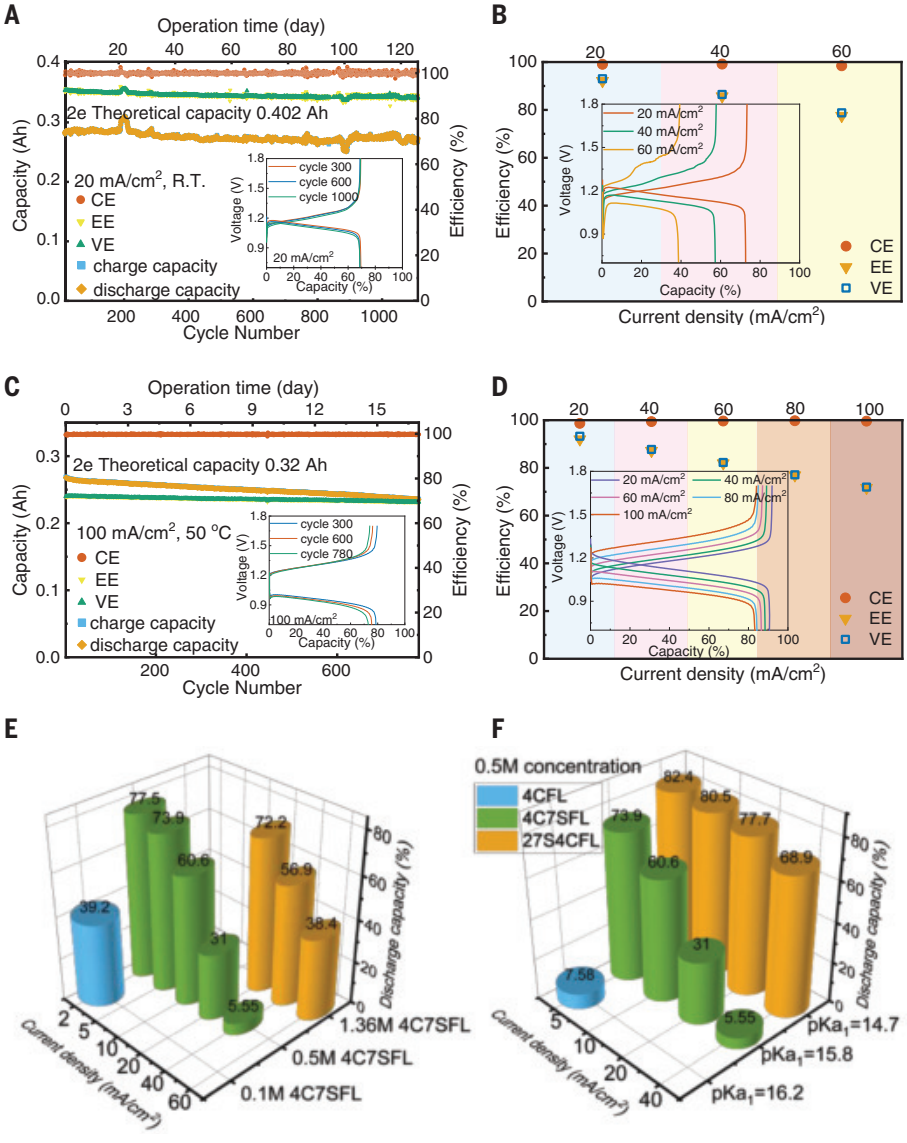


Fig. 3. High-concentration battery demonstration. (**A** and **B**) High-concentration battery demonstrated with 1.36 M 4C7SFL/1 equiv. NaOH anolyte cycled against an excess amount of ferro/ferricyanide catholyte. The detailed battery configuration is shown in the battery flow tests condition C in the materials and methods. (A) Battery operation across 120 days and polarization curve at selected cycles. (B) Efficiency and polarization curve at different current density. (**C** and **D**) High-concentration battery demonstrated with 1 M 4C7SFL/1 equiv. NaOH anolyte cycled against an excess amount of ferro/ferricyanide catholyte at 50°C outside of a glovebox. The detailed battery configuration is shown in the battery flow tests condition D in the materials and methods. (C) Battery operation across 17 days and polarization curve at selected cycles. (D) Efficiency and polarization curve at various current densities. (**E** and **F**) Battery performance reflected by discharge capacity (adjusted to percentage of theoretical capacity) as a function of discharge current density. (E) Performance with variation of material concentration. (F) Performance with variation of hydroxy pK_a.

cycling and 50% of discharge capacity point at ~1.10 V. As shown in Fig. 3A, the polarization curves of cycle 300 (day 35), 600 (day 69), and 1000 (day 113) reveal nearly identical operational discharge capacity, with most capacity loss observed during initial cycles. There is a net 2.62% observed capacity fade over 4 months of operation (calculated on the basis of cycle 17 and cycle 1111, equivalent to 0.0209%/day and 0.00239%/cycle). A detailed postcycling decomposition study using NMR and liquid chromatography–mass spectrometry suggested that only a minor amount of desulfonated product was formed (figs. S11 and S12). The average Coulombic efficiency (CE) is 99.96%, although a slight decrease of voltage efficiency (VE) was observed over extended cycling. As a result, the overall energy efficiency (EE) of the cell is ~90% for the majority of the cycles. The voltage profile and the efficiency data of the flow cell under various current densities are shown in Fig. 3B. In the range of 20 to 60 mA cm^{-2}, the material utilization percentage (calculation based on two-electron transfer) and VE/EE both decrease with increasing current density; at a current density of 20 mA cm^{-2} the utilization percentage was 72.2%, the VE was 93.0% and the EE was 92.1%, whereas at 60 mA cm^{-2} they were at 38.4, 78.8, and 77.6%, respectively. Although the increasing current causes an increase in the polarization, differences in the equilibration rate between protonated and deprotonated species also contribute to the observed performance. Nevertheless, the modified 4C7SFL provides sufficient kinetics for reversible battery charge and discharge at a reasonable rate (Fig. 3B). Battery cyclical stability study was further conducted on a flow cell using 1 M 4C7SFL with potentiostatic holds every 50 cycles (fig. S13A) (*1*). The stable cycling performance, combined with postcycling NMR analysis (fig. S13, B and C), as well as ex situ ^{1}H-NMR stability studies (fig. S14), provides evidence that FLs in their oxidized and reduced forms are stable (*29*).

In practical applications of RFBs, tolerance to fluctuations in operating temperature arising from ambient input and efficiency losses during operation is critical. For aqueous organic RFBs, although higher temperature may increase the solubility and lower the viscosity to improve the kinetics, it presents a threat to the stability of the organic active materials. For the same reason, flow battery tests of organic-based electrolytes reported so far are mostly conducted in an inert atmosphere, which is a substantial hurdle for large-scale deployment. We subjected another 1 M 4C7SFL/1 equiv. NaOH (equivalent to 2 M electron transfer) anolyte to electrochemical cycling at 50°C outside of a purge box (the detailed battery test condition is shown in the supplementary materials). Current density test was performed in the initial 25 cycles, detailed

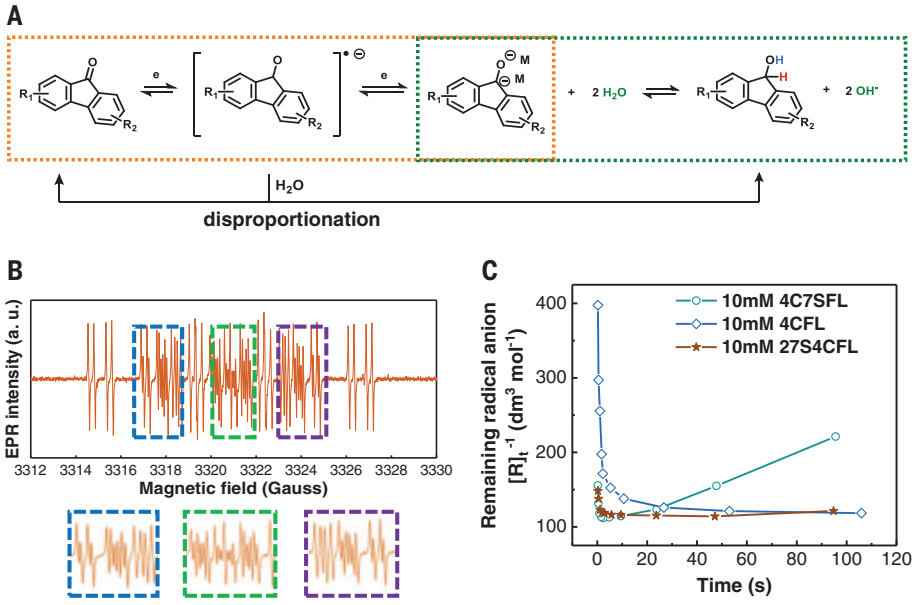


Fig. 4. Proposed mechanism, DFT calculation, and experimental data. (**A**) Proposed mechanism. Orange box: charging process with disproportionation involved; green box: proposed acid–base chemistry of fluorenol/fluorenolate. M = Na^{+} or K^{+}. (**B**) EPR detection for radical intermediate **2** with magnified views. The 64-splitting pattern observed in the spectrum is consistent with the compound structure, which has six different protons near the radical center. (**C**) 1/[radical anion]$_t$ versus *t* plot was generated to probe the complex reaction of the electrochemically generated radical anion. The data-processing procedure is described in detail in the supplementary materials. Reactions were probed at 10 mM 4CFL, 4C7SFL, and 27S4CFL, a subset of derivatives selected to represent the increase in the electron withdrawing-substitution effect on the aromatic ring.

cycling data for the first 30 cycles are provided in fig. S9B (Fig. 3C). A stable cycling was achieved throughout more than 700 cycles at 100 mA cm^{-2} with an average CE of 99.8%, VE of 70.8%, and EE of 70.6%. Slight capacity decay was observed as cycling proceeded, with capacity retention of 87.8% over 780 cycles (99.98% per cycle over 16 days of cycling) at 100 mA cm^{-2} and 50°C. Detailed postcycling analysis suggested that only a minor amount of desulfonated product was formed (figs. S15 and S16). Capacity decay is mainly attributed to the accelerated crossover at increased temperature, which was confirmed by NMR (fig. S15). The modified 4C7SFL also demonstrated substantially improved rate capability at increased temperature. The voltage profile and the efficiency data of the flow cell under various current densities are shown in Fig. 3D. At 50°C, the flow cell was able to cycle at 100 mA cm^{-2} with a material utilization of 83.7%, which is much higher than the cycling rate performance at room temperature.

Battery performance of FL derivatives at various concentrations and substitution patterns was investigated regarding the "observed reversibility" through discharge capacity as a function of discharge current density (Fig. 3, E and F). 4C7SFL demonstrated a concentration-dependent reversibility, as shown in Fig. 3E. This behavior is not typical in traditional RFB chemistries; however, it does support our hypothesis that a sufficient amount of deprotonated anionic species is needed to enable the battery discharge at a sufficiently low potential. The EWG effect is shown in Fig. 3F. As expected, with stronger EWGs, improved reversibility is observed, which also validates the design that stronger EWGs shift the pK_a more toward the generation of the deprotonated fluorenolate that supports the discharge process. Rotating disk electrode experiments (figs. S17 to 19 and table S4) showed a decrease in diffusion coefficient and kinetic reduction rate constant with increasing EWG functionalization. The kinetic properties, however, are advantageous compared with the cathode side of the vanadium flow batteries.

NMR aliquots (fig. S20) were taken during the charging process to identify possible intermediates formed (*15*, *17*). Within the NMR detection limit, no pinacol-type dimers could be confirmed. However, FL-OH was observed as the charged product even at a state of charge as low as 25% (fig. S20A, trace a), indicating the disproportionation of the charged radical anion species (*17*). Both ex situ EPR analysis of the battery electrolyte at various concentrations (0.1, 0.5, and 1 M) of 4C7SFL (Fig. 4B and fig. S21) and in situ H-cell EPR detection (fig. S22) further confirmed that disproportionation occurs during the charging process. Moreover, the comproportionation reaction is confirmed by the EPR study presented in fig. S4, in which

radical anions are detected in the chemically synthesized FL/FL-OH mixture in alkaline solution. Through synthesis of our test results and related prior studies, a possible reaction mechanism depicted in Fig. 4A (*16*, *17*, *25*, *26*) thus entails the electrochemical reduction–oxidation and accompanying disproportionation–comproportionation chemical reactions in the charge–discharge process. During the charge process, FL molecules are electrochemically reduced to radical anions, which then are chemically consumed through disproportionation to form FL and FL-OH. By contrast, the radical anions are electrochemically oxidized to FL during the discharge process while being chemically produced via comproportionation reaction. Aspects of the proposed mechanism have been confirmed by the NMR and EPR analyses discussed above, although more in-depth studies are warranted to elucidate the overall process.

Unlike an exclusively electrochemical redox reaction, the disproportionation–comproportionation chemical reactions may become the rate-limiting step. The competition between the electrochemical and chemical reactions largely explains the lower utilization at lower concentration, higher current density, and lower temperature illustrated in Fig. 3E and fig. S23, respectively, and the single plateau observed in the polarization curves of both battery cycling (Fig. 3, B and D) and H-cell tests with a reference electrode (fig. S24). At a much lower concentration (10 mM, figs. S5 and S6), two separate reduction events are observed in CV, suggesting that the electrochemical process is dominant. To investigate the disproportionation of generated radical species, we generated a plot of 1/[radical anion]$_t$ versus t (*30*) (Fig. 4C) on three FL derivatives with varying EWG strengths from their CVs. A V-shaped curve indicated a complicated mechanism instead of a simple second-order disproportionation of radical anion (*17*). The concentration effect on the disproportionation reaction is presented in figs. S25 and S26. By varying the functional group, a variation in the disproportionation reaction between different functionalized FL can be expected (*16*, *17*). Figure 4C shows that 4C7SFL has the fastest disproportionation reaction, represented by the fastest increase on the right portion of the curve, compared with 4CFL and 27S4CFL (*30*) (fig. S27).

We have demonstrated here the ability to pursue and exploit accelerated redox reactions enabled by molecular engineering of materials that would otherwise be unsuitable for flow batteries. These results suggest the potential for identifying other atypical organic redox molecules for energy storage.

REFERENCES AND NOTES

1. D. G. Kwabi, Y. Ji, M. J. Aziz, *Chem. Rev.* **120**, 6467–6489 (2020).
2. Y. Ding, C. Zhang, L. Zhang, Y. Zhou, G. Yu, *Chem. Soc. Rev.* **47**, 69–103 (2018).
3. M. Park, J. Ryu, W. Wang, J. Cho, *Nat. Rev. Mater.* **2**, 16080 (2016).
4. X. Zu, L. Zhang, Y. Qian, C. Zhang, G. Yu, *Angew. Chem. Int. Ed.* **59**, 22163–22170 (2020).
5. A. Hollas *et al.*, *Nat. Energy* **3**, 508–514 (2018).
6. T. Liu, X. Wei, Z. Nie, V. Sprenkle, W. Wang, *Adv. Energy Mater.* **6**, 1501449 (2016).
7. K. Lin *et al.*, *Science* **349**, 1529–1532 (2015).
8. D. C. Cantu *et al.*, *ACS Catal.* **8**, 7645–7658 (2018).
9. R. Kato *et al.*, *Nat. Commun.* **7**, 13032 (2016).
10. N. Weinberg, H. Weinberg, *Chem. Rev.* **68**, 449–523 (1968).
11. C. Bianchini, P. K. Shen, *Chem. Rev.* **109**, 4183–4206 (2009).
12. J. Rodriguez Jr., C. Niemet, L. D. Pozzo, *ECS Trans.* **89**, 49–59 (2019).
13. P. Leung *et al.*, *Appl. Energy* **197**, 318–326 (2017).
14. X. Xing, Q. Liu, B. Wang, J. P. Lemmon, W. Q. Xu, *J. Power Sources* **445**, 227330 (2020).
15. X. Wei *et al.*, *Angew. Chem. Int. Ed.* **54**, 8684–8687 (2015).
16. L. Nadjo, J. Saveant, *J. Electroanal. Chem. Interfacial Electrochem.* **33**, 419–451 (1971).
17. M. K. Kalinowski, Z. R. Grabowski, *J. Chem. Soc., Faraday Trans.* **62**, 926–934 (1966).
18. A. Shrestha, K. H. Hendriks, M. S. Sigman, S. D. Minteer, M. S. Sanford, *Chemistry* **26**, 5369–5373 (2020).
19. J. B. Gerken *et al.*, *Adv. Energy Mater.* **10**, 2000340 (2020).
20. F. Wang, S. S. Stahl, *Acc. Chem. Res.* **53**, 561–574 (2020).
21. X. Zhang *et al.*, *ChemPlusChem* **78**, 703–711 (2013).
22. B. Ariche, A. Rahmouni, *Can. J. Chem.* **96**, 1001–1009 (2018).
23. W. S. Matthews *et al.*, *J. Am. Chem. Soc.* **97**, 7006–7014 (1975).
24. E. C. Meister, M. Willeke, W. Angst, A. Togni, P. Walde, *Helv. Chim. Acta* **97**, 1–31 (2014).
25. M. Hirayama, H. Suzuki, H. Ohhata, *Chem. Lett.* **16**, 413–416 (1987).
26. A. S. Mendkovich, M. A. Syroeshkin, M. N. Mikhailov, D. V. Ranchina, A. I. Rusakov, *Russ. Chem. Bull.* **62**, 1668–1670 (2014).
27. K. S. Han *et al.*, *J. Phys. Chem. C* **120**, 27834–27839 (2016).
28. J. Luo *et al.*, *Nano Energy* **42**, 215–221 (2017).
29. M. Kamaura, J. Inanaga, *Tetrahedron Lett.* **40**, 7347–7350 (1999).
30. D. P. Hickey *et al.*, *J. Am. Chem. Soc.* **141**, 1382–1392 (2019).

ACKNOWLEDGMENTS

We acknowledge financial support primarily from the US Department of Energy (DOE) Office of Electricity through its Energy Storage Program at Pacific Northwest National Laboratory (PNNL) under Contract no. 57558 and support from Energy Storage Materials Initiative (ESMI), which is a Laboratory Directed Research and Development Project at PNNL, on the FL derivative asymmetric structure design. K.M.R. acknowledges support from the US DOE Office of Science, Office of Basic Energy Sciences, Chemical Sciences, Geosciences, and Biosciences Division, through its Geosciences program at PNNL. The mass spectrometry measurements, NMR measurements, and theoretical calculations were performed at the William R. Wiley Environmental Molecular Sciences Laboratory, a national scientific user facility sponsored by the US DOE's Office of Biological and Environmental Research and located at PNNL. We thank S. Burton and V. Lin for NMR instruments assistance, K. Duanmu and S. Hammes-Schiffer (Yale University) for DFT discussion, R. Chu for performing mass spectrometry analysis, and F. Thomas for performing LC-MS analysis. **Funding:** This work was supported by the US Department of Energy Office of Electricity under Contract no. 57558 and PNNL Laboratory Directed Research and Development project Energy Storage Materials Initiative. **Author contributions:** X.Z. and W.W. conceived the research. R.F., X.Z., and W.W. designed the experiments. R.F. performed the organic synthesis and electrochemical test with assistance from A.H., Y.S., N.W., E. W., and L.Y. V.M. performed DFT calculations. Y.C. performed EPR. All authors discussed the results. V.M., A.H., Y.S., and K.M.R. revised the manuscript. R.F., X.Z., and W.W. wrote the paper with input from all authors. **Competing interests:** The authors declare no competing interests. A patent application titled "Fluorenone/Fluorenol Derivatives for Aqueous Redox Flow Batteries" has been filed through Pacific Northwest National Laboratory (US patent application 17/097,715) **Data and materials availability:** All data are available in the main text or the supplementary materials.

SUPPLEMENTARY MATERIALS

science.sciencemag.org/content/372/6544/836/suppl/DC1
Materials and Methods
Supplementary Text
Tables S1 to S4
Figs. S1 to S27
NMR Spectra
References (*31*–*44*)

23 July 2020; resubmitted 14 January 2021
Accepted 18 March 2021
10.1126/science.abd9795

TRANSLATION

Imaging translation dynamics in live embryos reveals spatial heterogeneities

Jeremy Dufourt[1]*†, Maelle Bellec[1]†, Antonio Trullo[1], Matthieu Dejean[1], Sylvain De Rossi[2], Cyril Favard[3], Mounia Lagha[1]*

Much is known about the factors involved in the translation of messenger RNA (mRNA) into protein; however, this multistep process has not been imaged in living multicellular organisms. Here, we deploy the SunTag method to visualize and quantify the timing, location, and kinetics of the translation of single mRNAs in living *Drosophila* embryos. By focusing on the translation of the conserved major epithelial-mesenchymal transition–inducing transcription factor Twist, we identify spatial heterogeneity in mRNA translation efficiency and reveal the existence of translation factories, where clustered mRNAs are cotranslated preferentially at basal perinuclear regions. Observing the location and dynamics of mRNA translation in a living multicellular organism opens avenues for understanding gene regulation during development.

More than 60 years ago, it was established that mRNA is translated to make protein. However, studies have revealed that the level of a given mRNA and the amount of protein it encodes do not directly correlate (*1*). This lack of colinearity may partially result from differential translational regulation in subcellular compartments where mRNAs are targeted (*2*, *3*). To quantitate and compare mRNA and nascent protein, methods are needed to visualize these molecules in vivo. Live imaging of mRNA has been possible since 1998 (*4*), but a similar method to image many cycles of translation was only established in 2016 in cultured cells (*5*–*9*) and has yet to be established in an intact developing organism. With its rapid development and the simple arrangement of

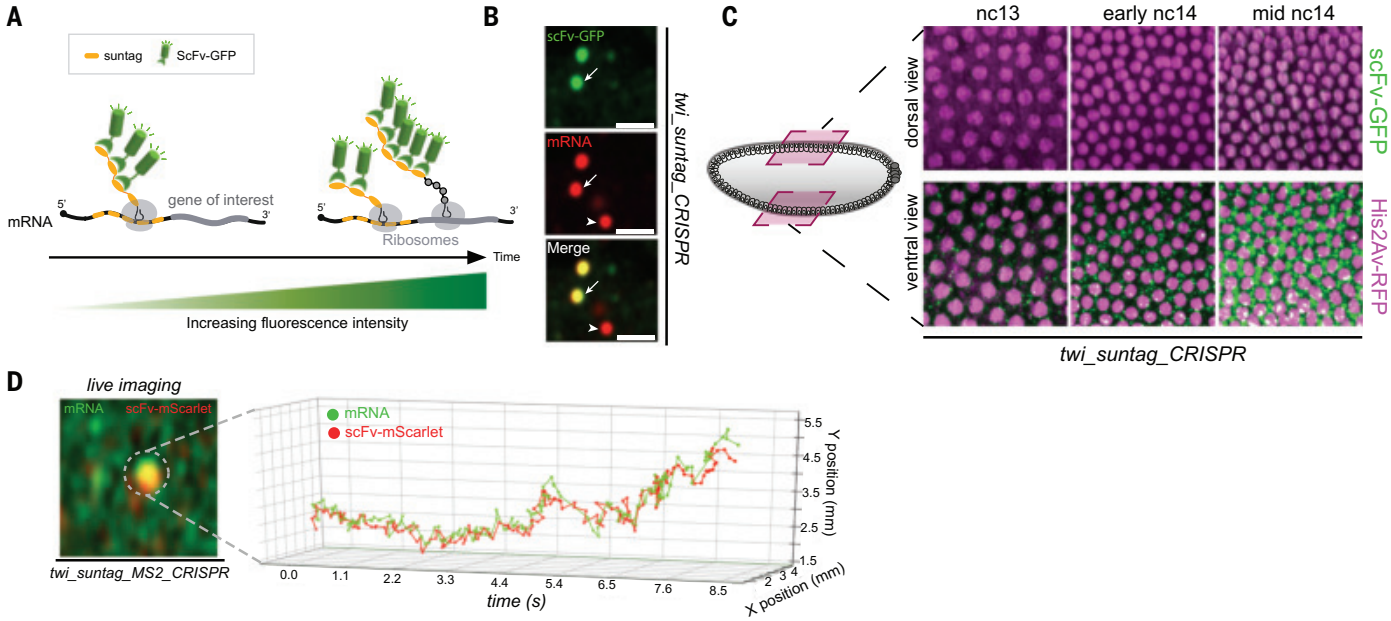


Fig. 1. Imaging translation of mRNAs in *Drosophila* embryos. (**A**) Principle of the SunTag system. Repetitions of suntag epitopes are added to the protein of interest and are detected with a single-chain antibody (scFv) fused to GFP. (**B**) Zoomed-in confocal images of n.c.14 *twi_suntag_CRISPR Drosophila* embryos expressing scFv-GFP (green) stained with suntag probes (red), exhibiting two groups of mRNA molecules: colocalizing with scFv-GFP signal (arrows) and not colocalizing with a GFP signal (arrowheads). Scale bars, 1 μm. (**C**) Live imaging of a *His2Av-mRFP/+;scFv-GFP-NLS/+>twi_suntag_CRISPR/+* embryo by MuViSPIM (multiview selective plane illumination microscope) (images from movie S1). (**D**) Spatiotemporal tracking of mRNA and translation signal from an *MCP-eGFP/+; scFv-mScarlet-NLS/+>twi_suntag_MS2_CRISPR/+* embryo (image from movie S3).

nuclei in the syncytial blastoderm stage, the *Drosophila melanogaster* embryo represents a model organism to image gene expression.

To visualize translation using a reporter transgene, we used the SunTag system, whereby repetitions of an epitope (named suntag) are added to the protein of interest and are detected with a genetically encoded single-chain antibody (called scFv) fused to a fluorescent protein (*10*) (Fig. 1A). To implement the SunTag method in *Drosophila* embryos, we focused on the gene *twist*, which encodes a conserved transcriptional activator of the mesodermal program in metazoans (*11*). In *Drosophila* early embryos, this gene is expressed during the activation of the zygotic genome in a specific ventral domain. We created a *twi_suntag* transgene (fig. S1F and supplementary text) that enables the labeling of Twi protein with 32 suntag repeats. Additionally, we created scFv-fluorescent lines to detect suntag peptides (fig. S1, A to E; movie S8; and supplementary text). In the presence of the *twi_suntag* transgene and scFv–green fluorescent protein (GFP) detector protein, distinct spots were detected within the presumptive mesoderm of living embryos (figs. S1 and S2, movie S9, and supplementary text). However, *twi_suntag* expression appeared stochastically in this domain (fig. S1G; fig. S2, B, E, and F; and supplementary text).

Having demonstrated our ability to observe translation with a reporter transgene, we then monitored *twi* translational dynamics from its endogenous locus with a *twi_suntag*_CRISPR allele (fig. S3, A and B). By performing single-molecule mRNA labeling [single-molecule fluorescence in situ hybridization (smFISH)] with the simultaneous detection of native scFv-GFP, we could detect two populations of cytoplasmic mRNA molecules: (i) those colocalizing with a bright GFP signal—i.e., 69 ± 3% in nuclear cycle 14 (n.c.14) (n = 5 embryos)—presumably corresponding to mRNAs being translated and (ii) those devoid of a GFP signal (Fig. 1B). Next, we questioned whether these bright scFv foci could be detected in living embryos with light sheet microscopy, and we found that *twi* translation was strongly induced during n.c.14 (Fig. 1C and movie S1) and was specific to the mesoderm. Bright but rare scFv-GFP foci appeared as early as n.c.12 and persisted during mitoses (fig. S3C).

To determine whether scFv-GFP spots correspond to nascent sites of translation, we imaged *twi_suntag_CRISPR* embryos injected with puromycin, a translation inhibitor. We did not observe scFv-GFP spots close to the injection site (fig. S3D and movie S10C). To observe nascent translation of single mRNA particles in live embryos, we engineered a *twi_suntag_MS2_CRISPR* and combined a *scFv-mScarlet* with an *MCP-GFP* transgenic line (fig. S4 and supplementary text). For this dual cytoplasmic imaging, single mRNA molecules are labeled with an MS2 array, visualized using the coat protein of bacteriophage MS2 (MCP) fused to GFP (*12*), while nascent proteins are labeled with the suntag peptides, recognized by the scFV antibody fused to mScarlet. Confocal imaging revealed distinct molecules of cytoplasmic mRNAs with, in some cases, a red scFv-mScarlet signal on top (fig. S4G and movie S2). This dual-color live imaging confirms the existence of two mRNA pools, with a subset of *twi* mRNA undergoing translation. It further shows that these mRNA and nascent proteins move together (Fig. 1D and movie S3), revealing that mRNAs in translation are not static.

By combining SunTag and MS2 labeling, it is possible to image transcription and translation and quantify their degree of correlation. In the case of *twi*, the timing of translation is consistent with its mRNA production (fig. S5A). Live imaging of the *twi_suntag_MS2_CRISPR* reveals that transcription peaks in n.c.13 (Fig. 2, A and B) (*13*). Thus, the largest wave of mRNA production precedes the timing of the largest burst of *twi* translation (Fig. 2,

[1]Institut de Génétique Moléculaire de Montpellier, University of Montpellier, CNRS-UMR 5535, Montpellier 34293 cedex 5, France. [2]MRI, BioCampus Montpellier, CNRS, INSERM, University of Montpellier, Montpellier, France. [3]Institut de Recherche en Infectiologie de Montpellier, CNRS UMR 9004, University of Montpellier, Montpellier 34293 cedex 5, France.
***Corresponding author. Email: jeremy.dufourt@igmm.cnrs.fr (J.D.); mounia.lagha@igmm.cnrs.fr (M.L.)**
†These authors contributed equally to this work.

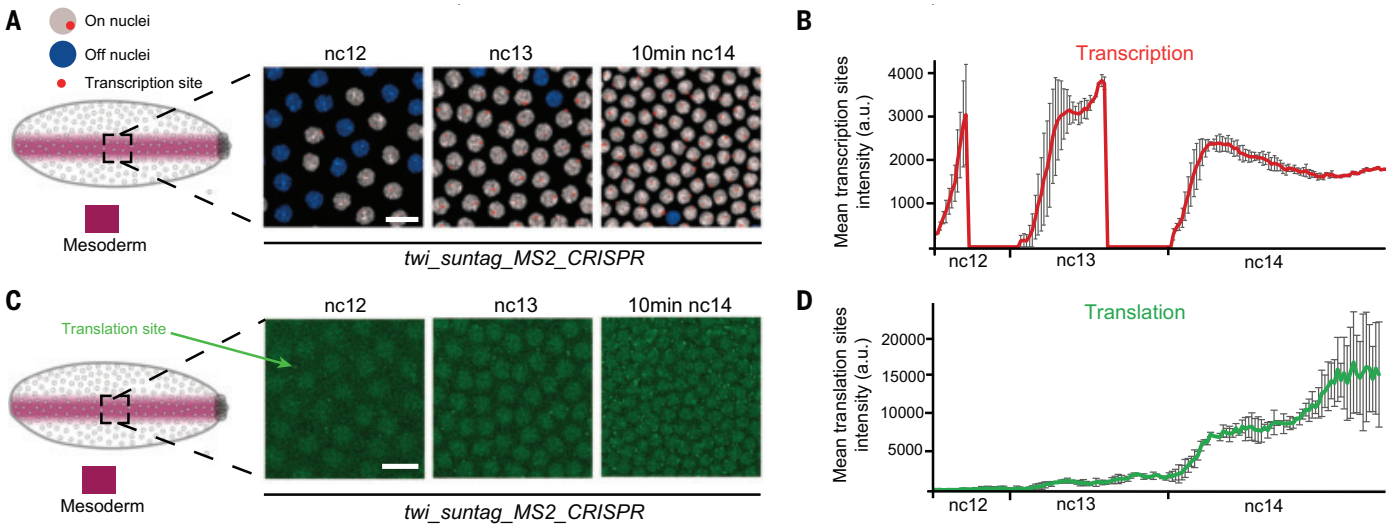


Fig. 2. Dynamics of transcription and translation. (**A** and **B**) Live imaging of an *MCP-eGFP-His2Av-mRFP>twi_suntag_MS2_CRISPR/+* embryo showing transcription sites (TSs) in red (A) and quantification of TS intensities (B) (n = 2 movies). Scale bar, 10 μm. a.u., arbitrary units. (**C** and **D**) Live imaging of a *scFv-GFP/+ >twi_suntag_MS2_CRISPR/+* embryo (C) and quantification of translation site intensities over time (D) (n = 2 movies). Scale bar, 10 μm.

C and D; fig. S4D; and movies S1 and S12A). Further, the timing of *twi* translation is consistent with the timing of nuclear Twi protein emergence (fig. S5B).

To gain more insight into the dynamics of *twi* translation, we used the SunTag method to reveal translation kinetics (*5*, *7*–*9*). We determined that Suntag-Twi fusion protein was fully translated (fig. S5C). Then, by correlating temporal intensity fluctuations of single spot scFv-GFP (*5*, *7*–*9*), elongation and initiation rates were estimated to be in the order of 35 amino acids per second and 13 s, respectively (fig. S5, D to H). These rates are probably upper estimates and do not reflect the variability between mRNAs. Nonetheless, these rates lead to an overall translation efficiency of seven ribosomes per mRNA (fig. S5I), consistent with ribosome profiling experiments (*14*). Collectively these data suggest that the relatively late timing of *twist* translational activation could be partly compensated by its fast translation kinetics.

Using a transverse view of a developing embryo, the sites of translation in n.c.14 appeared much more prominent in the basal perinuclear region (i.e., toward the interior of the embryo), although translation was also observed in the apical perinuclear space (Fig. 3A, fig. S6A, and movies S4 and S12B). To further investigate this apparent spatial bias, we quantified the scFv-GFP signal in these two compartments (fig. S6, B and C, and fig. S7). In contrast to earlier developmental stages—where translation is equivalent in the apical and basal cytoplasmic spaces—in n.c.14, the largest and brightest spots of *twi* translation appeared mainly in the basal cytoplasm. To estimate translation efficiency, we extracted the intensity of the scFv-GFP signal overlapping individual

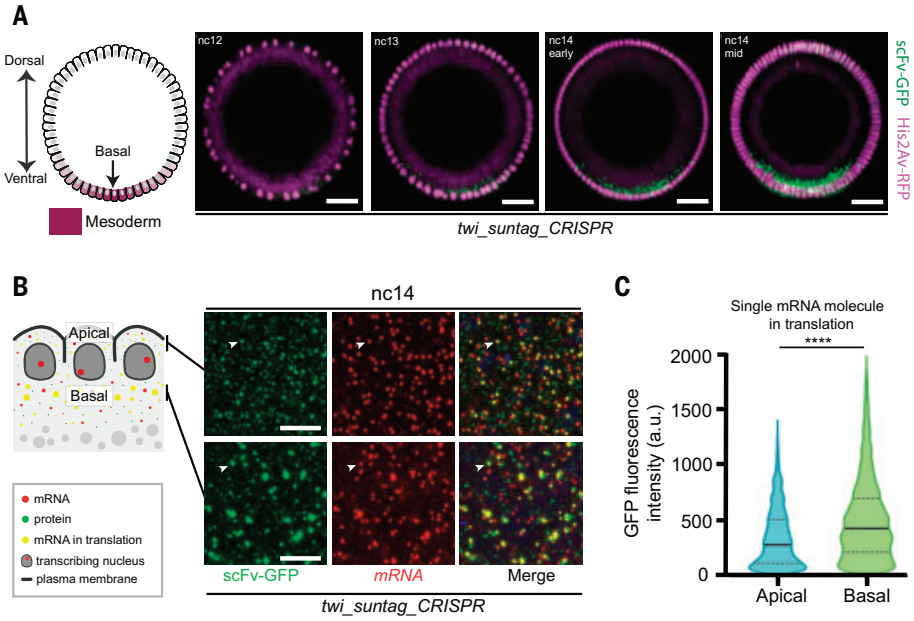


Fig. 3. Spatial heterogeneity of translation. (**A**) Live imaging of a *His2Av-mRFP/+;scFv-GFP-NLS/+ >twi_suntag_CRISPR/+* embryo (MuviSpim cross section) (images from movie S4). Scale bars, 30 μm. (**B** and **C**) Representative confocal image (apical and basal *z*-stacks shown separately) of an *scFv-GFP-NLS/+ >twi_suntag_CRISPR/+* embryo expressing scFv-GFP (green) labeled with suntag probes (red) (scale bars, 5 μm) (B) and quantification shown as a violin plot of the distribution of scFv-GFP intensities colocalizing with single mRNA molecules located apically (n = 2380; blue) and basally (n = 4202; green) (C). Two-tailed Welch's t test; ****P < 0.0001.

mRNA molecules (see materials and methods). We found that in the basal perinuclear space, a single molecule of mRNA is on average 50% more intense in the scFv-GFP channel than a single molecule located apically, which suggests an enhanced efficiency of translation (Fig. 3, B and C). This bias is also observed with *twi_suntag* transgene (fig. S6, D and E). Collectively, these data demonstrate that translation efficiency of identical mRNA molecules depends on their subcellular localization. This spatial heterogeneity does not seem to rely on a differential distribution of ribosomes and might be supported by a higher basal availability of mitochondria (fig. S6, F and G, and movie S5).

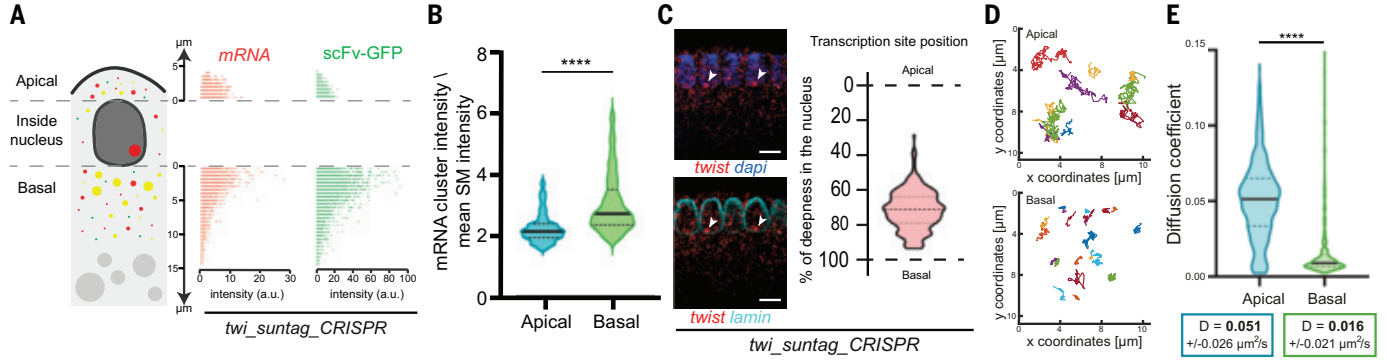


Fig. 4. Local translation of *twi* mRNA. (**A**) Intensity quantification of *scFv-GFP-NLS/+>twi_suntag_CRISPR/+* embryos labeled with suntag probes showing mRNA spots (red) and scFv-GFP spots (green) in 0.5-µm-spaced Z-planes of four n.c.14 embryos. (**B**) Distribution of the intensity of mRNA clusters in apical (n = 523; blue) and basal (n = 1384; green), normalized by the mean intensity of a single mRNA molecule. Two-tailed Welch's t test; ****P < 0.0001. (**C**) Sagittal views of *twi_suntag_CRISPR/+* embryos labeled with *suntag* probes, anti-lamin, and 4′,6-diamidino-2-phenylindole (DAPI) (scale bars, 5 µm) and corresponding quantification of TS positions along the apico-basal nuclear axis. (**D** and **E**) Single-particle tracking on *scFv-GFP-NLS/+>twi_suntag_CRISPR/+* embryos. (D) Examples of color-coded translation foci trajectories. (E) Violin plots of the estimated diffusion coefficient distributions of apical and basal particles. Two-tailed Welch's t test; ****P < 0.0001.

Live imaging data revealed the existence of large scFv-GFP foci predominantly present in the basal cytoplasm. Simultaneous detection of mRNA and translation foci shows that these large size translation foci overlap large mRNA foci (Fig. 3B and fig. S6D). To better characterize these large foci, we quantified mRNA densities and scFv-GFP signal. Although mRNA molecules were present along the entire depth of a cell volume, their intensity was clearly enhanced at the level of the basal perinuclear space (Fig. 4A), where they tend to assemble in clusters (fig. S8, A and B). These mRNA clusters were of varying sizes and were larger in the basal perinuclear cytoplasm (Fig. 4, A and B, and fig. S8, B and C). In total, 94 ± 3% of these mRNA clusters were engaged in translation (n = 4 embryos). Thus, we consider them as translation factories, echoing what has been shown in mammalian cells (*7*, *15*, *16*). Similar translation factories are observed with an *ilp4-suntag* transgenic reporter (fig. S9 and supplementary text).

Twi translation factories are distinct from germ plasm granules and processing bodies (P-bodies) (fig. S10, A and B, and movie S15). Clustering of *twi* mRNA in the basal cytoplasm is also observed in wild-type as well as in *twi* hemizygous embryos, albeit with a reduced frequency, which suggests that clustering partly depends on mRNA concentration (fig. S8D). Basal mRNA clustering is also detected for other mRNAs (fig. S11A). However, clustering of mRNAs is not a specific feature of the basal cytoplasm, as it is also observed apically (fig. S11, B and C) and largely documented for pair-rule genes (*17*, *18*).

The site of *twi* mRNA major clustering might be, in part, dictated by the localization of its site of transcription (Fig. 4C; fig. S12, A and B; and movie S6). A preferential export of mRNA toward the basal cytoplasm would favor basal *twi* mRNA clustering, which would be rapidly cotranslated in factories. In the case of a nuclear protein like Twi, its translation in factories nearby the nuclear periphery could favor rapid nuclear import of newly formed proteins, as suggested by Twi protein stainings (fig. S12C).

twi translation occurs before complete cellularization. Consequently, its messenger ribonucleoproteins (mRNPs) could theoretically diffuse between neighboring pseudocells. To gain insight into *twi* mRNP mobilities, we tracked *twi_suntag_CRISPR* mRNPs in different cytoplasmic locations (Fig. 4D and movie S7). The trajectories and the mean square displacement (MSD) revealed clear, distinct properties of apical versus basal particles (fig. S13 and supplementary text). For example, the diffusion coefficient of mRNPs is one-third as fast in the basal compartment compared with the apical (Fig. 4E). The sublinear growth of the MSD curves suggests subdiffusive behavior in both compartments (fig. S11, C to G). Thus, we conclude that, in the basal perinuclear cytoplasm, *twi* translation sites diffuse slower because of their larger size.

By focusing on *twi* mRNAs as a paradigm for transcription factor encoding transcripts, we have uncovered fundamental features of translation in a living organism such as heterogeneity in translation efficiencies of identical mRNAs and the existence of translation factories. Local translation of multiple mRNAs could have several benefits. First, it could favor the assembly of newly synthesized proteins in complexes. This is potentially the case for Twi, known to homodimerize (*19*). Second, localized protein synthesis could favor fast delivery of newly formed proteins to their destinations. Correlation between mRNA localization and protein function is well documented (*2*). The SunTag method now allows us to bridge the gap between mRNA and protein localization. In the case of *twi*, we propose that local and enhanced translation close to the nuclear envelope favor rapid nuclear import of neosynthesized Twi protein. This might be generalizable to other transcription factors, as proposed for pair-rule proteins (*18*).

Finally, the clustering of mRNAs and their cotranslation restricts the diffusion capacities of mRNPs. In the context of a syncytial embryo, this property could be exploited to limit the diffusion and allow spatial precision in cell fate decisions. As cellularization proceeds with an apico-basal directionality, apical anchoring of mRNAs represents an optimal strategy to limit diffusion. However, translation dynamics of these apical mRNAs remain to be demonstrated. In contrast, for mRNAs located basally in a compartment, where short-range diffusion lasts for a relatively long period of time, we propose that clustering and rapid local translation restrict the diffusion capacities of mRNPs. Thus, precision in the establishment of developmental patterns cannot only be attributed to precision in transcriptional activation. We anticipate that our approaches will pave the way to investigating previously inaccessible translation modalities during development and differentiation.

REFERENCES AND NOTES

1. K. Becker *et al.*, *Nat. Commun.* **9**, 4970 (2018).
2. E. Lécuyer *et al.*, *Cell* **131**, 174–187 (2007).
3. A. Chin, E. Lécuyer, *Biochim. Biophys. Acta Gen. Subj.* **1861**, 2956–2970 (2017).
4. E. Bertrand *et al.*, *Mol. Cell* **2**, 437–445 (1998).
5. X. Yan, T. A. Hoek, R. D. Vale, M. E. Tanenbaum, *Cell* **165**, 976–989 (2016).
6. T. Morisaki *et al.*, *Science* **352**, 1425–1429 (2016).
7. X. Pichon *et al.*, *J. Cell Biol.* **214**, 769–781 (2016).
8. B. Wu, C. Eliscovich, Y. J. Yoon, R. H. Singer, *Science* **352**, 1430–1435 (2016).
9. C. Wang, B. Han, R. Zhou, X. Zhuang, *Cell* **165**, 990–1001 (2016).
10. M. E. Tanenbaum, L. A. Gilbert, L. S. Qi, J. S. Weissman, R. D. Vale, *Cell* **159**, 635–646 (2014).
11. T. Sandmann *et al.*, *Genes Dev.* **21**, 436–449 (2007).
12. K. Tantale *et al.*, *Nat. Commun.* **7**, 12248 (2016).
13. J. E. Sandler, A. Stathopoulos, *Genetics* **202**, 1575–1584 (2016).
14. S. W. Eichhorn *et al.*, *eLife* **5**, e16955 (2016).

15. L. Chang, Y. Shav-Tal, T. Trcek, R. H. Singer, R. D. Goldman, *J. Cell Biol.* **172**, 747–758 (2006).
16. R. Chouaib *et al.*, *Dev. Cell* **54**, 773–791.e5 (2020).
17. I. Davis, D. Ish-Horowicz, *Cell* **67**, 927–940 (1991).
18. S. L. Bullock *et al.*, *Development* **131**, 4251–4261 (2004).
19. I. Castanon, S. Von Stetina, J. Kass, M. K. Baylies, *Development* **128**, 3145–3159 (2001).

ACKNOWLEDGMENTS

We are grateful to E. Bertrand, R. Zinzen, I. Izzedin, P. Lasko, T. Hurd, and X. Pichon for sharing flies, reagents, and software. We thank C. Desplan, J. Chubb, R. Bordonne, F. Besse, T. E. Saunders, J. Dejardin, and V. L. Pimmett, for their critical reading of the manuscript. We acknowledge L. Bellec, H. Lenden, and M. Goussard for technical assistance. We acknowledge the Montpellier Ressources Imagerie facility (France-BioImaging). **Funding:** M.B. is a recipient of an FRM fellowship. This work was supported by the ERC SyncDev starting grant and a HFSP-CDA grant to M.L. M.L., J.D., and C.F. are sponsored by CNRS. S.D.R. is sponsored by INSERM. **Author contributions:** M.L. conceived the project. M.L. and J.D. designed the experiments. J.D., M.B., and M.D. performed experiments. A.T. developed software. C.F., M.B., and J.D. performed kinetic analysis. S.D.R. and J.D. performed MuViSPIM imaging. J.D., M.L., A.T., M.B., and C.F. analyzed the data. J.D., M.L., and M.B. interpreted the results. M.B. created artwork. M.L. wrote the manuscript with help from J.D. and M.B. All authors discussed, approved, and reviewed the manuscript. **Competing interests:** The authors declare that they have no competing interests. **Data and materials availability:** All data are available in the main text and/or the supplementary materials, and fly stocks will be deposited at Vienna Drosophila Resource Center.

SUPPLEMENTARY MATERIALS

science.sciencemag.org/content/372/6544/840/suppl/DC1
Materials and Methods
Supplementary Text
Supplementary Sequences
Figs. S1 to S14
Table S1
References (*20*–*37*)
MDAR Reproducibility Checklist
Movies S1 to S15

29 April 2020; accepted 13 April 2021
Published online 29 April 2021
10.1126/science.abc3483

QUANTUM GASES

Observation of superfluidity in a strongly correlated two-dimensional Fermi gas

Lennart Sobirey[1,2]*, Niclas Luick[1,2], Markus Bohlen[1,2,3], Hauke Biss[1,2], Henning Moritz[1,2], Thomas Lompe[1,2]

Understanding how strongly correlated two-dimensional (2D) systems can give rise to unconventional superconductivity with high critical temperatures is one of the major unsolved problems in condensed matter physics. Ultracold 2D Fermi gases have emerged as clean and controllable model systems to study the interplay of strong correlations and reduced dimensionality, but direct evidence of superfluidity in these systems has been missing. We demonstrate superfluidity in an ultracold 2D Fermi gas by moving a periodic potential through the system and observing no dissipation below a critical velocity v_c. We measure v_c as a function of interaction strength and find a maximum in the crossover regime between bosonic and fermionic superfluidity. Our measurements enable systematic studies of the influence of reduced dimensionality on fermionic superfluidity.

Reducing the dimensionality of a quantum system from three to two dimensions drastically modifies its physical properties. One notable difference is the increased role of fluctuations in low-dimensional systems, which prevents long-range phase coherence (*1*) and makes two dimensions the marginal number of dimensions for the existence of superfluidity (*2*). Hence it is quite surprising that all known ambient-pressure high–critical temperature (T_c) superconductors are layered quasi–two-dimensional (2D) materials with superconductivity occurring in the 2D layers, such as the copper-oxide layers in cuprates (*3*).

Over the past decade, ultracold 2D Fermi gases (*4*–*9*) have been established as a model system that can provide insight into the interplay of strong correlations and reduced dimensionality (*10*–*15*). Recent experiments have observed pair condensation (*16*), algebraically decaying correlations (*17*), and phase coherence (*18*) at low temperatures. However, although all of these results support the presence of a superfluid, a direct observation of superfluid flow has not yet been made.

In this work, we obtain definitive evidence for superfluidity in a 2D Fermi gas by probing its excitation spectrum and observing frictionless flow below a critical velocity v_c. We measure the critical velocity as a function of interaction strength and show that the 2D Fermi gas is superfluid throughout the crossover from deeply bound dimers to weakly bound Cooper pairs. We also study the temperature dependence of the critical velocity and observe the phase transition from the superfluid to the normal state at a critical temperature T_c.

For our experiments, we used a Fermi gas of $N \approx 6000$ ultracold ^{6}Li atoms in the lowest two hyperfine states, trapped in a box potential (*19*). The gas is tightly confined along the z direction with a level spacing $\hbar\omega_z \approx h \cdot 9.2$ kHz that is larger than the thermal energy $k_B T$ and the chemical potential of the gas, where $h = 2\pi\hbar$ is Planck's constant and k_B is the Boltzmann constant. Therefore, our system is in the quasi-2D regime (*20*). To show that the system is superfluid, we verified that it fulfills the Landau criterion (*21*–*26*), which states that the dispersion $\epsilon(p)$ of a superfluid does not allow for the creation of excitations at velocities smaller than a nonzero critical velocity $v_c = \min_p \left[\frac{\epsilon(p)}{p}\right]$. Thus, an impurity

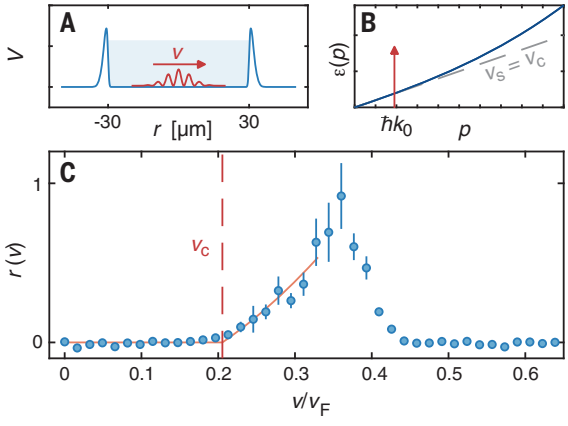


Fig. 1. Measuring the critical velocity of a 2D Fermi gas. (**A**) Sketch of the trapping potential. A 2D Fermi gas is trapped in a box potential (blue) projected through a high-resolution microscope objective. A periodic potential (red) can be moved through the gas at a variable velocity v. (**B**) Sketch of the Bogoliubov dispersion of a superfluid Bose gas. At small momentum transfer, excitations are phononic and the dispersion has a linear slope given by the speed of sound v_s, whereas for higher momentum transfers, single-particle excitations become dominant and the dispersion becomes quadratic. (**C**) Response $r(v)$ of a system at an interaction strength of $\ln(k_F a_{2D}) = -0.8$ to a moving optical lattice with wave vector $k_0 \approx 0.15 k_F$. No dissipation occurs at low lattice velocities, but there is a sharp increase in the response of the system above a critical velocity v_c. Note that the moving lattice probes the dispersion relation of the system along a vertical line, as visualized by the red arrow in (B). This results in a decrease of the response at high lattice velocities. The critical velocity is extracted by a fit (red solid line) to the expression $r(v) = A \max(0, v^2 - v_c^2)$ (*36*).

[1]Institut für Laserphysik, Universität Hamburg, Luruper Chaussee 149, 22761 Hamburg, Germany. [2]The Hamburg Centre for Ultrafast Imaging, Universität Hamburg, Luruper Chaussee 149, 22761 Hamburg, Germany. [3]Laboratoire Kastler Brossel, ENS-PSL Research University, CNRS, Sorbonne Université, Collège de France, 24 rue Lhomond, 75005 Paris, France.
*Corresponding author. Email: lsobirey@physnet.uni-hamburg.de

moving through a superfluid with a velocity $v < v_c$ creates no excitations, and the superfluid flows around it without friction. We created such an impurity by interfering two red-detuned laser beams in the center of the trap, resulting in a sinusoidal potential whose periodicity can be tuned by adjusting the crossing angle of the two beams. A frequency detuning Δv between the two laser beams causes this optical lattice to move at a constant speed $v = L\Delta v$, where L is the spacing between two maxima of the periodic potential.

To measure the critical velocity in our system, we moved the optical lattice through the gas at different velocities and observed the response of the system. To this end, we ramped the strength of the interatomic interaction to a value of $\ln(k_F a_{2D}) = -2.8$, where $k_F = \sqrt{4\pi n} = mv_F/\hbar$ is the Fermi wave vector of a gas with density n per spin state and Fermi velocity v_F, m is the mass of a ^{6}Li atom, and a_{2D} is the 2D scattering length (*27*). At this interaction strength, the system is deep in the Bose-Einstein condensation (BEC) regime, where the gas consists of weakly interacting dimers and it is straightforward to measure its momentum distribution $n(k)$ using matter wave focusing (*28*). As the occupation of the lowest momentum modes decreases with increasing temperature, we define the response $r(v) = [n(k = 0, v = 0)/n(k = 0, v)] - 1$ as a robust proxy for the energy deposited by the moving potential (*20*).

A typical measurement of the response of the system as a function of lattice velocity is shown in Fig. 1C. We observe that the gas is unaffected as the velocity of the optical lattice is increased until a critical velocity is reached and a sharp onset of dissipation occurs. In contrast to previous experiments (*22*–*25*), we observe that the response decreases again at higher velocities. This decrease is caused by the optical lattice transferring a specific momentum $\hbar k_0 = \hbar 2\pi/L$ to the superfluid, whereas the impurity in Landau's gedankenexperiment can excite the system at all momenta. Therefore, a moving optical lattice with varying velocity probes the dispersion relation of the gas on a vertical line of constant momentum $p = \hbar k_0$ (visualized in Fig. 1B).

We thus performed measurements at different spacings L of the periodic potential and thereby determined the response $r(v, k_0)$ as a function of both the lattice velocity v and the lattice wave vector k_0. In bosonic superfluids, the lowest velocity at which excitations can be created is found at small wave vectors. These long-wavelength excitations are phononic modes that are excited by an obstacle moving at a velocity close to the speed of sound of the system. In Bardeen-Cooper-Schrieffer (BCS) superfluids, phononic excitations at low k_0 can still be created, but the lowest onset velocity is found at $k_0 \approx 2k_F$. This is a consequence of pair-breaking excitations, which can occur at all momenta but according to BCS theory can be excited with the lowest velocities at a wave vector of $2k_F$. Our measurements in the BEC (Fig. 2A) and BCS (Fig. 2B) regimes directly show this difference in the excitation spectra of bosonic and fermionic superfluids. In both regimes, we clearly observe a critical velocity below which no excitations are created, which constitutes conclusive evidence of superfluidity.

After establishing that our system is superfluid in the BEC and BCS limits, we went on to study the evolution of the critical velocity in the crossover between these regimes. To take into account both the phononic and the pair-breaking excitations shown in Fig. 2, A and B, respectively, we measured the interaction dependence of the response $r(v)$ at two different lattice wave vectors of $k_0 \approx 0.3k_F$ and $k_0 \approx 2k_F$. The results are shown in Fig. 3, A and B.

For a lattice wave vector of $k_0 \approx 0.3k_F$, we clearly observe the presence of a well-defined sound mode with an onset velocity that increases as a function of interaction strength. In the crossover region [$\ln(k_F a_{2D}) \approx 0.5$], the peak smoothly broadens into a continuum as pair breaking becomes the dominant excitation in the system. For $k_0 \approx 2k_F$, the excitations on the BEC side are single-particle excitations of dimers, with pair breaking taking over toward the BCS side of the resonance. We fit the onset velocities for both datasets and used the smaller of the two values as the critical velocity of the system (Fig. 3C).

The measured critical velocities scale with the speed of sound on the BEC side of the resonance, show a maximum in the crossover, and decrease again as pair breaking becomes dominant in the BCS regime. We observe that the measured critical velocities become compatible with $v_c = 0$ at $\ln(k_F a_{2D}) \approx 2.3$, indicating that the phase transition to the normal state has been crossed (*29*). The maximum of v_c at an interaction strength of $\ln(k_F a_{2D}) \approx 0$

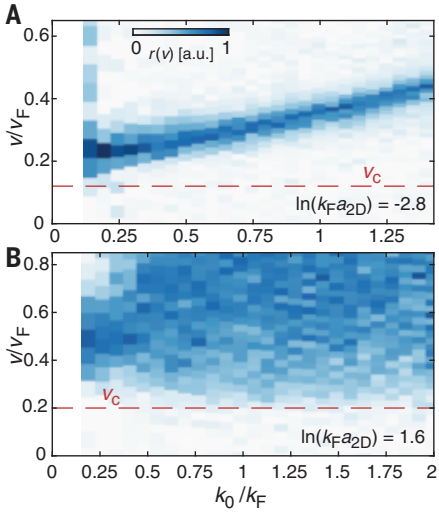


Fig. 2. Phononic and pair-breaking excitations in a 2D Fermi gas. (**A**) Response $r(v)$ of a gas in the BEC regime to excitations with lattice wave vector k_0 and velocity v. For small wave vectors, the moving lattice excites phononic modes at the sound velocity v_s. For larger wave vectors, the peak in the heating rate moves to higher velocities as the dispersion deviates from the linear phononic branch and single-particle excitations become dominant. a.u., arbitrary units. (**B**) In the BCS regime, we observe a continuum of pair-breaking excitations with a minimum of the onset velocity at $k_0 = 2k_F$. In both regimes, the heating rate is negligible for excitations that move slower than the critical velocity (red dashed lines, taken from Fig. 3C). To enhance the visibility of weaker excitations, each column in both panels has been linearly rescaled to range from 0 to 1.

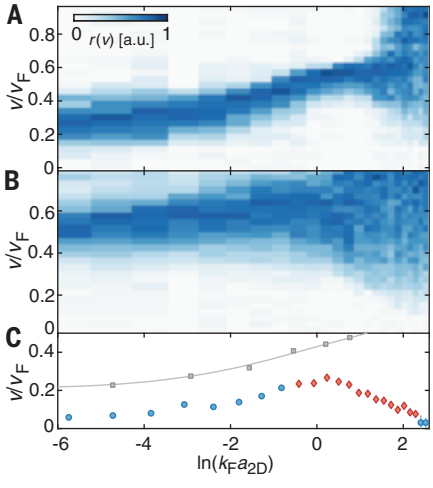


Fig. 3. Interaction dependence of the critical velocity. (**A** and **B**) Response of a 2D Fermi gas to a moving lattice with wave vectors $k_0 \approx 0.3k_F$ (A) and $k_0 \approx 2k_F$ (B) at different interaction strengths. In the BEC regime [$\ln(k_F a_{2D}) < -1$], we observe a well-defined excitation that corresponds to a sound mode for $k_0 \approx 0.3k_F$ and single-particle excitations for $k_0 \approx 2k_F$. When going to the BCS side of the crossover, the peak broadens into a continuum of pair-breaking excitations. To enhance the visibility of weaker excitations, each column has been linearly rescaled to range from 0 to 1. (**C**) We determine the critical velocity as a function of interaction strength as the lower of the two onset velocities obtained from the data shown in (A) and (B). In the BEC regime, the critical velocity is limited by excitations at small wave vectors (blue dots), whereas in the crossover, the lowest onset velocities occur at $2k_F$ (red diamonds). We find that the 2D Fermi gas is superfluid throughout the 2D BEC-BCS crossover, with the highest critical velocities found in the crossover regime at $\ln(k_F a_{2D}) \approx 0$. For comparison, we show the speed of sound v_s (gray squares) (*37*), as measured in (*38*). The gray line is a guide to the eye. The error bars denote the 1σ confidence intervals of the fit and are smaller than the symbol size for most data points.

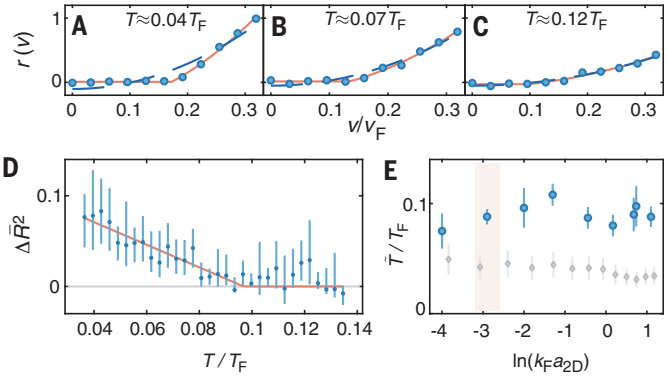


Fig. 4. Observing the superfluid phase transition. (**A** to **C**) Response of a gas in the BEC regime [$\ln(k_F a_{2D}) = -2.9$] to a moving periodic potential at different temperatures, which are indicated in the panels; the red and blue solid lines show fits to the data with $v_c > 0$ and $v_c = 0$, respectively. (**D**) The difference $\Delta\bar{R}^2 = \bar{R}^2_{v_c>0} - \bar{R}^2_{v_c=0}$ of the adjusted coefficients of determination of the two fits, which shows how allowing a critical velocity $v_c > 0$ improves the fit beyond the trivial effect of increasing the number of free parameters. We use a bilinear fit (red line) to determine the critical temperature T_c at which a nonzero v_c no longer improves the fit and find $T_c/T_F = 0.094 \pm 0.004_{stat} \pm 0.02_{sys}$ (*20*). The error bars show 1σ confidence intervals obtained by bootstrapping. (**E**) The gray diamonds show the temperature $\tilde{T}/T_F$ measured after preparing identical samples, holding them at different interaction strengths, and finally ramping to an interaction strength of $\ln(k_F a_{2D}) = -2.9$ in the BEC regime. We find only small variations of $\tilde{T}/T_F$, which establishes that this process is reasonably adiabatic and that we can use $\tilde{T}/T_F$ as a proxy for the entropy per particle in the system. The blue dots show the critical values $\tilde{T}_c/T_F$ for the onset of superfluidity in the 2D BEC-BCS crossover; the error bars show the 1σ uncertainty of the fit. Within the uncertainty of the measurement, we find no significant change in the critical entropy for superfluidity over a broad range of interaction strengths.

furthermore indicates that fermionic 2D superfluids are most stable in the strongly correlated crossover regime, which is similar to the behavior of 3D Fermi gases (*24*, *25*, *30*).

In our final set of measurements, we studied the phase transition from the superfluid to the normal state across the BEC-BCS crossover. In our first measurement, we determined the critical temperature T_c of a gas in the BEC regime [$\ln(k_F a_{2D}) = -2.9$] by preparing gases at different temperatures (*20*) and measuring the response of the system to the moving periodic potential at $k_0 \approx 0.6 k_F$. With increasing temperature, we expect the phononic branch of the dispersion to broaden and eventually become broad enough that excitations at arbitrarily small velocities can heat the gas (*31*). This broadening causes the critical velocity to decrease with temperature and vanish at $T = T_c$. Measurements of the response of the system for three different initial temperatures are shown in Fig. 4, A to C. Although the sharp onset of dissipation at the critical velocity is clearly visible in the colder data, it disappears at higher temperatures, signaling a phase transition from a superfluid to a normal state. We extracted a critical temperature of $T_c/T_F = 0.094 \pm 0.004_{stat} \pm 0.02_{sys}$, where T_F is the Fermi temperature and stat and sys denote the statistical and systematic error, respectively, of the measurement (*20*). This result is in very good agreement with theoretical predictions (*8*, *32*, *33*) and the observed onset of pair condensation (*16*).

After using this technique to measure T_c/T_F in the BEC regime, we applied it to systems in the 2D BEC-BCS crossover. We repeated the procedure outlined above at different interaction strengths and then ramped to an interaction strength of $\ln(k_F a_{2D}) \approx -2.9$ to measure the temperature $\tilde{T}$ of the system in the BEC regime (*20*). By ensuring that the interaction ramps are adiabatic, we can then use this temperature $\tilde{T}/T_F$ as a proxy for the entropy per particle of the system. The critical values of $\tilde{T}_c/T_F$ are shown in Fig. 4E as a function of interaction strength. Within the uncertainty of the measurement, we find no significant change in $\tilde{T}_c/T_F$ over a broad range of interaction strengths. This observation indicates that, although the critical temperature for pair condensation has been reported to increase in the strongly interacting regime (*16*), the critical entropy for superfluidity remains roughly constant. This is consistent with predictions for a finite-temperature equation of state where the temperature of a 2D Fermi gas with constant entropy increases as the system approaches the strongly interacting regime (*34*).

Our results can be extended to study the transition from a superfluid to strongly correlated pairs above T_c in a simple and accessible system (*35*). As the dimensionality of ultracold Fermi gases can be tuned continuously, they are furthermore particularly suited for studying the stability of the superfluid phase in the crossover from two to three dimensions.

REFERENCES AND NOTES

1. N. D. Mermin, H. Wagner, *Phys. Rev. Lett.* **17**, 1133–1136 (1966).
2. J. M. Kosterlitz, D. J. Thouless, *J. Phys. C Solid State Phys.* **6**, 1181–1203 (1973).
3. B. Keimer, S. A. Kivelson, M. R. Norman, S. Uchida, J. Zaanen, *Nature* **518**, 179–186 (2015).
4. B. Fröhlich *et al.*, *Phys. Rev. Lett.* **106**, 105301 (2011).
5. A. T. Sommer, L. W. Cheuk, M. J. Ku, W. S. Bakr, M. W. Zwierlein, *Phys. Rev. Lett.* **108**, 045302 (2012).
6. V. Makhalov, K. Martiyanov, A. Turlapov, *Phys. Rev. Lett.* **112**, 045301 (2014).
7. W. Ong, C. Cheng, I. Arakelyan, J. E. Thomas, *Phys. Rev. Lett.* **114**, 110403 (2015).
8. J. Levinsen, M. M. Parish, in *Annual Review of Cold Atoms and Molecules: Volume 3*, K. W. Madison, K. Bongs, L. D. Carr, A. M. Rey, H. Zhai, Eds. (World Scientific, 2015), pp. 1–75.
9. A. V. Turlapov, M. Yu Kagan, *J. Phys. Condens. Matter* **29**, 383004 (2017).
10. P. A. Murthy *et al.*, *Science* **359**, 452–455 (2018).
11. T. Peppler *et al.*, *Phys. Rev. Lett.* **121**, 120402 (2018).
12. M. Holten *et al.*, *Phys. Rev. Lett.* **121**, 120401 (2018).
13. D. Mitra, P. T. Brown, P. Schauß, S. S. Kondov, W. S. Bakr, *Phys. Rev. Lett.* **117**, 093601 (2016).
14. K. Fenech *et al.*, *Phys. Rev. Lett.* **116**, 045302 (2016).
15. I. Boettcher *et al.*, *Phys. Rev. Lett.* **116**, 045303 (2016).
16. M. G. Ries *et al.*, *Phys. Rev. Lett.* **114**, 230401 (2015).
17. P. A. Murthy *et al.*, *Phys. Rev. Lett.* **115**, 010401 (2015).
18. N. Luick *et al.*, *Science* **369**, 89–91 (2020).
19. K. Hueck *et al.*, *Phys. Rev. Lett.* **120**, 060402 (2018).
20. See supplementary materials.
21. L. Landau, *Phys. Rev.* **60**, 356–358 (1941).
22. C. Raman *et al.*, *Phys. Rev. Lett.* **83**, 2502–2505 (1999).
23. R. Desbuquois *et al.*, *Nat. Phys.* **8**, 645–648 (2012).
24. W. Weimer *et al.*, *Phys. Rev. Lett.* **114**, 095301 (2015).
25. D. E. Miller *et al.*, *Phys. Rev. Lett.* **99**, 070402 (2007).
26. L.-C. Ha, L. W. Clark, C. V. Parker, B. M. Anderson, C. Chin, *Phys. Rev. Lett.* **114**, 055301 (2015).
27. D. Petrov, G. Shlyapnikov, *Phys. Rev. A* **64**, 012706 (2001).
28. P. Murthy *et al.*, *Phys. Rev. A* **90**, 043611 (2014).
29. At this interaction strength, theoretical predictions give $T_c \approx 0.045 - 0.07 T_F$ (*32*, *33*, *39*), which is comparable to the temperature of our system in the BEC regime of $T = 0.04(1) T_F$ (*20*).
30. R. Combescot, M. Y. Kagan, S. Stringari, *Phys. Rev. A* **74**, 042717 (2006).
31. We are not aware of theoretical predictions for the damping of phonons in the 2D BEC-BCS crossover. However, we expect behavior similar to that predicted for liquid helium (*40*) and bosonic gases (*41*), which exhibit a linear dependence of the damping on the temperature in the relevant range of temperature and momentum.
32. B. C. Mulkerin *et al.*, *Phys. Rev. A* **96**, 053608 (2017).
33. G. Bighin, L. Salasnich, *Int. J. Mod. Phys. B* **32**, 1840022 (2018).
34. A. Tononi, A. Cappellaro, G. Bighin, L. Salasnich, arXiv:2009.06491 [cond-mat.quant-gas] (14 September 2020).
35. T. Kondo *et al.*, *Nat. Phys.* **7**, 21–25 (2011).
36. G. Astrakharchik, L. Pitaevskii, *Phys. Rev. A* **70**, 013608 (2004).
37. As shown in (*42*), the reduction of the critical velocity compared to the speed of sound can be explained by the damping of the sound mode as well as the finite potential height of the moving optical lattice.
38. M. Bohlen *et al.*, *Phys. Rev. Lett.* **124**, 240403 (2020).
39. M. Bauer, M. M. Parish, T. Enss, *Phys. Rev. Lett.* **112**, 135302 (2014).
40. C. Pethick, D. Ter Haar, *Physica* **32**, 1905–1920 (1966).
41. M.-C. Chung, A. B. Bhattacherjee, *New J. Phys.* **11**, 123012 (2009).
42. V. P. Singh, L. Mathey, Collective modes and superfluidity of a two-dimensional ultracold Bose gas. arXiv:2010.00013 [cond-mat.quant-gas] (30 September 2020).
43. L. Sobirey, N. Luick, M. Bohlen, H. Biss, H. Moritz, T. Lompe, Data for "Observation of superfluidity in a strongly correlated two-dimensional Fermi gas," Version 1, Zenodo (2021); https://doi.org/10.5281/zenodo.4613154.

ACKNOWLEDGMENTS

We thank L. Mathey and V. Singh for valuable insights and discussions. **Funding:** This work was supported by the European Union's Seventh Framework Programme (FP7/2007-2013) under grant 335431 and by the Deutsche Forschungsgemeinschaft (DFG, German Research Foundation) SFB-925 project 170620586 and the excellence cluster "Advanced Imaging of Matter" EXC 2056 project 390715994. M.B. acknowledges support by Labex ICFP of École Normale Supérieure Paris. **Author contributions:** L.S. performed the experiments and data analysis with support from all authors. L.S. and T.L. wrote the manuscript with input from all authors. T.L. and H.M. supervised the project. All authors contributed to the discussion and interpretation of the results. **Competing interests:** The authors declare no competing interests. **Data and materials availability:** All data presented in this paper are deposited at Zenodo (*43*).

SUPPLEMENTARY MATERIALS

science.sciencemag.org/content/372/6544/844/suppl/DC1
Supplementary Text
Figs. S1 to S4
Tables S1 and S2
References (*44*–*46*)

20 May 2020; accepted 17 April 2021
10.1126/science.abc8793

ORGANIC CHEMISTRY

Photocatalytic C–H activation and the subtle role of chlorine radical complexation in reactivity

Qiaomu Yang, Yu-Heng Wang, Yusen Qiao, Michael Gau, Patrick J. Carroll, Patrick J. Walsh*, Eric J. Schelter*

The functionalization of methane, ethane, and other alkanes derived from fossil fuels is a central goal in the chemical enterprise. Recently, a photocatalytic system comprising $[Ce^{IV}Cl_5(OR)]^{2-}$ [Ce^{IV}, cerium(IV); OR, $-OCH_3$ or $-OCCl_2CH_3$] was disclosed. The system was reportedly capable of alkane activation by alkoxy radicals (RO•) formed by Ce^{IV}–OR bond photolysis. In this work, we present evidence that the reported carbon-hydrogen (C–H) activation of alkanes is instead mediated by the photocatalyst $[NEt_4]_2[CeCl_6]$ (NEt_4^+, tetraethylammonium), and RO• are not intermediates. Spectroscopic analyses and kinetics were investigated for C–H activation to identify chlorine radical (Cl•) generation as the rate-limiting step. Density functional theory calculations support the formation of [Cl•][alcohol] adducts when alcohols are present, which can manifest a masked RO• character. This result serves as an important cautionary note for interpretation of radical trapping experiments.

The transformation of small molecules into value-added products is the chief enterprise of the chemical industry (*1*). Among readily available raw materials, methane and ethane are extremely attractive, given their abundances in natural gas. However, the catalytic C–H activation of methane has remained a major challenge because of the compound's low polarizability, large bond dissociation free energy of 105 kcal mol^{-1}, and tendency toward overfunctionalization (*1*–*4*). The reported catalysts for methane activation at mild temperatures (<200°C) include homogeneous and heterogeneous varieties, typically using low-abundance elements such as Ru, Ir, Pd, and Rh under thermo-, electro-, and photocatalytic conditions (*1*–*6*). Recent advances in methane activation include ruthenium, rhodium, and iridium borylation catalysis from Sanford's group and the team of Smith, Baik, and Mindiola (*7*, *8*), as well as Zuo's cerium photocatalytic reaction under blue light (*9*) and Noël and co-workers' decatungstate photocatalytic functionalization under ultraviolet A (UVA) light (*10*).

Zuo and co-workers introduced a homogeneous cerium-based catalyst for the photochemical amination of methane at room temperature (*9*). The result demonstrated that earth-abundant metal catalysts could efficiently mediate photocatalytic C–H functionalization of hydrocarbon substrates under mild conditions (*11*). A cerium(IV) alkoxide (Ce^{IV}–OR)–based system proposed by Zuo has been implemented in C–C and C–N coupling reactions, β-scission processes, and 1,5-hydrogen atom transfer (HAT) reactions (*9*, *12*–*18*). The proposed mechanism entailed the generation of alkoxy radicals (RO•) from Ce^{IV}–OR species under light irradiation, which were assumed to be the key species responsible for the HAT from hydrocarbons.

However, the UV-visible absorption spectrum of $[NEt_4]_2[CeCl_6]$ (**1**) (NEt_4, tetraethylammonium), a cerium-based photocatalyst studied recently by our group, was nearly identical to Zuo's putative catalyst, $[CeCl_5(OCH_2CCl_3)]^{2-}$ (**2**) (*9*, *19*). The similarity of these two UV-visible spectra and our continuing interest in development of cerium photoredox catalysts prompted us to investigate the identity of the cerium species operative for alkane C–H functionalization (*19*–*21*). In this context, previous studies by Costanzo and our group demonstrated that **1** produced a chlorine radical (Cl•) upon irradiation, leading us to question the involvement of alcohol in Zuo's C–H functionalization (*19*, *22*). In this work, we demonstrate that alcohol plays no substantial role in the observed activation of alkanes with $[NEt_4]_2[CeCl_6]$, as evidenced by studies of cerium speciation, kinetics, and trapping of the Cl• intermediate. A revised reaction mechanism for the reported cerium photocatalysis, predicated on the $[Ce^{IV}Cl_6]^{2-}/[Ce^{III}Cl_6]^{3-}$ system and the essential role of Cl•, is proposed. Beyond the applicability to Zuo's studies, our results provide important insights into the selectivity of Cl• adducts formed on interactions with donors, including alcohols and arenes. We posit that the adduct of Cl• with alcohols gives rise to Zuo's "alkoxy-radical trapping products" (ARTPs),

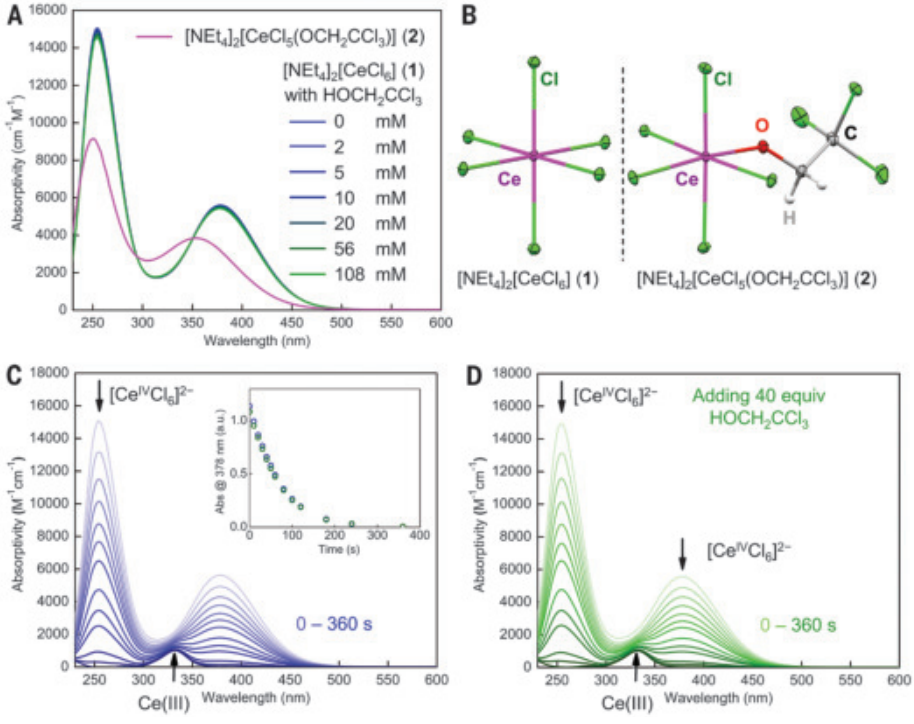


Fig. 1. Spectroscopic studies of the bona fide $[CeCl_5(OCH_2CCl_3)]^{2-}$ and mixtures of $[CeCl_6]^{2-}$ and $HOCH_2CCl_3$. (**A**) Absorption spectra of **1** (0.175 mM) with 0 to 600 equiv (108 mM) of $HOCH_2CCl_3$ (blue-greenish trace) and **2** (0.35 mM) in CH_3CN. (**B**) Thermal ellipsoid plots of **1** and **2** at the 50% probability level ($[NEt_4]^+$ countercations are omitted for clarity; H-atoms included as a riding model). (**C** and **D**) Time progression of UV-visible spectra for (C) **1** (0.20 mM) and (D) **1** (0.20 mM) with 40 equiv $HOCH_2CCl_3$ in CH_3CN under blue light (467 nm) irradiation. The inset of (C) shows an absorbance value of **1** at 378 nm at the given time intervals under 467 nm irradiation without (blue open circles) and with (green open circles) $HOCH_2CCl_3$ in CH_3CN. Abs, absorbance; a.u., arbitrary units.

P. Roy and Diana T. Vagelos Laboratories, Department of Chemistry, University of Pennsylvania, 231 South 34th Street, Philadelphia, PA 19104, USA.
*Corresponding author. Email: pwalsh@sas.upenn.edu (P.J.W.); schelter@sas.upenn.edu (E.J.S.)

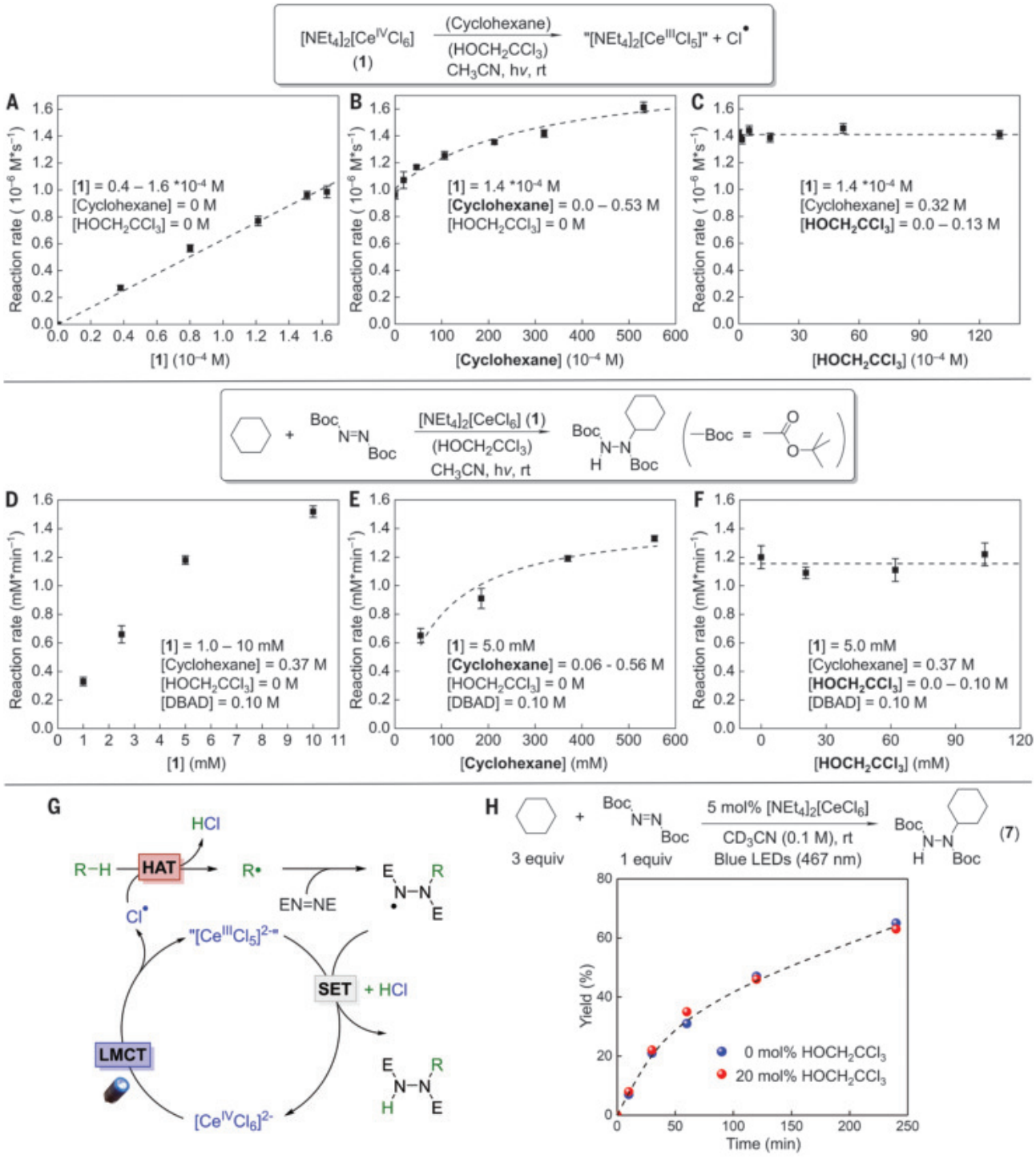


Fig. 2. Kinetic studies for the photochemical reactivity of 1. (**A** to **F**) The dependences of the stoichiometric photolytic depletion rates of **1** on the concentration of (A) [**1**], (B) [cyclohexane], and (C) [$HOCH_2CCl_3$] were measured at room temperature (rt). *hν*, photon energy. Dependences of photochemical cyclohexane amination rates on the concentration of (D) [**1**], (E) [cyclohexane], and (F) [$HOCH_2CCl_3$] using **1** as a catalyst were also measured at rt. The dashed lines for fitting and error bars are described in the SM (section III.A). Boc, *tert*-butyloxycarbonyl. (**G**) Revised catalytic cycle. In EN=NE, –E represents $–CO_2{}^{i}Pr$ or $–CO_2{}^{t}Bu$. ^{i}Pr, isopropyl; SET, single-electron transfer. (**H**) Time-course studies of the cyclohexane amination reaction. LEDs, light-emitting diodes.

highlighting that precise understanding of the mechanisms of trapping reactions is paramount to their use in providing insight into reaction intermediates.

According to Zuo and co-workers, the proposed catalyst, $[Ce^{IV}Cl_5(OCH_2CCl_3)]^{2-}$, was generated in situ from a mixture of $CeCl_3$, $[N^{n}Bu_4]Cl$, and $HOCH_2CCl_3$ under photocatalytic reaction conditions (*9*, *12*–*17*) (Bu, butyl). Mixtures of $CeCl_3$ and $[NEt_4]Cl$ were reported to form $[NEt_4]_3[CeCl_6]$ in CH_3CN, and $[NEt_4]_3[CeCl_6]$ is known to auto-oxidize

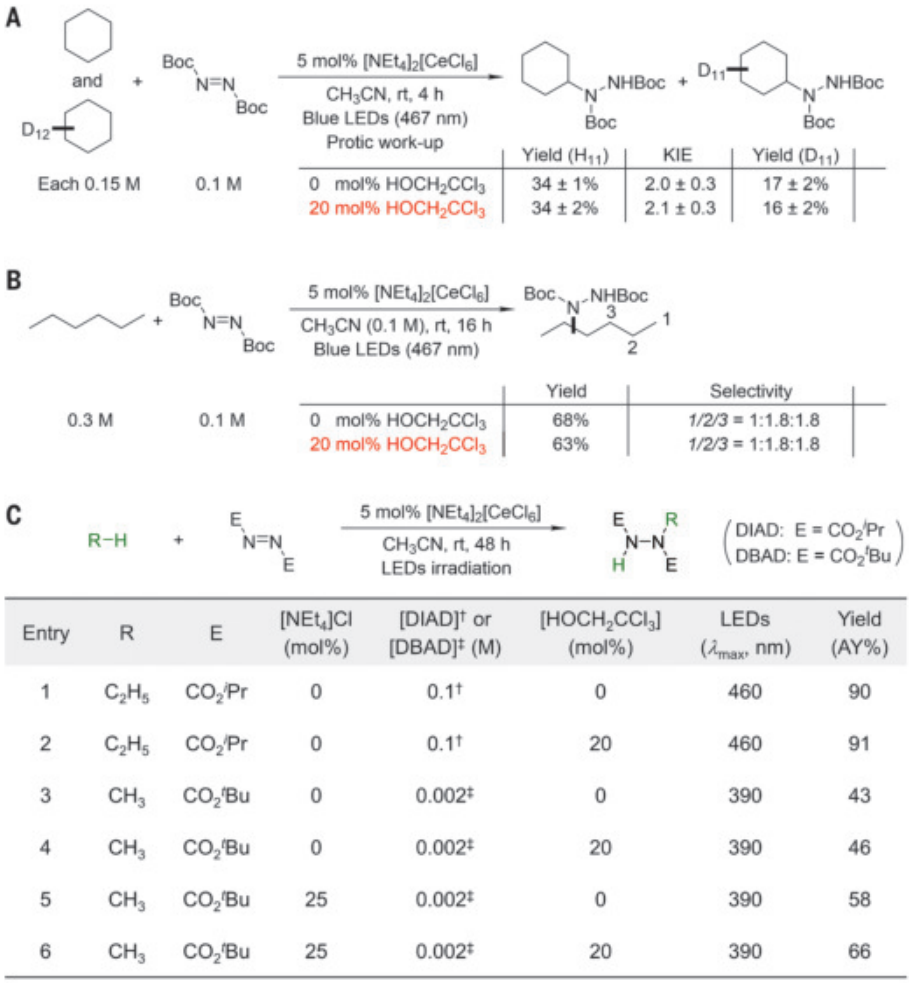
in air (*9*). To study the influence of the alcohol on the associated $[NEt_4]_2[CeCl_6]$ (**1**) speciation, we added $HOCH_2CCl_3$ to a solution of **1** in acetonitrile, and the mixture was evaluated by UV-visible spectroscopy (*23*). Negligible changes in the UV-visible spectrum of **1** (0.175 mM) were observed upon titration with $HOCH_2CCl_3$ [0.002 to 0.108 M, Fig. 1A; also see supplementary materials (SM), section II.C].

Independent synthesis and isolation of **2** was also pursued. The complex (**2**) was prepared by carefully mixing **1** and 1 equiv $NaOCH_2CCl_3$ in dry acetonitrile with the exclusion of light (SM, section VI). The resulting alkoxide **2** was then characterized crystallographically (Fig. 1B) and exhibited a UV-visible absorption spectrum with lower absorptivity and slight blue shift of the ligand-to-metal charge-transfer (LMCT) bands compared with **1** (Fig. 1A). Furthermore, this complex showed a characteristic peak in the ^{1}H nuclear magnetic resonance (NMR) spectrum at chemical shift (δ) = 5.63 parts per million for the methylene hydrogens, $[CeCl_5(OC\boldsymbol{H}_2CCl_3)]^{2-}$, that was not observed upon mixing **1** with 10 equiv $HOCH_2CCl_3$ (0.1 M) in a CD_3CN solution (SM, section II.A). These spectroscopic studies indicate that the formation of $[NEt_4]_2[Ce^{IV}Cl_5(OCH_2CCl_3)]$ (**2**) by the reaction of **1** and excess $HOCH_2CCl_3$ was unfavorable, at least without irradiation.

Similarly, time-resolved UV-visible studies were conducted to investigate whether **2** was photochemically generated under relevant conditions. In the absence and presence of 40 equiv $HOCH_2CCl_3$, **1** (0.20 mM) showed essentially identical UV-visible spectra (Fig. 1, C and D) and luminescence spectra (SM, section II.D). The depletion of **1** under visible-light irradiation is known to proceed by the formation of Cl• and a putative species, "$[Ce^{III}Cl_5]^{2-}$," through an LMCT transition of **1** (*22*). The luminescence spectra were characteristic for a mixture of two Ce^{III} species, $[NEt_4]_3[Ce_2Cl_9]$ (**3**) and $[NEt_4]_3[CeCl_6]$ (**4**), which is consistent with our previous findings (*19*). Furthermore, time-dependent–density functional theory (TD-DFT) calculations of **2** indicated an excited state leading to Cl• loss (SM, sections II.E and II.F) rather than RO• loss. Taken together, these spectroscopic results provide evidence that the photoreduction of **1** was not influenced by the presence of $HOCH_2CCl_3$ and that RO•, proposed to have been generated by irradiation of mixtures of $CeCl_3$, $[N^nBu_4]Cl$, and $HOCH_2CCl_3$, were not primary intermediates for the reported alkane activation.

To explore the mechanism for alkane functionalization, kinetics for the stoichiometric photolysis of **1** were monitored by following the decrease of [**1**] using UV-visible spectroscopy (Fig. 2, A to C, and SM, section III.C). The initial rates for photolysis of **1** showed a linear and positive dependence on [**1**], a positive dependence on [cyclohexane], and no dependence on $[HOCH_2CCl_3]$. At a low concentration of **1**, the photoreduction rate showed a linear, pseudo–first-order dependence (Fig. 2A). This observation confirmed that the generation of Cl• by an LMCT process for **1** is involved in the rate-limiting step (fig. S27). Increasing the cyclohexane concentration increased the rate of reaction in a nonlinear fashion (Fig. 2B). The dependence of the rate on [cyclohexane] was modeled by using steady-state conditions for the intermediate [Cl•] and was fitted to the observed reaction rate (figs. S28 and S35). Because Zuo emphasized the importance of $HOCH_2CCl_3$ among alcohols (*9*), we examined the kinetics of the reaction in the presence of $HOCH_2CCl_3$. A zero-order dependence on the concentration of $HOCH_2CCl_3$ (0 to 0.1 M) suggested that the alcohol did not influence the reaction kinetics (Fig. 2C). In the absence of cyclohexane, photolysis of **1** resulted in monochlorination of acetonitrile [20% assay yield (AY)] and radical dimer $NCCH_2CH_2CN$ (42% AY), as judged by ^{1}H NMR. In the presence of cyclohexane, formation of chlorocyclohexane was observed (56% AY) (figs. S20 to S22). We attribute this reaction difference to the better polarity matching of Cl• with cyclohexane than with CH_3CN (*24*).

To examine the mechanism for catalytic alkane functionalization, kinetic studies for the amination of cyclohexane with di-*tert*-butyl azodicarboxylate (DBAD) were performed (Fig. 2, D to F). Reaction rates were monitored by following the appearance of products by ^{1}H NMR spectroscopy (SM, section III.D). Similarly to the stoichiometric conditions, the initial rates of catalytic cyclohexane functionalization showed nonlinear, positive dependences on [**1**] and [cyclohexane] and no dependence on $[HOCH_2CCl_3]$. The radical trap (DBAD) exhibited zero-order behavior, indicating that it did not take part in the turnover-limiting step (fig. S34).



Entry	R	E	$[NEt_4]Cl$ (mol%)	[DIAD]† or [DBAD]‡ (M)	$[HOCH_2CCl_3]$ (mol%)	LEDs (λ_{max}, nm)	Yield (AY%)
1	C_2H_5	$CO_2{}^iPr$	0	0.1†	0	460	90
2	C_2H_5	$CO_2{}^iPr$	0	0.1†	20	460	91
3	CH_3	$CO_2{}^tBu$	0	0.002‡	0	390	43
4	CH_3	$CO_2{}^tBu$	0	0.002‡	20	390	46
5	CH_3	$CO_2{}^tBu$	25	0.002‡	0	390	58
6	CH_3	$CO_2{}^tBu$	25	0.002‡	20	390	66

Fig. 3. Reactions catalyzed by $[NEt_4]_2[CeCl_6]$ and the influence of $HOCH_2CCl_3$ as an additive. (**A**) Competition experiment using C_6H_{12} versus C_6D_{12}. (**B**) Selectivity studies of C–H activation with *n*-hexane. (**C**) Activation of ethane with DIAD (marked by †) and methane with DBAD (marked by ‡). λ_{max}, maximum wavelength.

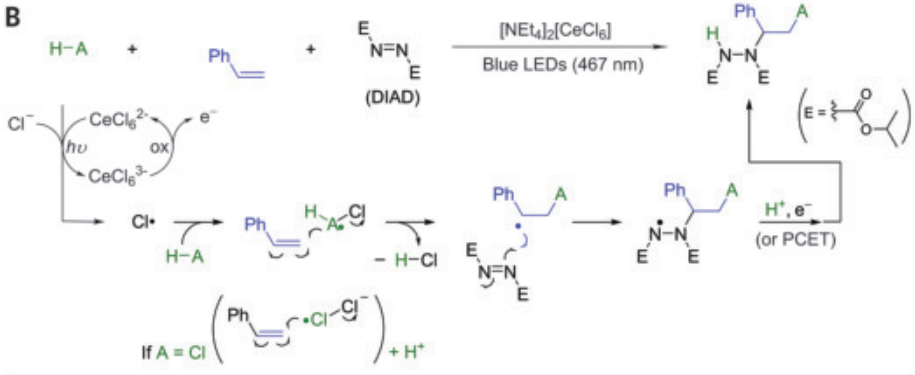
To understand the dependence of reaction rate on [cyclohexane] in Fig. 2E, kinetic isotope effect (KIE) studies were conducted. The reaction rates were measured by using cyclohexane (k_H) and cyclohexane-d_{12} (k_D) as substrates (fig. S37). A KIE value of 1.12 (k_H/k_D) was determined from parallel reactions (*25*), which indicated that the C–H/C–D activation by Cl• was not involved in the turnover-limiting step. This small parallel KIE is consistent with the small rate dependence on [cyclohexane] in Fig. 2E. A more challenging substrate to activate, such as methane, could alter the turnover-limiting step because of a stronger C–H bond. The reaction quantum yield of the photocatalytic amination of cyclohexane was 3.8%, as determined by actinometry. This value was smaller than that of stoichiometric photolysis of **1** (5.8%), suggesting that radical chain processes are not involved (SM, section III.G). These results indicated that the photochemical generation of Cl• by an LMCT process of **1** is the turnover-limiting step.

On the basis of the above-mentioned results, we propose a revised mechanism for the photocatalytic C–H activation by **1** (Fig. 2G). First, $[Ce^{IV}Cl_6]^{2-}$ undergoes a photoinduced LMCT transition to generate a Cl• and Ce^{III} product, "$[CeCl_5]^{2-}$." The Cl• then abstracts a hydrogen atom from an alkane substrate to generate a carbon-centered radical. This radical is trapped by the azodicarboxylate (e.g., DBAD), with C–N bond formation to produce a captodative, nitrogen-centered radical. We hypothesize that the nitrogen-centered radical is protonated by HCl and reduced by "$[CeCl_5]^{2-}$" through single-electron transfer to deliver the product and regenerate the Ce^{IV} photocatalyst **1**. A time-course study of the cyclohexane amination both in the absence and presence of alcohol gave identical results, indicating the absence of alcohol in reaction mechanism (Fig. 2H).

After we demonstrated that **1** was capable of photochemically generating Cl•, photocatalytic C–H activation of alkanes by **1** was investigated. The initial studies were conducted with 0.3 M cyclohexane as the substrate, 0.1 M DBAD as the trapping reagent, and 5 mol % **1** as the photocatalyst, which gave an optimized AY of 84% for compound **7** (*26*), indicating that alcohol was not required for this chemistry (SM, section IV.A). Equimolar mixtures of cyclohexane and cyclohexane-d_{12} were irradiated under catalytic conditions in the presence and absence of $HOCH_2CCl_3$ (20 mol %) (Fig. 3A), and identical AYs (50%) and product ratios ($[P_H]:[P_D] \approx 2.1$) were observed (*25*, *27*). The results indicated that alcohol had no influence on the yield or on the competitive rates between H- and D-atom abstraction from substrate, which suggests a common intermediate. Next, *n*-hexane was used to investigate the influence of alcohol on the chemoselectivity of



Entry	H–A	H–A (equiv)	[DIAD] (M)	$[NEt_4]_2[CeCl_6]$ (mol%)	Yield of **5a** (%)	Yield of **5b**/**5c** (%)
1	$[NEt_4]Cl$	1	0.1 M	5	< 5	\
2	HO_2CCF_3 $[NEt_4]Cl$	1 5	0.1 M	5	13	\
3	H–Cl	1	0.01 M	5	46	\
4	H–Cl $H–OCH_3$	2 2	0.01 M	5	44	< 5 (**5b**)
5	$H–OCH_3$	2	0.1 M	1	< 5	50 (**5b**)
6	$H–OCH_2CCl_3$	5	0.01 M	5	29	25 (**5c**)



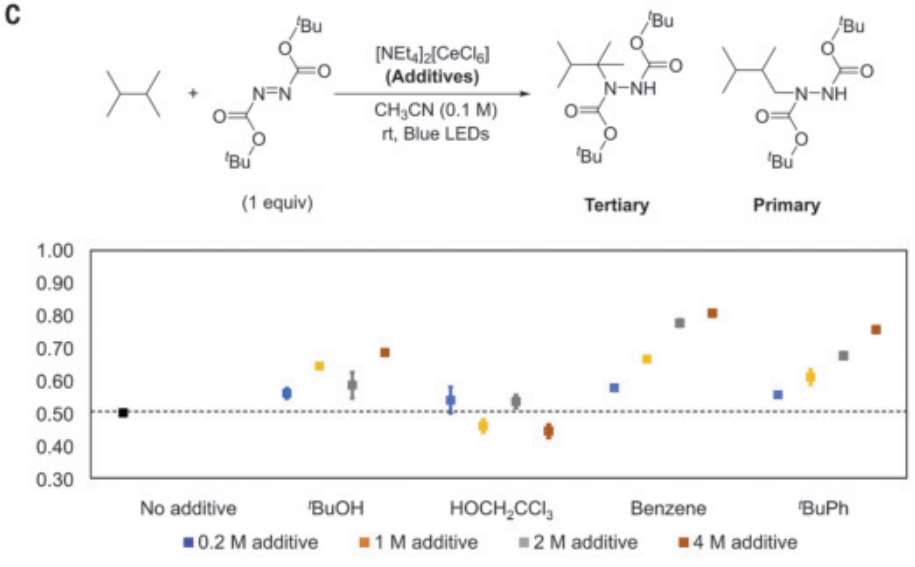


Fig. 4. Radical complexation experiments. (**A**) Radical trapping experiments with styrene, DIAD, and additives H–A, where –A represents –Cl (**5a**), $–OCH_3$ (**5b**), or $–OCH_2CCl_3$ (**5c**). In entries 3 and 4, HCl was added as a 12 M aqueous solution. (**B**) Proposed mechanism for the radical trapping experiments. ox, oxidation; PCET, proton-coupled electron transfer. (**C**) Selective activation of 2,3-dimethylbutane with additives in different concentrations. The dashed line indicates the standard conditions of selectivity without additives. Error bars come from the SD from three runs of each reaction. Unless otherwise specified, all reported yields in this section were determined by GC-MS.

C–H activation. In the presence and absence of alcohol, the selectivities of the three inequivalent C–H's were essentially identical (Fig. 3B, $C^1H_3C^2H_2C^3H_2C^3H_2C^2H_2C^1H_3$, C^1–H:C^2–H:C^3–H = 1.0:1.8:1.8). Overall, these experiments demonstrated that alcohol had negligible impact on the C–H activation yield or selectivity.

The performance of **1** and the influence of alcohol on its photocatalytic functionalization of light alkanes (i.e., ethane and methane) were studied in a customized pressure vessel (fig. S1) owing to the poor solubility of light alkanes in acetonitrile at ambient conditions (*28*). The yield of ethane activation with diisopropyl azodicarboxylate (DIAD) under 10 atm of ethane gas was 90% after 48 hours in the absence of $HOCH_2CCl_3$, and 91% in the presence of $HOCH_2CCl_3$ (Fig. 3C, entries 1 and 2). Methane activation was investigated in a similar manner, with the use of DBAD instead of DIAD (SM, section IV.B) (*29*). Zuo reported methane activation gave superior results using the Ce^{IV} salts $Ce(OTf)_4$ and $[N^nBu_4]_2[CeCl_6]$, together with 5 equiv $[N^nBu_4]Cl$, as starting materials (OTf, triflate). Despite the reactions being performed under 50 atm, our initial attempts toward methane activation afforded lower yields than that of ethane and other alkane products (table S5). This outcome is presumably due to the poor solubility of methane in acetonitrile combined with its high C–H bond dissociation energy (*1*). The amount of acetonitrile in the reaction vessel was increased to facilitate the reaction. A yield of methane functionalization of 43% was attained by adopting this strategy (Fig. 3C, entry 3). The influence of alcohol on methane functionalization was investigated and found to be insignificant (Fig. 3C, entries 3 and 4). Conducting the reaction in the presence of 25 mol % $[NEt_4]Cl$ led to a 58% AY (Fig. 3C, entry 5). The increase in yield in entry 5 is attributed to the excess chloride, which facilitates regeneration of the catalyst **1** (*19*). The yield of methane activation improved from 58 to 66% in the presence of $[NEt_4]Cl$ (25 mol %) and $HOCH_2CCl_3$ (20 mol %) (Fig. 3C, entries 5 and 6). These are the only conditions in which we detected a slight improvement in AY with the addition of alcohol. We hypothesize that this result is due to the characteristics of the highly reactive methyl radical, $\bullet CH_3$, which is reportedly stabilized by alcohol through hydrogen bonding (*30*, *31*). Overall, the experimental results presented in Fig. 3C consistently indicate that **1** is the active catalyst for this system, and the role of alcohols (i.e., trichloroethanol) was identified as an additive for methane activation through the stabilization of the highly reactive methyl radical by hydrogen bonding. The uses of different trapping agents with ethane are discussed in the SM (section VI).

Zuo and co-workers reported that RO• were crucial for the C–H activation and supported this claim by their isolation of what appear to be ARTPs (*9*). We conducted radical trapping experiments to further probe the hypothesis that Cl• was photochemically generated from **1** (SM, sections V.A to V.D) (*19*, *22*). Upon the reaction of DIAD, $[NEt_4]Cl$, and styrene with 5 mol % **1** in acetonitrile at room temperature for 24 hours under anaerobic irradiation conditions, no appreciable chlorine-radical trapping product (CRTP) was observed (Fig. 4A, entry 1). However, the addition of an external proton source, such as trifluoroacetic acid (CF_3CO_2H), afforded the CRTP (**5a**) in 13% AY [gas chromatography–mass spectrometry (GC-MS) conversion; Fig. 4A, entry 2]. The need for acid indicated that the protonation of the nitrogen atom is required for the formation of the CRTP. In the presence of 1 equiv of HCl, the CRTP was obtained in 46% yield (Fig. 4A, entry 3). The lower yield of CRTP was attributed to a side reaction between styrene and 2 equiv of DIAD that produced a Diels-Alder/conjugate addition product, **6** (SM, section V.B). An equimolar mixture of HCl and CH_3OH also afforded CRTP in 44% yield (Fig. 4A, entry 4), which is consistent with the spectroscopic results that demonstrated that Cl• was formed in the presence of alcohol. The generation of CRTP was also observed in the presence of $HOCH_2CCl_3$ (Fig. 4A, entry 6; also see SM, section V.C); the chlorine source was presumably from $HOCH_2CCl_3$ under these conditions because of alpha C–H abstraction (fig. S46). The CRTP was fully characterized by NMR spectroscopy, x-ray crystallography, and GC-MS. A proposed mechanism for CRTP (Fig. 4B) involves the reaction of photochemically generated Cl• with Cl^- to afford the $Cl_2\bullet^-$ complex (*22*, *32*), which adds to the terminal carbon of styrene to yield a stabilized benzyl radical. The resulting benzyl radical adds to the diazo linkage to form a captodative, *N*-centered radical. Next, the nitrogen radical is reduced by the Ce^{III} species with protonation to afford the product CRTP.

Repeating the reaction under Zuo's conditions for the ARTPs (*9*) indeed afforded the products **5b** in 50% GC yield and **5c** in 25% GC yield (Fig. 4A, entries 5 and 6). We hypothesized that a radical adduct between Cl• and the alcohols, [Cl–OHR]• (R, $-CH_3$ or $-CH_2CCl_3$), was generated in the presence of $HOCH_3$ or $HOCH_2CCl_3$ (SM, section V.C, and discussion below) (*33*, *34*). Indeed, Cl• has been established to interact with solvents such as benzene (*35*), haloalkanes (*36*), acetonitrile (*33*), pyridine (*37*), alcohols (*33*, *34*, *38*, *39*), and water (*38*), as well as anions such as Cl^- and Br^-, forming charge-transfer complexes (*32*, *36*). In this case, these [Cl–OHR]• intermediates were ultimately trapped, which led to **5b** and **5c** with elimination of HCl (Fig. 4B). The DFT calculations that we performed for Cl• adducts with the alcohols and acetonitrile revealed an increasing adduct stability $HOCH_3$ > $HOCH_2CCl_3$ > $NCCH_3$ (SM, section V.D) (*39*). We propose that a [Cl–OHMe]• species initially reacts with styrene at the oxygen atom. DFT computations of [Cl–OHMe]• revealed appreciable spin density on the oxygen atom (fig. S48). Next, a low-energy transition state for the reaction of [Cl–OHMe]• with styrene was optimized and confirmed through an internal reaction coordinate scan (fig. S49) (Me, methyl). This reaction is followed by the elimination of hydrogen chloride, leading to a benzylic radical intermediate. The intermediate is subsequently trapped by DIAD to afford the observed product **5b**. This proposed mechanism, which is controlled by the formation of radical adducts, accounts for the ARTPs (**5b** and **5c**) observed by Zuo, products that do not emerge directly from cerium alkoxides or RO•. Thus, photochemically generated Cl• are the primary reactive intermediate in this system, but charge-transfer adducts with Lewis bases can mask the Cl• character and give false-positive results for RO•.

One of the pillars of Zuo's mechanism is the observed change in selectivity in the presence of different alcohols, which is attributed to forming discrete RO• with notable selectivity. Cl•-induced charge-transfer complexes, however, are known to alter the selectivity in alkane activation (*40*, *41*). We investigated the activation of 2,3-dimethylbutane in the presence of additives and found that additives alter the ratio of tertiary:primary activation from 0.51:0.49 (no additive) to 0.69:0.31 (^{t}BuOH), 0.81:0.19 (benzene), and 0.76:0.24 (^{t}BuPh), respectively (Fig. 4C) (^{t}Bu, *tert*-butyl; Ph, phenyl). Higher concentrations of additives (0.04 to 4 M) resulted in a greater selectivity because of the equilibrium between Cl• and its radical adduct. Alcohols with alpha hydrogens were excluded from this study because of side reactions by means of alpha C–H abstraction at high concentrations. The changes in selectivity were examined by Russel for radical complexes induced by additive effects (*40*, *41*). For this work, DFT calculations performed on Cl• adducts with benzene confirmed an η^1 π-complex, as previously observed (SM, sections V.D and V.E) (*39*, *42*). These Cl• adducts are electronically more stable radicals with improved selectivity in alkane activation reactions. Our results support the hypothesis that alcohols in Zuo's system simply generate Cl• adducts that alter the selectivity in C–H activation, similar to benzene derivatives in the above reactions.

The apparent intermediacy of RO• in this case can be explained by adducts between the Cl• and alcohols, and this adduct could provide a platform to transfer the radical character from chlorine to heteroatoms for exploitation

in diverse reactivity. Given the current trends in catalysis of using Cl•, we suspect that the formation of Cl• adducts will play a larger role and advise that caution be used when basing reaction mechanisms on radical trapping products in the presence of additives.

REFERENCES AND NOTES

1. X. Meng *et al*., *Chem* **5**, 2296–2325 (2019).
2. M. Ravi, M. Ranocchiari, J. A. van Bokhoven, *Angew. Chem. Int. Ed.* **56**, 16464–16483 (2017).
3. N. J. Gunsalus *et al*., *Chem. Rev.* **117**, 8521–8573 (2017).
4. P. Schwach, X. Pan, X. Bao, *Chem. Rev.* **117**, 8497–8520 (2017).
5. R. A. Periana *et al*., *Science* **280**, 560–564 (1998).
6. M. E. O'Reilly, R. S. Kim, S. Oh, Y. Surendranath, *ACS Cent. Sci.* **3**, 1174–1179 (2017).
7. K. T. Smith *et al*., *Science* **351**, 1424–1427 (2016).
8. A. K. Cook, S. D. Schimler, A. J. Matzger, M. S. Sanford, *Science* **351**, 1421–1424 (2016).
9. A. Hu, J. J. Guo, H. Pan, Z. Zuo, *Science* **361**, 668–672 (2018).
10. G. Laudadio *et al*., *Science* **369**, 92–96 (2020).
11. O. S. Wenger, *J. Am. Chem. Soc.* **140**, 13522–13533 (2018).
12. J. J. Guo *et al*., *Angew. Chem. Int. Ed.* **55**, 15319–15322 (2016).
13. A. Hu *et al*., *J. Am. Chem. Soc.* **140**, 1612–1616 (2018).
14. A. Hu *et al*., *J. Am. Chem. Soc.* **140**, 13580–13585 (2018).
15. J. Guo, A. Hu, Z. Zuo, *Tetrahedron Lett.* **59**, 2103–2111 (2018).
16. K. Zhang, L. Chang, Q. An, X. Wang, Z. Zuo, *J. Am. Chem. Soc.* **141**, 10556–10564 (2019).
17. Q. An *et al*., *J. Am. Chem. Soc.* **142**, 6216–6226 (2020).
18. Y. Chen, J. Du, Z. Zuo, *Chem* **6**, 266–279 (2020).
19. H. Yin *et al*., *J. Am. Chem. Soc.* **138**, 16266–16273 (2016).
20. Y. Qiao, Q. Yang, E. J. Schelter, *Angew. Chem. Int. Ed.* **57**, 10999–11003 (2018).
21. Y. Qiao, E. J. Schelter, *Acc. Chem. Res.* **51**, 2926–2936 (2018).
22. L. L. Costanzo, S. Pistara, G. Condorelli, *J. Photochem.* **21**, 45–51 (1983).
23. The use of $[N^nBu_4]Cl$ by Zuo compared with the use of $[NEt_4]Cl$ in this study is not expected to have any impact on the speciation and relevant reactivity.
24. R. Zhao, L. Shi, *Org. Chem. Front.* **5**, 3018–3021 (2018).
25. N. S. Liebov *et al*., *ChemCatChem* **11**, 5045–5054 (2019).
26. The catalyst loading used by Zuo was 0.5 mol % cerium complex, which is lower than our 5 mol %. Using 0.5 mol % loading gave us a large variation in yield. We attribute these differences to mass measurement of the catalysts and differences in light flux.
27. M. Quant, "The Kinetics and Mechanism of Chlorine Atom Reactions with Cyclic Ethers," thesis, California State University, Fullerton, CA (2005).
28. A. Lannung, J. Gjaldbaek, S. Rundqvist, E. Varde, G. Westin, *Acta Chem. Scand.* **14**, 1124–1128 (1960).
29. The usage of either DIAD or DBAD for the photocatalytic alkane activation was in accordance with the experimental conditions in (*9*).
30. I. Alkorta, I. Rozas, J. Elguero, *Ber. Bunsenges. Phys. Chem* **102**, 429–435 (1998).
31. S. Hammerum, *J. Am. Chem. Soc.* **131**, 8627–8635 (2009).
32. E. Cervone, F. Diomedi Camassei, *J. Photochem.* **15**, 203–212 (1981).
33. A. S. Mereshchenko *et al*., *J. Phys. Chem. A* **120**, 1833–1844 (2016).
34. A. S. Mereshchenko, S. K. Pal, K. E. Karabaeva, P. Z. El-Khoury, A. N. Tarnovsky, *J. Phys. Chem. A* **116**, 2791–2799 (2012).
35. R. E. Bühler, M. Ebert, *Nature* **214**, 1220–1221 (1967).
36. L. Troian-Gautier *et al*., *Chem. Rev.* **119**, 4628–4683 (2019).
37. S. Rohe, A. O. Morris, T. McCallum, L. Barriault, *Angew. Chem. Int. Ed.* **57**, 15664–15669 (2018).
38. B. C. Gilbert, J. K. Stell, W. J. Peet, K. J. Radford, *J. Chem. Soc. Faraday Trans.* **84**, 3319–3330 (1988).
39. J. T. Jodkowski, M. T. Rayez, J. C. Rayez, T. Bérces, S. Dóbé, *J. Phys. Chem. A* **102**, 9230–9243 (1998).
40. G. A. Russell, *J. Am. Chem. Soc.* **79**, 2977–2978 (1957).
41. G. A. Russell, *J. Am. Chem. Soc.* **80**, 4987–4996 (1958).
42. M. L. Tsao, C. M. Hadad, M. S. Platz, *J. Am. Chem. Soc.* **125**, 8390–8399 (2003).

ACKNOWLEDGMENTS

K. I. Goldberg and N. Tomson (both University of Pennsylvania) and B. Flowers (Lehigh University) are gratefully acknowledged for helpful discussions. R. F. Higgins and G. Panetti (both University of Pennsylvania) are also acknowledged for helpful discussions and technical support. **Funding:** The project was supported by Vagelos Institute for Energy Science and Technology (VIEST), including support for Y.H.W.; Q.Y. was supported as part of the Center for Actinide Science and Technology (CAST), an Energy Frontier Research Center (EFRC) funded by the US Department of Energy (DOE), Office of Science, Basic Energy Sciences (BES), under award number DE-SC0016568. P.J.W. thanks the NSF (CHE-1902509) for financial support. We also thank the University of Pennsylvania for support of this work. **Author contributions:** Q.Y. performed syntheses, spectroscopy, reactivity, catalysis, selectivity, and kinetics experiments and DFT calculation and drafted and revised the manuscript; Y.H.W. conducted methane and ethane activation experiments and revised the manuscript; Y.Q. contributed to the methane reactor design, substrate activation, selectivity studies, DFT calculations, and revision of the manuscript; M.G. and P.J.C. conducted x-ray crystallography; and P.J.W. and E.J.S. supervised and administered all aspects of the project. **Competing interests:** The authors declare no competing interests. **Data and materials availability:** X-ray data are available free of charge from the Cambridge Structural Database under deposition number 2015363–2015364. NMR spectra, x-ray crystal structures, element analysis, UV-visible spectra, luminescence spectra, and mass spectra are included in the SM.

SUPPLEMENTARY MATERIALS

science.sciencemag.org/content/372/6544/847/suppl/DC1
Materials and Methods
Figs. S1 to S90
Tables S1 to S12
References (*43*–*53*)

15 July 2020; resubmitted 14 January 2021
Accepted 13 April 2021
10.1126/science.abd8408

NANOMATERIALS

Biphenylene network: A nonbenzenoid carbon allotrope

Qitang Fan[1]†, Linghao Yan[2]†, Matthias W. Tripp[1], Ondřej Krejčí[2], Stavrina Dimosthenous[2], Stefan R. Kachel[1], Mengyi Chen[1], Adam S. Foster[2,3], Ulrich Koert[1], Peter Liljeroth[2]*, J. Michael Gottfried[1]*

The quest for planar sp^2-hybridized carbon allotropes other than graphene, such as graphenylene and biphenylene networks, has stimulated substantial research efforts because of the materials' predicted mechanical, electronic, and transport properties. However, their syntheses remain challenging given the lack of reliable protocols for generating nonhexagonal rings during the in-plane tiling of carbon atoms. We report the bottom-up growth of an ultraflat biphenylene network with periodically arranged four-, six-, and eight-membered rings of sp^2-hybridized carbon atoms through an on-surface interpolymer dehydrofluorination (HF-zipping) reaction. The characterization of this biphenylene network by scanning probe methods reveals that it is metallic rather than a dielectric. We expect the interpolymer HF-zipping method to complement the toolbox for the synthesis of other nonbenzenoid carbon allotropes.

The synthesis of fullerenes (*1*), carbon nanotubes (*2*), graphene (*3*), and cyclo[18]carbon (*4*) from customized molecular precursors has initiated the era of designer carbon allotropes built from sp, sp^2, and sp^3-hybridized carbon atoms (*5*). Although numerous sp^2-hybridized planar carbon allotropes such as graphene (*6*), pentaheptite (*7*), and biphenylene network (*8*) were proposed (Fig. 1A), only graphene has been realized as a purely hexagonal net (*3*). Progress in the synthesis of other planar three-coordinate carbon nets (*6*) with nonhexagons such as four-, five-, seven-, and eight-membered rings has been very limited. Recently, expanding on the highly successful bottom-up synthesis of benzenoid graphene-related nanostructures (*9*–*13*), several nonbenzenoid nanographenes (*14*–*17*) and nanoribbons (*18*–*20*) with embedded nonhexagonal rings were reported.

Nonetheless, these carbon nanostructures only exhibit repeating nonhexagonal motifs along one dimension, which has hampered the study of the properties of planar nonbenzenoid carbon allotropes. For instance, the successful synthesis and characterization of biphenylene polymer chains cannot serve to clarify the theoretical debate on whether a biphenylene network is dielectric (*21*) or metallic (*22*, *23*). Attempts to add nonhexagonal carbon rings along the second dimension through hierarchical polymerization of nonbenzenoid molecules were of limited success. For example, the lateral fusion of polyazulene chains yielded only small segments of phagraphene (*24*), a planar carbon net with five-, six-, and seven-membered rings, because the orientation of the azulene moieties could not be controlled (*25*). Similarly, efforts toward the synthesis of a biphenylene network (BPN, Fig. 1B) through sequential deiodinative and debrominative coupling of 1,4,5,8-tetraiodo-2,3,6,7-tetrabromobiphenylene (TTBP, Fig. 1B) failed at the initial polymerization step (*26*).

[1]Department of Chemistry, Philipps-Universität Marburg, 35032 Marburg, Germany. [2]Department of Applied Physics, Aalto University, FI-00076 Aalto, Finland. [3]Nano Life Science Institute (WPI-NanoLSI), Kanazawa University, Kakuma-machi, 920-1192 Kanazawa, Japan.
†These authors contributed equally to this work.
***Corresponding author. Email: peter.liljeroth@aalto.fi (P.L.); michael.gottfried@chemie.uni-marburg.de (J.M.G.)**

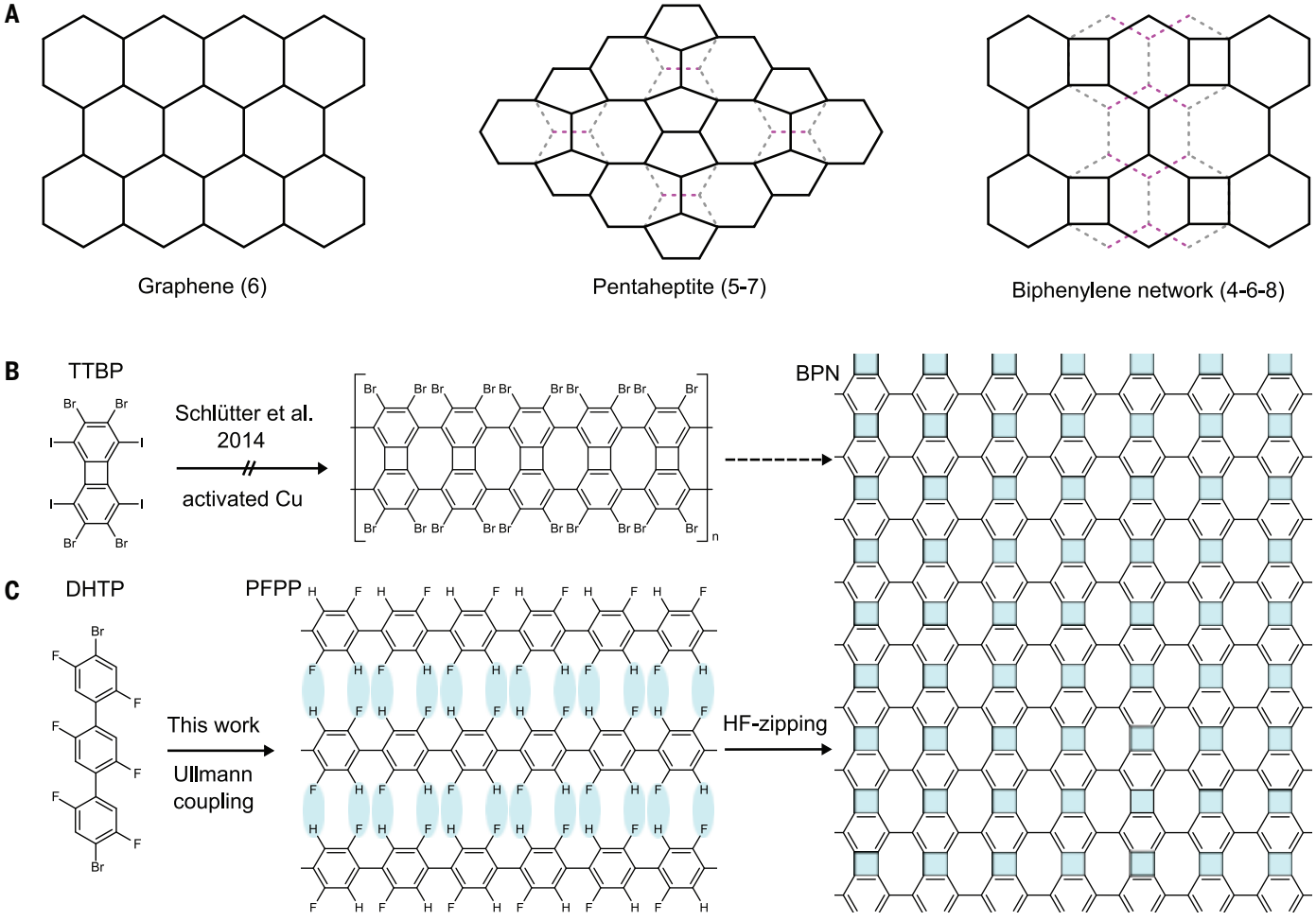


Fig. 1. Synthetic strategies toward the planar nonbenzenoid biphenylene network (BPN). (**A**) Lattice structures of three planar carbon allotropes: graphene, carbon pentaheptite (5-7), and biphenylene network (4-6-8). The latter two formally result from graphene by reorganization of bonds (magenta dotted lines). (**B**) Previous attempts toward the synthesis of BPN from the TTBP monomer. (**C**) DHTP monomer forming BPN by a two-step sequence consisting of linear polymerization followed by interchain HF-zipping.

Here, we demonstrate an alternative approach in which the nonbenzenoid structural elements were not contained in the precursor but were formed during the lateral dehydrofluorination (HF-zipping) fusion of benzenoid polyphenylene chains. As shown in Fig. 1C, 4,4″-dibromo-2,2′,2″,5,5′,5″-hexafluoro-1,1′:4′,1″-terphenyl (DHTP) first polymerized through debrominative coupling (*27*) on a Au(111) surface and formed well-aligned assemblies of poly(2,5-difluoro-*para*-phenylene) (PFPP) chains. In a second step, these chains underwent C-C coupling by HF-zipping (*28*–*31*) to form a biphenylene network. The interchain HF-zipping allowed C-C bond formation exclusively between a C-F and a C-H moiety (Fig. 1C, cyan ovals) but not between two C-H or two C-F moieties. As a result, four- and eight-membered rings formed selectively between the chains. Adequately positioned C-F moieties were essential for the formation of the nonbenzenoid structure. In their absence, such as in the case of plain poly(*para*-phenylene) chains, dehydrogenative C-C coupling led to the formation of six-membered rings and thus to regular graphene (*32*, *33*).

The monomer DHTP was synthesized in solution through a two-step sequence (see supplementary materials) and then vapor-deposited in ultrahigh vacuum onto a clean Au(111) surface held at 300 K. Related scanning tunneling microscopy (STM) images are shown in fig. S1. Subsequent annealing to 500 K induced the formation of PFPP chains by debrominative C-C coupling. An ordered island of well-aligned PFPP chains (Fig. 2A) exhibited a pronounced zigzag appearance in the zoom-in STM image in Fig. 2D. The periodicity of 8.8 ± 0.2 Å along the chain arose from alternating up-down tilting of the 2,5-difluoro-*para*-phenylene (FPP) units, as illustrated by the overlaid chemical structure in Fig. 2D. This model was confirmed by the noncontact atomic force microscopy (nc-AFM) image in fig. S2B.

The aligned PFPP chains fused laterally through HF-zipping to form a biphenylene network during annealing to 680 K, as shown by the STM image in Fig. 2B. This condensation reaction resulted in considerable lateral contraction. The high-resolution nc-AFM images (Fig. 2, E and F) of the regions marked by the white rectangles in Fig. 2B revealed armchair-edged biphenylene ribbons (BPRs) with widths of 12 and 18 carbon atoms (12-BPR and 18-BPR). These BPRs have alternating H/F edge termination rather than pure H termination, as illustrated by the chemical structure in Fig. 2E and confirmed by the simulated AFM images in figs. S3 and S4. The widest ribbon we observed (21-BPR) was achieved by further annealing the sample in Fig. 2B to 700 K (Fig. 2C).

The selectivity for biphenylene network formation is related to the two-dimensional (2D) chirality of the PFPP chains. Only HF-zipping between chains of identical handedness led to four- and eight-membered rings (4-8 type fusion; Fig. 2D). Otherwise, six-membered rings formed (6-6 type fusion; Fig. 2D), resulting

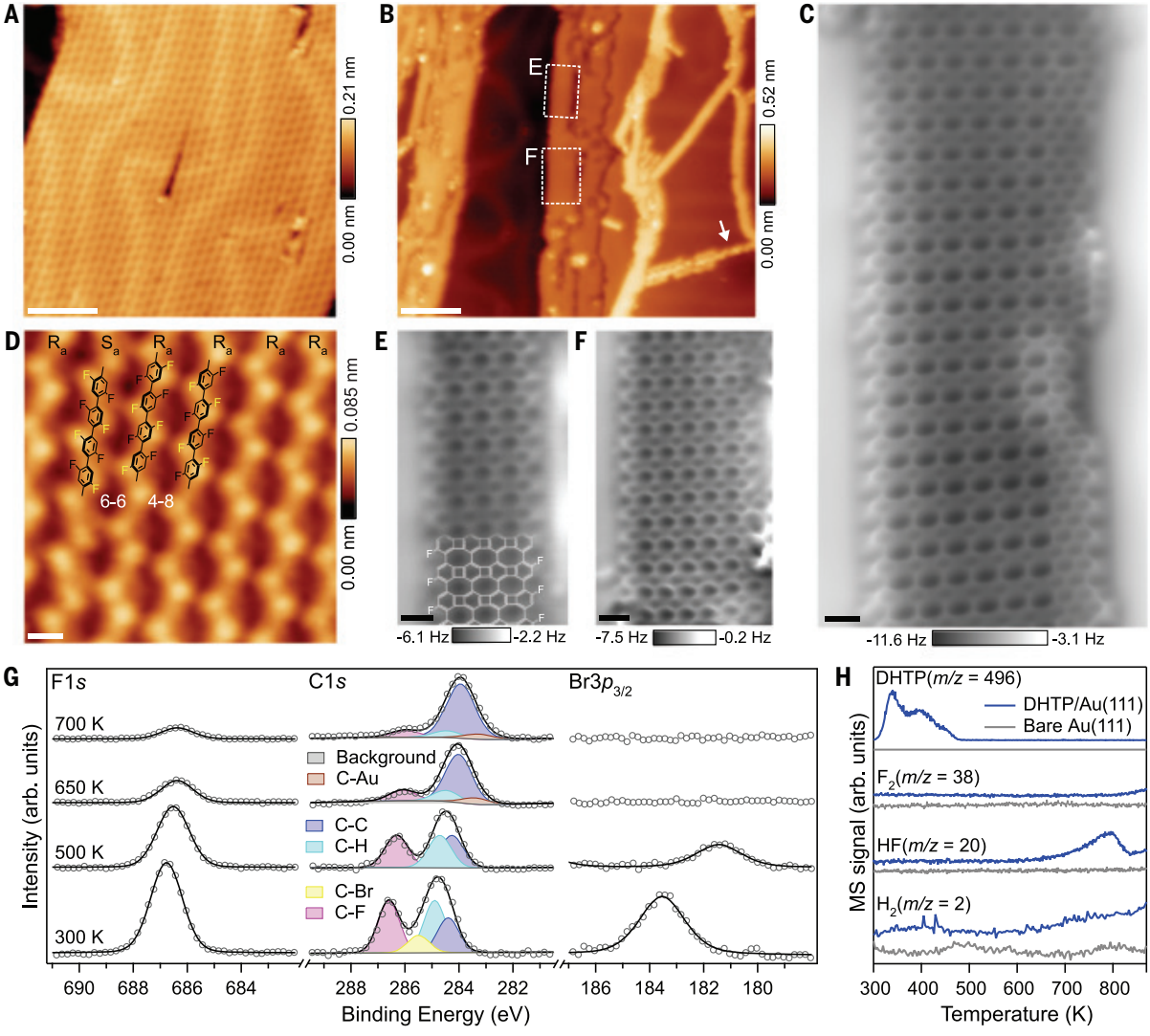


Fig. 2. Formation of biphenylene network by two-step polymerization of DHTP. (**A** and **B**) Overview STM images taken after deposition of DHTP onto Au(111) at 300 K followed by post-annealing to 500 K (A) and 680 K (B). The white arrow in (B) marks a remaining PFPP chain for comparison. (**C**) nc-AFM image of a wide biphenylene ribbon (BPR) obtained by further annealing of the sample in (B) to 700 K. Note that the BPR is jointed with regular graphene at the right side due to minor parasitic 6-6 type fusion. (**D**) Zoom-in STM image of the PFPP chains in (A) overlaid with chemical structures; 2D enantiomers labeled with R_a and S_a. (**E** and **F**) Zoom-in nc-AFM images of the BPRs outlined by the white rectangles in panel (B). The image in (E) is overlaid with the chemical structure. Scale bars, 5 nm [(A) and (B)], 0.5 nm [(C) to (F)]. (**G**) XPS spectra for the indicated core levels and annealing temperatures. (**H**) Mass spectrometer signals for the indicated *m/z* values recorded during controlled heating (1 K/s) of bare and monolayer DHTP-covered Au(111).

in the formation of an armchair-edged graphene nanoribbon (6-AGNR) with the normal benzenoid topology (fig. S6). The 4-8 type fusion was overall favored [2.4 (±0.3):1 over the 6-6 type; see supplementary text and fig. S8 for yield analysis] because each PFPP domain consisted mainly of chains with identical handedness, such as the R_a handedness in Fig. 2D (see also fig. S5). Therefore, the aggregation of the PFPP chains in almost homochiral domains was essential for the formation of a biphenylene network. Furthermore, sufficient length of the PFPP chains is a prerequisite for the formation of wide BPRs (see supplementary text).

The reaction progress was monitored by x-ray photoelectron spectroscopy (XPS) (Fig. 2G) and temperature-programmed desorption (TPD) mass spectrometry (Fig. 2H). For as-deposited DHTP on Au(111) at 300 K (Fig. 2G, 300 K), the F1s (686.8 eV) and Br3$p_{3/2}$ (183.5 eV) binding energies were typical for C-F and C-Br groups (*28*, *34*) and confirmed that carbon-halogen bonds were intact. The C1s signal could be consistently deconvoluted into four components attributed to C-F (pink), C-Br (yellow), C-H (cyan), and C-C (blue) with 1:3:3:2 intensity ratios, in agreement with the composition of DHTP. XPS also confirmed the formation of PFPP chains at 500 K: Lowering of the Br3$p_{3/2}$ binding energy by 2.1 eV indicates C-Br bond dissociation (*34*), and the C1s signal could be deconvoluted into three components (1:1:1) representing C-F, C-H, and C-C bonds (Fig. 2G, 500 K), in agreement with the chemical structure of the chains. We attributed the slight overall shifts (–0.3 eV) of C1s and F1s signals to a work-function change (*35*), whereas their attenuation (35% less) was caused by partial desorption of DHTP, as confirmed by the TPD signal of DHTP in Fig. 2H.

The gradual attenuation of the F1s and C-F–related C1s signals upon further annealing (Fig. 2G, 650 K and 700 K) was indicative of partial removal of fluorine from the C-F groups by HF-zipping. The corresponding TPD trace confirmed HF release above 600 K (Fig. 2H and Fig. S9). Note that the C1s spectra at 650 K

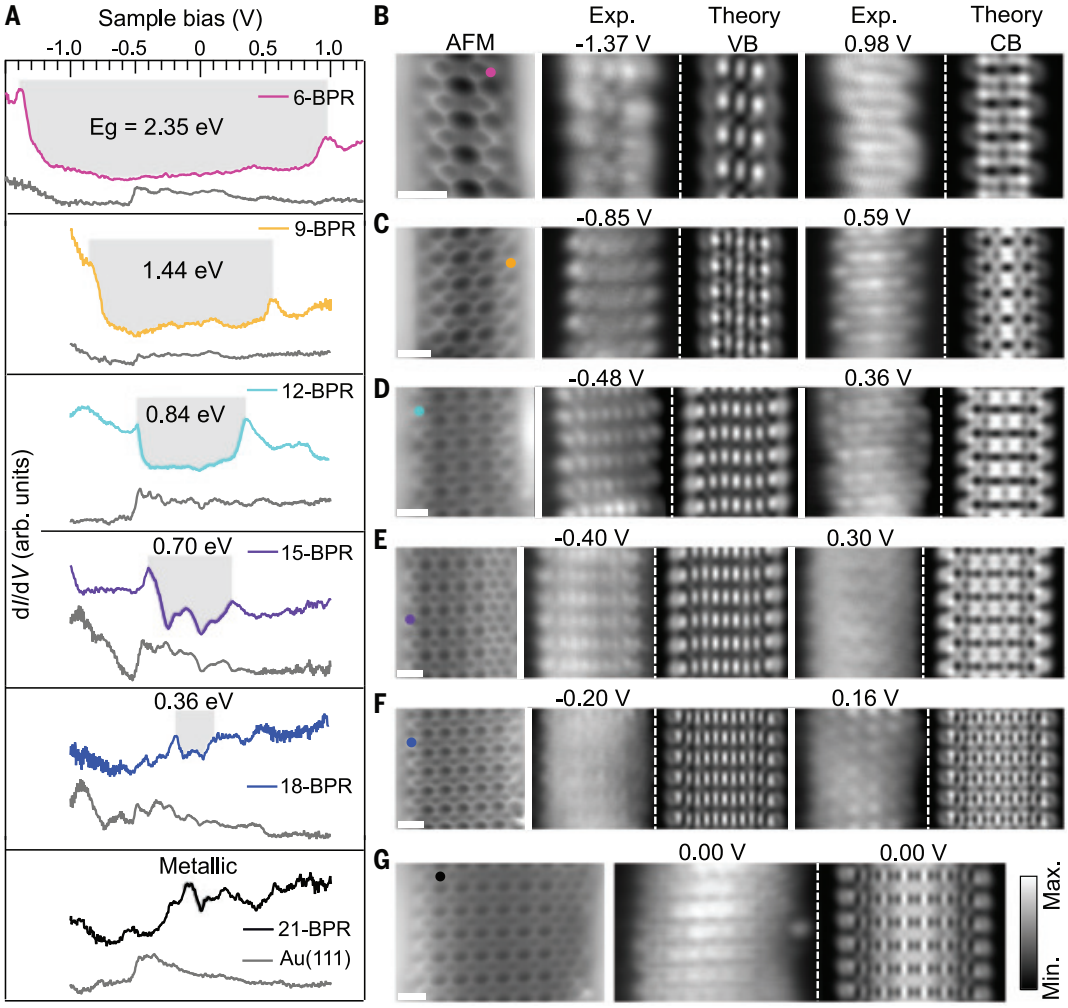


Fig. 3. Electronic properties of BPRs with different widths. (**A**) Differential conductance (d*I*/d*V*) spectra (colored curves) taken at the positions marked with corresponding colored dots in the leftmost panels of (B) to (G). The gray curves are reference d*I*/d*V* spectra taken at clean Au(111). The shaded regions denote the bandgaps between the peaks related to VB and CB onsets. (**B** to **G**) nc-AFM images, experimental and simulated d*I*/d*V* maps at the VB and CB onsets of the 6-BPR (B), 9-BPR (C), 12-BPR (D), 15-BPR (E), 18-BPR (F), and 21-BPR (G). These nc-AFM images are cutouts of the nc-AFM images in Fig. 2, C, E, and F and fig. S12, C to E. The simulated d*I*/d*V* maps are consistent with fluorine substituents at the edges (see fig. S18 for a detailed comparison), in agreement with the AFM images. All scale bars, 0.5 nm. The gray scale for all d*I*/d*V* maps is displayed to the right of (G). All d*I*/d*V* spectra and maps were recorded with CO-functionalized tips.

and 700 K showed a component at 283.4 eV, labeled C-Au, which we attributed to benzyne intermediates bonding to the surface after removal of H/F pairs in PFPP chains (fig. S11). This component decreased from 650 to 700 K because of the progressive fusion of the PFPP chains. Therefore, we tentatively propose the coexistence of HF-zipping (major reaction pathway) and the benzyne-based mechanism (minor reaction pathway) for the lateral fusion of PFPP chains (see supplementary text and fig. S10).

We systematically characterized BPRs of different widths with scanning tunneling spectroscopy and density functional theory (DFT) calculations. Figure 3A shows the normalized differential conductance (d*I*/d*V*) spectra of six different BPRs with widths from 6 to 21 carbon atoms. The spectra were taken at the positions marked by the colored dots in the AFM images on the left sides of Fig. 3, B to G. The narrower BPRs (6-BPR to 12-BPR) showed distinct valence band (VB) and conduction band (CB) onsets (see also additional d*I*/d*V* spectra and maps in figs. S13 and S14). Detecting the resonances in the d*I*/d*V* spectra corresponding to the band onsets in the wider BPRs (15-BPR to 21-BPR) was more difficult because of the narrow gaps and extra features around zero bias potentially arising from the Au(111) surface state.

We used d*I*/d*V* maps (Figs. 3, B to G, middle and right panels, Exp. column) to identity which features in the d*I*/d*V* spectra corresponded to states with similar symmetry relative to the VB and CB of the narrower BPRs (see also additional d*I*/d*V* spectra and maps in figs. S15 to S17). These features matched the simulated d*I*/d*V* maps of the VB and CB onsets (Fig. 3, B to G, middle and right panels, Theory column). For 21-BPR, we could detect orbital features in the d*I*/d*V* maps (Fig. 3G and fig. S17B) at all bias voltages, indicating the closing of the gap corresponding to metallic electronic structure. In addition, as assessed by comparison with simulation, the zero-bias d*I*/d*V* map corresponded to a mixture of the VB and CB features (arising from states at different momenta; see fig. S19 for calculated band structures), again consistent with the metallic response.

The bandgap evolution of the BPRs with different widths is summarized in Fig. 4. The measured gaps are overall somewhat larger than the values predicted by DFT at the HSE06 level, but the trend of decreasing bandgaps with increasing widths of the BPRs (Fig. 4, magenta line) agreed well with calculations (black line). This decrease was much steeper than that for the corresponding AGNR series reported previously (Fig. 4, blue line) (*33*, *36*). In contrast to the benzenoid AGNRs, the bandgap of the nonbenzenoid BPRs closed completely between 18-BPR and 21-BPR. According to the DFT calculations, the edge termination has no substantial influence on the bandgaps of the BPRs (fig. S19). This result was also consistent with the predicted bandgaps of pure H-terminated BPRs in previous work (*22*) (fig. S20). The rapid decrease of the measured gaps (from 2.35 to 0 eV) of biphenylene networks with increasing sizes provided strong evidence that this material had metallic character, rather than being dielectric with a gap of 2 eV, as was reported in a previous theoretical study (*21*).

Our interpolymer HF-zipping technique for the formation of rings with nonbenzenoid topology in a periodic arrangement paves the way for the exploration of new planar sp^2

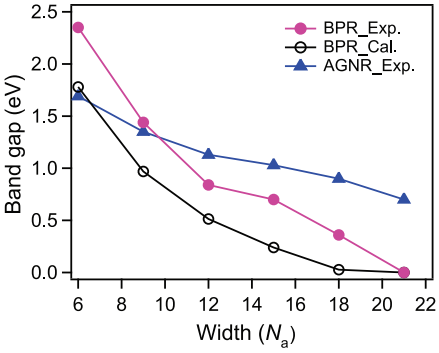


Fig. 4. Bandgaps of BPRs and AGNRs. Comparison between experimental (BPR_Exp.) and calculated (BPR_Cal.) bandgaps of BPRs with AGNRs (AGNR_Exp.) of the same width, as given by the number of carbon atoms, N_a. The AGNR values are adapted from (*33*) on Au(111) and (*36*) on monolayer gold silicide on Au(111).

carbon allotropes and their properties. Further synthesis progress will focus on increasing yield and selectivity, where the on-surface approach can offer distinct advantages over solution-based reactions (*37*). The HF-zipping reaction is also expected to work on metal-oxide surfaces (*28*, *30*), offering decoupling from the metallic substrate. Further direct potential for applications arises from transfer to other substrates or media. For instance, nonbenzenoid 2D carbon allotropes with large rings (>6 members) may represent superior anode materials in lithium-ion batteries because of their predicted larger lithium storage capacity relative to graphene (*38*). The revealed metallicity of the biphenylene network also makes it a candidate for conducting wires in future carbon-based circuitry.

REFERENCES AND NOTES

1. H. W. Kroto, J. R. Heath, S. C. O'Brien, R. F. Curl, R. E. Smalley, *Nature* **318**, 162–163 (1985).
2. S. Iijima, T. Ichihashi, *Nature* **363**, 603–605 (1993).
3. K. S. Novoselov *et al.*, *Science* **306**, 666–669 (2004).
4. K. Kaiser *et al.*, *Science* **365**, 1299–1301 (2019).
5. A. Hirsch, *Nat. Mater.* **9**, 868–871 (2010).
6. A. T. Balaban, *Comput. Math. Appl.* **17**, 397–416 (1989).
7. V. H. Crespi, L. X. Benedict, M. L. Cohen, S. G. Louie, *Phys. Rev. B* **53**, R13303–R13305 (1996).
8. A. T. Balaban, C. C. Rentia, E. Ciupitu, *Rev. Roum. Chim.* **13**, 231–247 (1968).
9. J. Cai *et al.*, *Nature* **466**, 470–473 (2010).
10. D. J. Rizzo *et al.*, *Nature* **560**, 204–208 (2018).
11. P. Ruffieux *et al.*, *Nature* **531**, 489–492 (2016).
12. L. Yan, P. Liljeroth, *Adv. Phys. X* **4**, 1651672 (2019).
13. Z. Chen, A. Narita, K. Müllen, *Adv. Mater.* **32**, e2001893 (2020).
14. S. Mishra *et al.*, *Nat. Commun.* **9**, 1714 (2018).
15. J. Liu *et al.*, *J. Am. Chem. Soc.* **141**, 12011–12020 (2019).
16. J. Hieulle *et al.*, *Nano Lett.* **18**, 418–423 (2018).
17. I. C.-Y. Hou *et al.*, *J. Am. Chem. Soc.* **142**, 10291–10296 (2020).
18. M. Liu *et al.*, *Nat. Commun.* **8**, 14924 (2017).
19. C. Sánchez-Sánchez *et al.*, *Chem. Eur. J.* **25**, 12074–12082 (2019).
20. J. I. Urgel *et al.*, *Angew. Chem. Int. Ed.* **59**, 13281–13287 (2020).
21. N. Tyutyulkov, F. Dietz, K. Müllen, M. Baumgarten, *Chem. Phys. Lett.* **272**, 111–114 (1997).
22. M. A. Hudspeth, B. W. Whitman, V. Barone, J. E. Peralta, *ACS Nano* **4**, 4565–4570 (2010).
23. N. N. Karaush, G. V. Baryshnikov, B. F. Minaev, *Chem. Phys. Lett.* **612**, 229–233 (2014).
24. Z. Wang *et al.*, *Nano Lett.* **15**, 6182–6186 (2015).
25. Q. Fan *et al.*, *J. Am. Chem. Soc.* **141**, 17713–17720 (2019).
26. F. Schlütter, T. Nishiuchi, V. Enkelmann, K. Müllen, *Angew. Chem. Int. Ed.* **53**, 1538–1542 (2014).
27. W. Wang, X. Shi, S. Wang, M. A. Van Hove, N. Lin, *J. Am. Chem. Soc.* **133**, 13264–13267 (2011).
28. M. Kolmer *et al.*, *Science* **363**, 57–60 (2019).
29. A.-K. Steiner, K. Y. Amsharov, *Angew. Chem. Int. Ed.* **56**, 14732–14736 (2017).
30. M. Kolmer *et al.*, *Science* **369**, 571–575 (2020).
31. K. Y. Amsharov, P. Merz, *J. Org. Chem.* **77**, 5445–5448 (2012).
32. A. Basagni *et al.*, *J. Am. Chem. Soc.* **137**, 1802–1808 (2015).
33. N. Merino-Díez *et al.*, *ACS Nano* **11**, 11661–11668 (2017).
34. D. Han *et al.*, *J. Phys. Chem. C* **124**, 5248–5256 (2020).
35. M. Chen *et al.*, *J. Phys. Chem. C* **118**, 6820–6830 (2014).
36. O. Deniz *et al.*, *Nano Lett.* **17**, 2197–2203 (2017).
37. S. Clair, D. G. de Oteyza, *Chem. Rev.* **119**, 4717–4776 (2019).
38. A. Lherbier *et al.*, *Phys. Rev. Mater.* **2**, 085408 (2018).

ACKNOWLEDGMENTS

This research made use of the Aalto Nanomicroscopy Center (Aalto NMC) facilities. Computing resources from the Aalto Science-IT Project and CSC, Helsinki, are gratefully acknowledged. **Funding:** Supported by the Deutsche Forschungsgemeinschaft through projects 223848855-SFB1083 and GO1812/2-1; the State of Hessen (LOEWE Focus Group PriOSS); the European Research Council (ERC-2017-AdG no. 788185); the Academy of Finland (Academy professor funding nos. 318995 and 320555 and project nos. 311012 and 314882); an Alexander von Humboldt Foundation research fellowship for postdoctoral researchers (Q.F.); the European Union's Horizon 2020 research and innovation program (Marie Skłodowska-Curie Actions Individual Fellowship nos. 839242 and 845060) (L.Y. and O.K.); and the World Premier International Research Center Initiative (WPI), MEXT, Japan (A.S.F.). **Author contributions:** J.M.G., P.L., and U.K. conceived and supervised the experiments; Q.F., L.Y., and M.C. developed the on-surface synthesis protocols and did the STM/AFM measurements and the spectroscopic analysis; M.W.T. synthesized the precursor monomers; S.R.K. did the TPD experiments; O.K. and S.D. performed the simulations under the supervision of A.S.F.; Q.F., L.Y., O.K., and S.D. made the figures; and Q.F., L.Y., P.L., and J.M.G. cowrote the paper. All authors discussed the results and commented on the manuscript at all stages. **Competing interests:** The authors declare no competing financial interests. **Data and materials availability:** All data are available in the main text or the supplementary materials. Data and metadata for all simulations are openly available at doi.org/10.5281/zenodo.4740196 under a CC-BY 4.0 license.

SUPPLEMENTARY MATERIALS

science.sciencemag.org/content/372/6544/852/suppl/DC1
Materials and Methods
Supplementary Text
Figs. S1 to S24
References (*39*–*51*)

6 January 2021; accepted 14 April 2021
10.1126/science.abg4509

CONSERVATION

Balancing conservation priorities for nature and for people in Europe

Louise M. J. O'Connor[1]*, Laura J. Pollock[1,2], Julien Renaud[1], Willem Verhagen[3,4], Peter H. Verburg[3,5], Sandra Lavorel[1], Luigi Maiorano[6], Wilfried Thuiller[1]

There is an urgent need to protect key areas for biodiversity and nature's contributions to people (NCP). However, different values of nature are rarely considered together in conservation planning. Here, we explore potential priority areas in Europe for biodiversity (all terrestrial vertebrates) and a set of cultural and regulating NCP while considering demand for these NCP. We quantify the spatial overlap between these priorities and their performance in representing different values of nature. We show that different priorities rarely coincide, except in certain irreplaceable ecosystems. Notably, priorities for biodiversity better represent NCP than the reverse. Theoretically, protecting an extra 5% of land has the potential to double conservation gains for biodiversity while also maintaining some essential NCP, leading to co-benefits for both nature and people.

There have been recent policy calls to expand protection to at least 30% of the world's area by 2030 to halt the extinction of species and degradation of nature's contributions to people (NCP) (*1*, *2*), but exactly where and how to focus conservation efforts is unclear (*3*). Biodiversity underpins functioning ecosystems, which sustain NCP essential to human life (*4*, *5*). These include critical regulating NCP, such as pollination, carbon sequestration, flood prevention, and regulation of air quality. Beyond material benefits, ecosystems also contribute to invaluable parts of human culture: Foraging for wild foods, nature-based tourism, and heritage landscapes are examples of cultural NCP (*5*). Protected areas have been shown to safeguard not only biodiversity (*6*) but also regulating and cultural NCP (*7*). However, although they are conceptually linked, different values of nature [intrinsic, cultural, and regulating (fig. S1)] are likely to be tied to different conservation outcomes (*8*, *9*). So, how can we maximize conservation gains across the spectrum of nature's values?

There is a need to conserve key, irreplaceable ecosystems that are not only particularly diverse but that also sustain rare species and provide locally valuable NCP. So far, few studies

[1]Univ. Grenoble Alpes, Univ. Savoie Mont Blanc, CNRS, LECA, Laboratoire d'Écologie Alpine, F-38000 Grenoble, France. [2]Department of Biology, McGill University, Montreal, QC H3A 1B1, Canada. [3]Environmental Geography Group, Institute for Environmental Studies, Vrije Universiteit Amsterdam, De Boelelaan 1085, 1081HV Amsterdam, Netherlands. [4]Frederick S. Pardee Center for International Futures, Josef Korbel School of International Studies, University of Denver, Denver, CO 80208, USA. [5]Swiss Federal Research Institute WSL, Zürcherstrasse 111, CH-8903 Birmensdorf, Switzerland. [6]Department of Biology and Biotechnologies "Charles Darwin," University of Rome "La Sapienza," Rome, Italy.
*Corresponding author. Email: louise.mj.oconnor@gmail.com

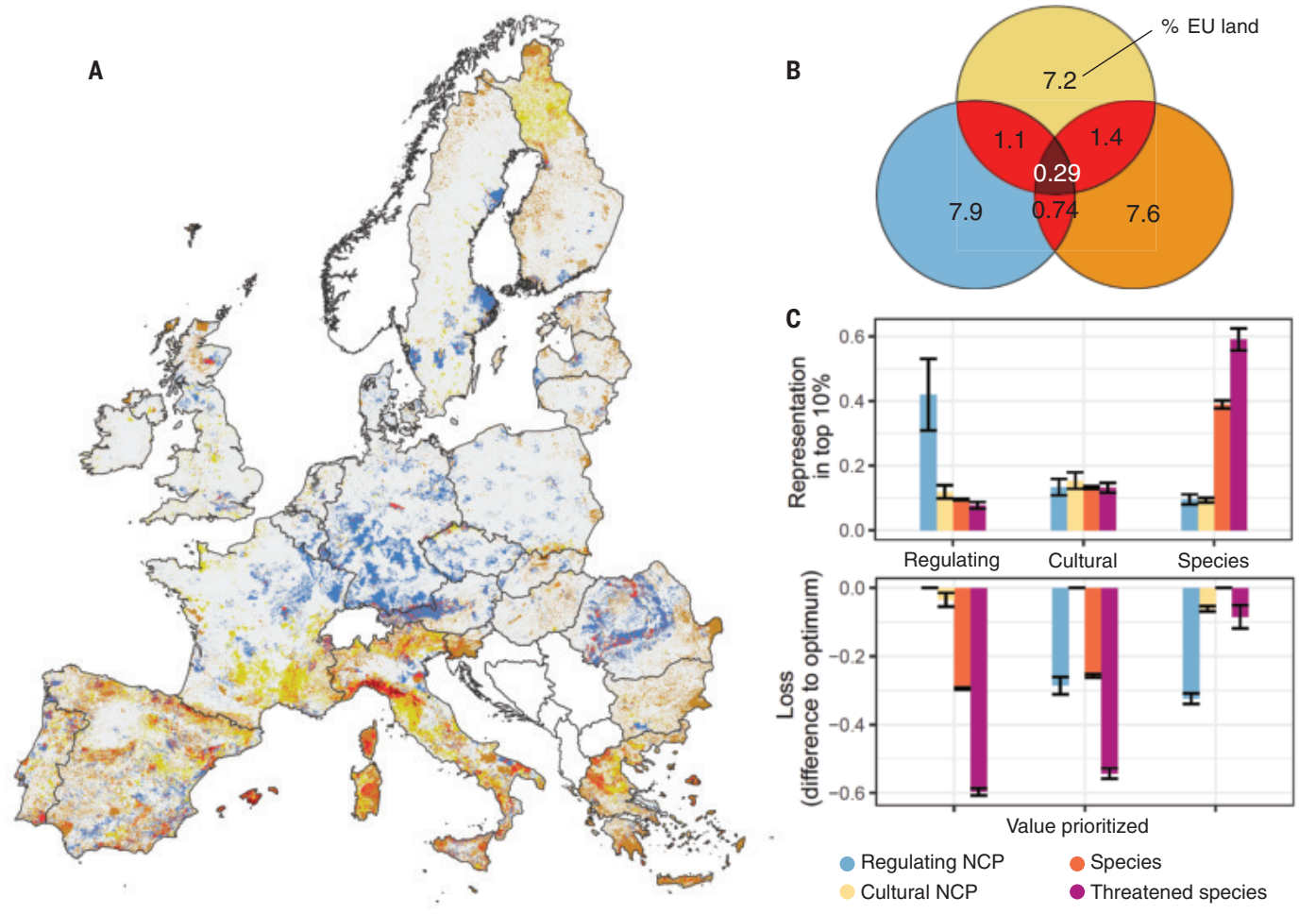
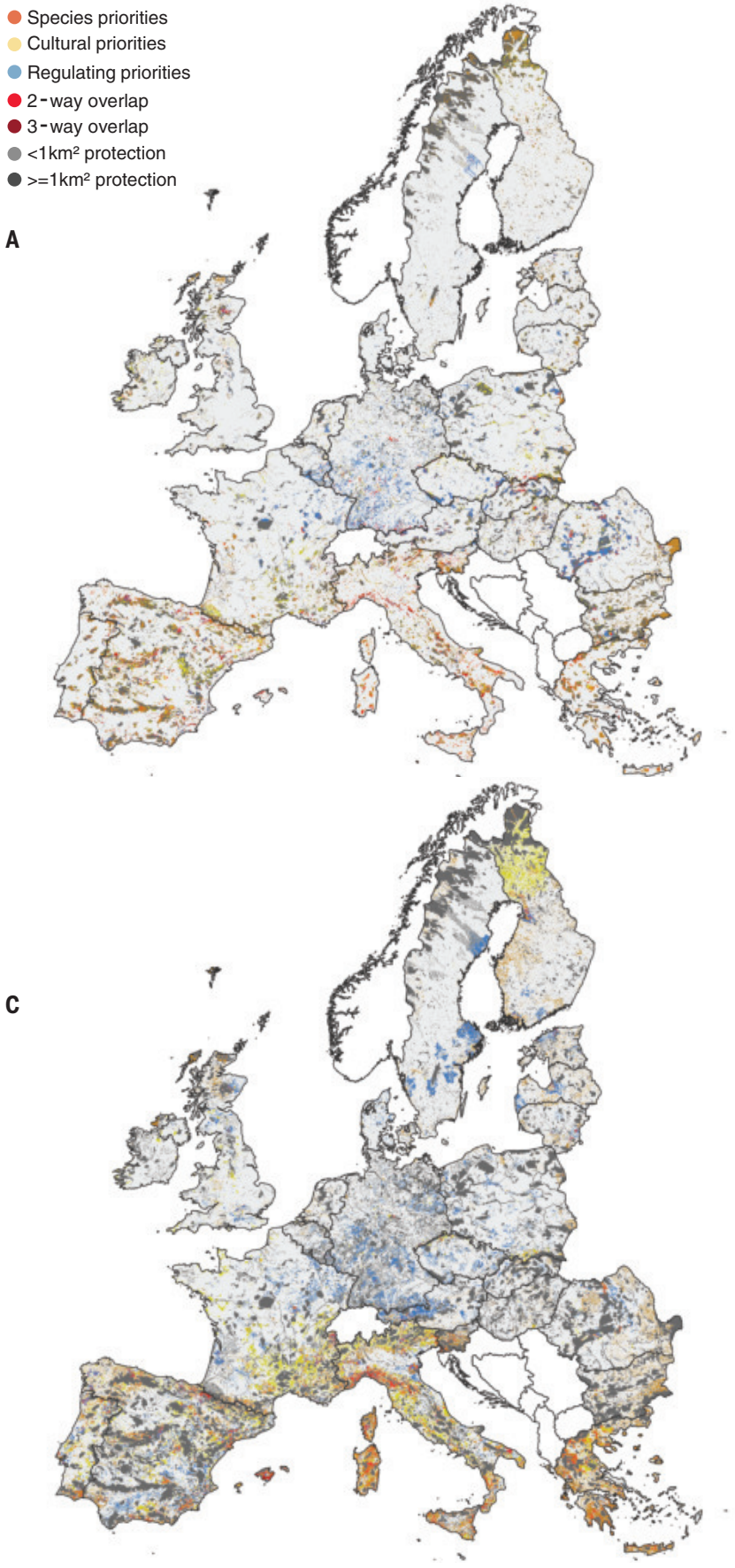


Fig. 1. Spatial coverage and ecological value of top 10% priorities in the optimal scenario. (**A**) Map locating the top 10% priorities for all three nature's values considered. Top priorities for vertebrate species are shown in orange, cultural NCP are in yellow, and regulating NCP are in blue. Areas of overlap between top priorities for two different values are bright red (3.2% of entire study region); areas of overlap between top priorities for all three values are brown (0.29% of entire study region). (**B**) Percentages of the study region (EU27) covered by different priorities and areas of spatial overlap. Color scheme is the same as in (A). (**C**) Bar plots quantifying the proportion of all distributions represented (*y* axis) in the top 10% of each prioritization (*x* axis) on average (error bars represent the SE) and the corresponding loss (i.e., the difference between the incidental representation in the prioritization and the optimal representation of a given value). The colors represent the value: magenta, threatened species; orange, all species; yellow, cultural NCP; blue, regulating NCP.

have combined biodiversity and NCP in spatial conservation planning at large spatial scales (*8*–*10*). Many conservation studies place high value on exceptionally biodiverse locations, which risks overlooking endemic or threatened species (*11*) and might not lead to the most efficient selection of sites (e.g., if biodiverse sites all contain similar species). Consideration of irreplaceability and complementarity between priority areas is crucial to maximize conservation gains in limited amounts of land (*12*, *13*).

Spatial conservation planning also needs to account for existing protected areas. In Europe, high levels of habitat fragmentation and a long history of human development have shaped the continent's biodiversity. Natura 2000, the densest network of protected areas on the planet (fig. S2), incorporates a diversity of management practices, from strict nature reserves to multiuse areas. This variety of management types is relevant for the conservation of different values of nature, especially in a context where human-induced environmental changes already dominate landscapes. However, the designation and management of Natura 2000 protected areas only consider certain rare species and ecosystem types, do not explicitly consider NCP (*14*), and have been repeatedly criticized for not integrating local beneficiaries (*15*).

Here, in line with the Intergovernmental Science-Policy Platform on Biodiversity and Ecosystem Services framework (*5*, *16*) and based on the principles of complementarity and irreplaceability, we contrast conservation priorities at 1-km^2 resolution for three important values of nature in Europe (fig. S1): (i) biodiversity, represented here by all 785 vertebrate species occurring in the study area, including 124 threatened species (fig. S3); (ii) regulating NCP, represented here by carbon sequestration, air quality regulation, flood control, and pollination (fig. S4); and (iii) cultural NCP, represented here by heritage agriculture, heritage forests, foraging areas for wild foods, and nature tourism (fig. S5 and table S1) (*17*). We considered the demand for NCP, so that NCP priorities are ecosystems where a high capacity of providing NCP coincides with a high demand, consistent with the Convention on Biological Diversity targets (*18*). We first identified spatial priorities separately for each value (species, cultural, and regulating NCP) for the entire European Union (EU) regardless of protection status, and we quantified the incidental gains and losses for different nature values within these top priorities. Second, we assessed how well these values of nature are currently represented in the Natura 2000 network of protected areas. As a preliminary step to integrate multiple values of nature into conservation planning, we identified priorities



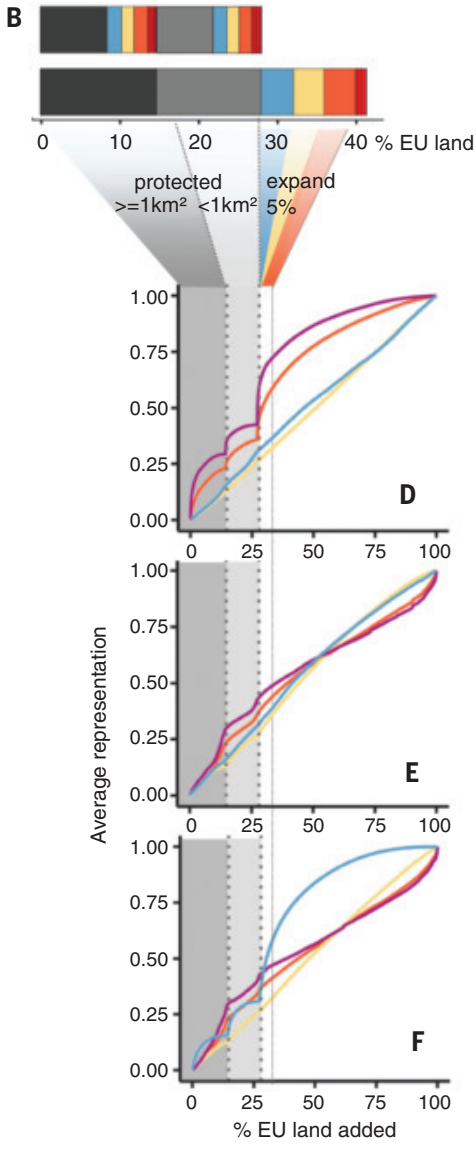


Fig. 2. Key areas for species and NCP within and outside the Natura 2000 protected area network. (**A**) The top 5% value areas within Natura 2000 sites [both large (dark gray) and small (lighter gray)]. (**B**) Bar plots quantifying the surface (percentage of EU land) occupied by each type of priority and their spatial overlap for the top 5% of area within Natura 2000 (top) and the top 5% of area outside Natura 2000 (bottom). (**C**) The top 5% priority areas for the expansion of Natura 2000 for the different nature's values. (**D** to **F**) Performance curves accounting for existing Natura 2000 areas, which quantify the representation (average proportion of distributions) gained for each value as land is added in each scenario, prioritizing species (D), cultural NCP (E), and regulating NCP (F). The colors represent the value: magenta, threatened species; orange, all species; yellow, cultural NCP; blue, regulating NCP. The gray shading indicates the land covered by Natura 2000, and the thin vertical line indicates the top 5% threshold for Natura 2000 expansion.

outside Natura 2000 that would best complement the existing network.

We found that, in an optimal allocation of EU land for conservation, top priorities (the highest-ranked 10% of area) for different values of nature rarely coincide: Areas where top priorities for two values overlap cover 3.2% of EU land, and areas where top priorities for all three values overlap only cover 0.29% of EU land, mostly in Mediterranean woodlands (Fig. 1, A and B; and fig. S9A). Cultural benefits are gained linearly as more area is protected (Fig. 2C and fig. S10A), because of the broad spatial distribution of the cultural NCP considered here. On the contrary, for the vertebrate species and the regulating NCP considered, a few key areas could yield high conservation gains (Fig. 1C and fig. S10A), but not in the same places. Top 10% priorities for species include on average 39% (SE = 1.2%) of all species distributions [including 59% of threatened species distributions but only 10% of regulating NCP (Fig. 1C and fig. S11)], and they are mostly located in Mediterranean countries, Eastern Europe, and Scandinavia (Fig. 1A and fig. S12). By contrast, top priority areas for regulating NCP (Fig. 1C) include on average 42% (SE = 11%) of key ecosystems for the regulating NCP considered (but only 9.5% of all species distributions) and are mostly located in forests of Romania, seminatural habitats of Spain, peri-urban vegetation in Sweden, and riparian ecosystems in central Europe (Fig. 1A and figs. S9A and S12). This analysis shows that simultaneously conserving vertebrate species and regulating NCP can only be achieved through considering them both. Further, species priorities coincide more often with cultural priorities than with regulating priorities (Fig. 1B and figs. S13 and S18) and incidentally represent a much higher proportion of threatened species distributions than priorities for regulating NCP (Fig. 1C and fig. S11). Even though species priorities do not optimally represent regulating NCP, the losses in relation to the optimal representation are smaller when prioritizing species than when prioritizing regulating NCP (Fig. 1C and fig. S19). Our results suggest that focusing on species could be more effective to maximize conservation gains across the spectrum of nature's values than any other value considered here (fig. S19). These results are robust to variations in the top priority threshold, input data, and spatial resolution (figs. S13 to S19).

A gap analysis revealed that half of the Natura 2000 sites are of high conservation value (the highest-ranked 5% of area within the network) for species, regulating, and cultural NCP. A quarter of these top priorities overlap for at least two values (Fig. 2, A and B), mostly in Mediterranean countries (fig. S12). Half of these "protected" cells of high conservation value actually contain less than 100 ha of Natura 2000 (Fig. 2B and figs. S10B and S20). However, despite covering one-fifth of EU land, Natura 2000 does not optimally represent any of nature's values considered here. On average, 70% of key ecosystems for regulating NCP and 64% of all vertebrate species' ranges (and 57% of threatened species' ranges) are not protected (Fig. 2, D to F). Our results suggest that large conservation gains are within reach: If the Natura 2000 network were to be expanded by 5%, the protection of species and key ecosystems for the considered NCP would become equivalent to the optimal scenario (Fig. 2, D to F). If protected, these key areas have the potential to double the current representation of vertebrate species and of regulating NCP in Natura 2000 and also to protect almost 75% of threatened species ranges on average. Locations that complement the existing Natura 2000 areas simultaneously for species and NCP represent 1.38% of EU land, and they are concentrated in Mediterranean woodlands and extensive agricultural areas (Fig. 2C and fig. S9B). This analysis is a preliminary step to integrate different values of nature into conservation planning, but it demonstrates that the protection of small, but well-selected, areas can yield large benefits to both species and NCP.

Here, we harnessed fundamental principles of spatial conservation planning while recognizing the multiplicity of relationships that link humans to nature (*5*) at a continental scale. Despite fundamental differences between key ecosystems for species and NCP, our results indicate that top priorities for species incidentally represent NCP better than the reverse (figs. S11 and S19). This is because there are highly irreplaceable areas for species (particularly for rare or endemic species), and vertebrates occur in a diverse set of ecosystems, including those that provide NCP. By contrast, most NCP are more widespread, and priorities for NCP are unlikely to capture the areas crucial for all vertebrates. Most regulating NCP are primarily provided by forests (fig. S9), whereas protecting the full set of European species requires a complementary set of habitats, of which forests are only one example, alongside grasslands, bare areas, and aquatic ecosystems (fig. S9). Our findings support recent calls that multiple targets are needed to protect the spectrum of nature's values (*19*), but we also show that larger conservation gains are possible, in more specific and ecologically diverse areas, when species are prioritized rather than NCP. Furthermore, terrestrial vertebrates have been shown to play a key role in the provision of both cultural and regulating NCP (*20*, *21*), including threatened species (*22*, *23*), which are efficiently represented in top priorities for all species.

The full set of vertebrate species considered here (many of which are understudied) represent a much broader diversity of ecological niches and evolutionary histories than most conservation planning studies, but these species are still only a subset of Earth's biodiversity. A variety of other taxa (invertebrates, plants, fungi, bacteria) and other biodiversity facets, such as functional or phylogenetic diversity (*24*) (figs. S15 and S18), are even less represented in conservation policies (*25*). Improving knowledge on the spatial distribution of biodiversity and integrating different ecological datasets are paramount to inform conservation (*26*). There is a discrepancy between the currently moderate quality of biodiversity data at large spatial scales and the limited areas available for conservation in Europe. Here, we used a resolution of 1 km^2, which is based on the trade-offs between the uncertainty in species distribution data (*17*), data on locally valuable NCP (e.g., pollination, air quality regulation), and the needed resolution to be sufficiently relevant for conservation planning. Working at a coarser resolution (e.g., 100 km^2) would lead to problems when assessing the Natura 2000 areas (many of which are smaller than 100 ha), especially given the mosaic nature of Europe's landscapes.

Most NCP are currently decreasing except those related to the production of material goods (*27*). Therefore, protecting key ecosystems that provide cultural and regulating NCP is especially urgent. We identified priorities where high NCP capacity overlaps with high demand, but conserving the capacity of ecosystems to provide NCP independently of current demand can be beneficial. Priority areas could shift in future conditions as a result of shifting human demand for NCP [for instance, with increasing population concentration in Europe's more productive regions (*28*)]. In addition, pressures such as climate change and habitat loss will further threaten biodiversity and NCP. Improved biodiversity models and innovative conservation approaches (*29*) are needed to protect biodiversity and NCP into the future as species ranges shift and ecosystems are modified (*30*).

The expansion of agriculture and periurbanization restricts wilderness to ever smaller areas, jeopardizing both biodiversity and NCP. In this context, protected areas should exist along a continuum of human presence, from untouched wilderness to sustainable use of nature. In Europe, Natura 2000 allows precisely this flexibility in management, and our results indicate where to ideally expand protection, in ecosystems that potentially sustain a majority of European vertebrate species and some essential NCP. Our results also highlight the potential ecological value of certain small Natura 2000 sites and the borders of larger Natura 2000 sites. Ensuring that these sites are sufficiently large and adequately connected across space will be crucial to sustain ecological processes and

maintain viable populations for the long term (*31*). But to make realistic recommendations for the expansion of protected areas, further issues will need to be addressed. First, different stakeholders need to take part in the process, and economic and opportunity costs for varying sectors should be considered alongside potential ecological value (*32*). Our prioritization does not include spatial costs (e.g., market value, opportunity costs) (*12*), which would be necessary to designate protected areas but are likely to reduce the ecological value of the conservation solution (*33*). Second, the designation of protected areas takes place at national or local levels, despite widespread recognition that spatial prioritization across broader spatial scales (e.g., continents, ecoregions) is more efficient to conserve the total biodiversity across a region (*13*, *34*). In our study, conservation priorities defined at the level of the EU optimize the representation of both species and NCP and would ultimately be more efficient at preventing widespread losses at the continental scale. Finally, our results highlight the complementary roles that different countries need to play to conserve ecosystems for nature and for people (fig. S12) (*35*). Governing conservation in a concerted manner on much broader taxonomical and geographical scales is crucial to meet global conservation needs but will require mechanisms to efficiently share the responsibilities of conservation management (*36*).

REFERENCES AND NOTES

1. G. M. Mace *et al.*, *Nat. Sustain.* **1**, 448–451 (2018).
2. S. L. Maxwell *et al.*, *Nature* **586**, 217–227 (2020).
3. R. G. Pearson, *Trends Ecol. Evol.* **31**, 366–371 (2016).
4. B. J. Cardinale *et al.*, *Nature* **486**, 59–67 (2012).
5. U. Pascual *et al.*, *Curr. Opin. Environ. Sustain.* **26–27**, 7–16 (2017).
6. F. C. Bolam *et al.*, *Conserv. Lett.* **14**, e12762 (2020).
7. A. Eastwood *et al.*, *Ecosyst. Serv.* **17**, 152–162 (2016).
8. M. Girardello *et al.*, *Sci. Rep.* **9**, 5636 (2019).
9. R. Naidoo *et al.*, *Proc. Natl. Acad. Sci. U.S.A.* **105**, 9495–9500 (2008).
10. W. Xu *et al.*, *Proc. Natl. Acad. Sci. U.S.A.* **114**, 1601–1606 (2017).
11. C. D. L. Orme *et al.*, *Nature* **436**, 1016–1019 (2005).
12. A. S. Kukkala, A. Moilanen, *Biol. Rev. Camb. Philos. Soc.* **88**, 443–464 (2013).
13. F. Montesino Pouzols *et al.*, *Nature* **516**, 383–386 (2014).
14. L. Maiorano *et al.*, *Conserv. Biol.* **29**, 986–995 (2015).
15. G. Louette *et al.*, *J. Nat. Conserv.* **19**, 224–235 (2011).
16. L. M. Pereira *et al.*, *People Nat.* **2**, 1172–1195 (2020).
17. Materials and methods are available in the supplementary materials.
18. W. Verhagen, A. S. Kukkala, A. Moilanen, A. J. A. van Teeffelen, P. H. Verburg, *Conserv. Biol.* **31**, 860–871 (2017).
19. A. Purvis, *Nat. Ecol. Evol.* **4**, 768–769 (2020).
20. S. Lavorel, P. L. Rey, K. Grigulis, M. Zawada, C. Byczek, *Ecosyst. Serv.* **45**, 101155 (2020).
21. D. Hocking, K. Babbitt, *Herpetol. Conserv. Biol.* **9**, 1–17 (2014).
22. P. Mateo-Tomás, P. P. Olea, M. Moleón, N. Selva, J. A. Sánchez-Zapata, *Glob. Ecol. Biogeogr.* **26**, 1459–1470 (2017).
23. L. E. Dee *et al.*, *Trends Ecol. Evol.* **34**, 746–758 (2019).
24. L. J. Pollock, W. Thuiller, W. Jetz, *Nature* **546**, 141–144 (2017).
25. S. Mammola *et al.*, *Proc. Biol. Sci.* **287**, 20202166 (2020).
26. J. M. Heberling, J. T. Miller, D. Noesgaard, S. B. Weingart, D. Schigel, *Proc. Natl. Acad. Sci. U.S.A.* **118**, e2018093118 (2021).
27. K. A. Brauman *et al.*, *Proc. Natl. Acad. Sci. U.S.A.* **117**, 32799–32805 (2020).
28. P. J. Verkerk *et al.*, *Reg. Environ. Change* **18**, 817–830 (2018).
29. L. J. Pollock *et al.*, *Trends Ecol. Evol.* **35**, 1119–1128 (2020).
30. A. Arneth *et al.*, *Proc. Natl. Acad. Sci. U.S.A.* **117**, 30882–30891 (2020).
31. L. Maiorano, A. Falcucci, L. Boitani, *Proc. Biol. Sci.* **275**, 1297–1304 (2008).
32. J. Schleicher *et al.*, *Nat. Sustain.* **2**, 1094–1096 (2019).
33. H. Kujala, J. J. Lahoz-Monfort, J. Elith, A. Moilanen, *Methods Ecol. Evol.* **9**, 2249–2261 (2018).
34. A. S. Kukkala *et al.*, *Biol. Conserv.* **198**, 193–201 (2016).
35. B. B. N. Strassburg *et al.*, *Nature* **586**, 724–729 (2020).
36. E. Dinerstein *et al.*, *Sci. Adv.* **5**, eaaw2869 (2019).
37. L. O'Connor, Spatial priorities for vertebrate species and nature's contributions to people in Europe, Version 1, DataverseNL (2021); https://doi.org/10.34894/TCNKPJ.

ACKNOWLEDGMENTS

The authors are grateful to C. Martinez-Almoyna for creating fig. S1. We also thank L. Zupan, M. Cabeza, and J. Maes for previous discussions on the project. **Funding:** This research was funded through the 2017–2018 Belmont Forum and BiodivERsA joint call for research proposals, under the BiodivScen ERA-Net COFUND program, and with the funding organizations Agence Nationale pour la Recherche (FutureWeb, ANR-18-EBI4–0009) and the Dutch Research Council (FutureWeb, grant E10005). **Author contributions:** W.T. initially conceptualized the research with the help of S.L. W.T., L.J.P., and L.M.J.O. designed the analyses. L.M.J.O. ran the analyses, prepared the figures, and drafted the manuscript with the help of L.J.P. and W.T. P.H.V. and W.V. provided the spatial data for NCP. L.M. provided the data for species distributions and carried out additional spatial analyses. J.R. harmonized the spatial data for NCP and species. All authors contributed to data interpretation and to improving the manuscript. **Competing interests:** The authors declare no competing interests. **Data and materials availability:** Data products and script to analyze the data and produce the figures are accessible online at Dataverse NL (*37*).

SUPPLEMENTARY MATERIALS

science.sciencemag.org/content/372/6544/856/suppl/DC1
Materials and Methods
Appendices S1 to S4
Figs. S1 to S21
Tables S1 to S4
References (*38*–*59*)

29 April 2020; accepted 14 April 2021
10.1126/science.abc4896

PALEOECOLOGY

Global acceleration in rates of vegetation change over the past 18,000 years

Ondřej Mottl[1]*†, Suzette G. A. Flantua[1,2]*†, Kuber P. Bhatta[1], Vivian A. Felde[1,2], Thomas Giesecke[3], Simon Goring[4,5], Eric C. Grimm[6]‡, Simon Haberle[7,8], Henry Hooghiemstra[9], Sarah Ivory[10], Petr Kuneš[11], Steffen Wolters[12], Alistair W. R. Seddon[1,2], John W. Williams[4,5]

Global vegetation over the past 18,000 years has been transformed first by the climate changes that accompanied the last deglaciation and again by increasing human pressures; however, the magnitude and patterns of rates of vegetation change are poorly understood globally. Using a compilation of 1181 fossil pollen sequences and newly developed statistical methods, we detect a worldwide acceleration in the rates of vegetation compositional change beginning between 4.6 and 2.9 thousand years ago that is globally unprecedented over the past 18,000 years in both magnitude and extent. Late Holocene rates of change equal or exceed the deglacial rates for all continents, which suggests that the scale of human effects on terrestrial ecosystems exceeds even the climate-driven transformations of the last deglaciation. The acceleration of biodiversity change demonstrated in ecological datasets from the past century began millennia ago.

One of the clearest forms of biodiversity change during the past century has been the increased rates of species turnover across the marine and terrestrial biospheres (*1*–*3*). Today, >75% of Earth's ice-free land surface has been altered by human land use (*4*), with profound effects on the composition and functioning of ecosystems. Globally, extinction rates are increasing (*5*), although trends in local species richness are ambiguous (*6*).

These increased rates of species turnover, as signified by local and regional changes in community composition, are embedded in a longer-term context in which humanity's footprint has steadily grown since humans first began to alter landscapes for food, energy, and other resources. Hominid use of fire began at least 700,000 years ago (*7*), low-intensity but extensive agricultural land use began ~8000 years ago, and intensive agricultural land use expanded after 6000 years ago (*8*) (Fig. 1B). Detectable human imprints on vegetation began thousands of years ago (*9*, *10*), and the composition and carbon sequestration of many contemporary ecosystems remain profoundly influenced by the legacies of anthropogenic

[1]Department of Biological Sciences, University of Bergen, N-5020 Bergen, Norway. [2]Bjerknes Centre for Climate Research, University of Bergen, N-5020 Bergen, Norway. [3]Department of Physical Geography, Utrecht University, 3508 TC, Utrecht, Netherlands. [4]Department of Geography, University of Wisconsin-Madison, Madison, WI, USA. [5]Center for Climatic Research, University of Wisconsin-Madison, Madison, WI, USA. [6]Department of Earth and Environmental Sciences, University of Minnesota, Minneapolis, MN, USA. [7]Department of Archaeology and Natural History, Australian National University, Canberra, ACT 2601, Australia. [8]Australian Research Council Centre of Excellence in Australian Biodiversity and Heritage, Australian National University, Canberra, ACT 2601, Australia. [9]Department of Ecosystem and Landscape Dynamics, University of Amsterdam, 1098 XH, Amsterdam, Netherlands. [10]Department of Geosciences and the Earth and Environmental Systems Institute (EESI), Penn State University, University Park, PA, USA. [11]Department of Botany, Faculty of Science, Charles University, Prague, Czech Republic. [12]Lower Saxony Institute for Historical Coastal Research, Wilhelmshaven, Germany.
***Corresponding author. Email: ondrej.mottl@gmail.com (O.M.); s.g.a.flantua@gmail.com (S.G.A.F.)**
†These authors contributed equally to this work.
‡Deceased.

land use over the past centuries to millennia (*11*). Nonetheless, there remains a notable knowledge and scale gap between contemporary studies of global biodiversity trends of the past century (*2*) and studies examining early anthropogenic effects on ecosystems. Observational syntheses of global biodiversity trends are limited to the past several centuries, whereas macroscale syntheses of vegetation changes from fossil pollen data have been limited to continental scales (*9*) or are largely qualitative (*12*). Consequently, global patterns and magnitudes of vegetation compositional change, which are important for understanding how biodiversity and ecosystem dynamics have been shaped by climate change and early human activity, are poorly understood.

In parallel, paleoecological studies have shown the high sensitivity of terrestrial ecosystems to the climate changes that accompanied and followed the last deglaciation [~20,000 to 8200 calibrated years before radiocarbon present (cal yr BP, where 0 yr BP is 1950 CE); 20 to 8.2 thousand calibrated years BP (ka); Fig. 1, C and D] (*12*, *13*). In temperate and boreal regions, forest expanded from glacial refugia as temperatures rose and precipitation patterns shifted, with widespread leading-edge range expansions and, for some taxa, trailing-edge range contractions (*14*). Novel ecosystems emerged in response to novel climates and the Late Pleistocene extinction of megaherbivores (*15*). Tropical and subtropical ecosystems responded to rising temperatures linked to increasing greenhouse gases (Fig. 1D) and hydrological shifts driven by precessional controls on monsoons and the Intertropical Convergence Zone (*16*). Consequently, during the Pleistocene-Holocene transition, tropical ecosystems substantially

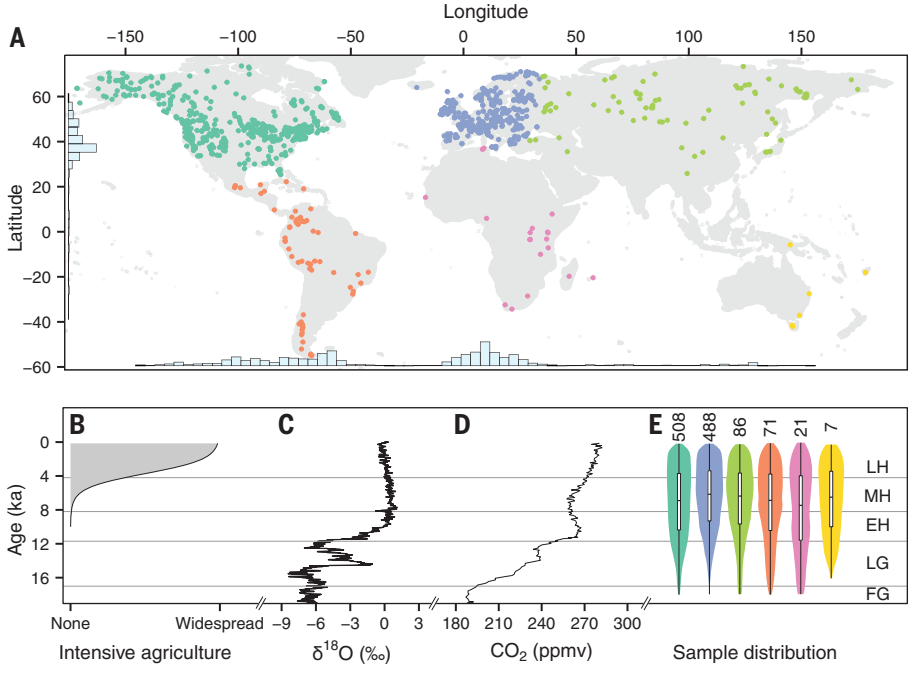


Fig. 1. Spatiotemporal distribution of the fossil pollen sequences analyzed here and climate and anthropogenic changes during the past 18,000 years. (**A**) Spatial distribution of pollen sequences used in this work. Histograms indicate the frequency of sequences across longitude and latitude. (**B**) Development of intensive agriculture based on archaeological expert elicitation (*8*). (**C**) $\delta^{18}O$, a temperature proxy, from the North Greenland Ice Core Project (NGRIP) (*38*). ‰, per mil. (**D**) Atmospheric CO_2 concentration [EPICA DOME C (*39*)]. ppmv, parts per million volume. (**E**) The number of pollen sequences per continent [colors match those in (A)] and sample density over the studied period. FG, full glacial; LG, Lateglacial; EH, Early Holocene; MH, Middle Holocene; LH, Late Holocene.

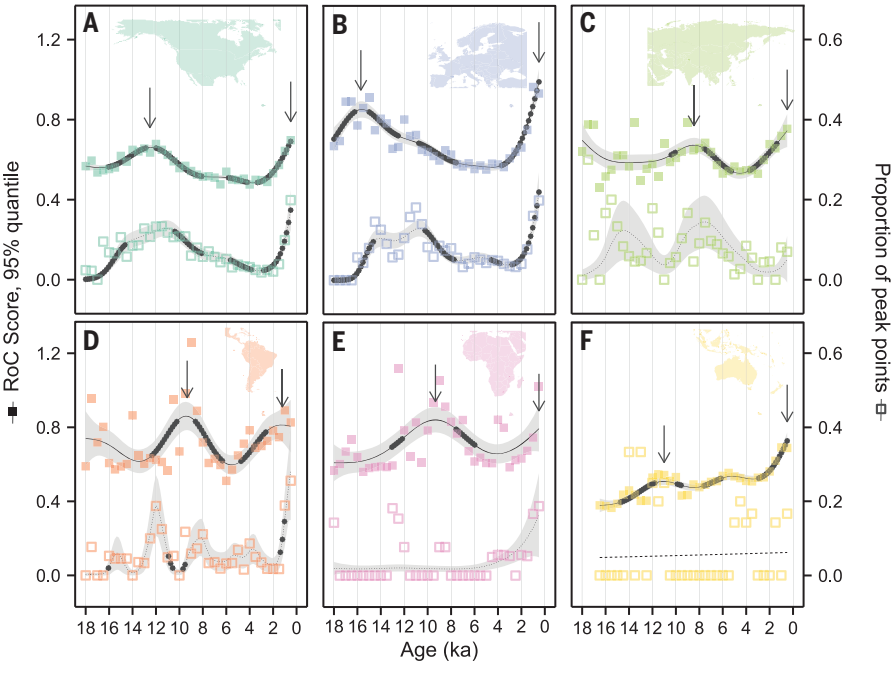


Fig. 2. RoC analyses by continent. (**A** to **F**) The filled squares represent the upper 95% quantile RoC score (left *y* axis) per 500-year time bin, with the solid curve representing the corresponding generalized additive model (GAM) (*22*). High values indicate high rates of vegetation change. Empty squares represent the proportion of peak points within each time bin (right *y* axis), with the corresponding GAM curve indicated by a dotted line. High values indicate a high synchrony in RoC among sequences (*22*). When the relationship is not significant, the GAM line is shown as dashed, and the error envelope is absent. Black asterisks on the GAM curves identify periods of significant acceleration in vegetation RoCs (i.e., where the derivative significantly differs from zero). Arrows indicate maximum RoC values for the Late Holocene and the Pleistocene-Holocene transition (table S1).

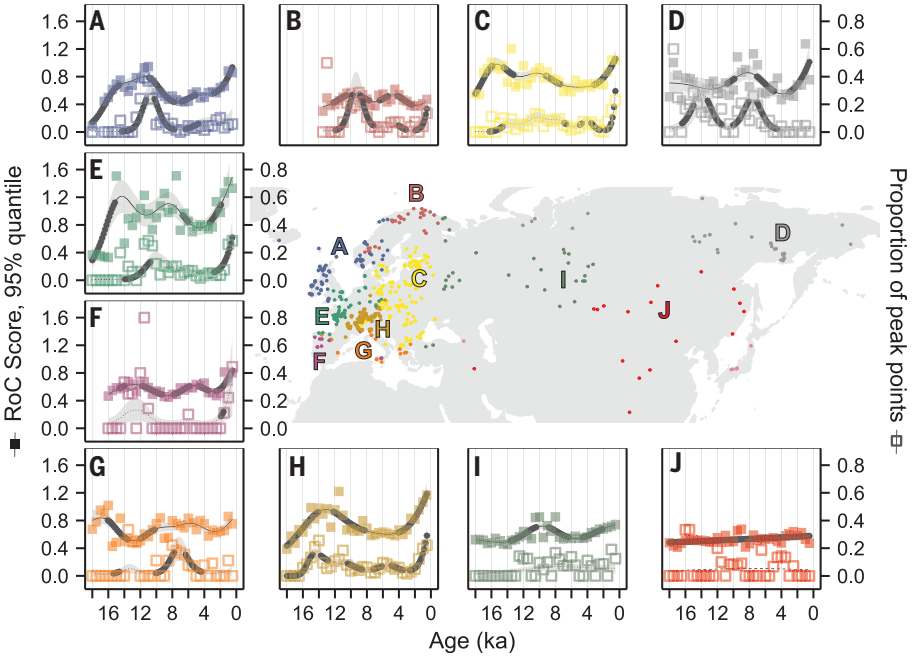


Fig. 3. RoC analyses by region across Eurasia. (**A** to **J**) Figure design follows that of Fig. 2.

changed in species composition and canopy structures across all elevations (*17*), whereas millennial- and centennial-scale hydroclimate variability caused abrupt changes in global vegetation during the Holocene (*18*).

Ecosystem responses to humans and climate change over long time scales can now be assessed globally, thanks to the century-long expansion of a global network of fossil pollen sequences anchored by increasingly precise radiocarbon chronologies (*19*); the building of open, community-curated data resources (*20*); and the development of new rate-of-change techniques (*21*). Here, we assess the global patterns and rates of vegetation change from the last deglaciation, through the Holocene, and up to the current Anthropocene on the basis of 1181 fossil pollen sequences from the Neotoma Paleoecology Database (*20*) covering all continents except Antarctica (Fig. 1 and data S1). These analyses are based on continentally harmonized taxonomies and updated Bayesian chronologies with age-depth model uncertainties and an improved algorithm [R package *R-Ratepol*; (*21*, *22*)] for estimating rates of change (RoCs) for paleoecological time series. RoCs are calculated as the compositional dissimilarity between consecutive time intervals (using the chi-squared coefficient) standardized by the length of time between samples, thereby providing an indicator of compositional change per unit of time. *R-Ratepol* uses a moving-window approach (instead of the traditional calculation of dissimilarities between individual levels), which minimizes artifactual alterations in RoC resulting from variations in sample density and sedimentation rate (*21*). *R-Ratepol* also incorporates temporal uncertainty resulting from age-depth modeling calculations through randomization (*21*, *22*). For each pollen sequence, we pooled data into 500-year time bins [see also our 250-year sensitivity experiment in the supplementary materials (*22*)] and calculated RoCs between bins to represent the rate of compositional change through time. For each sequence, we also identified time intervals with a large increase in RoC, called peak points [for more detailed information, see materials and methods (*22*)].

We analyzed RoCs at the scale of continents and subcontinental clusters, defined by climatic and geographic variables (*22*). For each continent and subcontinental region, we binned the RoC scores per 500-year time bins [with a 250-year sensitivity experiment in the supplementary materials (*22*)] and calculated the 95% RoC quantile to highlight intervals and places with large vegetation changes while filtering out outliers [see (*22*) for a comparison of the 95% quantile to median trends]. Similarly, we calculated the proportion of sequences with a peak point in each time bin. The clustering of peak points among sequences indicates a synchronous period of abrupt vegetation change within a region. Generalized additive models were fitted to all RoCs and peak point curves to summarize trends and test for significant accelerations [simultaneous confidence intervals of the first derivative differ from zero (*22*)].

We detect an unequivocal global acceleration of vegetation change during the Late Holocene (4.2 to 0 ka; Fig. 2). The estimated start of acceleration differs among continents and ranges from 4.6 to 3.1 ka (table S1). This estimated start is well supported by the dense availability of samples during the Middle to Late Holocene (Fig. 1E), but continental-scale estimates vary by ~500 to 1000 years (*22*). For most continents, Late Holocene RoCs are close to or exceed RoCs over the past 18 ka, with a percent differential ranging from −6.3 to 22.2% (Fig. 2 and table S1). Increases in RoC during the Lateglacial and Early Holocene can be linked to temperature and atmospheric CO_2 variations (Fig. 1, C and D) and hydrological variations. Rapid vegetation changes concentrate near the onset of the Holocene (11.7 ka) for most continents, expressed as a maximum in RoC or in peak points (Fig. 2). In North America and Europe, RoCs reached maxima during the abrupt millennial-scale climate oscillations characteristic of the North Atlantic and adjacent regions (~15 to 11 ka) and then substantially declined during the Early Holocene (Fig. 2, A and B). The heightened rates of deglacial vegetation change resemble the patterns of increased temperature variability in the North Atlantic and elsewhere in the Northern Hemisphere that were driven by a combination of orbital forcing, atmospheric greenhouse gas concentrations, meltwater pulses to the North Atlantic, and shifting patterns of heat transport (*23*). In Asia, rapid but asynchronous change characterizes the Lateglacial and deglaciation period, with a maximum in RoCs or a clustering of peak points between 10 and 8 ka (Fig. 2C). In Latin America and Africa, RoCs also reach maxima between 10 and 8 ka, which can be linked to altered monsoonal rainfall associated with declining Northern Hemisphere summer insolation (*24*).

RoC patterns at subcontinental scales are consistent with known histories of climate change and human land use. For example, in Eurasia, the western and northern European clusters show strong peaks in the rate of vegetation change between 15 and 10 ka (Fig. 3, A and E), which is consistent with the response of vegetation to North Atlantic climate variations and the retreating Eurasian ice sheets (Fig. 1C). Late Holocene rates of vegetation change are high across western and central Europe, particularly in areas of high present and past agricultural activity (*10*). In Asia, high rates of vegetation change during the Early Holocene can be linked to postglacial forest expansion in northern Asia (*25*) and millennial-scale variability in temperature and monsoonal rainfall in eastern Asia (*26*) (Fig. 3, C, D, and I). Seven of 10 Eurasian clusters show increased RoCs during the Late Holocene.

In the Americas, vegetation RoCs vary by latitude and between Atlantic- and Pacific-adjacent regions (Fig. 4). Eastern North America resembles western Europe in its high vegetation RoCs between 15 and 10 ka, with a strong signal of synchronous vegetation change over the past millennium (Fig. 4, G, H, and I). All North American regions show increased RoCs during the Late Holocene except for the high-latitude clusters. Driven by the topographic

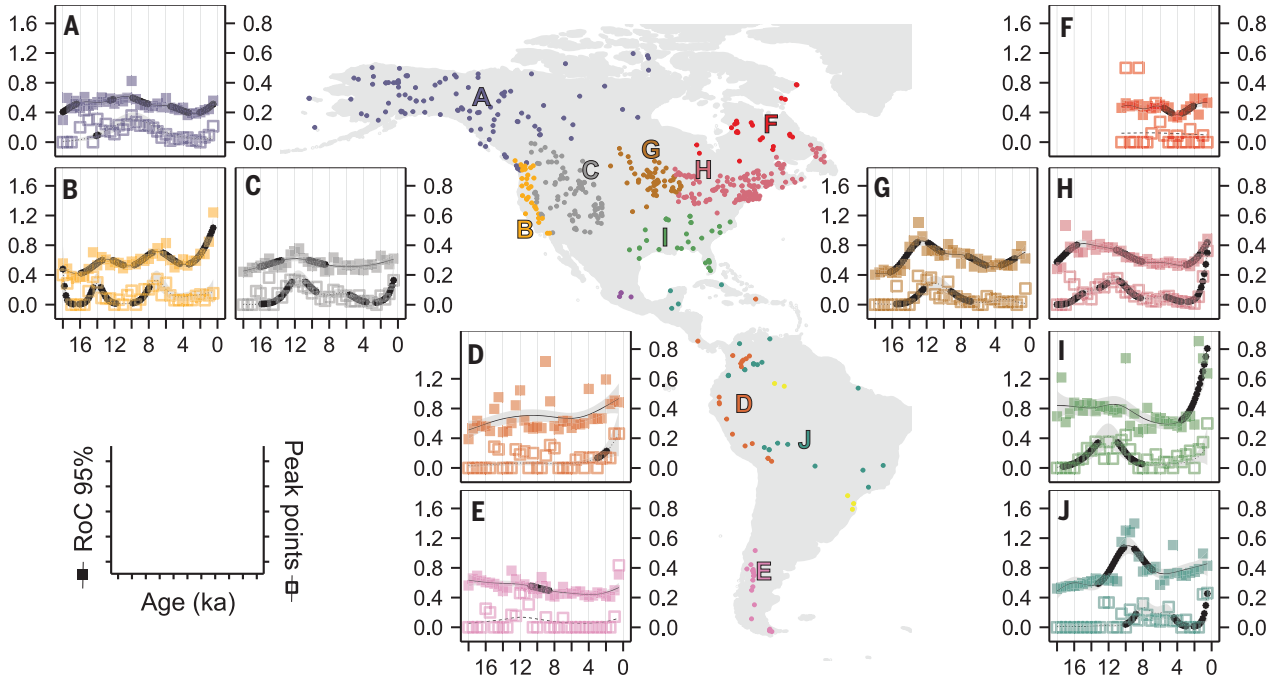


Fig. 4. RoC analyses by region across the Americas. (**A** to **J**) Figure design follows that of Fig. 2.

complexity of the Andes, vegetation responses in the Neotropical highlands were highly variable and asynchronous (Fig. 4D)—likely a combined effect of changes in temperature, hydroclimate variability, and atmospheric CO_2 (*27*, *28*). In the lowlands, a peak in vegetation RoCs at 10 ka is likely the result of hydrological variability linked to shifting monsoons (Fig. 4J) (*27*). These large vegetation changes challenge the common myth of the stable tropics and suggest a strong sensitivity of the Neotropics to temperature, hydroclimate variability, and orbital precession during the Early Holocene (*27*, *28*). In temperate South America, a period of synchronous vegetation change in the Holocene (Fig. 4E) is asynchronous with warm Neotropical regions (Fig. 4J), likely because of varying climate modes influencing different parts of the continent (*29*). The Late Holocene acceleration of vegetation change is clearly manifested across most of the latitudinal gradient of the Americas, except for the high northern latitudes, with the highest RoCs in coastal western North America and eastern North America (Fig. 4).

The detection of globally accelerating rates of vegetation change during the Late Holocene provides a longer-term perspective to the well-documented increase in species turnover during the 20th and 21st centuries (*6*). For terrestrial ecosystems at least, these recent increases in species turnover are the continuation of a longer acceleration that began millennia ago (Fig. 2). Moreover, this work suggests that contemporary communities and some current biodiversity trends may be partially resulting from legacies of past land use or environmental forcing (*11*) in combination with the strong anthropogenic imprint of the past decades. Hence, recent changes in biodiversity patterns represent only the most recent interval of our used planet (*30*) that has been altered by millennia of changing environments and human activities.

Our study focused primarily on detecting patterns of rates of vegetation compositional changes over the past 18,000 years and secondarily on attributing causes. This approach follows the standard delineation in climate change research between detection studies that focus on establishing the significance and fingerprints of observed climate trends (*31*) and attribution studies that explore the potential causes of the observed events and patterns (*32*). Biodiversity research is now achieving the capability for global detection analyses (*2*, *6*) across an increasingly broad range of time scales. The next frontier is to disentangle and attribute the contributions of climatic variability and anthropogenic impacts to past vegetation changes. This attribution is challenged by the complex interplay between climatic, anthropogenic, and vegetation dynamics that varies within and among ecosystems, particularly at local to regional scales. For example, in the Holocene in East Africa, land cover changes over the past 6000 years were driven by multiple cultural and technological innovations and by changes in rainfall amount and seasonality (*33*). In South America, Holocene climate variability contributed to regime shifts in human demography and displacement, which in turn affected ecosystems regionally (*34*). The worldwide spread of agricultural land use over the past 3000 years suggests intensified resource management (*8*) but was accompanied in some regions by substantial climate changes (*16*, *33*). Deglacial vegetation dynamics, although strongly climate driven, were also affected by global megaherbivore extinctions during the late Quaternary (*15*), which likely resulted from synergistic anthropogenic and climatic drivers (*35*). These interactions provide evidence against single-cause attributions of rates of vegetation change.

A key next step is to integrate these paleovegetation sequences with other paleoclimatic and archaeological records to better understand the past feedbacks among the climate, ecosystems, and humans (*3*, *10*, *13*, *36*) and the legacy effects of these past interactions on the trajectory of contemporary ecosystems. Assembled networks of paleovegetation, paleoclimatic, and anthropogenic records need to be harmonized and quality checked to do this attribution correctly and handle the spatial variations in vegetation, climate, and human histories within and among continents (*36*). Such an integration will also need carefully chosen numerical techniques to formally detect the onset of detectable human influence in paleoenvironmental time series and the variation in timing within and among ecosystems (*29*). Additionally, a higher density of paleoecological records is still needed, especially in topographically rich regions such as the Himalayas and the Andes, where climate heterogeneity is highest and human activities span millennia.

Despite these complexities, it is well known that the mean global temperature increases during the last deglaciation (~6°C) were several times as large as those of the Middle to Late Holocene [~1°C (*37*)]. Thus, a reasonable working inference is that the globally enhanced rates of vegetation change over the past several thousand years were caused primarily by anthropogenic activities, whereas vegetation changes during the Late Pleistocene to Early Holocene were driven primarily by changing climates. If so, the magnitude and extent of Late Holocene rates of vegetation change suggests that the global transformation of the terrestrial biosphere by humans now resembles or exceeds in rate and scope even the profound ecosystem transitions associated with the end of the last glacial period. Moreover, the global ecosystem changes for this century may be greater yet given current climate commitments and given that the climate changes expected for higher-end emission scenarios are similar in magnitude to those of the last deglaciation.

REFERENCES AND NOTES

1. B. J. McGill, M. Dornelas, N. J. Gotelli, A. E. Magurran, *Trends Ecol. Evol.* **30**, 104–113 (2015).
2. M. Dornelas *et al.*, *Glob. Ecol. Biogeogr.* **27**, 760–786 (2018).
3. J. Woodbridge *et al.*, *J. Ecol.* **109**, 1396–1410 (2021).
4. E. C. Ellis, N. Ramankutty, *Front. Ecol. Environ.* **6**, 439–447 (2008).
5. S. L. Pimm *et al.*, *Science* **344**, 1246752 (2014).
6. S. A. Blowes *et al.*, *Science* **366**, 339–345 (2019).
7. D. M. J. S. Bowman *et al.*, *J. Biogeogr.* **38**, 2223–2236 (2011).
8. L. Stephens *et al.*, *Science* **365**, 897–902 (2019).
9. T. Giesecke *et al.*, *Nat. Commun.* **10**, 5422 (2019).
10. L. Marquer *et al.*, *Quat. Sci. Rev.* **171**, 20–37 (2017).
11. C. N. H. McMichael, *New Phytol.* **229**, 2492–2496 (2021).
12. C. Nolan *et al.*, *Science* **361**, 920–923 (2018).
13. D. A. Fordham *et al.*, *Science* **369**, eabc5654 (2020).
14. J. W. Williams, B. N. Shuman, T. Webb III, P. J. Bartlein, P. L. Leduc, *Ecol. Monogr.* **74**, 309–334 (2004).
15. Y. Malhi *et al.*, *Proc. Natl. Acad. Sci. U.S.A.* **113**, 838–846 (2016).
16. F. E. Mayle, D. J. Beerling, W. D. Gosling, M. B. Bush, *Phil. Trans. R. Soc. Lond. B* **359**, 499–514 (2004).
17. F. E. Mayle, M. J. Burn, M. Power, D. H. Urrego, in *Past Climate Variability in South America and Surrounding Regions*, F. Vimeux, F. Sylvestre, M. Khodri, Eds., vol. 14 of *Developments in Paleoenvironmental Research* (Springer, 2009), pp. 89–112.
18. A. W. Seddon, M. Macias-Fauria, K. J. Willis, *Holocene* **25**, 25–36 (2015).
19. S. G. A. Flantua *et al.*, *Rev. Palaeobot. Palynol.* **223**, 104–115 (2015).
20. J. W. Williams *et al.*, *Quat. Res.* **89**, 156–177 (2018).
21. O. Mottl *et al.*, bioRxiv 2020.12.16.422943 [Preprint]. 24 February 2021. https://doi.org/10.1101/2020.12.16.422943.
22. See supplementary materials online.
23. Z. Liu *et al.*, *Science* **325**, 310–314 (2009).
24. T. M. Shanahan *et al.*, *Nat. Geosci.* **8**, 140–144 (2015).
25. G. M. MacDonald, K. V. Kremenetski, D. W. Beilman, *Phil. Trans. R. Soc. B* **363**, 2283–2299 (2008).
26. H. Zhang *et al.*, *Quaternary* **2**, 26 (2019).
27. V. F. Novello *et al.*, *Earth Planet. Sci. Lett.* **524**, 115717 (2019).
28. M. H. M. Groot *et al.*, *Clim. Past* **7**, 299–316 (2011).
29. S. G. A. Flantua *et al.*, *Clim. Past* **12**, 483–523 (2016).
30. E. C. Ellis *et al.*, *Proc. Natl. Acad. Sci. U.S.A.* **110**, 7978–7985 (2013).
31. PAGES 2k Consortium, *Nat. Geosci.* **6**, 339–346 (2013).
32. K. E. Trenberth, J. T. Fasullo, T. G. Shepherd, *Nat. Clim. Chang.* **5**, 725–730 (2015).
33. R. Marchant *et al.*, *Earth Sci. Rev.* **178**, 322–378 (2018).
34. P. Riris, M. Arroyo-Kalin, *Sci. Rep.* **9**, 6850 (2019).
35. E. D. Lorenzen *et al.*, *Nature* **479**, 359–364 (2011).
36. A. Bevan *et al.*, *Proc. Natl. Acad. Sci. U.S.A.* **114**, E10524–E10531 (2017).
37. J. E. Tierney *et al.*, *Nature* **584**, 569–573 (2020).
38. North Greenland Ice Core Project members, *Nature* **431**, 147–151 (2004).
39. E. Monnin *et al.*, *Science* **291**, 112–114 (2001).
40. O. Mottl, S. Flantua, HOPE-UIB-BIO/Global_RoC: First public release, version v1.0, Zenodo (2021); http://doi.org/10.5281/zenodo.4650239.
41. S. G. A. Flantua *et al.*, "Mottl et al. (2021, Science) Taxonomic harmonization tables for North America, Latin America, Europe, Asia, Africa," Figshare, dataset (2021); https://doi.org/10.6084/m9.figshare.13049735.

ACKNOWLEDGMENTS

We are grateful to all data contributors to the Neotoma Paleoecology Database and data stewards for the constituent databases—African Pollen Database, European Pollen Database, IndoPacific Palaeoecology Database, Latin American Pollen Database, and North American Pollen Database—for supporting open-access data. We thank H. J. B. Birks for making suggestions on the analyses and for providing advice on the Asian taxonomic harmonization. **Funding:** O.M., S.G.A.F., K.P.B., V.A.F., and A.W.R.S. acknowledge support from the European Research Council (ERC) under the European Union's Horizon 2020 research and innovation program (grant agreement no. 741413) to H. J. B. Birks. Neotoma development has been supported by the National Science Foundation (1550707, 1550805, and 1948926) and Belmont Forum (1929476). **Author contributions:** O.M., S.G.A.F., A.W.R.S., and J.W.W. co-led and designed the study. S.G.A.F., K.P.B., V.A.F., A.W.R.S., and O.M. developed the data extraction workflow, and O.M. performed the numerical analyses. J.W.W., H.H., S.G.A.F., K.P.B., and S.I. led the compilation and taxonomic harmonization of continental-scale pollen datasets. E.C.G., T.G., S.H., H.H., S.I., S.G.A.F., and J.W.W. led Neotoma data mobilization efforts. S.G.A.F. and J.W.W. led the writing. All authors contributed to the article and approved the submitted version. **Competing interests:** The authors declare no competing interests. **Data and materials availability:** All the data and R codes are publicly available at Zenodo (*40*) and at https://github.com/HOPE-UIB-BIO/Global_RoC. Harmonization tables are available at Figshare (*41*).

SUPPLEMENTARY MATERIALS

science.sciencemag.org/content/372/6544/860/suppl/DC1
Materials and Methods
Figs. S1 to S7
Tables S1 to S3
References (*42*–*77*)
Data S1

19 December 2020; accepted 8 April 2021
10.1126/science.abg1685

PLANT SCIENCE

Lipid exchanges drove the evolution of mutualism during plant terrestrialization

Mélanie K. Rich[1]†, Nicolas Vigneron[1]†, Cyril Libourel[1], Jean Keller[1], Li Xue[2,3], Mohsen Hajheidari[2], Guru V. Radhakrishnan[4], Aurélie Le Ru[5], Seydina Issa Diop[6,7], Giacomo Potente[6,7], Elena Conti[6,7], Danny Duijsings[8], Aurélie Batut[9], Pauline Le Faouder[9], Kyoichi Kodama[10], Junko Kyozuka[10], Erika Sallet[11], Guillaume Bécard[1], Marta Rodriguez-Franco[12], Thomas Ott[12,13], Justine Bertrand-Michel[9], Giles E. D. Oldroyd[4,14], Péter Szövényi[6,7], Marcel Bucher[2], Pierre-Marc Delaux[1]*

Symbiosis with arbuscular mycorrhizal fungi (AMF) improves plant nutrition in most land plants, and its contribution to the colonization of land by plants has been hypothesized. Here, we identify a conserved transcriptomic response to AMF among land plants, including the activation of lipid metabolism. Using gain of function, we show the transfer of lipids from the liverwort *Marchantia paleacea* to AMF and its direct regulation by the transcription factor WRINKLED (WRI). Arbuscules, the nutrient-exchange structures, were not formed in loss-of-function *wri* mutants in *M. paleacea*, leading to aborted mutualism. Our results show the orthology of the symbiotic transfer of lipids across land plants and demonstrate that mutualism with arbuscular mycorrhizal fungi was present in the most recent ancestor of land plants 450 million years ago.

The stunning diversity of extant terrestrial ecosystems results from the diversification of plants after their colonization of emerged land 450 million years ago (*1*). This singular terrestrialization event required the aquatic algal ancestor of land plants to adapt to desiccation, direct ultraviolet radiation, and a nutrient-poor habitat (*2*). Although they remain elusive, the evolutionary innovations that allowed terrestrialization to occur are predicted to be shared across the two main clades of land plants, the nonvascular Bryophytes and the vascular plants, and absent from their close algal relatives (*2*).

Most land plants benefit from associations with the mutualistic arbuscular mycorrhizal fungi (AMF), which facilitate nutrient and water uptake (*3*). Fossil records indicate that

[1]Laboratoire de Recherche en Sciences Végétales (LRSV), Université de Toulouse, CNRS, UPS, 31326 Castanet-Tolosan, France. [2]Institute for Plant Sciences, Cologne Biocenter, Cluster of Excellence on Plant Sciences, University of Cologne, D-50674 Cologne, Germany. [3]College of Chemistry and Life Sciences, Zhejiang Normal University, Jinhua 321004, China. [4]John Innes Centre, Norwich NR4 7UH, UK. [5]Fédération de Recherche 3450, Plateforme Imagerie, Pôle de Biotechnologie Végétale, 31326 Castanet-Tolosan, France. [6]Department of Systematic and Evolutionary Botany, University of Zurich, 8008 Zurich, Switzerland. [7]Zurich-Basel Plant Science Center, 8092 Zurich, Switzerland. [8]BaseClear BV, 2333 Leiden, Netherlands. [9]MetaToulLipidomics Facility, INSERM UMR1048, 31432 Toulouse, France. [10]Graduate School of Life Sciences, Tohoku University, Sendai 980-8577, Japan. [11]Laboratory of Plant-Microbe Interactions (LIPM), Université de Toulouse, INRA, CNRS, 31326 Castanet-Tolosan, France. [12]Cell Biology, Faculty of Biology, University of Freiburg, 79104 Freiburg, Germany. [13]CIBSS – Centre for Integrative Biological Signalling Studies, University of Freiburg, 79104 Freiburg, Germany. [14]Crop Science Centre, University of Cambridge, Cambridge CB2 3EA, UK.
***Corresponding author. Email: pierre-marc.delaux@lrsv.ups-tlse.fr** †These authors contributed equally to this work.

spores morphologically similar to those of extant AMF were present when terrestrialization occurred (*4*). The earliest plant macrofossils, which belong to an extinct plant lineage that preceded vascular plants, harbor intracellular structures morphologically similar to extant symbiotic structures (*5*, *6*). In addition, plant genes known to be essential for the symbiosis with AMF in angiosperms have coevolved with the ability to associate with these fungi across land plants (*7*, *8*). These data support the original hypothesis that the association with AMF might represent one of the traits facilitating terrestrialization (*9*). However, definitive evidence of the ancestral character of the symbiosis

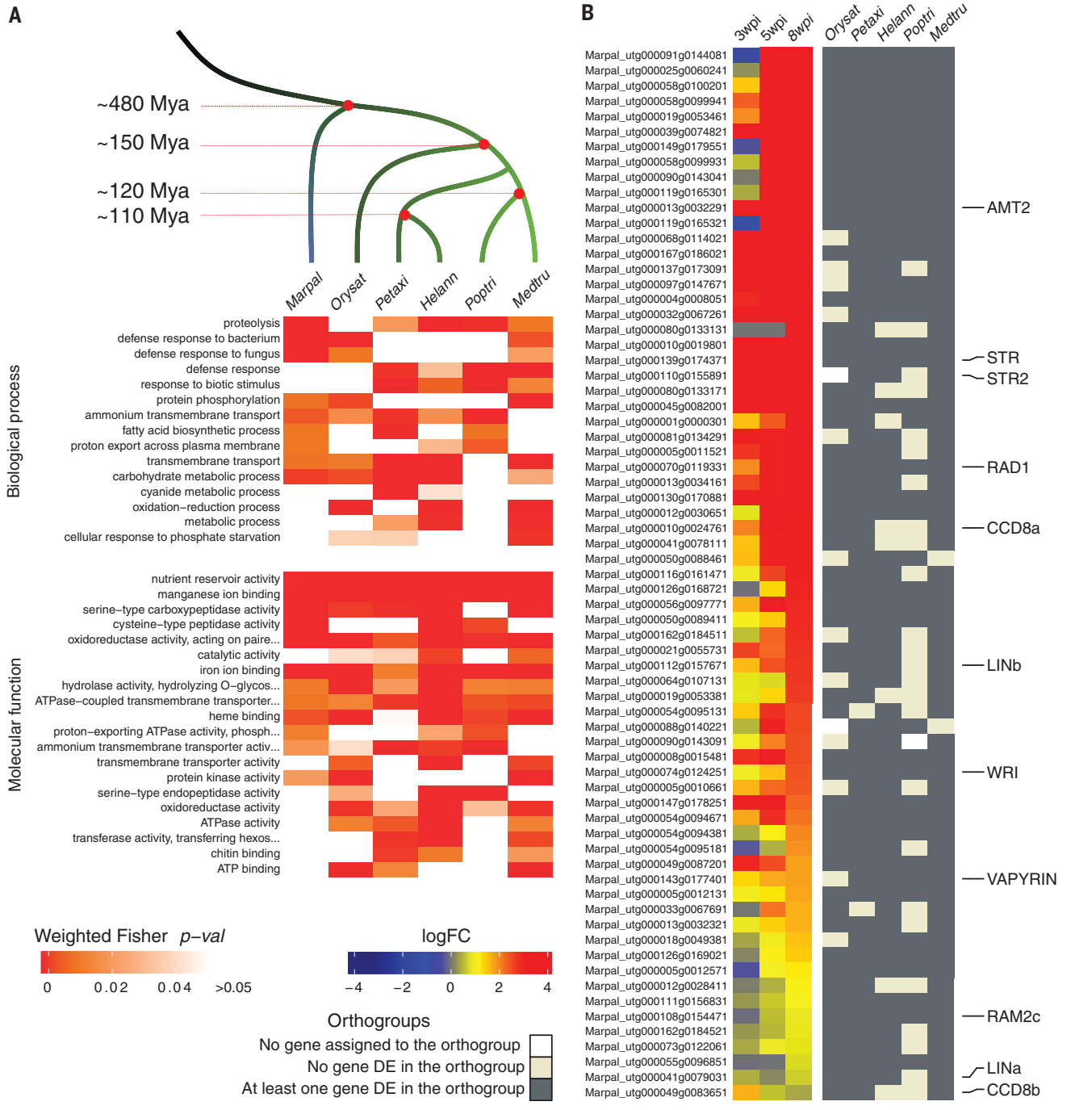


Fig. 1. Conserved transcriptomic response to arbuscular mycorrhizal fungi across land plants. (**A**) Comparison of GO term enrichment during AMS in different plant species. GO terms enriched in at least two species are shown. Colors of the heatmap are weighted Fisher *P* values of the respective GO terms. Approximation of divergence time between species is shown (*26*, *27*). Marpal, *Marchantia paleacea*; Orysat, *Oryza sativa*; Petaxi, *Petunia axillaris*; Helann, *Helianthus annuus*; Poptri, *Populus trichocarpa*; Medtru, *Medicago truncatula*. Mya, million years ago; logFC, log fold change; DE, differentially expressed. (**B**) Heatmap of gene expression during AMS in *M. paleacea*. Up-regulation of genes from the same orthogroups as the *M. paleacea* genes in five angiosperm species is indicated. Genes shown in this graph are significantly up-regulated during AMS in *M. paleacea* in at least one of the time points and belong to an orthogroup where at least three other species present with AMS–up-regulated genes (false discovery rate < 0.05). Heatmap is shown as $\log_2$ fold change compared with mock-treated plants. wpi, weeks postinoculation.

with AMF in the most recent common ancestor of the land plants, and the molecular mechanisms at its origin, remain to be discovered.

If symbiosis with AMF indeed predated the divergence between Bryophytes and vascular plants, we hypothesized that there would be a shared transcriptional response to AMF in those two clades. To test this, we generated RNA sequencing data of the Bryophyte *Marchantia paleacea* collected 3, 5, and 8 weeks after either inoculation with the AMF *Rhizophagus irregularis* or mock treatment (Fig. 1 and table S1). Reads were mapped on a *M. paleacea* genome assembly generated by augmenting a previous Illumina-based assembly (*8*) with long-read sequencing (table S2). Increasing transcriptional response was observed along the time course of the interaction, leading to more than 1200 differentially regulated genes with more than 1000 up-regulated genes at 8 weeks postinoculation (Fig. 1 and table S3). We cross-referenced these results with transcriptomic datasets available for five phylogenetically diverse angiosperms (*10*–*14*). Gene Ontology (GO) term enrichment analysis revealed a set of conserved processes up-regulated during the symbiosis across land plants, including fatty acid biosynthesis, transmembrane transport, oxidoreductase activity, and proteolysis (Fig. 1A and table S1). To further investigate the conservation of the response, we computed groups of orthologous genes across land plants and identified, for each orthogroup, whether one or more genes were up-regulated during the symbiosis in each species (fig. S1 and table S3). We found 47 orthogroups corresponding to 69 *M. paleacea* genes up-regulated during the symbiosis with AMF both in this liverwort and in at least three of the five investigated angiosperms (Fig. 1B). These orthogroups contain genes with functions in diverse aspects of the symbiosis in angiosperms, such as strigolactone biosynthesis, infection, and lipid exchanges (Fig. 1B and table S3). Such conservation of cellular reprogramming shows that the induction of a core genetic program during AM symbiosis (AMS) is conserved between land plant lineages spanning 450 million years of diversification.

In angiosperms, *Required for Arbuscular Mycorrhization 2* (*RAM2*), *Stunted Arbuscule* (*STR*), and *STR2* are expressed in arbuscule-containing cells where they are essential for the biosynthesis and transfer of lipids to the AMF partners (*14*, *15*–*17*), which are fatty acid auxotrophs (*18*, *19*). In addition to the up-regulation of *MpaRAM2c* and *MpaSTR/STR2*, genes corresponding to the GO term "fatty acid biosynthesis" (GO:006633) were enriched in the subset of AMS–up-regulated genes across

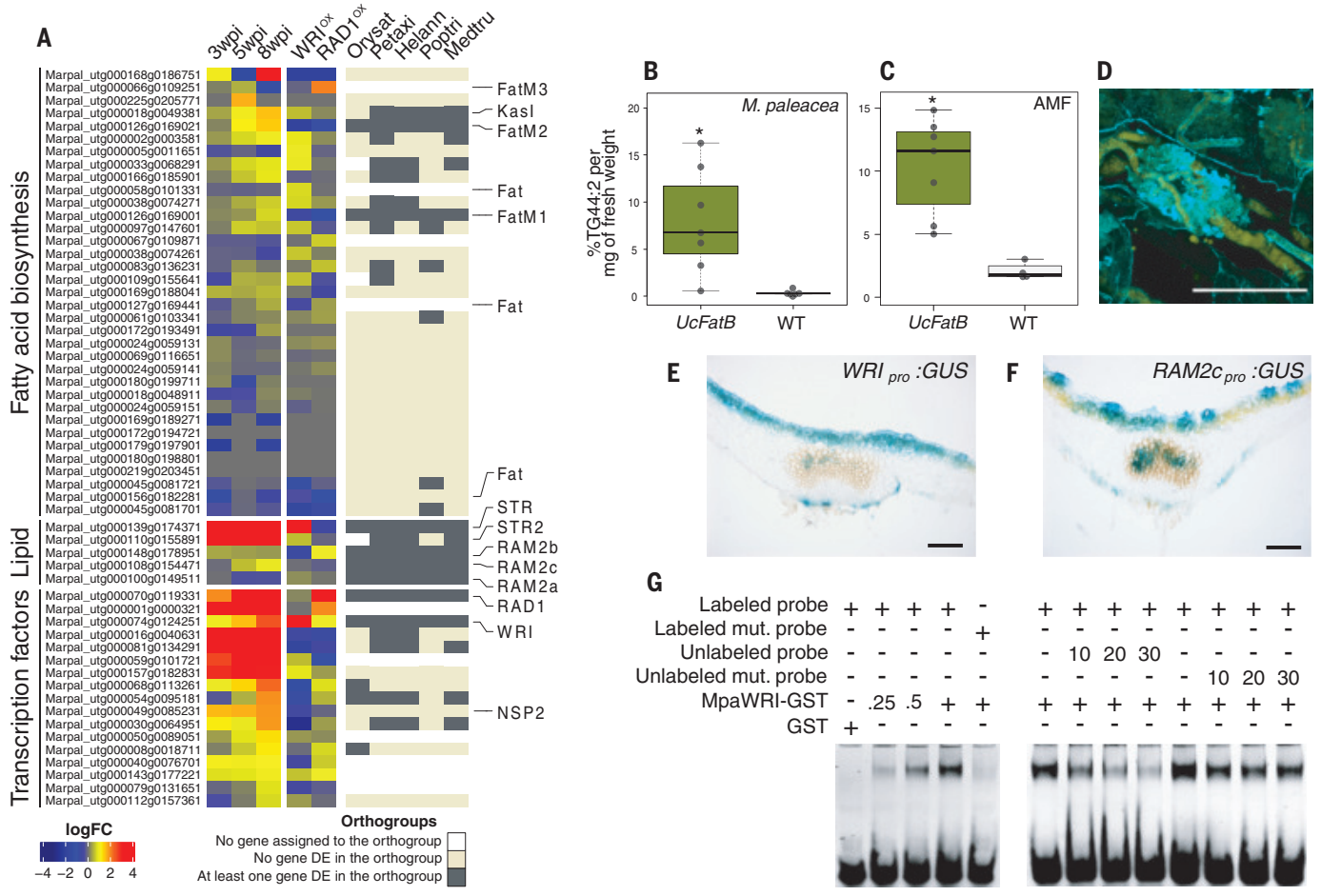


Fig. 2. WRI-induced symbiotic transfer of lipids is conserved across land plants. (**A**) Heatmap of $\log_2$ fold change of *M. paleacea* genes in a time-course of AMF-inoculated compared with mock-treated plants, and in the *MpaWRI*^{OX} and *MpaRAD1*^{OX} lines. Genes from the fatty acid biosynthesis GO term (006633), from the symbiotic lipid-transfer pathway, and *M. paleacea* transcription factors up-regulated in response to AMF are indicated. Up-regulation of genes from the same orthogroups as the *M. paleacea* genes in five angiosperm species is indicated. (**B** and **C**) Quantification of the C12 containing TAG 44:2 in samples from colonized wild-type (WT) and UcFatB *M. paleacea* lines (B) and the associated AMF (C). *P < 0.01; Student's t test. (**D**) Arbusculated cell from a section of *M. paleacea* stained with Nile red (yellow, neutral lipids) and calcofluor (blue, cell walls). Scale bar, 50 μm. (**E** and **F**) GUS reporter fusion of *MpaWRI* and *MpaRAM2c* promoters. Scale bars, 0.5 mm. (**G**) EMSA with GST-MpaWRI on a fragment of the *MpaRAM2c*$_{pro}$ (probe) and a mutated version (mut. probe).

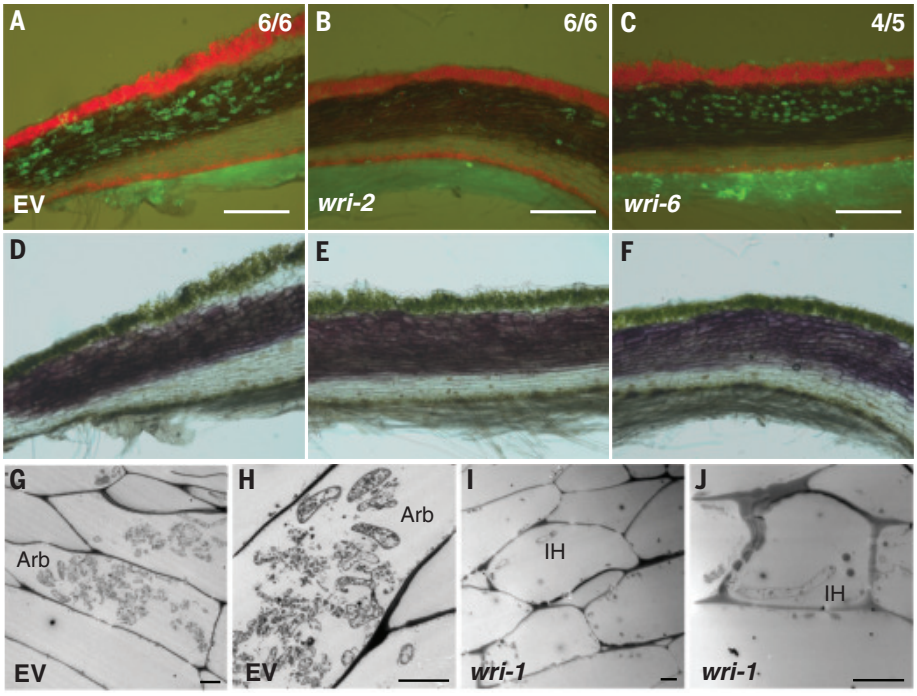


Fig. 3. WRI is necessary for AMS in *M. paleacea*. (**A** to **F**) Transversal sections of empty-vector (EV) control [(A) and (D)], *wri* null [(B) and (E)], or *wri* edited [(C) and (F)] *M. paleacea* thalli stained with WGA-FITC (top) or bright field (bottom). Proportion of thalli with the presented phenotype is indicated. Scale bars, 0.5 mm. (**G** to **I**) Transmission electron microscopy pictures of cells from empty-vector control lines [(G) and (H)] or *wri-1* [(I) and (J)]. In control plants, the central part of the thallus contains arbuscules (Arb), whereas only intracellular hyphae (IH) are seen in the mutant. Scale bars, 10 μm.

host plants (Fig. 2A). The prevalence of lipid genes up-regulated in *M. paleacea* suggests that lipid transfer from the host plant to the AMF occurs in Bryophytes, as is the case in angiosperms. To test this hypothesis, we compared the amount of triacylglycerol (TAG) in AMF or mock-inoculated *M. paleacea* thalli. TAGs acylated with two or three palmitic acids (C16) were enriched in AMF-colonized *M. paleacea* thalli when compared with mock-treated plants (fig. S2). To determine whether this accumulation of TAGs was mirrored by the presence of lipids in the AMF intracellular structures, sections of AMF-colonized *M. paleacea* were stained with a lipid-specific dye (Nile red). Staining in the arbuscules and intracellular fungal hyphae was observed, indicating the accumulation of lipids in the AMF during the association with *M. paleacea* (Fig. 2D). Staining in the tissue area where arbuscules are hosted during symbiosis was absent in noncolonized plants (fig. S3). To test whether the lipids observed in the AMF originate from *M. paleacea,* the fatty acid metabolism in the arbuscule-containing cells was rewired by the expression of *Umbellularia californica Fatty Acid Thioestherase B* (*UcFatB*) under an arbuscule-containing cell-specific promoter (fig. S4) to produce a rare C12 acyl group, lauric acid (*14*). If transfer of lipids occurs between *M. paleacea* and the colonizing AMF, TAGs acylated with C12 should accumulate in both the colonized *UcFatB*-expressing plant tissues and the associated newly produced AMF spores. Mass spectrometry analyses of AMF-inoculated wild-type and *UcFatB* lines revealed the accumulation of C44:2, a TAG containing one C12 and two C16, in the *UcFatB* lines, a compound barely detectable in the wild-type samples (Fig. 2B). Analysis of the AMF spores and hyphae connected to the *UcFatB* lines showed a similar enrichment (Fig. 2C). This demonstrates that lipids biosynthesized in arbuscule-containing cells of *M. paleacea* are transferred to the AMF. Altogether, these results indicate that, as in vascular plants, the symbiotic transfer of lipids from the host plant to AMF occurs in Bryophytes.

To dissect the mechanisms underlying the symbiotic transfer of lipids, we mined the cross-referenced RNA sequencing (RNA-seq) data to identify potential transcriptional regulators of the symbiotic lipid pathway in arbuscule-containing cells (Fig. 2A). Two orthogroups contained transcriptional regulators up-regulated in all six species colonized by AMF. These orthogroups contained genes known for their involvement in AMS in angiosperms: *Required for Arbuscular Development 1* (*RAD1*), a GRAS transcriptional regulator (*20*), and the *WRINKLED* family of AP2 transcription factors (*21*, *22*). The *RAD1* orthogroup contained three *M. paleacea* genes, and previous phylogenies (*8*) had identified two of those genes (Marpal_utg000070 g0119331, Marpal_utg000071 g0120271) as putative RAD1 orthologs. From those two genes, only the latter (now renamed *MpaRAD1*) was up-regulated during symbiosis (Fig. 2A and table S3). Although members of the GRAS family are present in Zygnematophyceae, the closest algal relative to land plants, *RAD1* originates from a land plant–specific duplication and is absent from all the investigated algal genomes (fig. S5). Only one *WRINKLED* gene was found in *M. paleacea* (*MpaWRI*, Marpal_utg000074 g0124251) and no *WRI* gene was found in algae (figs. S6 to S8). Thus, the origin of *RAD1* and *WRI* coincides with terrestrialization. Fusion of *MpaRAD1* and *MpaWRI* promoters to a GUS reporter showed that both genes are expressed in arbuscule-containing cells (fig. S9). To determine whether MpaRAD1 or MpaWRI could regulate the symbiotic biosynthesis of fatty acids in *M. paleacea*, we generated lines overexpressing *MpaWRI* ($MpaWRI^{OX}$) and *MpaRAD1* ($MpaRAD1^{OX}$) and compared their transcriptome in the absence of AMF to empty-vector controls (Fig. 2A and table S3). Whereas in the $MpaRAD1^{OX}$ lines no major gene expression reprogramming was observed, in $MpaWRI^{OX}$ lines, an enrichment of the GO term "fatty acid biosynthesis" was observed among the differentially expressed genes (Fig. 2A and table S1). This enrichment is reminiscent of the role of *WRINKLED* genes in controlling lipid biosynthesis in angiosperms, both in developmental and symbiotic contexts (*22*, *23*). Transient expression of *MpaWRI* in leaves of *Nicotiana benthamiana* led to accumulation of TAG, further confirming the link with the lipid metabolism (fig. S10). In addition, the putative symbiosis-specific lipid transporter *STR* was also up-regulated in $MpaWRI^{OX}$ lines in absence of AMF (Fig. 2A). Taking the reverse approach, we expressed a version of *MpaWRI* fused to the artificial repressor domain SRDX ($MpaWRI^{SRDX}$) (*24*). $MpaWRI^{SRDX}$ lines showed developmental defects and a significant decrease in the expression of *MpaRAM2c*, the *RAM2* paralog from *M. paleacea*, which is up-regulated during AMS (Fig. 2A and figs. S11 and S12) and whose expression pattern overlaps with that of *MpaWRI* (Fig. 2, E and F). Within a 1-kb portion of the $MpaRAM2c_{pro}$ that was sufficient for induction in arbuscules (fig. S13), we identified a region containing known target sequences of angiosperm *WRINKLED* promoters (*25*). Using electrophoretic mobility shift assay (EMSA), a 25-bp-long DNA sequence within this region was found to be sufficient for the direct binding of MpaWRI on $MpaRAM2c_{pro}$ (Fig. 2G and fig. S13). Altogether, these data indicate that MpaWRI directly regulates the expression of the lipid metabolism in arbuscule-containing cells in *M. paleacea*, leading to the transfer of fatty acids to the AMF.

To determine whether the function of *MpaWRI* is required for AMS, we generated a series of CRISPR-Cas9 *wri* mutants in *M. paleacea*. Five weeks after inoculation with the AMF *R. irregularis*, all inoculated empty-vector control thalli were fully colonized and showed high density of arbuscules (Fig. 3A). By contrast, in five *wri* null mutants (*wri-1* to *wri-5*), no fully developed arbuscules were found, and AMF colonization structures were restricted to intraradical hyphae (Fig. 3). Similarly, absence of arbuscules was observed in the $MpaWRI^{SRDX}$ lines (fig. S12) and in the single *wri* allele obtained in another *M. paleacea* subspecies (fig. S14). Two additional CRISPR alleles, *wri-6* and *wri-7*, with edited alleles of *MpaWRI* that did not impair the open reading frame of the gene (fig. S15) showed an almost wild-type phenotype with more than 50 and 75% of the thalli harboring arbuscules, respectively (Fig. 3C).

Our results demonstrate that the symbiotic regulation by *MpaWRI* of the biosynthesis of fatty acids and their transfer to the symbiont are essential for mutualism with AMF in *M. paleacea*. In angiosperms, the *WRINKLED* orthogroup encompasses multiple paralogs (fig. S6), including several that contribute to AMS (*21*, *22*). The less-pronounced symbiotic defect observed in the angiosperm mutants compared with their liverwort counterpart is likely due to partial genetic redundancy. The fact that the same trait is regulated by orthologous genetic pathways in Bryophytes and in angiosperms indicates its conservation across land plants, covering 450 million years of diversification and dispersion. These results validate the long-standing proposed hypothesis that the mutualistic arbuscular mycorrhizal symbiosis was one of the traits that evolved in the first land plants, enabling terrestrialization.

REFERENCES AND NOTES

1. D. J. Beerling, *The Emerald Planet: How Plants Changed Earth's History* (Oxford Univ. Press, 2007).
2. S. A. Rensing, *Cell* **181**, 964–966 (2020).
3. S. E. Smith, D. Read, in *Mycorrhizal Symbiosis* (Academic Press, ed. 3, 2008), pp. 91–116.
4. D. Redecker, R. Kodner, L. E. Graham, *Science* **289**, 1920–1921 (2000).
5. W. Remy, T. N. Taylor, H. Hass, H. Kerp, *Proc. Natl. Acad. Sci. U.S.A.* **91**, 11841–11843 (1994).
6. P. Kenrick, P. R. Crane, *Nature* **389**, 33–39 (1997).
7. P.-M. Delaux *et al.*, *Proc. Natl. Acad. Sci. U.S.A.* **112**, 13390–13395 (2015).
8. G. V. Radhakrishnan *et al.*, *Nat. Plants* **6**, 280–289 (2020).
9. K. A. Pirozynski, D. W. Malloch, *Biosystems* **6**, 153–164 (1975).
10. V. Fiorilli *et al.*, *Front Plant Sci* **6**, 636 (2015).
11. M. K. Rich, P.-E. Courty, C. Roux, D. Reinhardt, *BMC Genomics* **18**, 589 (2017).
12. A. Vangelisti *et al.*, *Mycorrhiza* **30**, 373–387 (2020).
13. S. Calabrese *et al.*, *Plant Cell Physiol.* **58**, 1003–1017 (2017).
14. L. H. Luginbuehl *et al.*, *Science* **356**, 1175–1178 (2017).
15. Y. Jiang *et al.*, *Science* **356**, 1172–1175 (2017).
16. A. Bravo, M. Brands, V. Wewer, P. Dörmann, M. J. Harrison, *New Phytol.* **214**, 1631–1645 (2017).
17. A. Keymer *et al.*, *eLife* **6**, e29107 (2017).
18. V. Wewer, M. Brands, P. Dörmann, *Plant J.* **79**, 398–412 (2014).
19. M. Malar C *et al.*, *Curr. Biol.* **31**, 1570–1577.e4 (2021).
20. L. Xue *et al.*, *Plant Physiol.* **167**, 854–871 (2015).
21. Y. Jiang *et al.*, *Mol. Plant* **11**, 1344–1359 (2018).
22. L. Xue *et al.*, *Proc. Natl. Acad. Sci. U.S.A.* **115**, E9239–E9246 (2018).
23. A. To *et al.*, *Plant Cell* **24**, 5007–5023 (2012).
24. K. Hiratsu, K. Matsui, T. Koyama, M. Ohme-Takagi, *Plant J.* **34**, 733–739 (2003).
25. N. Fukuda, Y. Ikawa, T. Aoyagi, A. Kozaki, *Plant Mol. Biol.* **82**, 473–483 (2013).
26. J. L. Morris *et al.*, *Proc. Natl. Acad. Sci. U.S.A.* **115**, E2274–E2283 (2018).
27. F. Lutzoni *et al.*, *Nat. Commun.* **9**, 5451 (2018).
28. GenoToul Bioinformatics Facility, GenoToul Bioinfo (INRAE, 2018); https://doi.org/10.15454/1.5572369328961167E12.

ACKNOWLEDGMENTS

We thank T. Vernié and S. Schornack for fruitful discussions and comments on the manuscript and B. Miller for providing the Cas9 Level-0 construct. We are grateful to the GenoToul bioinformatics platform Toulouse Occitanie [Bioinfo GenoToul (*28*)] for providing computing resources and to the MetaToul-Lipidomique Core Facility (I2MC, Inserm 1048, Toulouse, France). **Funding:** This work was supported by the Bill and Melinda Gates Foundation; the UK Foreign, Commonwealth and Development Office as Engineering Nitrogen Symbiosis for Africa (OPP1172165) to G.E.D.O., P.-M.D., and T.O.; Agence Nationale de la Recherche (ANR) grant EVOLSYM (ANR-17-CE20-0006-01); Université Paul Sabatier ATP2016 grant to P.-M.D.; the MetaboHUB-ANR-11-INBS-0010 grant to J.B.-M.; the URPP Evolution in Action of the University of Zurich (P.S. and I.S.D.); funding from the Forschungskredit (University of Zurich; P.S. and I.S.D.); Swiss National Science Foundation grants 160004 and 131726 (P.S.); the EU's Horizon 2020 Research and Innovation Programme (PlantHUB-No. 722338; I.S.D., G.P., P.S., E.C., and D.U.); and the Georges and Antoine Claraz Foundation (G.P., I.S.D., and P.S.). This work was also supported by the German Research Foundation (DFG) under Germany's Excellence Strategy (CIBSS – EXC-2189 – Project ID 39093984). The TEM (funded by DFG grant INST 39/1153-1) is operated by the University of Freiburg, Faculty of Biology, as a partner unit within the Microscopy and Image Analysis Platform (MIAP) and the Life Imaging Center (LIC), Freiburg. This research was supported by the German Science Foundation grant BU-2250/12-1 (M.B.) and by the German Ministry of Education and Research (BMBF, project no. 031B0200 A to M.B.) within the frame of RECONSTRUCT. The Laboratoire de Recherche en Sciences Végétales (LRSV) and the Laboratory of Plant-Microbe Interactions (LIPM) belong to the TULIP Laboratoire d'Excellence (ANR-10-LABX-41). **Author contributions:** M.K.R., N.V., P.-M.D., P.S., E.C., D.D., J.Ke., J.Ky., C.L., G.E.D.O., J.B.-M., G.B., M.B., M.H., and L.X. designed the experiments. M.K.R., N.V., G.V.R., C.L., J.Ke., K.K., I.S.D., E.S., M.R.-F., A.L.R., P.L.F., A.B., M.H., L.X., G.P., and P.S. conducted the experiments. M.K.R., N.V., P.-M.D., C.L., J.Ke., T.O., J.B.-M., P.L.F., A.B., M.B., M.H., and L.X. analyzed the results. M.K.R., N.V., and P.-M.D. wrote the manuscript. All coauthors edited and commented on the initial draft. **Competing interests:** The authors declare no competing interests. **Data and materials availability:** Genome assembly, annotation file, and gene models are available through a genome browser at Marpal_GenomeBrowser and on NCBI (BioProject PRJNA362997). Raw Oxford Nanopore data were submitted under NCBI SRA accession SRR13188886. Raw RNA-seq data can be found under NCBI SRA accession numbers SRR13077953 to SRR13077969 corresponding to BioProject PRJNA362997 (*M. paleacea* genome). This Whole Genome Shotgun project has been deposited at DDBJ/ENA/GenBank under the accession MUAA00000000. The version described in this paper is version MUAA02000000. All other data are available in the main paper or the supplementary materials.

SUPPLEMENTARY MATERIALS

science.sciencemag.org/content/372/6544/864/suppl/DC1
Materials and Methods
Figs. S1 to S18
Tables S1 to S8
References (*29*–*77*)
MDAR Reproducibility Checklist

10 December 2020; accepted 26 March 2021
10.1126/science.abg0929

NATIONAL UNIVERSITY OF DEFENSE TECHNOLOGY

Discover Your FUTURE at National University of Defense Technology

Systems Science, Computer Science and Technology,
Software Engineering, Management Science and Engineering
Optical Engineering, Information and Communication Engineering,
Control Science and Engineering
Mechanical Engineering
.....

Join us and build your career with us.



Find out more at **www.nudt.edu.cn**

Email: rcfw@nudt.edu.cn Tel: +86-0731-8700-0655

OPPORTUNITIES IN CHINA

ScienceCareers online @sciencecareers.org

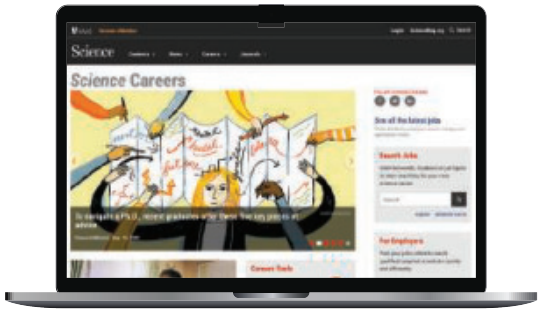
Science Careers online @sciencecareers.org



Science Careers helps you advance your career. Learn how!

- Register for a free online account on **ScienceCareers.org**.
- Search hundreds of job postings and find your perfect job.
- Sign up to receive e-mail alerts about job postings that match your criteria.
- Upload your resume into our database and connect with employers.
- Watch one of our many webinars on different career topics such as job searching, networking, and more.
- Download our career booklets, including Career Basics, Careers Beyond the Bench, and Developing Your Skills.
- Complete an interactive, personalized career plan at "my IDP."
- Visit our Employer Profiles to learn more about prospective employers.
- Read relevant career advice articles from our library of thousands.

Visit **ScienceCareers.org** today — all resources are free



SCIENCECAREERS.ORG

ScienceCareers
FROM THE JOURNAL SCIENCE AAAS



南昌大学
NANCHANG UNIVERSITY

Announcement of Nanchang University on Open Recruitment for Domestic and Foreign High-level Medical Talents

Jointly established by the Ministry of Education and Jiangxi Province, Nanchang University has been included into China's construction of first-class universities and disciplines of the world, the "Project 211", and Jiangxi provincial overall construction of high-level universities.

Nanchang University Medical Department has currently set up 14 schools (Basic Medical School, School of Public Health, School of Pharmacy, School of Nursing, Queen Mary School, Huankui School, No. 1 Clinical Medical School, No. 2 Clinical Medical School, No. 3 Clinical Medical School, No. 4 Clinical Medical School, School of Stomatology, School of Ophthalmology and Optometry, and People's Clinical Medical School), and 2 centers (Clinical Medical Experiment Teaching Center, and Animal Science Center). It has 5 directly affiliated hospitals, with 9 national key clinical departments.

Nanchang University Medical Department currently employs 311 full-time preclinical-phase medical teachers, including 89 with senior titles; and 1,172 clinical medical teachers, including 234 with senior titles. Among the talents of the University, there are 2 teachers included in the national overseas high-level talent introduction program, 1 teacher included into the national special support program for high-level talents, 1 winner of the "National Science Fund for Distinguished Young Scholars", 3 specially-appointed professors of the talent program of the Ministry of Education, 5 candidates shortlisted for the national "Millions of Talents Project", 1 candidate shortlisted for the "Program for New Century (Trans-Century) Excellent Talents in University" of the Ministry of Education, 5 specially-appointed professors with the title of "Jinggang Scholars" of Jiangxi Province.

In order to promote the construction of "Double First-class" disciplines, further enhance the level of scientific research and talent training, and focus on the goal of constructing a high-level university to vigorously bring in and gather high-level talents (especially national high-level innovative talents) in the fields of basic medicine, clinical medicine, public health and preventive medicine, pharmacy, biology and inter-disciplines, the University has carried out research and then decided to open-recruit domestic and foreign high-level medical talents. Experts and scholars at home and abroad are sincerely welcome to apply for jobs. The relevant matters are now announced as follows:

I. Recruiting positions

Position:

Positions for outstanding talents、Positions for disciplinary leading talents (concurrently serving as dean of the secondary school)、Positions for disciplinary guiding talents、Positions for disciplinary excellent talents.

Disciplines:

Cardiovascular and cerebrovascular diseases, digestive system diseases, malignant tumors, nervous system diseases, cytobiology, structural biology, neurobiology, biochemistry and molecular biology, physiology, epidemiology, health statistics, social medicine, occupational and environmental health, child and adolescent health, pharmacology, pharmaceutical chemistry, pharmacy, pharmaceutical analysis, biopharmaceuticals, genomics, bioinformatics, and rehabilitation medicine.

II. Contact information

Correspondence address:

HR Department of Nanchang University, 999 Xuefu Avenue, Nanchang, Jiangxi Province

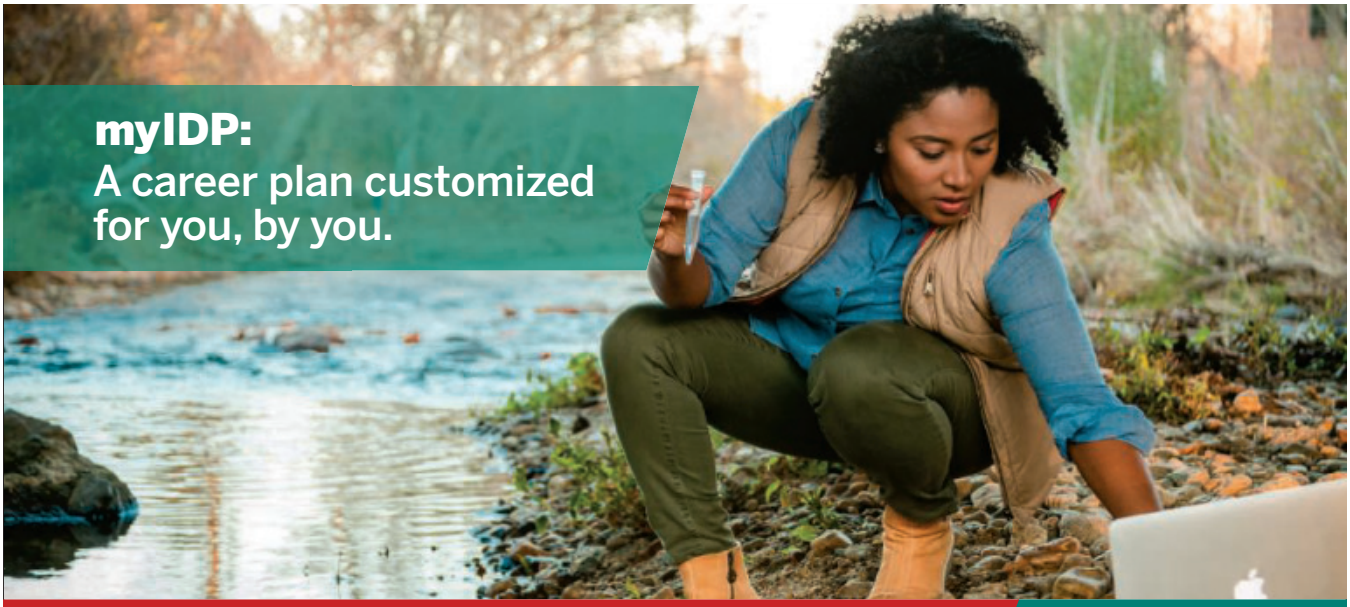
Postal code: 330031 Contact person: Mr. Yang

Tel: 0791-83969074 Fax: 0791-83968717

E-mail: rscrsk@ncu.edu.cn



Science Careers online @sciencecareers.org



For your career in science, there's only one Science

Features in myIDP include:

- Exercises to help you examine your skills, interests, and values.
- A list of 20 scientific career paths with a prediction of which ones best fit your skills and interests.
- A tool for setting strategic goals for the coming year, with optional reminders to keep you on track.
- Articles and resources to guide you through the process.
- Options to save materials online and print them for further review and discussion.
- Ability to select which portion of your IDP you wish to share with advisors, mentors, or others.
- A certificate of completion for users that finish myIDP.

myIDP

Visit the website and start planning today!
myIDP.sciencecareers.org

Science Careers AAAS In partnership with:

FASEB Federation of American Societies for Experimental Biology
UMASS University of Massachusetts Medical School
UCSF University of California San Francisco
UIC
BURROUGHS WELLCOME FUND

The National Academies of | SCIENCES ENGINEERING MEDICINE

POSTDOCTORAL RESEARCH FELLOWS

Air Force Science & Technology Fellowship Program

The National Academies of Sciences, Engineering, and Medicine administers **postdoctoral and senior fellowship awards** at the U.S. Air Force Research Laboratory (AFRL), the U.S. Air Force Institute of Technology (AFIT), and the U.S. Air Force Academy (USAFA) under the Air Force Science & Technology Fellowship Program (AF STFP).

We are seeking highly qualified candidates who are U.S. citizens and hold, or anticipate earning, a doctorate in a variety of fields of science or engineering.

Application deadline dates (four annual review cycles):

- February 1
- May 1
- August 1
- November 1

Awardees have the opportunity to:

- Conduct independent research in an area compatible with the interests of the Air Force laboratories
- Devote full-time effort to research and publication
- Access the excellent and often unique Air Force research facilities
- Collaborate with leading scientists and engineers

Awardee benefits:

- Base stipend starting at $76,542; may be higher based on experience
- Health insurance (including dental and vision), relocation benefits, and professional travel allowance

For detailed program information, to search for AFRL, AFIT, and USAFA Research Opportunities, and to contact prospective Research Adviser(s), visit **www.nas.edu/afstfp**.

The National Academies of | SCIENCES ENGINEERING MEDICINE

POSTDOCTORAL RESEARCH ASSOCIATES

NRC Research Associateship Programs

The National Academies of Sciences, Engineering, and Medicine administers **postdoctoral and senior research awards** at participating federal laboratories and affiliated institutions at locations throughout the U.S and abroad.

We are seeking highly qualified candidates who hold, or anticipate earning, a doctorate in a variety of fields of science or engineering. Degrees from foreign universities should be equivalent in training and research experience to a doctoral degree from a U.S. institution. Citizenship eligibility varies among the sponsoring laboratories.

Application deadline dates (four annual review cycles):

- February 1
- May 1
- August 1
- November 1

Awardees have the opportunity to:

- Conduct independent research in an area compatible with the interests of the sponsoring laboratory
- Devote full-time effort to research and publication
- Access the excellent and often unique facilities of the federal research enterprise
- Collaborate with leading scientists and engineers at the sponsoring laboratories

Awardee benefits include:

- Stipends ranging from $45,000 to $86,000; may be higher based on experience
- Health insurance (including dental and vision), relocation benefits, and a professional travel allowance

For detailed program information, to search Research Opportunities, and to contact prospective Research Adviser(s) visit **www.nas.edu/rap**.

YOU'D SMILE TOO IF YOU JUST ADVANCED YOUR CAREER.



Find your next job at ScienceCareers.org

There's scientific proof that when you're happy with what you do, you're better at what you do. Access career opportunities, see who's hiring and take advantage of our proprietary career-search tools. Get tailored job alerts, post your resume and manage your applications all in one place: sciencecareers.org

ScienceCareers

FROM THE JOURNAL SCIENCE AAAS

By **Ananya Sen**

The problem with 'follow your dream'

I walked into my adviser's office, overflowing with frustration and confusion about the advice I had received at a recent career development workshop. It reiterated what I had heard so many times before: I should follow my dream, and if I didn't yet know what that was, I should live with career uncertainty until I figured it out. But as an international student working in the United States, taking time to explore wasn't an option for me. After listening to me rant, my adviser calmly looked across his desk. He told me that instead of focusing on finding a dream job, I should think about what I am good at and what makes me happy at least 80% of the time. This advice surprised me at first, but it ended up being exactly what I needed to hear.

I had spent the previous 22 years following my childhood dream—becoming a professor of marine biology. However, in grad school I saw how applying for grants is a constant source of worry for many professors. I realized I did not want to be responsible for the salaries of my hypothetical lab members. About 4 years into the program, I decided I did not want to pursue a career in research after all.

I began to attend career panels, which all followed a worryingly similar template. I would walk into the room with other excited graduate students and collect my free cookies and coffee, confident that the panelists would have the magical answers I needed. Instead, they would talk—again—about following their dreams. The message: I just needed to find a new dream. It would mean taking time off from work to self-reflect and discover a new path. But I couldn't stay in the country without a visa. For most academic researchers, obtaining a university-sponsored visa is relatively straightforward. But outside of academia, it is infinitely more complex, requiring a company that has a job opening and is willing to foot the bill for a work visa. As well-meaning as the panelists were, they fell silent when I brought up this dilemma. I felt totally lost.

Finally, I went to my adviser for help. We hadn't talked much about my career plans over the years, but I felt I needed a new perspective from someone who knew me well. When he offered his advice, I was taken aback at first. What happened to "if you love what you do, you'll never work a day in your life"? My adviser assured me there is seldom such a job. Every job has its ugly bits. But as long as you're happy most of the time, you can struggle through the parts you don't like. He also said it was important to find a job I was good at, especially because my visa applications required me to make the case that I would benefit the country.



"I should think about what I am good at and what makes me happy at least 80% of the time."

I was relieved to finally have helpful, practical advice. But I discovered that finding overlap between what I like and what I'm good at was not easy. I love scuba diving, but the physical demands are a challenge for me. I'm good at teaching, as evidenced by my friends nagging me to teach them chemistry and microbiology during my high school and undergraduate years and getting rave reviews from my students when I was a teaching assistant, but I don't like repeating the same content every year. Through my teaching experience, however, I also learned that I love telling stories about science. Maybe science communication would offer the overlap I was looking for.

To test the waters, during my "spare time" in grad school I started a blog about the history of scientific discoveries. I found that I loved the freedom to choose what to write about, and I never encountered a challenge I didn't enjoy. As for whether I was any good at it, the signs were promising. My writing got noticed, eventually by people at my institution, and I was given opportunities to write press releases and stories for the university's news bureau. After 3 years of writing, I was offered a position as a science writer. It's nothing like my childhood dream. But I am happy—more than 80% of the time. ■

Ananya Sen is a science writer for the Carl R. Woese Institute for Genomic Biology at the University of Illinois, Urbana-Champaign.
Send your career story to SciCareerEditor@aaas.org.

ILLUSTRATION: ROBERT NEUBECKER

CALL FOR PAPERS

SPJ
SCIENCE PARTNER JOURNALS



Journal of Remote Sensing

The *Journal of Remote Sensing* is an online-only Open Access Science Partner Journal published in affiliation with **Aerospace Information Research Institute, Chinese Academy of Sciences (AIR-CAS)** and distributed by the **American Association for the Advancement of Science (AAAS)**. Like all partners participating in the Science Partner Journal program, the *Journal of Remote Sensing* is editorially independent from the *Science* family of journals and AIR-CAS is responsible for all content published in the journal. This journal covers multiple research areas that include theory, science, technology of remote sensing, and interdisciplinary research with earth science and information science. Particular topics of interest within the journal include radiative transfer modeling, biogeosciences remote sensing, remote sensing of energy, and more.

Submit your research to the *Journal of Remote Sensing* today!

Learn more at **spj.sciencemag.org/remotesensing**

The Science Partner Journal (SPJ) program was established by the American Association for the Advancement of Science (AAAS), the nonprofit publisher of the *Science* family of journals. The SPJ program features high-quality, online-only, Open Access publications produced in collaboration with international research institutions, foundations, funders and societies. Through these collaborations, AAAS furthers its mission to communicate science broadly and for the benefit of all people by providing top-tier international research organizations with the technology, visibility, and publishing expertise that AAAS is uniquely positioned to offer as the world's largest general science membership society.

Visit us at **spj.sciencemag.org**

@SPJournals **@SPJournals**

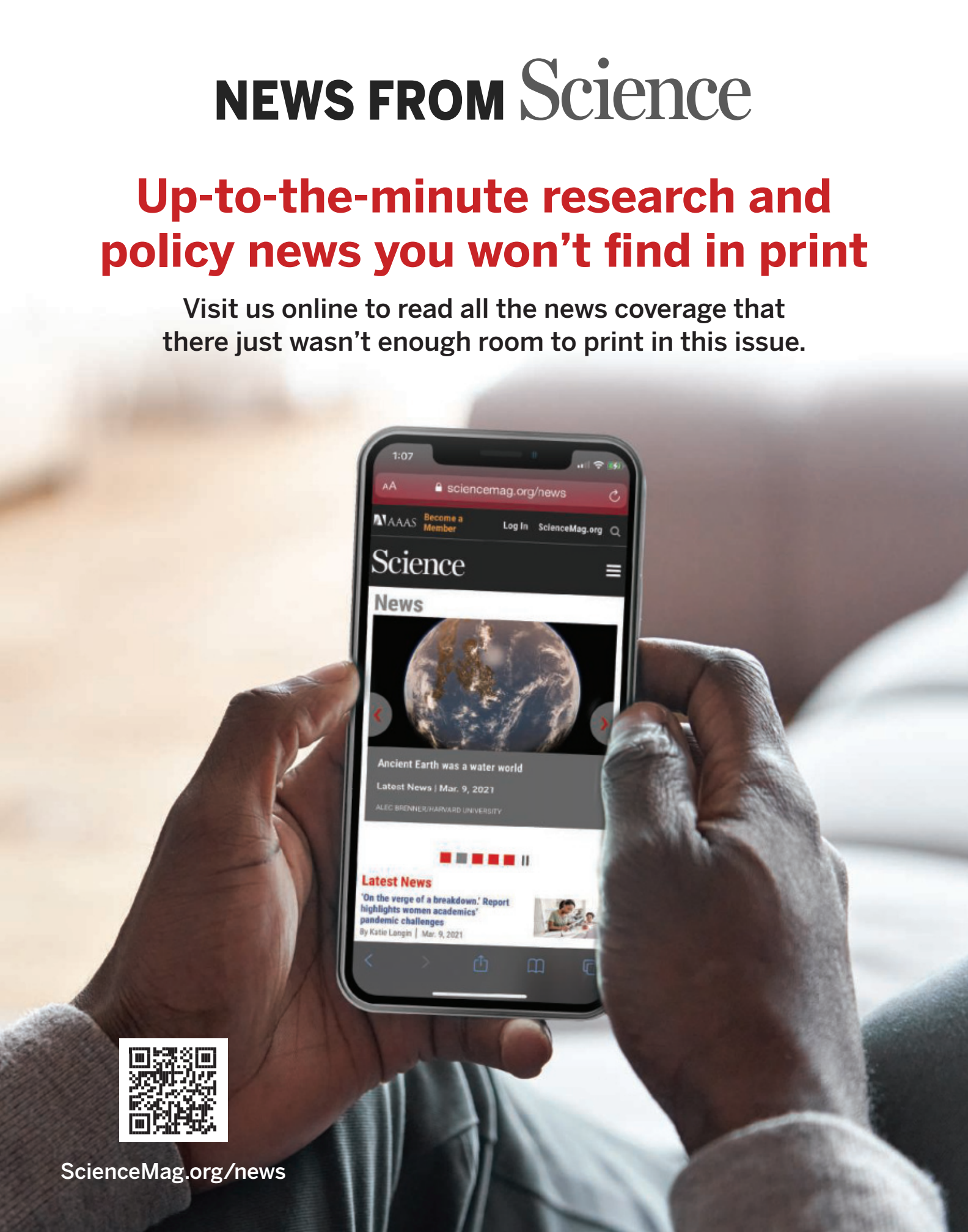
OPEN ACCESS

ARTICLE PROCESSING CHARGES WAIVED UNTIL JULY 2023

NEWS FROM Science

Up-to-the-minute research and policy news you won't find in print

Visit us online to read all the news coverage that there just wasn't enough room to print in this issue.



ScienceMag.org/news